An Experimental and Modelling Study of The Effect of Surface Roughness on Mass Transfer and Corrosion in CO_2 Saturated Oilfield Environments

Mohammed Ali Mohammed Jawad Al-Khateeb

Submitted in accordance with the requirements for the degree of
Doctor of Philosophy

The University of Leeds
School of Mechanical Engineering

Institute of Thermofluids

January 2019

Publication Statement

The candidate confirms that the work submitted is his own, except where work which has formed part of jointly-authored publications has been included. The contribution of the candidate and the other authors to this work has been explicitly indicated below. The candidate confirms that appropriate credit has been given within the thesis where reference has been made to the work of others.

In all papers listed below, the primary author completed all experimental studies, evaluation of data and preparation of publications. All authors contributed to proof reading of the articles prior to publication. Papers contributing to this thesis:

Al-Khateeb, M., Barker, R., Neville, A., & Thompson, H. M. (2018). The effect of surface roughness on diffusion and chemical reaction controlled limiting currents on a Rotating Cylinder Electrode in deaerated solutions with and without CO_2. *Corrosion*, *74*(9), 971-983.

Al-Khateeb, M., Barker, R., Neville, A., & Thompson, H. "An experimental and theoretical investigation of the influence of surface roughness on corrosion in CO_2 environments." *Journal of Corrosion Science and Engineering* 20 (2018).

Acknowledgements

First, I would like to thank the Almighty God for granting me the power and patience to accomplish this work. Without the will of Allah, nothing is possible.

I would like to express my deepest gratitude to my supervisors Prof. Harvey Thompson, Prof. Anne Neville and Dr. Richard Barker for their unlimited support throughout my PhD journey. I has been an honour of working with distinguished and knowledgeable supervisors like you. Special thanks to Harvey for always being available to discuss the project, fix my Python code and his invaluable advice and support when writing my thesis and papers and to Anne for her invaluable advice and guidance and to Rick for his invaluable daily advice and support in the lab.

I would like to thank my sponsor the Higher Committee for Education Development (HCED) for their continuous support and funding through the PhD.

I am truly grateful to the iFS technicians that supported my research work: Jordan, Mick, Paul and Andrew. Thanks a lot guys.

A big thanks go to all my family, Mum (Mrs. Nada Alkhassaki), Dad (Dr. Ali Alkhateeb), and my brothers Hassan and Jaffer for their unlimited support. My dear parents, I hope that I have achieved what you have dreamed of and compensated a small part of your endless efforts to raise me. Without your love, kindness, prayers and inspiration I would not have been able to accomplish this. Special thanks go to my aunties Shatha and Dalal for believing in me and accepting to be my guarantors.

A massive thank you to my lovely wife (Afnan Alsaeed), thanks for your love and patience and for withstanding my moody temper. Thanks for being so supportive during my PhD.

My princess Aya, the most valuable gift I have gotten in my life. You are the most beautiful gift that I have received during my PhD journey. Thanks a lot for always smiling. Your smile has given me further motivation and hope.

Finally, I would also like to thank my colleagues and friends at the school of mechanical engineering for their help and support and in particular Ben, Josh, Giuseppe, Amir, Rehan, Olujide, Andy, Ogbemi, Wassim and Sikiru.

Abstract

In the oil and gas industry, internal corrosion of carbon steel is commonly encountered during production and transportation of hydrocarbons and water saturated with corrosive gases such as CO_2 and H_2S, with CO_2 corrosion (termed sweet corrosion) the most common one.

This thesis presents an experimental and modelling approach to study the effect of surface roughness on the mass transfer and corrosion of carbon steel.

The influence of surface roughness on mass transfer on a rotating cylinder electrode apparatus is investigated experimentally. Mass transfer from four different samples, with roughness values of 0.5, 6, 20 and 34 μm, is measured using the limiting current technique for a range of rotational speeds in NaCl solutions saturated with N_2 at pH=3 and 4. A new correlation for Sherwood number as a function of the Reynolds number, Schmidt number and surface roughness is proposed. Complementary experiments in CO_2 environments were used to assess the combined limiting current associated with H^+ and H_2CO_3 reduction. In the CO_2 environments considered, surface roughness is found to have no significant influence on the limiting current contribution from H_2CO_3, which can therefore be determined from Vetter's correlation.

Novel surface pH measurement methods are also developed to measure surface pH. These were implemented to study the surface pH during CO_2 corrosion. Comparisons between mesh capped probes and iridium oxide probes showed that the results in both cases were very similar.

Two mechanistic models were implemented to predict corrosion rates in the CO_2 environments. The models were validated against the experimental results from both the literature and the current study. The first, multi-node model is used to predict the concentration of species within the boundary layer. While, the second, two-node model was used to explore the effect of roughness in the CO_2 environment. Agreement between experimental and theoretical corrosion rates was good and demonstrated clearly how increased surface roughness accentuates corrosion rates and mass transfer coefficients, and that the latter need to be accounted when implementing theoretical models.

Table of Contents

List of Tables

List of Figures

List of Units, Chemicals, Symbols and Abbreviations

Units

A	ampere
Bar	x10^5 Pascal
˚C	degrees Celsius
cm	centimetre
g	grams
Hz	Hertz
J/mol	Joule per mole
K	Kelvin
kg/m^3	Kilogram per cubic metre
kV	Kilovolts
m/s	Metres per second
mA/cm^2	milliamp per centimetre squared
mm/year	millimetre per year
Molar	Mole per litre
Pa	Pascal
rpm	Revolutions per minute
s	Seconds
V	Volt
wt.%	Weight percent
μm	micrometre

Chemicals

Ag/AgCl	Silver/Sliver chloride
Au, Au^{3+}	Gold, Gold ion
CE	Calomel Electrode

CO_2, CO_3^{2-}	Carbon dioxide, carbonate ions
Cu	Copper
Cr, Cr^{3+}	Chromium, Chromium ion
e^-	Electron
Fe, Fe^{2+}	Iron, Iron ion
$FeCO_3$	Iron carbonate
H^+	Hydrogen ion
HCl	Hydrochloric acid
HCO_3^-, H_2CO_3	Bicarbonates, carbonic acid
H_2SO_4	Sulfuric acid
H_2O	Water
IrO_2	Iridium oxide
Mo	Molybdenum
NaCl	Sodium chloride
$NaHCO_3$	Sodium bicarbonate
Ni, Ni^{2+}	Nickel, Nickel ion
N_2	Nitrogen
OH^-	Hydroxide
O_2	Oxygen
Pt	Platinum
Ti	Titanium
Zn, Zn^{2+}	Zinc, Zinc ion

Symbols and Abbreviations

AR	Attack Ratio
a_1,a_2	Reaction constants

B	Stern-Geary coefficient
$c_{bulk,j}$	Bulk concentration of species j (mol/m^3)
$C_{b,H2CO3}$	Bulk concentration of carbonic acid (mol/m^3)
C_j	Concentration of species j (mol/m^3)
$c_{surface,j}$	Surface concentration of species j (mol/m^3)
CRAS	Corrosion Resistance Alloys
CV	Cyclic voltammetry
d	Diameter of the rotating cylinder electrode (m)
$\overline{d}$	Diameter of the pipe (m)
d^+	Friction length
DC	Direct Current
D_{H2CO3}	Diffusion coefficient of carbonic acid (m^2/s)
D_j	Molecular diffusion coefficient (m^2/s)
e	Average distance from peak to valley (µm)
E	Potential difference (Volts)
EDL	Electrical Double Layer
EIS	Electrochemical Impedance Spectroscopy
EOR	Enhanced Oil Recovery
E°	Potential difference at standard conditions (Volts)
E_{anodic}	Potential of the cathodic reaction (Volts)
$E_{applied}$	External power source (Volts)
$E_{cathodic}$	Potential of the anodic reaction (Volts)
E_{cell}	Cell potential (Volts)
E_{corr}	Free corrosion potential (Volts)
F	Faraday’s constant (Coulombs/mole)

UFHWA	US Federal Highway Administration
FILC	Flow-Induced Localised Corrosion
f_c	Rotating cylinder electrode friction factor
f_p	Pipe friction factor
GDP	Gross Domestic Product
GNP	Gross National Product
HSE	Health and Safety and the Environment
IHP	Inner Helmholtz Plane
IMPACT	International Measures of Prevention, Application and Economics of Corrosion Technology
i_{lim}	Limiting current (A/m^2)
$i_{lim\ H2CO3}$	Limiting current of carbonic acid (A/m^2)
i_0	Current density (A/m^2)
i_{corr}	Corrosion current density (A/m^2)
K_{corr}	Corrosion constant
K_m	Mass transfer coefficient (m/s)
L	Length of the transfer surface (m)
LPR	Linear Polarisation Resistance
n	number of the electrons exchanged
NACE	National Association of Corrosion Engineers
NIST	National Institute of Science and Technology
OCP	Open Circuit Potential
OHP	Outer Helmholtz Plane
OPEC	Organization of the Petroleum Exporting Countries
pH	potential Hydrogen
PHMSA	Pipeline and Hazardous Materials Safety Administration

ppm	Parts per million
p_{CO2}	Partial pressure of carbon dioxide (Bar)
p_{total}	Total pressure in system (Bar)
Q	Total electric charge passed through the substance
R	Ideal gas constant (J/ mol.K)
RCE	Rotating cylinder electrode
R_{ct}	Resistance Charge Transfer (Ohm.cm^2)
R_j	Rate of reaction of species j
R_s	Solution Resistance (Ohm.cm^2)
R_p	Polarisation Resistance (Ohm.cm^2)
Re	Reynolds number
$\mathrm{Re}_{\mathrm{crit}}$	Critical Reynolds number
SHE	Standard Hydrogen Potential
Sc	Schmidt number
Sh	Sherwood number
St	Stanton number
ST	Scaling Tendency
T	Absolute temperature (°C)
TCFC	Thin Flow Channel Cell
V	Velocity of flow (m/s)
Z	Ratio of the alternating potential to the alternating current
z_j	electrical charge of species j
α	Charge transfer coefficient
ΔG	Gibbs free energy change (kJ/mol)
ΔG°	Gibbs free energy change at standard conditions (kJ/mol)
β_a	Anodic Tafel constant

β_c	Cathodic Tafel constant
δ	Thickness of the boundary layer (m)
f_{CO2}	CO_2 fugacity (Bar)
ρ	Density (Kg/m^3)
μ	Viscosity (Kg/m.s)
$\emptyset$	Electric potential
τ	Shear stress (Pa)
ζ	ratio of the diffusion layer to the reaction layer

Chapter 1 Introduction

1.1 Background of Corrosion in Petroleum Industry

The significant growth in the global economy has led to an increase in energy consumption. The energy demand keeps increasing worldwide, and in 2017 the global energy demands rose by 2.1%, twice the rate of growth in 2016 [2]. The boosted consumption in global energy was mainly met by oil and natural gas. Oil and gas are estimated to provide 70% of the energy resources needed to cover the increase in energy demand [2]. The global oil consumption has increased from 85.3 million barrels per day in (2006) to 97.8 million barrels per day in (2017). As shown in Figure **1-1**, in the last ten years, the percentage annual growth in oil demand is estimated at 0.7% [3].

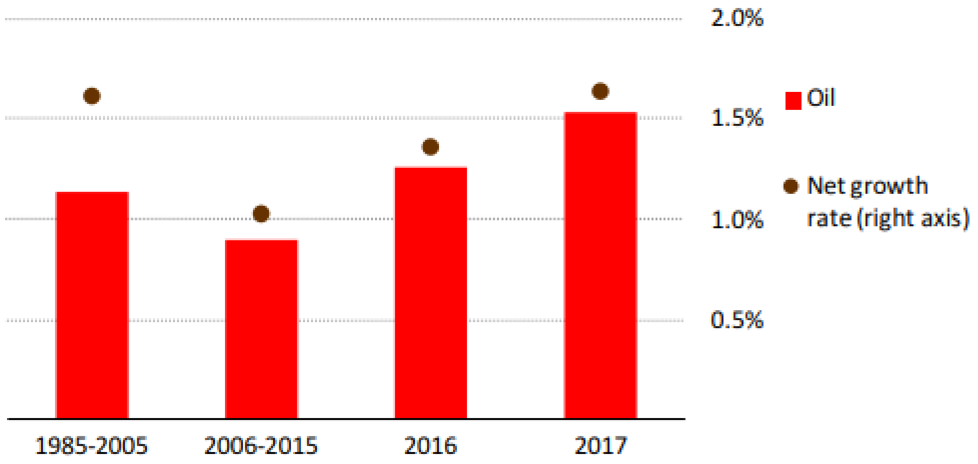

Figure 1-1 Average growth in oil demand [3].

The relatively slow development of renewable energy and high demands of energy makes a surge in supply for petroleum products inevitable [2]. Thus, hydrocarbons remain the primary source of energy globally. The Organization of the Petroleum Exporting Countries (OPEC) is expecting an increase in oil demand as a result of the expansion in the petrochemical sectors in the U.S. and China. Therefore, sustaining petroleum production is vital to cover the global energy demand [4].

The petroleum industry is one of the most essential and complex global industries. This industry is divided into two parts; the first part is called upstream referring to the drilling and production of oil and gas and the second part is called downstream referring to the transportation, refining and marketing of oil and gas [5]. In the petroleum production and transportation, a key challenge is ensuring process safety and compliance to government environmental regulations [6].

Oil is pumped out of the ground and the produced oil is transported from the oil wells to refineries and from refineries to the consumers mainly through long pipelines. Sometimes these pipelines are in several kilometres long. For example, oil and natural gas are transported in 0.4 to 1.2 meter diameter pipes through distances of 10-20 kilometres downstream for post-processing [7]. Thus, a country such as Russia has hundreds pipelines of kilometres long to transport hydrocarbons from very remote locations to consumers [8].

The ultimate goal of the hydrocarbons industry is to maintain and maximise the production and reduce risks through improving process safety. There are many challenges relating to asset integrity control and cost-effective operational performance. Corrosion is one of the major problems. Among 50 various major oil and gas failures between 1977 and 2007, corrosion-related failures represent more than one-third of these failures [9]. In a more up to date study, in 2015, the Pipeline and Hazardous Materials Safety Administration (PHMSA) has surveyed the causes of pipelines failures in the USA including natural force damage (i.e., Hurricane Katrina). The study has revealed that despite the use of advanced technologies, corrosion is still one of the main causes of the failures in pipelines. The corrosion-related failures (as shown in Figure **1-2**) are estimated to be 18.2% of the total pipes incidents [10]. The study also showed that the majority of the failures relating to corrosion arise as a result of inadequate predictive capabilities, poor resistance of the material and lack of control to the various forms of attack. Thus, a stringent corrosion management strategy is important not only to reduce cost but also to prevent safety and environmental implications [10].

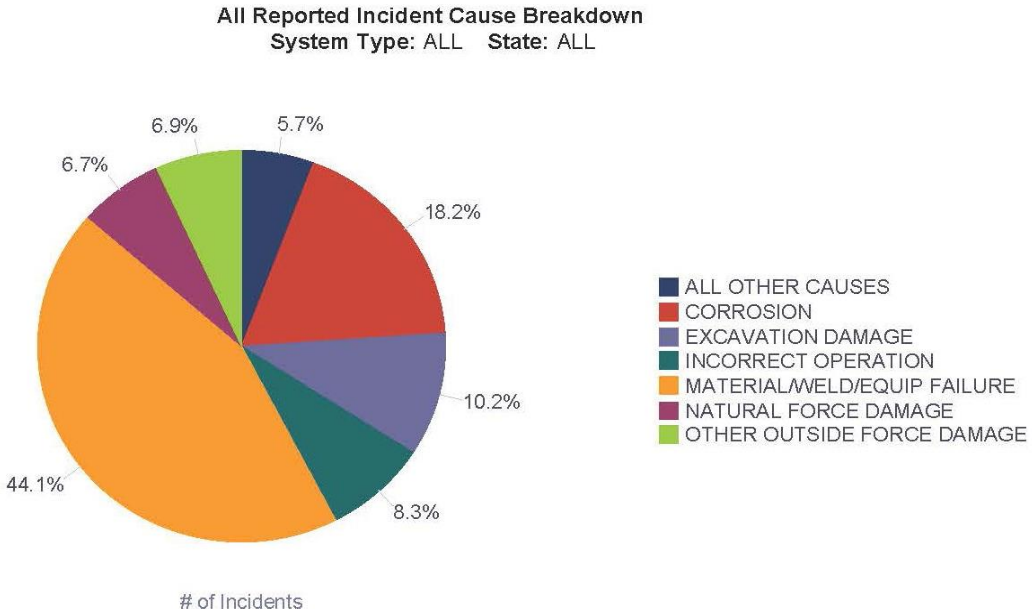

Figure 1-2 Types of failures in pipelines in the USA [10].

Corrosion has direct and indirect effects on our daily lives. These impacts vary from economic to health and safety [6]. The direct impact is due to the costs to repair the damaged parts and expenses associated with stopping production to maintain and fix the corroded pipe.

Corrosion is still one of the major obstacles in the operation of hydrocarbon production and management is considered necessary for the cost-effective design of the facilities [11]. However, quantifying the cost of corrosion is no easy task. In 1975, the National Institute of Science and Technology (NIST) found that the cost of corrosion in the U.S.A was about $70 billion which represented 4.2% of the Gross National Product (GNP). Furthermore, this report suggested that these expenses were able to be avoided by applying new technologies and best practices [12, 13]. In 2002, the US Federal Highway Administration (FHWA) published a two-year study on expenditures related to metallic corrosion in nearly every U.S. sector [14]. The results of this study (as shown in Figure **1-3**) revealed that the total estimated direct expenditures of corrosion in the U.S. amounted to 3.1% of Gross Domestic Product (GDP). As a part of this research, the losses in production and manufacturing were reviewed and found to cost around $17.6 billion where those in the oil and gas industry represents 10% of this value [14].

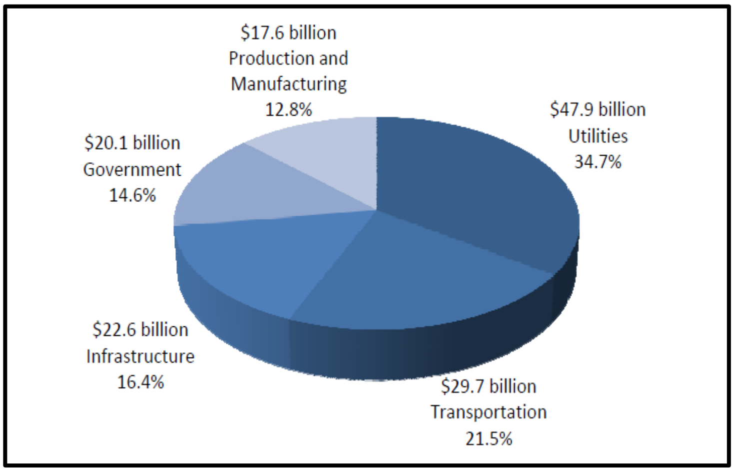

Figure 1-3 Percentage and dollar contribution to the total cost of corrosion for the five U.S. economic sectors [14].

Nevertheless, in 2016, the National Association of Corrosion Engineers (NACE) released the study "International Measures of Prevention, Application and Economics of Corrosion Technology (IMPACT). The study estimated the global corrosion cost $2.5 trillion which approximately equal to 2.4% of the global Gross Domestic Product (GDP). The (IMPACT) study emphasised that oil and gas corrosion remains at the top of the corrosion expenditures. Also, the study forecasted that the use of new corrosion control practices could save between 15-35% of the total global corrosion cost.

1.2 Health, Safety and Environmental Impact

The indirect impact of corrosion is related to the environmental and health implications. Oil may spill outside the pipelines and cause pollution to the environment close to the pipes [15].

Of even higher importance is Health and Safety and the Environment (HSE). Since the 1980’s, there has been an increase in the environmental awareness of using chemicals. Nowadays the use of the chemicals is an essential requirement for the successful operation of oil and gas fields, therefore increasing the risk of liquid and gas leaks. These chemicals might be toxic and contaminate the surrounding environments. As a result of this risk, governments have resorted to stronger legislation [6]. For example, in 2006 as a result of a corrosion failure in the pipeline in Prudhoe Bay, Alaska, BP suffered a loss estimated as $100 million to replace 16 miles of corroded pipes. Furthermore, the government fined the company \$320 million due to the risk of endangering the safety of the public and the environment [16]. The impact of this corrosion incident was costly both economically and reputationally not only for the oil and gas industry but also for the public and environment. This highlights the importance of managing corrosion effectively and efficiently. Therefore, the governments enforce rigorous regulations to ensure the safety of the environment and the population where these pipes run [6, 16].

1.3 Types of Oil and Gas Corrosion

Pipelines are exposed to corrosion on a daily basis. At the source of petroleum production, when companies pump crude oil out of the ground, a mixture of water, CO_2, sulphur and solid particles also pump with the oil. The exposure of these chemicals with the internal surface of pipes is the cause of corrosion. Corrosion deteriorates the basic useful properties of materials such as strength and permeability to liquid and gas. The nature and the degree of damage mainly depend on the concentration of and particular combinations of these various chemicals and the operating conditions within the pipe [11, 17].

Researchers have identified seven different corrosive environments that can be found in the petroleum industry. The environmental parameters which mainly control this types of corrosion are partial pressure, fluid temperature, flow, salinity and pH [18].

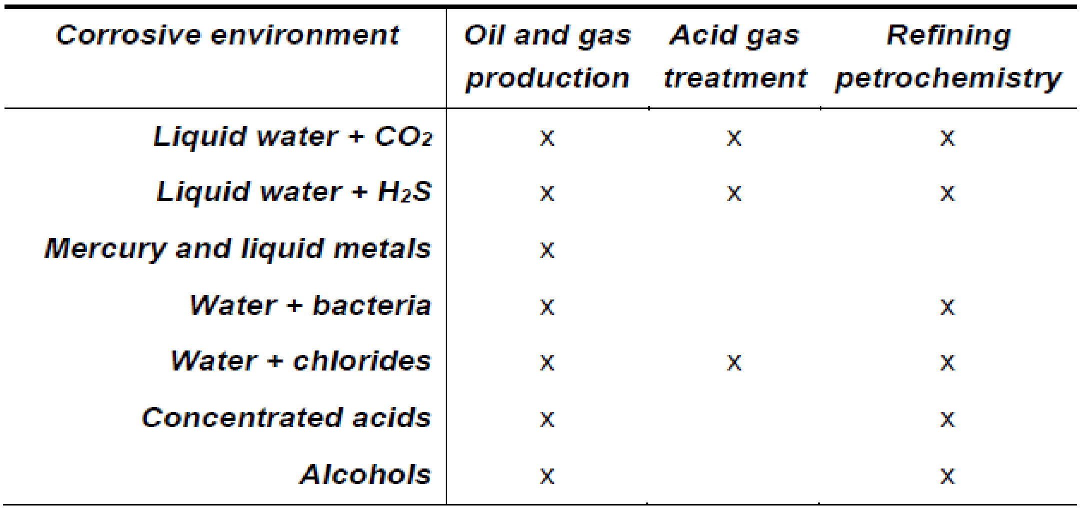

Corrosive environment	*Oil and gas production*	*Acid gas treatment*	*Refining petrochemistry*
Liquid water + CO_2	x	x	x
Liquid water + H_2S	x	x	x
Mercury and liquid metals	x		
Water + bacteria	x		x
Water + chlorides	x	x	x
Concentrated acids	x		x
Alcohols	x		x

Table 1-1 List of oil field corrosive environments during oil and gas production [18].

Table **1-1** displays seven of these types of corrosion which occur in the petroleum industry. These seven types of corrosion are most common when CO_2, H_2S and various microorganisms are the dominant fluid phase [18].

Also, corrosion can be categorised according to the attack mechanism. Various corrosion modes such as preferential weld, galvanic, pitting, crevice, intergranular and stress corrosion can be found in the oil fields. Furthermore, erosion-corrosion and bacterial corrosion can also occur when sand and biofilms are present respectively. The corrosion can initiate on both outside surfaces (external corrosion) and inside surfaces (internal corrosion). However, internal corrosion is the focus of this research.

Types of Corrosion Failure	Frequency (%)
CO_2 related	28
H_2S related	18
Preferential Weld	18
Pitting	12
Erosion-corrosion	9
Galvanic	6
Crevice	3
Impingement	3
Stress corrosion	3

Table 1-2 Causes of corrosion-related failures in the oil and gas industry [6].

Kermani et al. [6] studied corrosion failures in oil fields. Their results presented in Table **1-2** show that CO_2 corrosion is one the most common type of corrosion. CO_2 corrosion was estimated to be 28% of the total corrosion failures in the oil and gas industry. CO_2 remains an essential constituent of the petroleum production fluid, directly connected to the most predominant type of corrosive degradation in the petroleum industry.

CO_2 corrosion or sweet corrosion is not a recent problem and was first documented in the USA in 1940s [6]. As a consequence, the mechanism of CO_2

corrosion has been studied by many researchers. Although CO_2 occurs naturally, the level of the dissolved gas with the produced fluids can increase through using the new techniques such as Enhanced Oil Recovery (EOR) by injecting CO_2 (as shown in Figure1-4) [6].

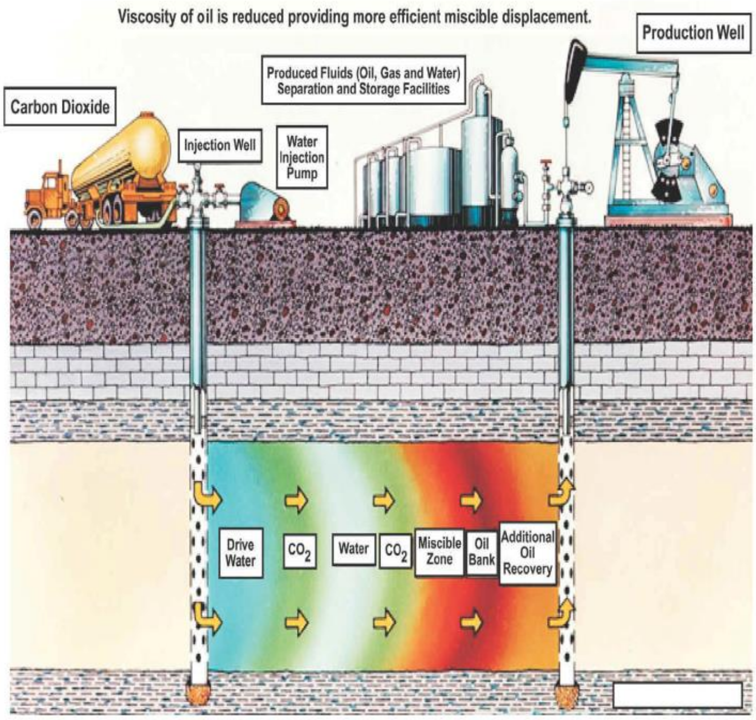

Figure 1-4 CO_2 injection as an enhanced oil recovery technique [19].

Despite the importance and extensive research into the overall CO_2 corrosion mechanism, there are still a number of questions that remain unanswered. Thus, the influence of CO_2 on oil field corrosion will be reviewed in the next section.

1.4 Influence of Carbon Dioxide in the Petroleum Industry

Carbon dioxide has been considered one of the major problems in the petroleum industry. Carbon dioxide is non-corrosive in the gas phase. However, once CO_2 dissolves in water, it hydrates to form carbonic acid which is corrosive to the inner walls of pipeline steel.

Despite the development of Corrosion Resistant Alloys (CRAS) to resist corrosion, carbon steel is still the most common metal used in the oil and gas production. Carbon steel has been used as a pipework material due to its mechanical properties, ease of fabrication and low cost. However, its low corrosion resistance has led to corrosion being widely studied to ensure the operational integrity of facilities and equipment [20].

At the design stage, corrosion mitigation must be taken into consideration. Corrosion management is a part of capital expenditures of a project to judge the feasibility of using carbon steel for the operational field environment. Also, to judge the amount and type of inhibitor need to be used or if coating needs to be applied [21, 22].

Corrosion can be controlled through studying the operational conditions such as flow rate, concentration of different corrosive species, partial pressure, temperature, pH and mechanical forces. Corrosion rate is usually estimated using flow assurance software. The software computes the maximum allowance for corrosion rate in mm/year. Furthermore, the predicted corrosion rate in mm/year multiplied by the desired lifetime which should remain above a certain thickness in years of service. These steps are called modelling of corrosion [21, 22].

Models have been developed to control and estimate the corrosion rates of carbon steel. Accurate prediction of the corrosion rate can help engineers in the design of pipelines and their related infrastructure. Although these models have been widely used, their application is still limited to specific conditions in which models are built and tested which mean unexpected failures in some cases [6, 20]. In recent years, advances in mechanistic models of CO_2 corrosion have provided more robust calculations to predict the corrosion rates through including various working conditions and processes during carbon dioxide corrosion.

The mechanistic models divide corrosion of carbon steel in CO_2 environments into three parts. The first part is the chemical reactions in bulk, the second part is the mass transfer of species from the bulk to the surface, and the third part is the electrochemical reactions at the surface [23]. These three mechanistic components have been studied extensively over the past 35 years. The mechanistic models have been used to predict uniform CO_2 corrosion. Good agreement was achieved between these models and the experimental results in labs [24-27]. The experiments which were used to validate the mechanistic models were performed by immersing smooth carbon steel samples in a solution saturated with carbon dioxide and testing them in different working conditions [24-27].

The mechanistic models predict the corrosion rates through calculating the concentration of species in bulk, mass transfer between the bulk and the surface and concentration of the species at the surface. Most of the models were focused on specific aspects such the effect of water chemistry on the corrosion rates, the effect of working conditions such as flow velocity, temperature and partial pressure on the corrosion rates and the effect of protective layers on the corrosion rates [24-27].

Corrosion by carbon dioxide is highly controlled by mass transfer. Parameters such as flow velocity and temperature that affect the transfer and control the corrosion rates are well studied. Researchers have suggested correlations to calculate the mass transfer for different test set-ups such as the Eisenberg et al. [28] correlation to predict mass transfer for RCE and the Berger and Hau [29] correlation to predict mass transfer for pipes. However, many researchers demonstrated that the mass transfer is significantly affected by the surface roughness. The increase in surface roughness will generally increase the mass transfer [30, 31].

Also, CO_2 corrosion is an electrochemical process. This means hydrogen ions are consumed at the surface. Thus, surface pH differs from that of the bulk. Surface pH is recognised as a key parameter that influences the electrochemical reactions at the surface. Quantifying surface pH could help to improve the understanding of heterogeneous reactions at the surface that control the corrosion rates. The mechanistic models have been used to estimate the surface pH [32, 33].

The next section will describe the objectives of the project which will address outstanding research questions in the field

1.5 Research Objectives

Despite the extensive research studies into the mechanism of CO_2 corrosion, there are key questions which are of interest for both researchers and industry.

CO_2 corrosion has been measured by immersing smooth samples in a solution, what will happen when the surface roughness increases? Will this affect the mass transfer coefficient? Will the corrosion rate increase or decrease? Models have been used to predict surface pH and the corrosion rates in CO_2 corrosion, how accurate are these models? Can these models predict the surface pH? Can these models predict the corrosion rate for samples with different surface roughness?

As the surface pH differs from the bulk, how much does the surface pH differ from the bulk? Can the surface pH be measured experimentally? In this light, the overall objectives of this research are defined:

- To understand the effect of surface roughness in CO_2 environments on both mass transfer and corrosion rate.
- To develop a new mass transfer correlation to predict mass transfer for surfaces with different roughness.
- To develop a new novel experimental method to measure the near surface pH in CO_2 environments and compare different methods to measure the surface pH.
- To assess the validity of the existing CO_2 corrosion models highlighting their limitations and applicability.
- To predict the corrosion rates for samples with different roughness and working conditions.

1.6 Thesis Outline

This work contributes to the literature by providing an experimental and modelling approach to study the effect of surface roughness on the mass transfer and corrosion rates of carbon steel in CO_2 environments. Also, surface pH measurement methods are implemented to study the surface pH during CO_2 corrosion. There are seven chapters in this thesis, including the current one.

Chapter 2 includes the fundamentals of corrosion and the review of previous studies in the literature related to corrosion of carbon steel in a CO_2 environment which includes mechanism of CO_2 corrosion, modelling the process of corrosion and the experimental studies to measure the surface pH. **Chapter 3** covers in details the experimental protocol. This chapter describes the experimental methods and techniques used in this work to investigate the effect of surface roughness on mass transfer and corrosion rates. Also, it reveals the preparation procedure of the iridium oxide probes which includes the preparation of the iridium oxide solution, the electrodeposition method and the equipment and test conditions. **Chapter 4** provides the experimental results of the smooth surfaces. This results chapter includes the validation of the mass transfer results in N_2 environments against the correlation from the literature, corrosion rate measurements under dynamic conditions and the surface pH measurements of both mesh capped probes and iridium oxide probes. **Chapter 5** focuses on the obtained experimental results aiming to understand how the surface roughness affects the mass transfer coefficients in both N_2 and CO_2 environments. This chapter presents the results of the surface profilometry of the samples used in this study to characterise the roughness of each sample. It also provides new insights into the effect of surface roughness on both of the mass transfer components in the CO_2 environments which are H^+ and H_2CO_3. **Chapter 6** describes the modelling work where a numerical model developed to predict corrosion rates for both smooth and rough surfaces in CO_2 environments is detailed. Discussions and conclusions are provided at the end of chapters 4, 5 and 6. However, **Chapter 7** provides a summary of the findings, conclusions and possible future directions of research.

Chapter 2 Fundamentals of Corrosion and Literature Review

2.1 Fundamentals of Corrosion

The integrity of the oil and gas equipment and operation is of paramount importance during production and transportation. As mentioned earlier, corrosion is the most common cause of failures in the petroleum industry [1]. Corrosion is the destructive attack of a metal, a chemical effect, in particular, the metal dissolves/degrades over time due to surface electrochemical and chemical reactions brought about by the aqueous environment [13]. Corrosion is generally defined as the deterioration of a metal caused by its environment. Most aqueous environments can cause corrosion. Some known types of corrosion are electrochemical corrosion caused by current flow and electron transfer, cracking caused by stress, fretting caused by wear and cavitation caused by erosion. CO_2 corrosion which is studied in detail within this project is one of the electrochemical corrosion processes [34]. This means corrosion does not occur by direct chemical reaction of a metal with its environment but rather through coupled electrochemical reactions [1]. The process of electrochemical corrosion consists of four essential components (as shown in Figure **2-1**). If any of these components is absent corrosion will not occur. These components are classified as follows:

- The anode: is the corroding metal which usually corrodes by the loss of electrons from electronically neutral metal atoms to form ions. These ions either stay in the solution or react to form insoluble corrosion product [35].

  The corrosion reaction of metal M which is known as anodic reaction can be expressed by the equation:

  $$\mathbf{M} \rightarrow \mathbf{M^{n+}} + \mathbf{ne^{-}} \qquad (2\text{-}1)$$

  Where n is the number of the electrons (e^-) released by the metal. The produced electrons do not flow into the solution. They remain at the surface of the corroding metal and flow through the electronic conductor to the cathode [20, 35].

- The cathode: usually does not corrode, it is a part of the same metal surface or another metal surface which is in contact with it. The cathode consumes the electrons which are produced by the anode. This can be achieved by the reducible species in the electrolyte that reach the metal surface and remove the electrons [20, 35, 36].

- The electrolyte is the name of the aqueous environment which must conduct electricity. The electrolyte is in contact with the anode and the cathode to provide a path for ionic conduction [20, 35].
- The electrical connection between the anode and the cathode allows the electrons to flow through in the corrosion cell [35].

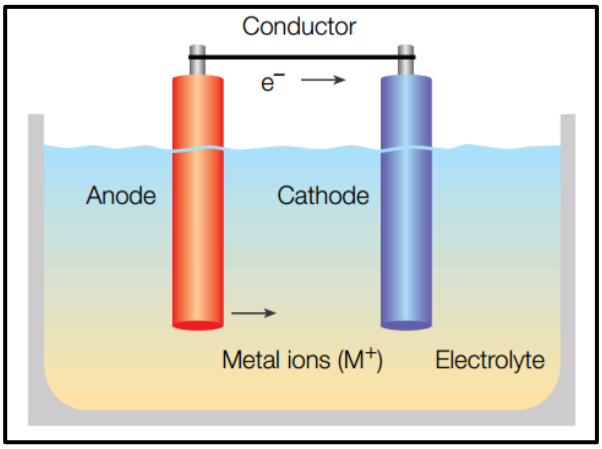

Figure 2-1 The basic four components in a corrosion cell [37].

Sometimes these components vary slightly, in other words, at a corroding metal, anode and cathode represent different places at the same metal surface. For example, when an iron surface immerses in an acidic aqueous environment (as shown in Figure **2-2**), the iron (Fe) tends to dissolve so iron passes into the solution as iron ions (Fe^{2+}) (similar to equation (2-2)). The two electrons produced by the anode flow away from the anode region to a site where they form the cathode to reduce two hydrogen ions to one H_2 molecule (equation (2-3)).

$$\mathbf{Fe \rightarrow Fe^{2+} + 2e^{-}} \tag{2-2}$$

$$\mathbf{2\,H^{+} + 2e^{-} \rightarrow H_2} \tag{2-3}$$

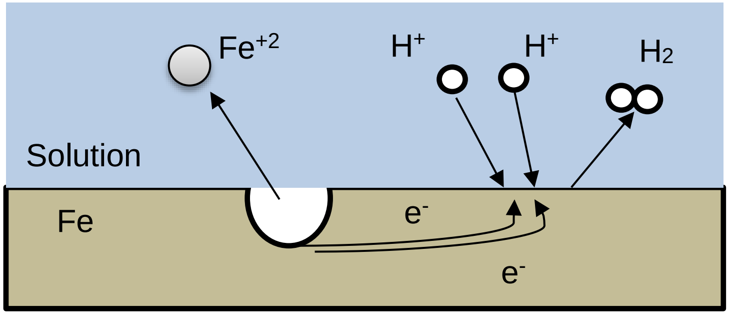

Figure 2-2 Coupled electrochemical reactions which are occurring at the same surface of iron in an acid solution [1].

The fact that both electrochemical reactions (anodic and cathodic reactions) can propagate at the same surface can be attributed to the heterogeneous nature of a metal surface. The difference between the free energy of each reaction is quantifiable as electrical potential and current flow [38]. The metal can be considered as an array of ions with the valence electrons of each atom having transferred to the crystal lattice as a whole. These electrons account for electrical conductivity of the metal and other electronic properties [20].

2.2 Corrosion Thermodynamics of Aqueous Reactions

Metals usually exist in metal ores thus most metals are unstable and always try to lower their energy by reacting to form a solution or compound with higher thermodynamical stability [20, 35]. The driving force in corrosion is the Gibbs free energy, which provides a quantitative measurement of the tendency of the reaction in a given direction. Furthermore, the change in free energy of the metal and the aqueous environment is brought about by corrosion. The change in Gibbs free energy represents the difference between Gibbs energies of the final and initial stages of the reaction process which is independent of the different intermediate stages. The change in Gibbs free energy (ΔG) can be used to assess the spontaneity of the reaction. Thus, ΔG must be negative if the reaction is spontaneous [20, 34].

When metals are immersed in the aqueous solution, the developed potential is called the free corrosion potential. Faraday presented the equation that relates the potential difference and the change in Gibbs free energy of the corrosion process [20]:

$$\mathbf{\Delta G = (-n\ F)E.} \tag{2-4}$$

Where ΔG is the change in the free energy for the corrosion reaction (kJ/mol), n is the number of the electrons exchanged in the corrosion reaction, F is the Faraday's constant which equals 96485 (Coulombs/mole) and E is the potential difference at non-standard conditions (Volts).

At standard condition (temperature 25°C and pressure of 1 atm), the standard redox potential $\mathring{E}$ replaces E.

$$\mathbf{\Delta \mathring{G} = (-n\ F)\mathring{E}.} \tag{2-5}$$

Values of $\mathring{E}$ are available for all metals and are listed in electrochemical series. Examples of the half-cell potentials are provided in Table **2-1**. Metals with negative potential corrode readily and tend to be anodes. While metals with a positive potential such as gold tends to be a noble metal.

Electrode	**Standard Electrode Potentials $\mathring{E}$ (V) (SHE)**
$Au^{3+} + 3e^- \rightarrow Au$	+1.50
$Fe^{3+} + e^- \rightarrow Fe^{2+}$	+0.771
$2H^+ + 2e^- \rightarrow H_2$	0.000 (by definition)
$Ni^{2+} + 2e^- \rightarrow Ni$	-0.250
$Fe^{2+} + 2e^- \rightarrow Fe$	-0.440
$Cr^{3+} + 3e^- \rightarrow Cr$	-0.740
$Zn^{2+} + 2e^- \rightarrow Zn$	-0.763

Table 2-1 Standard electrode reduction potentials versus a standard hydrogen potential (SHE) [38].

The change in Gibbs Free energy depends on temperature. Additionally, half-cell potential changes with the concentrations of the ions present in the reaction. The relation between ΔG and the concentrations at a given temperature can be written as:

$$\mathbf{\Delta G = \Delta \mathring{G} - R\ T \ln \frac{[Products]}{[Reactants]}.} \tag{2-6}$$

Where R is the ideal gas constant (8.314 J/mol K), T is the absolute temperature Kelvin (K), [Products] and [Reactants] are the concentrations of the products and the reactants simultaneously (Molar).

The current tends to flow in the direction that will decrease the concentration difference and the metal exposed to the low concentration will behave as an anode and corrode [39].

By substituting equation (2-4) and equation (2-5) with equation (2-7) the new equation is called the Nernst equation. The Nernst equation was first published in 1888 by the German chemist Nernst who won later the Nobel prize in chemistry [40]. The equation is used to find the potential of metals in a solution; the equation can be written:

$$\mathbf{E} = \mathbf{E}^{\circ} - \frac{\mathbf{R\ T}}{\mathbf{n\ F}}\ \mathbf{ln}\ \frac{[\mathbf{Products}]}{[\mathbf{Reactants}]}. \tag{2-7}$$

To get the potentials of a cell consisting of the cathodic and the anodic reactions, electrode potentials can be combined mathematically. For galvanic cells which operate spontaneously the voltage will be positive if it is calculated as follows:

$$\mathbf{E_{cell}} = \mathbf{E_{cathodic}} - \mathbf{E_{anodic}}. \tag{2-8}$$

Where $\mathbf{E_{cell}}$ is the cell potential (Volts), $\mathbf{E_{cathodic}}$ is the reduction potential of the cathodic reaction (Volts) and $\mathbf{E_{anodic}}$ is the anodic potential of the anodic reaction (Volts). In the case of corrosion, which is a spontaneous reaction, the cell potential should be positive because corrosion must result in a reduction in Gibbs energy, therefore ΔG must be negative [39].

2.3 Electrical Double Layer (EDL)

The significance of studying the electrical double layer (EDL) is to understand the nature of the metal-electrolyte interface. When a metal is immersed in an aqueous solution local cathodic and anodic regions will generate at the interface.

As previously discussed, when a metal corrodes, ions leave their lattice leaving behind their electrons. After that, water molecules surround the metal ions that left their lattice and hydrate them. The hydrated ions are then free to diffuse away from the metal. The surface of the metal becomes negatively charged due to excess electrons and tends to attract some positive ions. This means that a certain amount of ions remain near the surface instead of diffusing away to the electrolyte. The water layer around the ions acts as a barrier to prevent them from contacting the excess surface electrons and subsequently being reduced to the metal surface. Positive ions already in the electrolyte are also attracted to the negatively charged surface [41].

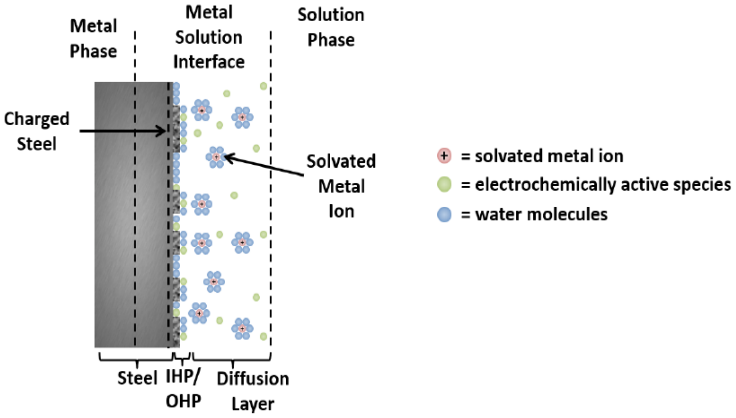

Figure 2-3 Schematic of the electrical double layer (EDL) at the metal-electrolyte interface [41].

Figure **2-3** shows a simple schematic of the electrical double layer (EDL) at the metal-electrolyte interface. The electrolyte layer adjacent to an electrode surface contains water molecules and ions from both the metal and bulk electrolyte providing it with a different chemical composition than the bulk solution. This layer of specifically absorbed ions forms with the inner Helmholtz plane (IHP) balancing the associated electron charge at the surface. A layer of solvated ions, which are free to diffuse into the bulk solution forms the adjacent region known as the Outer Helmholtz Plane (OHP). The negatively charged surface and the adjacent electrolyte layer are collectively referred to the electrical double layer (EDL) [42].

EDL (as shown in Figure **2-4**) acts as a capacitor due to its oppositely charged properties. On the other hand, the metal also resists the excess electrons from transferring to the active ions which allow the EDL to act as a resistor [42].

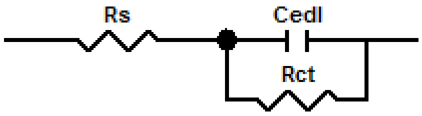

Figure 2-4 Simple equivalent circuit of the electrical double layer. C_{edl} is the double layer capacitance, R_{ct} is the resistance to charge across the edl and R_s is the resistance of the solution [42].

The electrical double layer is the origin of the potential difference across the interface and accordingly of the electrode potential. Changes of the metal (electrode potential) can produce changes in anodic and cathodic reactions. Any change should pass through the EDL as the metal ions should pass through the EDL towards the solution and the solution ions should cross the EDL towards the metal. Thus, the EDL controls the process of corrosion [42].

2.4 Corrosion Kinetics

The rate of corrosion is usually defined as a penetration rate in millimetres per year. The corrosion rate is proportional to the rate of electron transfer. The term current density has been used to describe the current flow where the surface area of the corroding metal is considered. The corrosion can be quantified via various techniques such as: weight loss, change in thickness or commonly implemented electrochemical techniques. Both mixed potential theory and the Butler-Volmer equation (which will be discussed later) are used to explain polarisation curves which describe the basic kinetic law for any electrochemical reaction [43].

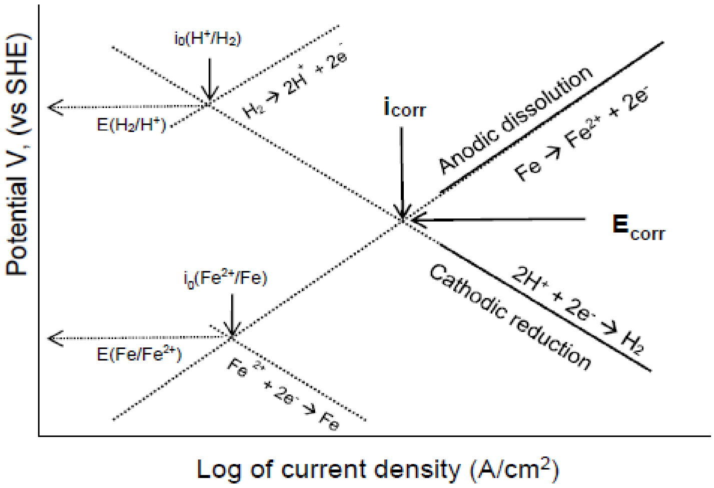

Figure 2-5 Schematic of Evans plot for iron immersed in a deaerated acid [44].

The Evans' diagram (as shown in Figure **2-5**) is a graphical representation of the polarisation curves for the anodic and cathodic reactions and their relationship with corrosion potential and current. Evans' diagram is also known as mixed potential plot or polarisation plot. The diagram reveals metal corrosion as a reaction of two electrodes working simultaneously and defines the shape of both anodic and cathodic polarisation curves [45]. The diagram demonstrates that most of the factors affecting the corrosion rate can be explained from the superposition of the potential and current curves. It is worth noting that the current densities and reaction kinetics shapes/gradients for cathodic reactions can be different when exchange currents are modified. Many environmental factors affect the corrosion rates such as temperature, flow, pressure..etc [46]. Figure **2-5** shows the Evans' diagram of corrosion of iron in the acid solution where the anodic reaction is the dissolution of iron while the cathodic reaction is the reduction of the hydrogen ions. The current flowing in a single electrode at E_0 is known as the exchange current density i_0. The intersection of both corrosion potentials (cathodic and anodic) is known as the corrosion potential of the system E_{corr} and the measured current is called corrosion current I_{corr} [45].

As discussed earlier in previous sections, any change in metal potential should pass across the EDL. Thus, the value of E_{corr} changes with the change in the composition of EDL. The measured potential depends on the concentrations of metal ions and electrochemically active species in the EDL. When the bulk solution changes, this will alter the EDL composition, hence, E_{corr} will be changed [41].

The Nernst equation (2-7) relates the EDL to the electrical potential. However, this equation only expresses the tendency of a metal to corrode. Thus, the Nernst equation cannot be used to predict the rate at which a metal corrodes. Thus, the Butler-Volmer equation can be used instead to calculate the corrosion rate.

The Butler-Volmer equation (equation (2-9)) draws a theoretical model of the current and overvoltage reaction.

$$\mathbf{i_o} = \mathbf{i_{corr}} \left[\mathbf{e}^{\left(\frac{(1-\alpha)\, \mathrm{n\, F\, (E-E_{corr})}}{\mathrm{R\, T}}\right)} - \mathbf{e}^{\left(\frac{-\alpha\, \mathrm{n\, F\, (E-E_{corr})}}{\mathrm{R\, T}}\right)} \right]. \tag{2-9}$$

where E_{corr} is the free corrosion potential (Volts), i_o is the external current (Amps/cm^2) flowing to or from the electrode because of an applied potential, i_{corr} is the corrosion current density (Amps/cm^2) that occurs when the electrode is at E_{corr}, E is the applied potential (Volts), α is a coefficient ranging from 0 to 1 and R, T, n and F have been defined previously. The first term in the Butler-Volmer equation describes the forward, anodic reaction while the second term describes the backward, cathodic reaction [41, 47].

In the case of equilibrium, the anodic current is equal to the cathodic current (Equation (2-10)). However, when a potential is applied, it will disturb the system equilibrium, and the rate of anodic reactions will no longer equal the rate of cathodic reactions. The difference between the new applied potential (E) and the equilibrium potential (E_{eq}) is called polarisation or over potential and the net current equation will be either cathodic controlled ($i_{cathodic}$) or anodic controlled (i_{anodic}) (equations (2-11) and (2-12)) depending on the applied voltage charge.

$$\mathbf{i_o = i_{anodic} = i_{cathodic}}. \qquad (2\text{-}10)$$

$$\mathbf{i_o = i_{anodic} - i_{cathodic}}. \qquad (2\text{-}11)$$

$$\mathbf{i_o = i_{cathodic} - i_{anodic}}. \qquad (2\text{-}12)$$

where

$$\mathbf{i_{cathodic} = i_{corr}\left[e^{\left(\frac{(1-\alpha)\, n\, F\, (E-E_{corr})}{R\, T}\right)}\right]}. \qquad (2\text{-}13)$$

$$\mathbf{i_{anodic} = i_{corr}\left[e^{\left(\frac{-\alpha\, n\, F\, (E-E_{corr})}{R\, T}\right)}\right]}. \qquad (2\text{-}14)$$

2.5 Electrochemical Methods to Monitor Corrosion

Corrosion of metals in an aqueous solution is an electrochemical process which involves the exchange of electrons. As a result, studying this phenomenon using electrochemistry measurements is the preferred methodology. The use of electrochemical methods could describe the reaction of reactive species on a metal surface due to electrochemical reactions. Also, these methods express the effect of different factors on the corrosion rates.

Different techniques were used to record electrochemical responses in this study such as: Linear Polarisation Resistance (LPR), Tafel Polarisation and Electrochemical Impedance Spectroscopy (EIS).

2.5.1 Three Electrode Cell

In this study, as in most previous electrochemical studies, a ‘three-electrode cell setup’ is used similar to the one shown in Figure **2-6**. The configuration comprises of: a working electrode (metal which corrodes), a counter electrode is usually an inert electrode with a current carrying function to study the working electrode and a reference electrode, which has a reproducible interfacial potential to measure against the working electrode. Nowadays, both the reference electrode and the counter electrode are combined in a single redox electrode readily available such as silver-silver chloride or saturated calomel electrode. The potentiostat allows to measure the voltage between the working electrode and the reference electrode using a voltmeter and the flow of current between the counter electrode and the working electrode using an ammeter. This setup tends to minimise the current that passes through the reference electrode while the counter electrode allows the application of the desired current or potential through the working electrode [41].

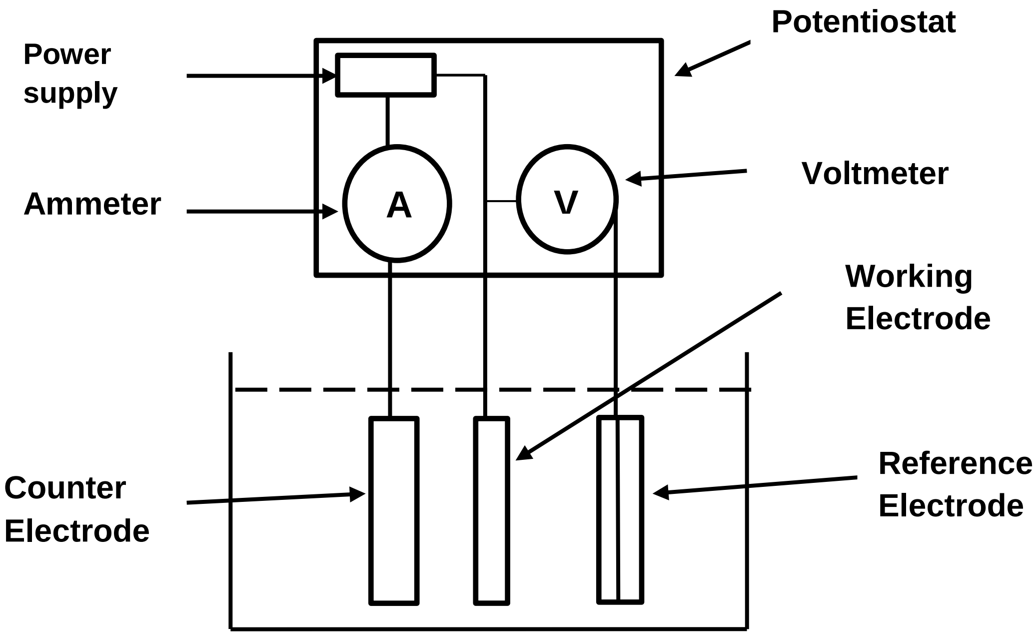

Figure 2-6 Schematic diagram of a three electrode cell set up.

2.5.2 Direct Current- Linear Polarisation Resistance (LPR)

Many studies have detected the linear relationship between applied voltage and current within a few millivolts of corrosion potential (E_{corr}). Stern and Geary provided an approximation to the charge transfer controlled reaction using the Butler-Volmer equation. When a small potential of ±5-20 mV is applied with respect to E_{corr}, the Butler-Volmer equation can be linearised mathematically using the McLaurin series expansion of e^X [48]. Thus, the new simplified equation can be written in the following form:

$$\mathbf{R_p} = \left[\frac{\Delta \mathbf{E}}{\Delta \mathbf{i}}\right]_{(\mathbf{E}-\mathbf{E_{corr}})\rightarrow 0} = \frac{\mathbf{1}}{\mathbf{2.303\ i_{corr}}}\left[\frac{\boldsymbol{\beta}_\mathbf{a}\,\boldsymbol{\beta}_\mathbf{c}}{\boldsymbol{\beta}_\mathbf{a}+\boldsymbol{\beta}_\mathbf{c}}\right]. \qquad (2\text{-}15)$$

Rearranging this equation gives:

$$\mathbf{i_{corr}} = \frac{\mathbf{1}}{\mathbf{2.303\ R_p}}\left[\frac{\boldsymbol{\beta}_\mathbf{a}\,\boldsymbol{\beta}_\mathbf{c}}{\boldsymbol{\beta}_\mathbf{a}+\boldsymbol{\beta}_\mathbf{c}}\right] = \frac{\mathbf{B}}{\mathbf{R_p}}. \qquad (2\text{-}16)$$

where R_p is the polarisation resistance (Ohm·cm^2) calculated by the gradient of the polarisation plot at small overpotentials (dE/di) for a plot of E vs I. R_p is equal to the charge-transfer resistance. The B factor is dominated by the smaller of the two anodic and cathodic Tafel slopes (β_a and β_c) if unequal.

This approach allows carrying non-destructive low overvoltage laboratory studies of reactions with the assumption that activation control is the dominant process. The main advantage of this technique is the use of small voltage amplitudes which allows for testing repeatedly without affecting the evolution of corrosion rate because metal surfaces change when high potential is applied to the cell [48].

2.5.3 Direct Current – Tafel Plots

Although the linear polarisation technique is useful to measure the corrosion rate for long-term without having to replace the electrodes, it is also sometimes necessary to know more about corrosion than just the rate. Tafel plots give more information than the LPR. They use a wide DC potential around 200 to 500 mV.

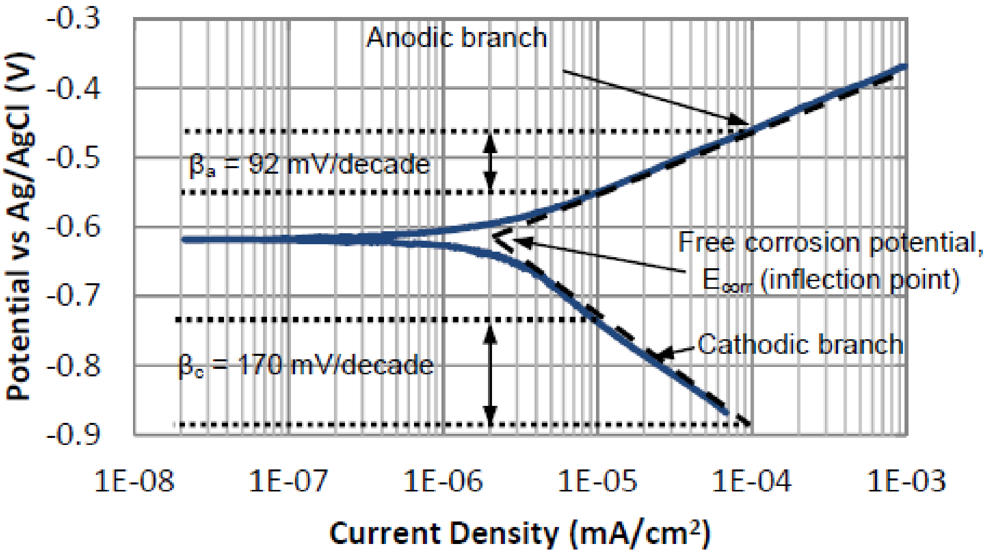

Figure 2-7 Tafel plot for activation controlled corrosion rates, indicating how to determine Tafel slopes [17].

As shown in Figure **2-7**, Tafel plots display the results of currents versus different potentials on a logarithmic scale. Polarisation plot structures can vary in that they can be activation controlled (controlled by the reaction rate) or diffusion controlled (controlled by the rate of diffusion of species to and from the surface).

Determining the Tafel slopes can give the corrosion rate of the metal. Tafel slopes have units of mV/decade (the decade is associated with the current) and this can easily be found by determining the gradient of the anodic and cathodic slopes from the linear parts of the E-log(i) plot, as shown in Figure **2-7**.

When this information is used in conjunction with linear polarisation data and the Stern-Geary equation, the value of corrosion rate can be calculated [49]. Otherwise, the corrosion current density, i_{corr}, can be read directly from a Tafel plot and the rate of corrosion of a metal can be determined using Faraday's Law. Faraday stated that the mass of a substance altered at an electrode during electrolysis is directly proportional to the quantity of electricity transferred at that electrode. Faraday also stated that for a given quantity of electric charge, the mass loss of an elemental material altered at an electrode is directly proportional to the element's equivalent weight [49]. This law can be summarised using the following equation:

$$\mathbf{m} = \frac{\mathbf{Q\,M}}{\mathbf{n\,F}}. \tag{2-17}$$

where m is the mass of the substance liberated at an electrode in (g), Q is the total electric charge passed through the substance in (Coulombs) and M is the molar mass (g/mol).

Similarly:

$$\mathbf{Corrosion\ Rate\ (moles\ /m^2\ s)} = \frac{\mathbf{i_{corr}}}{\mathbf{n\,F}}. \tag{2-18}$$

Applying conversion factors, the corrosion rate can be expressed in (mm/year)

$$\mathbf{Corrosion\ Rate\ (mm\ /year)} = \frac{\mathbf{K_{corr}\ M\ i_{corr}}}{\mathbf{n\ \rho}}. \tag{2-19}$$

where K_{corr} is a corrosion constant =3.27 $\times 10^{-3}$ (mm.g/μA/cm/year)and ρ is the metal density in (g/cm^3).

It is important to note that Tafel plots cannot be used to measure localised corrosion [41].

2.5.4 Electrochemical Impedance Spectroscopy (EIS)

Electrochemical impedance spectroscopy or EIS is one of the most common AC techniques. The method is conducted over a range of low magnitude AC polarisation voltages. The amplitude typically ranges from 5 to 20 millivolts and are usually centred around OCP. Frequencies of the applied voltages range from 100 kilohertz to several millihertz. The relations applicable in EIS are shown in equations (2-20) and (2-21) where Z is defined as the ratio of the alternating potential to the alternating current. The voltage depends on the frequency and time, while the current depends on the phase angle.

$$\mathbf{E = I.Z.} \tag{2-20}$$

$$\mathbf{Z} = \frac{\mathbf{\Delta E}}{\mathbf{\Delta I}} \tag{2-21}$$

EIS method has three types of graphs: complex plane plots, Bode magnitude and Bode phase plots. Complex plane plots or Nyquist plots are used in this study to measure the solution resistance. The Nyquist plot shown in Figure **2-8** reveals the data extracted from EIS tests run with AC sinusoidal waveform with frequency range from 10 kHz to 10 mHz. The plot shows the imaginary part of the impedance (Z’) on the Y-axis and the real part of the impedance (Z’’) on the X-axis. The unit should be in Ohms. However, the values shown here have incorporated the surface area of the corroded sample. On this plot, the high frequencies are on the left, while the low frequencies are on the right. The solution resistance (R_S) was taken from the Nyquist plot by determining the first value of Z’ when Z’’ = 0.

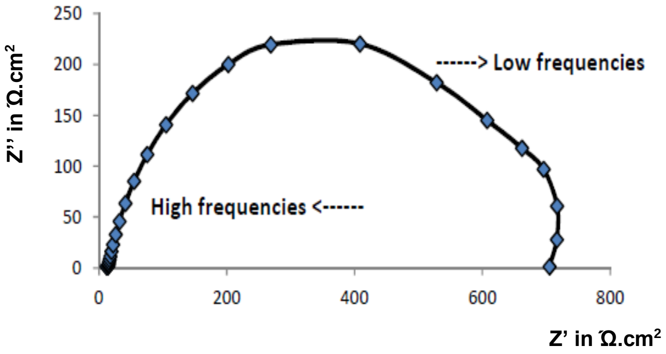

Figure 2-8 Nyquist plot for carbon steel in a CO_2 environment after 15 hours, pH 6.8, 50°C [50].

CO_2 Corrosion

Depending on the gas which is abundantly present in the liquid phase, three types of aqueous corrosion are described in the literature. CO_2 corrosion or ‘’sweet corrosion’’ starts when carbon dioxide dissolves in water, H_2S corrosion or “sour corrosion” initiates when hydrogen sulphide is present while oxygen corrosion can be found during water injection [51].

In the oil and gas industry, hydrocarbons are transported through long connected pipes where a high concentration of dissolved gases such as CO_2 and H_2S and a significant amount of water are common. Thus, providing the environment for corrosion to initiate. Usually, both CO_2 and H_2S can be found together. However, when the H_2S partial pressure is less than 0.3 kPa, the oil well is considered to suffer from carbon dioxide corrosion according to the material standard published by National Association of Corrosion Engineers (NACE) entitled “NACE MR0175 / ISO 15156” [52].

CO_2 corrosion is considered a major problem in the oil and gas industry. CO_2 is non corrosive as a dry gas but it becomes corrosive when it dissolves in water [11, 53]. To adequately assess its impact, it is essential to understand the mechanism of CO_2 corrosion and the factors that affect the corrosion rate. This part reveals the mechanism of CO_2 corrosion and highlights the critical parameters affecting CO_2 corrosion behaviour.

2.6 CO_2 Corrosion Mechanisms

CO_2 corrosion is a complicated process. Various mechanisms have been proposed. According to Dugstad et al. [54] the "CO_2 corrosion" terminology and the effect of CO_2 is not solely related to one mechanism. It contains a number of chemical reactions, electrochemical reactions and transport of species between the bulk and the surface [11, 54].

2.6.1 Bulk Chemical Reactions

In general, oil and gas contain significant percentages of carbon dioxide and water. CO_2 is inert and non-corrosive in the gas phase. When CO_2 dissolves in water a series of chemical reactions occur. Carbonic acid (H_2CO_3) is formed. Carbonic acid is a diprotic weak acid which dissociates to form different species according to the following reactions [54].

$$\mathbf{CO_{2\,(gas)} \rightarrow CO_{2\,(aq)}} \tag{2-22}$$

$$\mathbf{CO_{2\,(aq)} + H_2O \leftrightarrow H_2CO_{3\,(aq)}} \tag{2-23}$$

$$\mathbf{H_2CO_{3\,(aq)} \leftrightarrow H^+{}_{(aq)} + HCO_3^-{}_{(aq)}} \tag{2-24}$$

$$\mathbf{HCO_3^-{}_{(aq)} \leftrightarrow H^+{}_{(aq)} + CO_3^{2-}{}_{(aq)}} \tag{2-25}$$

$$\mathbf{H_2O_{(l)} \leftrightarrow H^+{}_{(aq)} + OH^-{}_{(aq)}} \tag{2-26}$$

2.6.2 Electrochemical Reactions

Corrosion is an electrochemical process involving the transfer of electrons at metal surfaces. In CO_2 corrosion, there are two essential reactions at the surface of the metal which are the cathodic and anodic reactions.

2.6.2.1 Cathodic reactions

A large number of papers have discussed and debated the cathodic reactions at the metal surface in the presence of CO_2. Nesic et al. [26, 55] summarised the cathodic reactions and referred to three main cathodic reactions.

- **The Hydrogen Evolution Reaction**

$$\mathbf{2H^{+} + 2e^{-} \rightarrow H_2} \qquad (2\text{-}27)$$

In a strong acid, the rate of hydrogen evolution occurs according to the equation (2-27) and cannot exceed the rate of hydrogen ions transported from the bulk solution to the surface [54]. The same equation can be used to explain the hydrogen evolution reaction in CO_2 corrosion. This reaction is strongly dependent on the pH value of the system. The reaction depends on the protons (H^+) transport from bulk to surface which makes it flow dependent [56]. When the pH<4 the dominant reaction is the cathodic reaction of H^+ due to the high concentration of hydrogen ions. While at intermediate pH value (4<pH<6) the limiting mass transfer current of hydrogen ions is lower due to its low concentration.

- **Cathodic reaction of carbonic acid**

Carbonic acid is a weak acid which dissociates as a function of temperature and pH of the solution. Carbonic acid increases the cathodic reaction at the steel surface. Therefore, the corrosion rate will increase. The mechanism of reduction of carbonic acid is still being studied [54]. When the carbonic acid directly reduces at the metal surface the process is called ‘direct reduction’. DeWaard and Milliams [57] proposed the following explanation. They assumed that the rate determining step is the release of hydrogen from carbonic acid similar to equation (2-28). Also, they suggested that the adsorbed bicarbonate would then combine with hydrogen ions to reproduce carbonic acid.

$$\mathbf{2\,H_2CO_3 + 2e^{-} \rightarrow H_2 + 2\,HCO_3^{-}} \qquad (2\text{-}28)$$

While the other mechanism is called the ‘buffering effect’ where the hydrogen evolution reaction is the dominant cathodic reaction. The term “buffer” refers to the assumption that the carbonic acid acts as a “reservoir” of hydrogen ions and is able to supply extra protons when they get consumed by the reduction reaction at the metal surface [58].

The buffering effect and direct reduction processes are similar from the thermodynamic viewpoint. The difference between them is the pathway. If the reaction is the direct reduction of carbonic acid, this means the increase in CO_2 partial pressure will steadily increase the corrosion rate, and this process is called charge transfer controlled [59]. On the other hand at constant pH, the increase in partial pressure of specified value of CO_2 will not increase the corrosion rate this process is called limiting current control.

Figure **2-9** reveals the difference between both pathways [59].

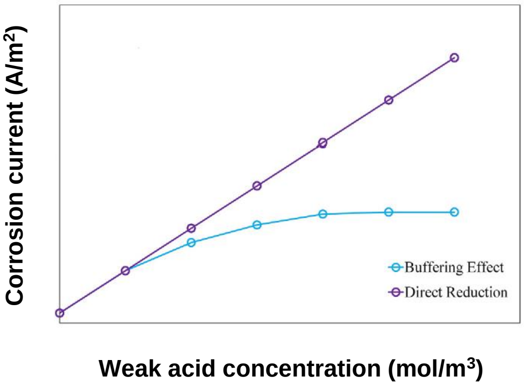

Figure 2-9 Illustration of the corrosion current behaviour for the different cathodic reaction mechanisms [59].

It is challenging to distinguish between the buffering effect and the direct reduction due to the difficulties of resolving the issue of charge transfer of the reduction of hydrogen ions. In this region, the hydrogen reduction curve overlaps with the region where the dominant reaction is the anodic dissolution of iron which cannot be easily characterised [59].

- **Direct reduction of water**

Some researchers have assumed that there is water reduction at corroding surfaces especially at pH>5. George and Nesic [60] have assumed that water is reduced on the electrode, releasing hydroxide ions into the solution. The process of direct reduction of water at the surface is similar to the following reaction:

$$\mathbf{2H_2O + 2e^- \rightarrow H_2 + 2OH^-_{(aq)}} \tag{2-29}$$

The direct reduction of water occurs when the steel surface is negatively polarised to the reversible potential of water and it requires a relatively large overvoltage [61, 62].

2.6.2.2 Anodic reaction

$$\mathbf{Fe} \rightarrow \mathbf{Fe^{2+} + 2\,e^-} \tag{2-30}$$

The only anodic reaction is given in equation (2-30). Bockris [63] suggested the mechanism of anodic iron dissolution reaction for strong acids. The anodic reaction steps are as follows:

$$\mathbf{Fe + H_2O \leftrightarrow FeOH + H^+ + e^-} \tag{2-31a}$$

$$\mathbf{FeOH \Rightarrow FeOH^+ + e^-} \tag{2-31b}$$

$$\mathbf{FeOH^+ + H^+ \leftrightarrow Fe^{2+} + H_2O} \tag{2-31c}$$

In a CO_2 environment, the mechanism of the anodic reaction was studied by many researchers [57, 64-66]. De Waard and Milliams [57] suggested that the mechanism of iron dissolution is similar to the mechanism of a strong acid. Also, they debated that CO_2 has no affect on the iron dissolution. Later, Hurlen and Gunvaldsen [65] found CO_2 has a minor effect on the anodic reaction of iron in the active state.

Based on experiments and previous work, Nesic [66] proposed the following equation for the rate of iron dissolution in CO_2 systems:

$$\mathbf{i_a = k\,[OH^-]^{a1}\,(P_{CO2})^{a2}\,10^{\frac{E}{b_a}}} \tag{2-32}$$

where for: PH<4 a_1=2 b_a=0.03 V per decade

4<PH<5 a_1=2-0 b_a=0.03-0.12 V per decade

PH>5 a_1=0 b_a=0.12 V per decade

$P_{CO2}< 10^{-3}$ MPa a_2=0

$10^{-2} <P_{CO2}<$ 0.1MPa a_2=1

$P_{CO2}>$ 0.1MPa a_2=0

Finally, Nesic [67] suggested that the reaction rate for the active iron dissolution is independent of flow and not a strong function of pCO_2 and pH, but increases with the increase of temperature in a CO_2 environment.

2.7 Key Factors Affecting CO_2 Corrosion

A range of different factors have an effect on metals that corrode in CO_2 aqueous solutions. These factors include environmental, physical and metallurgical ones. The main factors are water chemistry, pH, CO_2 partial pressure, operating temperature, the effect of surface films and flow effects. The next section provides an overview of the existing literature on the effect of these parameters on the corrosion rates in CO_2 containing brines.

2.7.1 Effect of Water Chemistry and its Content

Water chemistry plays a vital role in CO_2 corrosion. The composition of the solution may vary from simple to very complex ones such as in the formation of water emerging together with crude oil [23]. Water which pumps out with the production of oil and gas may contain different types of salts with a different range of concentrations. Typical dissolved species comprise ions such as carbonic, bicarbonate, hydrogen, hydroxide, chloride, sodium, potassium, calcium, magnesium, barium, strontium, acetate and sulphate ones in addition to dissolved gases such as carbon dioxide and hydrogen sulfide [23, 68]. An increase in the concentration of dissolved salts reduces the solubility of gases. Since the general corrosion rate depends on the concentration of carbonic acid which depends on the partial pressure of CO_2, therefore an increase in the concentration of dissolved solids and ionic strength reduces the solubility of carbonic acid and will cause the corrosion rate to decrease. This has been found by Fang et al. in their study when the corrosion rate decreased from 0.27 mm/year to 0.06 mm/year when they changed the NaCl concentration from 3wt.% to 25wt.% [69].

In cases where oil-water emulsions are formed, the presence of oil reduces the water wetting of steel and lowers the corrosion rate because the crude oil decreases the corrosion rate of CO_2 through its interaction with the steel surface in addition to reducing the surface wettability [23]. Understanding of water chemistry can explain its effect on the corrosion rate due to CO_2 corrosion and maintain a controlled environment.

2.7.2 Effect of pH

pH has a strong influence on the corrosion rate. The solution pH represents the concentration of hydrogen ions which directly diffuse, reduce at the surface and cause corrosion. A lower pH means a higher H^+ concentration so a higher corrosion rate and vice versa. Nesic [70] has demonstrated this computationally and experimentally. Moreover, pH has an indirect effect through its influence on the formation of iron carbonate. Research has shown that the increase in pH from 4 to 5 reduces the solubility of Fe^{2+} by about five times. A further increase from 5 to 6 reduces the solubility to factor about 100 times. A low solubility can lead to higher supersaturation which accelerates the formation of $FeCO_3$ which can reduce the corrosion rate [23, 54].

2.7.3 Operating Temperature

In all chemical processes, an increase in temperature accelerates the chemical reactions. Similarly, in corrosion, temperature accelerates all processes influenced in corrosion such as chemical reactions in the bulk, electrochemical reactions at the surface and transport of species between bulk and the corroding surface. Thus, at low pH in the absence of a protective film, the corrosion rate increases steadily with an increase in the operating temperature. The situation changes markedly in the case of the protective film which occurs at high pH [23]. In this situation increasing temperature accelerates the kinetics of precipitation and formation of the protective film and reduces the corrosion rate. At higher temperatures, the film becomes more crystalline and generally more protective [71]. These effects are shown in Figure **2-10**.

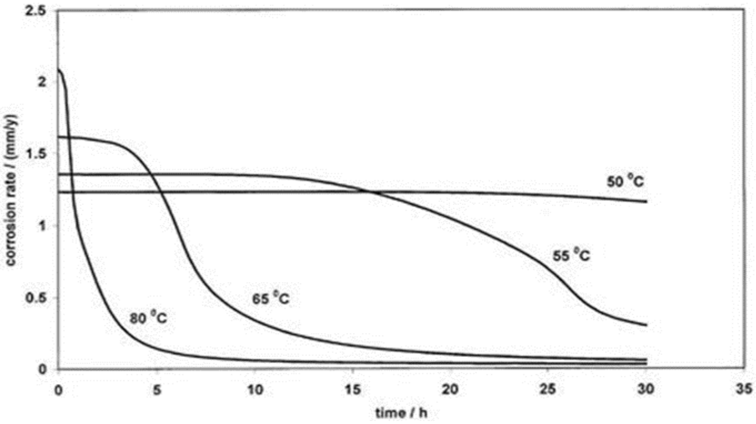

Figure 2-10 The effect of temperature on the corrosion rate over a period of 30 hours for pH=6.6, P_{CO2}=0.54 bar, cFe^{2+} =250 ppm and v=1m/s [23].

The adherence of iron carbonate may be related to the kinetics of precipitation. At high temperatures, iron carbonate may rapidly nucleate and grow to form a tight protective layer. In contrast, at low temperature crystals may grow irregularly. Therefore any increase in temperature, carbonate concentration or ferrous concentration increases the precipitation rate thus improving the protectiveness of the film [72].

2.7.4 Effect of CO_2 Partial Pressure

In the case when protective films are absent, an increase in CO_2 partial pressure enhances the corrosion rate as a result of increasing the concentration of H_2CO_3. Thus the cathodic reaction accelerates. Wang et al. [73] have agreed on this conclusion experimentally and computationally in their work. They found that increasing pCO_2 from 3 bar to 10 bar increases the corrosion rate by a factor of 5. The work of Wang et al. is summarised in Figure **2-11**.

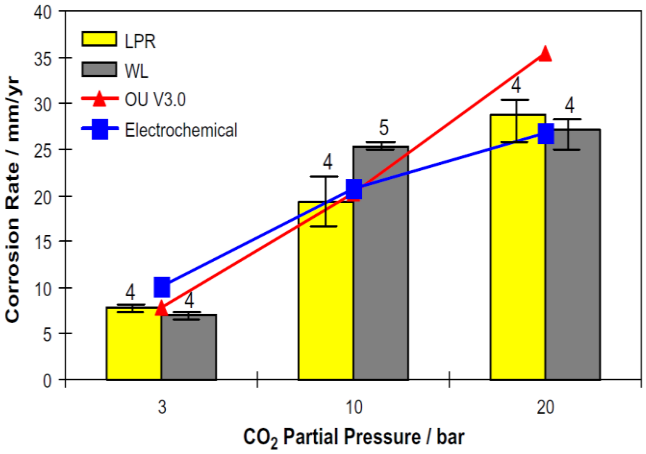

Figure 2-11 Predicted and experimentally measured corrosion rates showing the effect of CO_2 partial pressure [73].

However, in the conditions which are favourable for the formation of protective films, increasing partial pressure plays a significant role through increasing the bicarbonate and carbonate ions concentration to accelerate the formation of protective film and reduce the corrosion rate [11]. These conclusions are supported by the work of Suhor et al. [74] (as shown in Figure **2-12**) on the effect of partial pressure on the corrosion rate over a period of 25 hours.

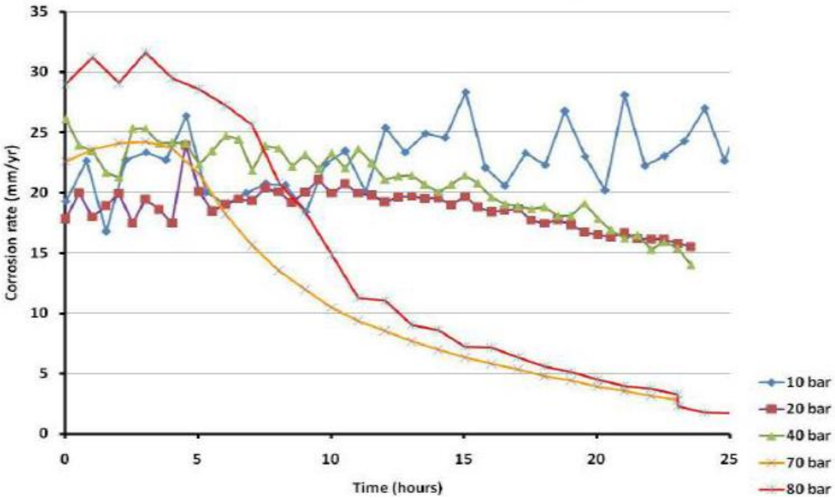

Figure 2-12 Corrosion rate over time for a static experiment at high temperature 80°C and pCO2 ranging from 10 to 80 bar [74].

2.7.5 Effect of Corrosion Products

CO_2 corrosion is strongly dependent on the surface films which form during the corrosion process. The precipitation of iron carbonate is very important in the sweet corrosion of mild steel because it acts as a barrier to reduce the corrosion rate. Researchers have studied the degree of protectiveness of iron carbonate films and they found it depends on a large number of factors such as: the nucleation kinetics, morphology, nature of the alloy, temperature, pH, partial pressure and dynamic effects [75, 76].

In 2014, a newly developed mechanistic model to study the nucleation of iron carbonate has revealed that the nucleation rate changes with the supersaturation of iron carbonate, ferrous ions concentration and partial pressure of CO_2 [75]. Furthermore, it was found that an increase in operating temperature increases the nucleation rate. Higher nucleation rates produce denser and more protective iron carbonate [75].

The protectiveness of iron carbonate depends on the stability of the film, porosity and precipitation rate. Models of iron carbonate precipitation kinetics are part of prediction models of CO_2 corrosion. For example, scaling tendency ST, is a simple parameter to check the protectiveness of $FeCO_3$ which defines the ratio of precipitation rate to the corrosion rate [77].

$$\mathbf{ST} = \frac{\mathbf{P_{FeCO3}}}{\mathbf{CR}}. \tag{2-33}$$

When ST < 1 the iron carbonate layer is very porous and unprotective, however protective $FeCO_3$ forms when the ST > 1 [77].

The formation of iron carbonate is subject to many factors. However, the solution pH and the operating temperature are the most influential factors. The study by Sun et al. suggested that pH = 6.6 and temperature 80°C are the best working condition for the formation of iron carbonate [78].

Despite the fact that the surface films have a significant effect on the corrosion rate. However, it is not the focus of this project.

2.7.6 Effect of Flow

The effect of flow on CO_2 corrosion depends on the surface condition whether there is a protective scale or not.

In the presence of a protective film, a high flow velocity will reduce the corrosion rates by obstructing the transport of reactive species involved in electrochemical reactions. However, the mechanical removal of the film is often encountered in single and multiphase flow [23].

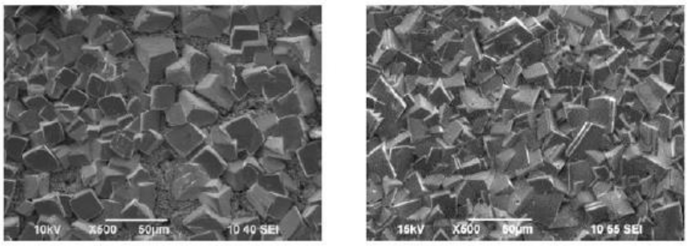

(a) 0 rpm (b) 100 rpm

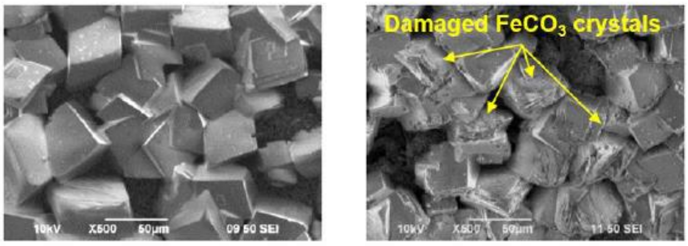

(c) 500 rpm (d) 1000 rpm

Figure 2-13 SEM images showing the effect of flow velocity on the morphology of $FeCO_3$ [51].

Tanupabrungsun [79] studied the effect of flow on the removal of iron carbonate film. SEM images have shown that the increase of the velocity of the system could damage the crystals of iron carbonate. Figure 2-13 SEM images showing the effect of flow velocity on the morphology of FeCO3 [51]. Figure **2-13** (a) shows the tests conducted in static conditions where the Fe^{2+} will increase the pH. However, in the tests run under flowing conditions (Figure **2-13** (b), (c) and (d)), the mass transfer of reactive species reduces the local pH at the steel surface. In other words, the decrease in pH leads to a reduction in the supersaturation of a surface. Thus, the solution becomes under saturated with respect to iron carbonate. Therefore, the crystals of $FeCO_3$ that appear to be damaged in Figure **2-13** (d) are as a result of chemical dissolution instead of mechanical removal. The decrease in near-wall pH as the velocity increases was also demonstrated by Ning et al. [80].

In the absence of a protective film (typically at low pH), the flow has a significant contribution through the mass transfer of the species involved in the electrochemical reactions. An increase of flow velocity leads to an enhanced mass transfer process and the release of Fe^{2+} ions due to corrosion can be more easily transported away from the steel surface, whilst H^+ ions are transported to the surface leading to a decrease in the local pH and an increase in the rate of corrosion. Results by Nesic et al. (shown in Figure **2-14**) found that the corrosion rates increased almost threefold as the velocity increased from 1 m/s to 10 m/s [81].

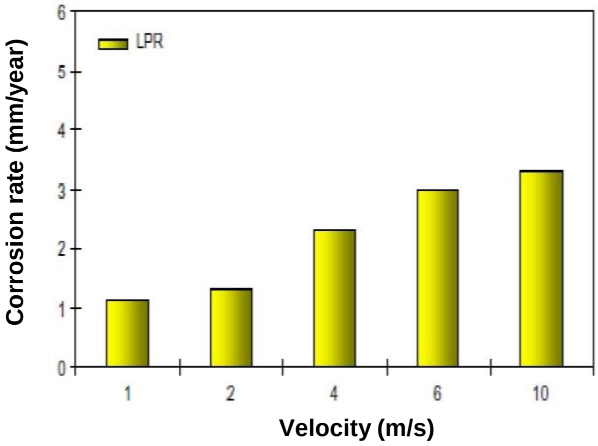

Figure 2-14 Experimentally measured corrosion rates showing the effect of velocity in the absence of iron carbonate film, Test conditions: 20°C, P_{CO2}= 1 bar, c_{Fe2+}<2 ppm [81].

In turbulent flow, the change in concentration occurs in a small region adjacent to the surface called the mass transfer boundary layer. The thickness of the boundary layer is a function of flow geometry and flow rate [81]. Davis [82] presented a semi-empirical correlation (equation (2-34)) to calculate the thickness of the boundary layer for pipes.

$$\boldsymbol{\delta = 25\ \frac{\mathrm{Re}^{\frac{-7}{8}}}{\mathrm{d}}}. \tag{2-34}$$

where: δ is the thickness of the boundary layer (m), Re is the Reynolds number and d is the diameter of the pipe (m).

The mass transfer can be affected by near wall conditions such as surface roughness. Few studies have focused on the effect of surface roughness on mass transfer. Furthermore, no previous studies have focused of the effect of surface roughness on mass transfer in a CO_2 environment. Thus, this will be reviewed in detail later in this chapter.

2.8 Forms and Types of Corrosion Attack

Corrosion has been classified according to the attack ratio AR, of the depth to the width. Corrosion is considered as general corrosion if AR<1. In contrast, the corrosion is termed as localised corrosion if AR>1, furthermore when AR>>1 corrosion is defined as pitting corrosion [34, 83]. There are many classifications of corrosion according to the way that metal is affected by nature and the precise environment condition. Four major types of corrosion (as shown in Figure 2-15) are identified and clarified in the next paragraphs. More detailed information on the form of corrosion attack can be found in reference [34, 36].

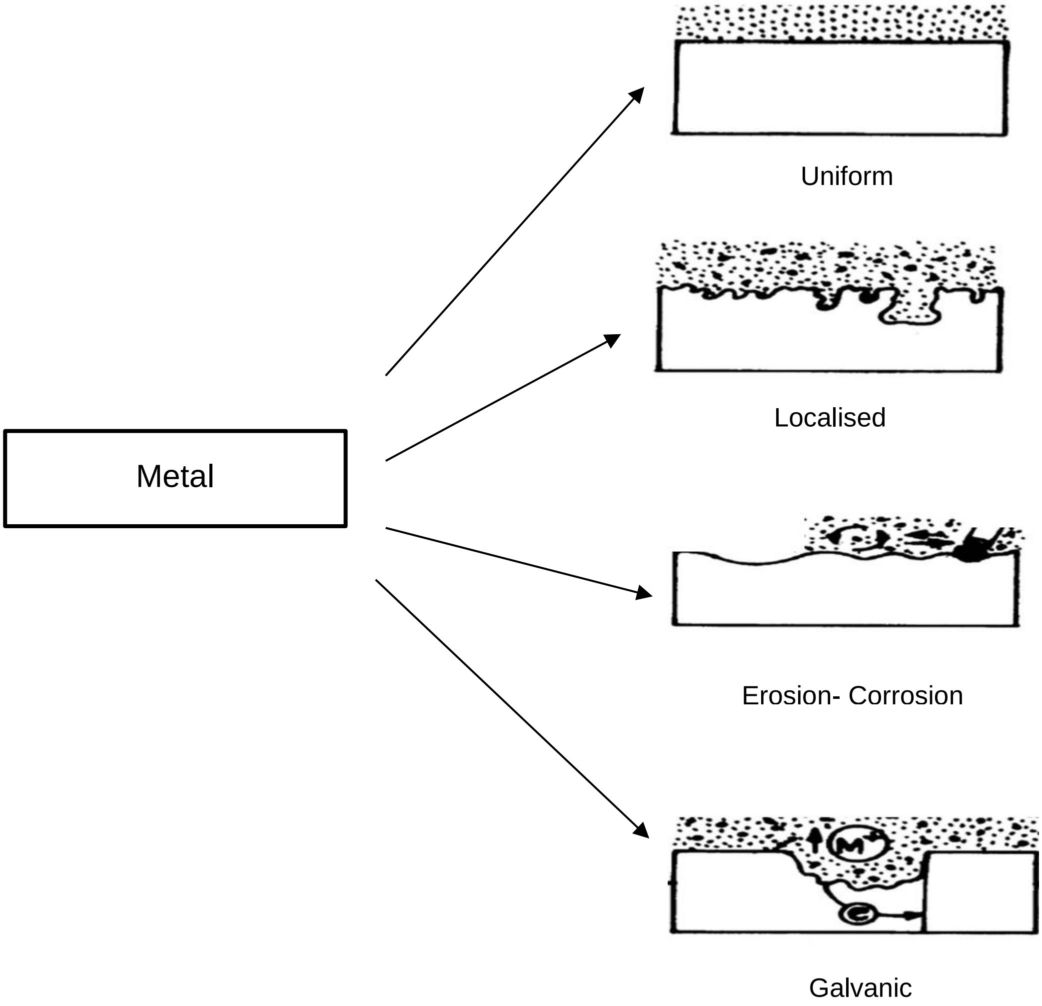

Figure 2-15 Schematic representation of types of corrosion [1].

2.8.1 Uniform Corrosion

Uniform corrosion is defined as corrosion of all areas of the metal at the same time at a similar rate. Corrosion is reasonably uniform particularly in the natural environment where no film or scale can form. Uniform corrosion is easier to be measured compared to localised corrosion. Wall thickness measurement and corrosion rates caused by uniform corrosion can be monitored using different techniques such as weight loss and linear polarisation resistance (LPR). Examples of uniform corrosion are corrosion of zinc in hydrochloric acid and the atmospheric corrosion of steel in the aggressive outdoor environment [34].

2.8.2 Localised Corrosion

Corrosion can appear as a localised attack. The form of localised corrosion observed in field pipelines is typically characterised by flat, film-free regions, separated by sharp steps. Thus, the literature has categorised the localised corrosion into three types which are pitting corrosion, mesa attack and Flow-Induced Localised Corrosion (FILC).

2.8.2.1 Pitting Corrosion

Pitting is an extremely localised form of corrosion where local metal dissolution leads to the formation of cavities within the surface. The environmental conditions within the pit can quickly become aggressive causing corrosion pits to increase through the wall while the other surfaces of the pipe or vessel remain unaffected. The highly localised attack can result in small pits which penetrate the metal and may lead to wall perforations. This type of corrosion can be found in corrosion resistant alloys. However, it also occurs in carbon steel. As shown in Figure **2-16**, pitting corrosion can be divided into a number of types depending on the shape of the pit [84].

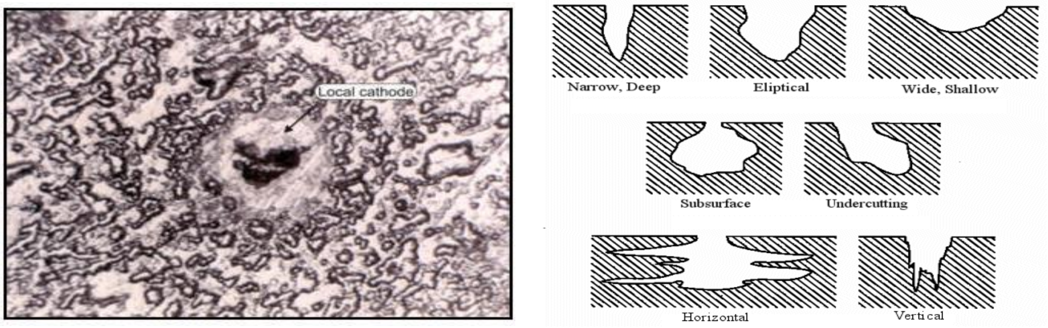

Figure 2-16 Types of pitting corrosion [85].

Pitting corrosion likely occurs at low velocities and around the dew-point temperatures. Local defects in the corrosion product and/or hydrodynamics effects are the factors controlling the initiation of pits [86].

2.8.2.2 Mesa-Type Attack

This is a type of localised corrosion that occurs in low to average flow rates where the protective film forms but it is still unable to bear the mechanical forces from the flow. Such a failure is shown in Figure **2-17**. When the film breaks down, it establishes a galvanic cell between the bare steel (anode) and the film (cathode) which leads to severe localised corrosion [86, 87].

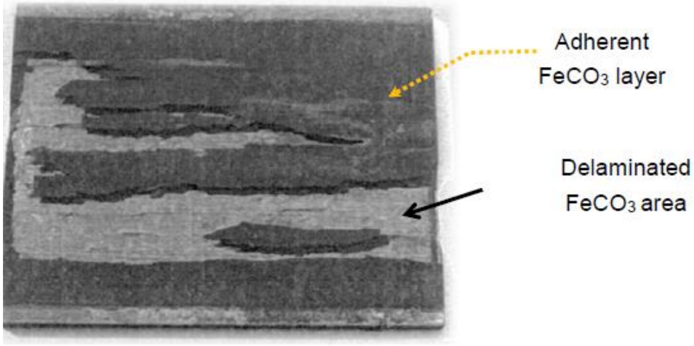

Figure 2-17 An overview of carbon steel sample with mesa attack [86].

2.8.2.3 Flow-induced localised corrosion (FILC)

This type of localised corrosion starts forming pits and/or areas of mesa attack. FILC occurs during turbulent flow when high flow removes the protective iron carbonate ($FeCO_3$) leaving a small area of exposed steel for corrosion to take place.

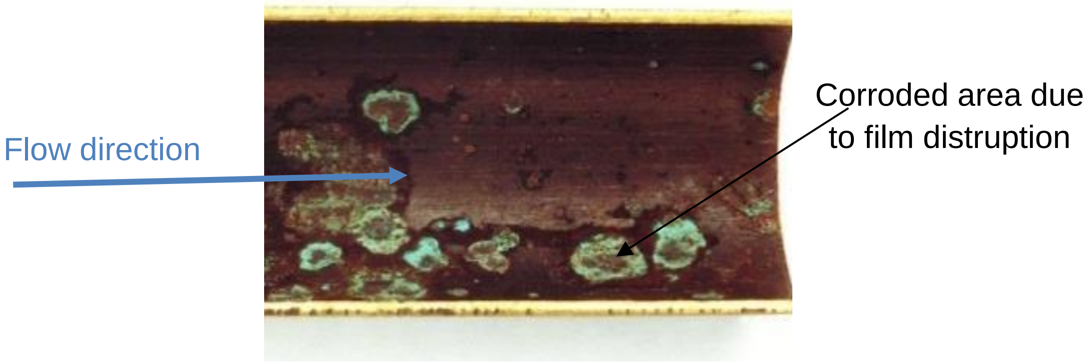

Figure 2-18 Example of pipe corroded as a result of flow induced localised corrosion [88].

Figure **2-18** depicts such a process where the high flow velocity is wearing off the protective film leaving behind the metal surface to corrode. FILC usually contributes to the metal corrosion by removing the scale. The flow induced corrosion was studied in more details in 2000 by Schmitt et al. [89].

2.8.3 Galvanic Corrosion

The corrosion of dissimilar metals when two different metals are coupled together to form the basic corrosion cell is called galvanic corrosion. When two metals are in electrical contact with each other the junction between them is under galvanic contact. One metal will be protected while the other will be under corrosion attack according to their relative position in the galvanic series which is shown in Figure **2-19**. The example of this type of corrosion can be found in preferential weld corrosion (PWC). Figure **2-20** reveals the probability of galvanic corrosion of different metals. Metals with red colour are more probable to corrode due to galvanic corrosion. To prevent galvanic corrosion attacking the weld, more noble elements such as (Ni, Cr, Mo and Cu) should be added to make the weld more cathodic [83, 84].

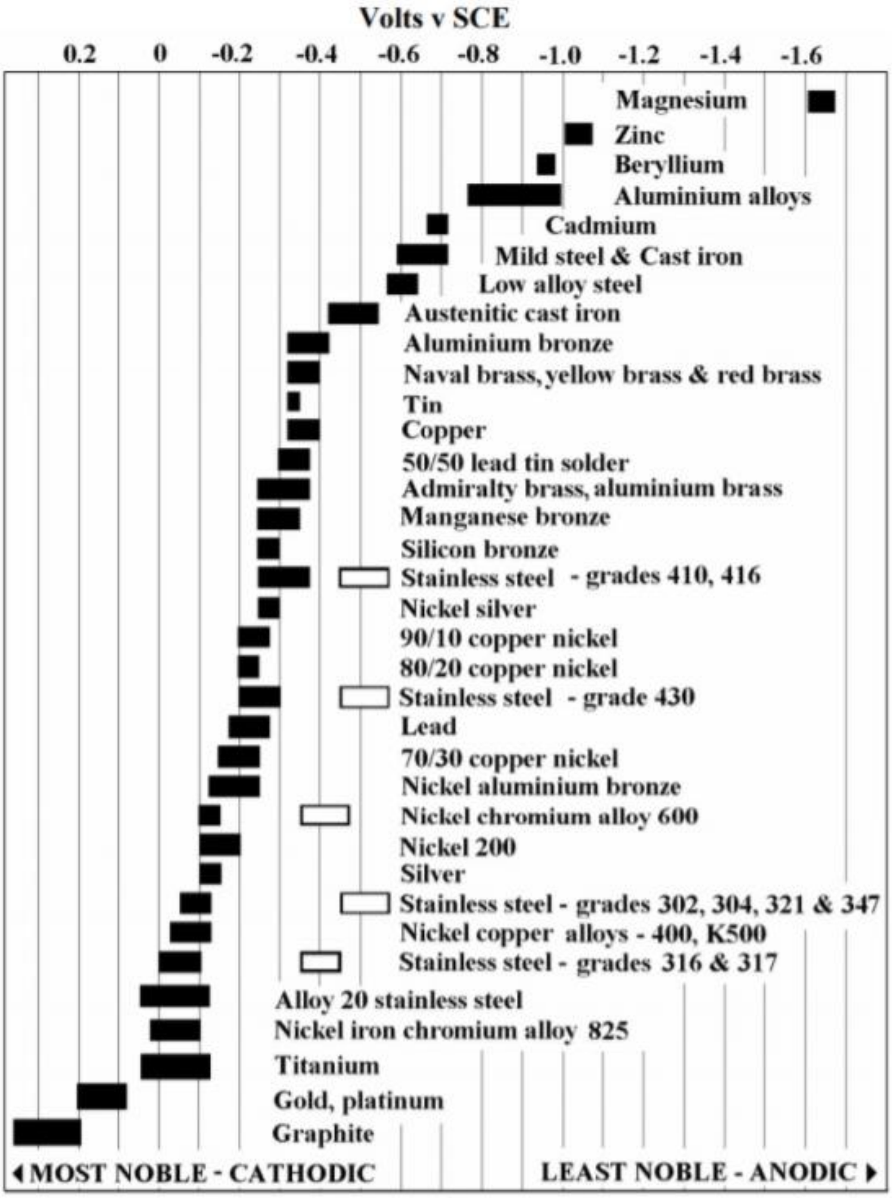

Figure 2-19 Galvanic series of metals [90].

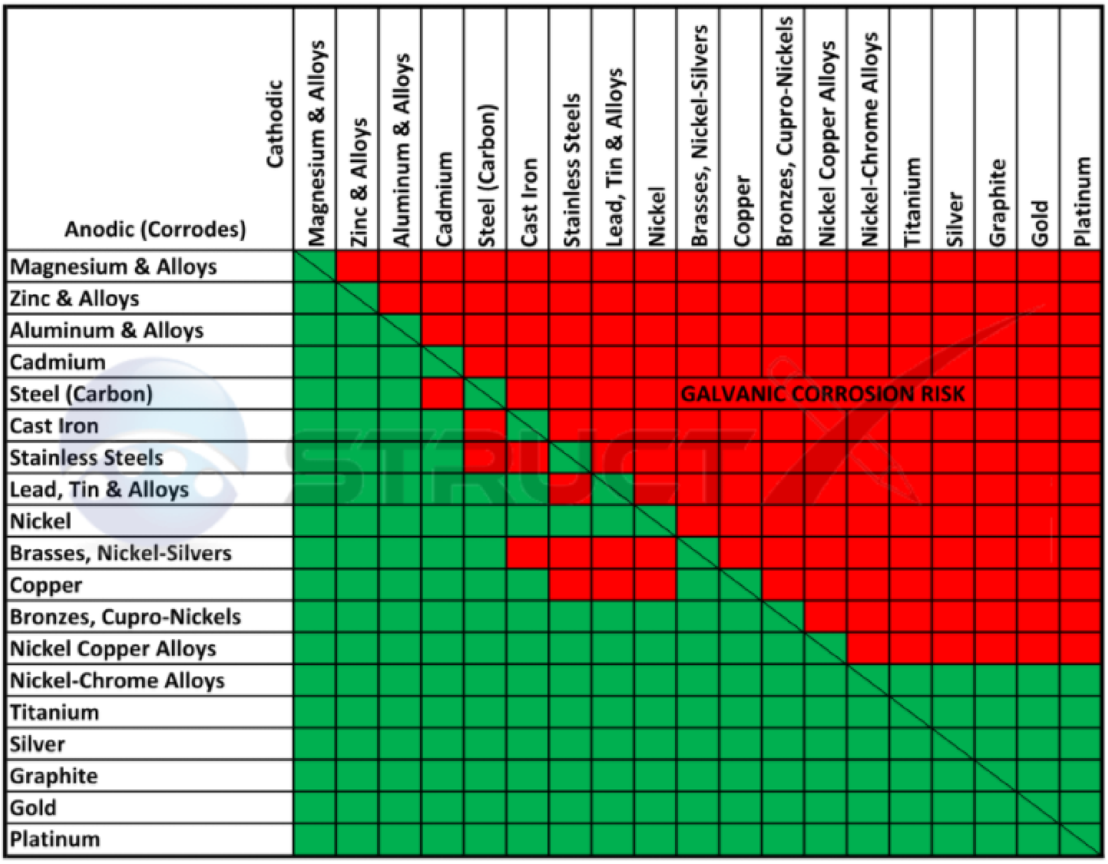

Cathodic Anodic (Corrodes)	Magnesium & Alloys	Zinc & Alloys	Aluminum & Alloys	Cadmium	Steel (Carbon)	Cast Iron	Stainless Steels	Lead, Tin & Alloys	Nickel	Brasses, Nickel-Silvers	Copper	Bronzes, Cupro-Nickels	Nickel Copper Alloys	Nickel-Chrome Alloys	Titanium	Silver	Graphite	Gold	Platinum
Magnesium & Alloys	🟩	🟥	🟥	🟥	🟥	🟥	🟥	🟥	🟥	🟥	🟥	🟥	🟥	🟥	🟥	🟥	🟥	🟥	🟥
Zinc & Alloys	🟩	🟩	🟥	🟥	🟥	🟥	🟥	🟥	🟥	🟥	🟥	🟥	🟥	🟥	🟥	🟥	🟥	🟥	🟥
Aluminum & Alloys	🟩	🟩	🟩	🟥	🟥	🟥	🟥	🟥	🟥	🟥	🟥	🟥	🟥	🟥	🟥	🟥	🟥	🟥	🟥
Cadmium	🟩	🟩	🟩	🟩	🟥	🟥	🟥	🟥	🟥	🟥	🟥	🟥	🟥	🟥	🟥	🟥	🟥	🟥	🟥
Steel (Carbon)	🟩	🟩	🟩	🟥	🟩	🟥	🟥	🟥	🟥	🟥	🟥	🟥	🟥	🟥	🟥	🟥	🟥	🟥	🟥
Cast Iron	🟩	🟩	🟩	🟩	🟥	🟩	🟥	🟥	🟥	🟥	🟥	🟥	🟥	🟥	🟥	🟥	🟥	🟥	🟥
Stainless Steels	🟩	🟩	🟩	🟩	🟥	🟥	🟩	🟥	🟥	🟥	🟥	🟥	🟥	🟥	🟥	🟥	🟥	🟥	🟥
Lead, Tin & Alloys	🟩	🟩	🟩	🟩	🟩	🟩	🟥	🟩	🟥	🟥	🟥	🟥	🟥	🟥	🟥	🟥	🟥	🟥	🟥
Nickel	🟩	🟩	🟩	🟩	🟩	🟩	🟩	🟩	🟩	🟥	🟥	🟥	🟥	🟥	🟥	🟥	🟥	🟥	🟥
Brasses, Nickel-Silvers	🟩	🟩	🟩	🟩	🟩	🟥	🟥	🟥	🟥	🟩	🟥	🟥	🟥	🟥	🟥	🟥	🟥	🟥	🟥
Copper	🟩	🟩	🟩	🟩	🟩	🟩	🟥	🟥	🟥	🟩	🟩	🟥	🟥	🟥	🟥	🟥	🟥	🟥	🟥
Bronzes, Cupro-Nickels	🟩	🟩	🟩	🟩	🟩	🟩	🟩	🟩	🟩	🟩	🟩	🟩	🟥	🟥	🟥	🟥	🟥	🟥	🟥
Nickel Copper Alloys	🟩	🟩	🟩	🟩	🟩	🟩	🟩	🟩	🟩	🟩	🟩	🟩	🟩	🟥	🟥	🟥	🟥	🟥	🟥
Nickel-Chrome Alloys	🟩	🟩	🟩	🟩	🟩	🟩	🟩	🟩	🟩	🟩	🟩	🟩	🟩	🟩	🟩	🟩	🟩	🟩	🟩
Titanium	🟩	🟩	🟩	🟩	🟩	🟩	🟩	🟩	🟩	🟩	🟩	🟩	🟩	🟩	🟩	🟩	🟩	🟩	🟩
Silver	🟩	🟩	🟩	🟩	🟩	🟩	🟩	🟩	🟩	🟩	🟩	🟩	🟩	🟩	🟩	🟩	🟩	🟩	🟩
Graphite	🟩	🟩	🟩	🟩	🟩	🟩	🟩	🟩	🟩	🟩	🟩	🟩	🟩	🟩	🟩	🟩	🟩	🟩	🟩
Gold	🟩	🟩	🟩	🟩	🟩	🟩	🟩	🟩	🟩	🟩	🟩	🟩	🟩	🟩	🟩	🟩	🟩	🟩	🟩
Platinum	🟩	🟩	🟩	🟩	🟩	🟩	🟩	🟩	🟩	🟩	🟩	🟩	🟩	🟩	🟩	🟩	🟩	🟩	🟩

Figure 2-20 Risk of galvanic corrosion for different materials where red area represents the corrosion area while green area represents safe or non-corrosion area [90].

2.8.4 Erosion-Corrosion

Erosion corrosion results when the metal is corroded because of the motion between an electrolyte and the metal surface. Flowing fluid can damage the protective film and lead to accelerated corrosion. The increased corrosion damage results from high shear stress that removes the protective films.

The most severe condition occurs when corrosion and erosion act together in a CO_2 environment. The combined effects of electrochemical reactions and mechanical forces due to solid particles impingement enhance metal loss from surfaces. Erosion-corrosion removes the protective scale by the sand particles impingement then allows the corrosive solution to react with the surface. Erosion-corrosion is the main cause of failures in safety valves, chokes, tee and elbow joints [83]. The poor understanding of the mechanism can cause a serious safety threat to the petroleum industry. It can be prevented by using resistant alloys, changing the design, cathodic protection and removal of suspended solid away from the flow [35, 84].

CO_2 Corrosion Modelling

This section will review the main CO_2 corrosion models that have been used since 1970. They are many available CO_2 corrosion models; some of these models are available in literature and others are proprietary models. The models discussed here have been chosen because they are either well known or widely used by industry and reflected the variety of different categories of models available. These models are organised according to the theoretical background. Nesic has classified CO_2 corrosion models into three categories: empirical, semi-empirical and mechanistic [91].

2.9 Empirical CO_2 Corrosion Models

These models have very little theoretical background. Most of the constants in these models have no physical meaning and are used simply to fit the experimental results. These models cannot be used outside the parameter range for which they are calibrated. However, correction factors can be added with a high degree of uncertainty. Important examples of empirical models are presented below.

The Norsok M-506 Model (1995)

This model was developed by the Norwegian oil companies Statoil, Norsk Hydro and Saga Petroleum. The model is a result of fitting lab data. The first version of the model was limited to 1 bar CO_2 partial pressure and low-temperature environment. However, the latest version can be used for high temperature and pressure environment. The model takes into account the effect of a protective film. The model is quite sensitive to the change in pH. The model calculates both wall shear stress and pH [92, 93]. There are three options to calculate pH. One for condensed water when there is no corrosion product where pH is a function of partial pressure and temperature. Second where condensed water is saturated with iron carbonate. Third for formation water where pH calculations are based on ionic strength and bicarbonate concentration. The limitation of this model that it does not take into account the effect of oil wetting [92, 93].

The Mishra et al. model (1997)

Mishra et al. [94] developed a model where corrosion of carbon steel in CO_2 environments is considered as a chemical controlled reaction. The model is a combination of fundamentals of reaction rate theory and empirical equations in the literature. The model requires inputs such as pH, temperature and CO_2 partial pressure. The predictive equation takes the following form:

$$\mathbf{CR = C\,[H^{+}]^{1.33}\,pCO_2{}^{0.67}\,e^{\frac{-Q}{k\,T}}} \tag{2-35}$$

where CR is the corrosion rate (mm/year), C is a constant, $[H^+]$ is the concentration of hydrogen ions ($kmol/m^3$), pCO_2 is the partial pressure of CO_2 in (Pa), Q is the instantaneous reaction rate constant of CO_2 dissolution in water, k is the Boltzman constant (J/K) and T is the temperature (K).

The drawback of this equation is that it cannot be modified to capture the diffusion-controlled system especially after the formation of a stable film on the corroded surfaces.

2.10 Semi-Empirical Models

These models have some theoretical background. They are for practical purposes where there is limited physical data and understanding. Constants in these models sometimes have a physical meaning while in others cases they are simply calibration constants. These models can be modified more easily to account for new experimental data.

The De Waard et al. model (1975)

This model has been widely used to predict CO_2 corrosion. This model was revised many times. The first version was published in 1975 [57] which is later modified in 1991 and 1995 [71, 95] to take into account different parameters such as mass transport, flow velocity and steel composition by introducing new correction factors. The final version was calibrated against a significant amount of flow loop data tested by the authors.

The corrosion rate is calculated by multiplying the initial value by a number of correction factors. These factors include:

- System pressure: the effect of high pressure was modelled by taking in account the non-ideality of the natural gas (fugacity). The fugacity coefficient can be calculated by solving an equation for a mixture of CO_2 and natural gas. After that, the fugacity coefficient can be used instead of CO_2 partial pressure in the model calculations.
- Flow velocity: in the absence of a protective film, the effect of flow was solved using the Lotz harmonic mean [96]:

$$\frac{1}{V_{cor}} = \frac{1}{V_r} + \frac{1}{V_m} \tag{2-36}$$

where V_r represents the rate of the electrochemical processes and V_m denotes mass transfer.

- Protective film: A scale factor was obtained by applying a multidimensional regression analysis of the results at high temperature by Ikeda et al. [97] to get the best fit with experimental results:

$$\log F_{scale} = \frac{2400}{T} - 0.6 \log(f_{CO2}) - 6.7 \tag{2-37}$$

where T is the absolute Temperature (K) and f_{CO2} is the CO_2 fugacity (bar). The maximum value of scale F_{scale}=1

The De Waard et al. [93] model has been considered as a vital contribution in CO_2 corrosion research over the past three decades, and it is still being used widely by industry.

2.11 Mechanistic Models

Mechanistic models are based on a firm theoretical background. Most of the constants in these models have a physical meaning and they can be found in the literature [91]. Mechanistic models are entirely different from other models because they do not depend on the measured corrosion rates. The majority of mechanistic models were created by researchers in universities [7].

2.11.1 Theory of Mechanistic Models

The core of all mechanistic models is the electrochemical kinetic equation. CO_2 dissolves in water, hydrates and forms carbonic acid which is weak acid and dissociates to form H^+, $HCO_3{}^-$ and $CO_3{}^{2-}$ ions. Species diffuse from the bulk to the wall and react cathodically as shown in the figure below [7].

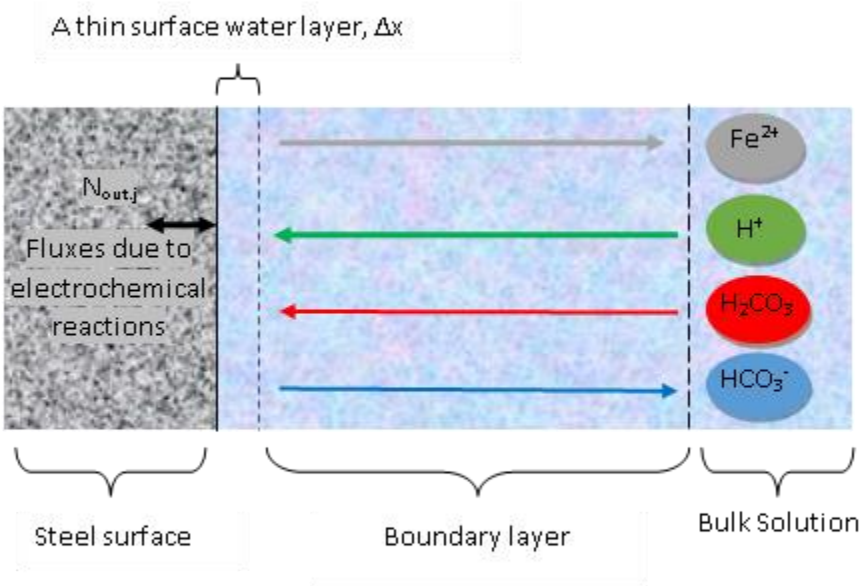

Figure 2-21 Principles of mechanistic CO_2 corrosion models.

The produced species diffuse away from the surface. At certain conditions $FeCO_3$ forms and acts as a diffusion barrier to reduce corrosion and prevent the species from reacting at the surface [54].

It is worth mentioning that all these models provide time and space averaged representations of the system especially turbulence and boundary layer thickness.

2.11.2 An Assessment and Comparison of CO_2 Mechanistic Models

Many mechanistic models exist for CO_2 corrosion. Some of these models are used by engineers in the oil and gas industry [23]. With so many models existing, only these have had a significant contribution to the development of CO_2 corrosion modelling are considered in this study.

Gray et al. Model (1989)

Gray and his co-workers published one of the first mechanistic models. The model was based on theoretical background from literature where constants have physical meaning. The electrochemical reactions in their model are hydrogen evolution reaction and carbonic acid reduction as the cathodic reactions and iron dissolution as the anodic reaction [98]. The first model was limited to low pH environment. Later in 1990, the model was expanded toward more alkaline environments up to pH=10 [99]. They assumed that at pH range between (6<pH<10) there is a direct reduction of bicarbonate ions. Thus, the model was expanded and included direct reduction of bicarbonate ions as cathodic reaction. The two published studies by Gray et al. [98, 99] were studied and further developed by other researchers.

Dayalan et al. Model (1995)

This model took the form of a comprehensive computational program to predict the CO_2 corrosion rate of carbon steel. The model was built to predict the uniform corrosion of CO_2 in the absence of the protective layer and then extended to cover the formation of iron carbonate [100].

In the absence of $FeCO_3$, the overall corrosion process was divided into four steps; the first step is the dissolution of carbon dioxide in the aqueous solution to form various species. The second step is the transport of these species from the bulk to the surface. The third step is the electrochemical reactions (anodic and cathodic) at the surface. The last step is the transportation of products from the surface to the bulk. By modifying a number of steps, similar procedure was used when iron carbonate starts to form as shown in Figure **2-22**:

Step 1: Formation of Reactants

(Chemical species in the Bulk)

$CO_2 + H_2O = H_2CO_3$

$H_2CO_3 = H^+ + HCO_3^-$

HCO_3^- = H+ + CO_3^{2-}

Step 2: Transportation of Reactants

(Bulk to Scale surface)

H_2CO_3 (bulk) → H_2CO_3 (Scale surface)

HCO_3^- (bulk) → HCO_3^- (Scale surface)

H^+ (bulk) → H^+ (Scale surface)

Step 3: Transportation of Reactants

(Scale surface to Metal surface)

H_2CO_3 (Scale surface) → H_2CO_3 (Metal surface)

HCO_3^- (Scale surface) → HCO_3^- (Metal surface)

H^+ (Scale surface) → H^+ (Metal surface)

Step 4: Electrochemical Reactions at the Scale Surface

$2H_2CO_3 + 2e = H_2 + 2HCO_3^-$

$2HCO_3^- + 2e = H_2 + 2CO_3^{2-}$

$2H^+ + 2e = H_2$

Step 5: Electrochemical Reactions at the Metal Surface

Cathodic Reactions

$2H_2CO_3 + 2e = H_2 + 2HCO_3^-$

$2HCO_3^- + 2e = H_2 + 2CO_3^{2-}$

$2H^+ + 2e = H_2$

Anodic Reactions

$Fe = Fe^{2+} + 2e$

Step 6: Transportation of Products

(Metal Surface to Scale surface)

Fe^{2+} (Metal surface) → Fe^{2+} (Scale surface)

CO_3^{2-} (Metal Surface) → CO_3^{2-} (Scale surface)

Step 7: Transportation of Products

(Scale Surface to Bulk)

Fe^{2+} (Scale surface) → Fe^{2+} (Bulk)

CO_3^{2-} (Scale Surface) → CO_3^{2-} (Bulk)

Figure 2-22 Steps in the CO_2 corrosion process on carbon steel with scale [100].

The model was validated against experimental flow loop results and field data from the literature. However, the model does not consider any temperature or CO_2 hydration effect and suffers from some errors in calculating charge transfer rates.

The Nordsveen et al. Model (2003)

This mechanistic model was proposed to predict the corrosion rate as well as the flux and concentration profile of the species. The model covered the following: chemical reactions including precipitation of surface film, electrochemical reactions, diffusion of species between the bulk and the surface, diffusion through the porous film and migration due to potential gradients [33].

The model utilises the Nernst-Planck equation (Equation (2-38)) to solve the mass transfer and homogeneous chemical reactions at the solution near the metal surface.

$$\frac{\partial\, \mathbf{c_j}}{\partial\, \mathbf{t}} = -\frac{\partial \mathbf{N_j}}{\partial\, \mathbf{x}} + \mathbf{R_j} \qquad (2\text{-}38)$$

where c_j is the concentration of the species j, R_j is the source or sink of species j due to all the chemical reactions in which the particular species is involved; t is time; and x is the normal distance away from the steel surface and Nj is the flux of species j which has three components: diffusion, migration and convection:

$$\mathbf{N_j} = -\mathbf{D_j}\,\frac{\partial \mathbf{C_j}}{\partial \mathbf{x}} - \mathbf{z_j}\,\mathbf{u_j}\,\mathbf{F}\,\mathbf{C_j}\,\frac{\partial \emptyset}{\partial \mathbf{x}} + \mathbf{C_j}\,\mathbf{v} \qquad (2\text{-}39)$$

where D_j is the molecular diffusion coefficient of species j, z_j is the electrical charge of species j, u_j is the mobility of species j, F is the Faraday constant, $\emptyset$ is the electric potential in the solution and v is the instantaneous velocity.

In addition to the use of the above equation to describe the concentration profile of the chemical species in the solution, the chemical reactions and electrochemical reactions were treated in greater detail than other previous models. The chemical model is well validated in this model. Furthermore, this model can be used in both low and high pH environments. The model was expanded to include the formation of corrosion product films. The model covers not only the film growth but also, determining the porosity distribution throughout that layer [33]. However, the model proposed in this study suffers from miscalculations in charge transfer rate such as equations to calculate the cathodic and anodic Tafel constants. Despite these drawbacks, the model is considered to be one of the best mechanistic models due to its robust theoretical background [101].

The Model of Remita et al. (2008)

Remita et al. [58] have studied the CO_2 corrosion extensively and suggested their model which studied the rotating disc electrode immersed in CO_2 solution as shown in Figure **2-23**. The model is a revised version of the one by Nordsveen et al. [33].

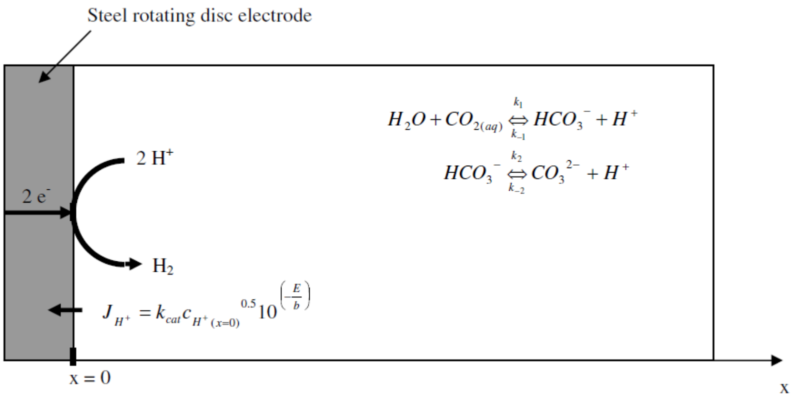

Figure 2-23 Schematic diagram of the system modelled [58].

One of the general assumptions in this model is that the only cathodic reaction at the steel surface is the hydrogen evolution reaction. This assumption is in agreement with Linter [102] and the model was validated against the experimental data of a solution saturated with CO_2 at 25°C and pH=3.95 with different rotation speeds. The final experimental results confirmed the buffering effect of carbonic acid. However, the model was limited to cases with low pH values.

The Zheng et al. Model (2015)

In 2015, Zheng and co-workers developed a new more computationally efficient modelling approach covering both CO_2 and H_2S corrosion. CO_2/H_2S corrosion is a complicated process involving multiple processes which occur simultaneously. These processes are chemical reactions in the bulk of the solution, electrochemical reactions at the steel and mass transport of species through the liquid boundary layer [53]. All of these processes must be taken into account in the model to provide the correct values of the corrosion rate.

The concentration of the species can vary between the bulk and at the surface because of the mass transfer effects and the electrochemical reactions. The concentration in the bulk could be easily computed using a standard water chemistry model; however, the electrochemical reactions depend on the surface concentrations. Therefore, the surface concentrations need to be calculated explicitly [53].

In this model (shown Figure **2-24**) two nodes were used in the computational domain: one for the bulk to calculate the concentrations in the bulk and the second for the surface to calculate the concentrations at the corroding surface.

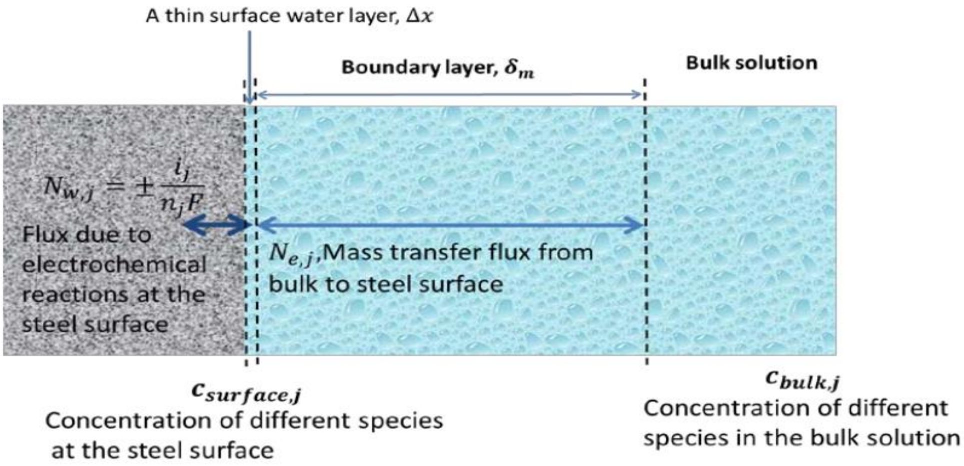

Figure 2-24 Illustration of the computational domain and governing equations for mass transport simulation [53].

According to Figure **2-24** the physicochemical processes that affect the surface concentrations are:

1) Homogeneous chemical reactions close to the steel surface
2) Electrochemical reactions at the steel surface
3) Transport of species between the surface and the bulk.

Therefore, the general equation for these processes can be written as

$$\frac{\partial\, c_{surface,j}}{\partial\, t} = \frac{N_{e,j} - N_{w,j}}{\Delta x} + R_j \quad (2\text{-}40)$$

where $c_{surface,j}$ is the concentration of species j at the steel surface, $N_{e,j}$ is the flux of species j on the east boundary due to mass transfer from the bulk solution to the surface, $N_{w,j}$ is the flux of species j on the west boundary due to electrochemical reactions at the steel surface, Δx is the concentration boundary layer (m) and R_j is the source/sink term due to homogeneous chemical reactions involving species j.

The electrochemical reactions considered in this model were

$$\mathbf{Fe} \rightarrow \mathbf{Fe^{2+}} + \mathbf{2e^-} \tag{2-41}$$

$$\mathbf{2H^+} + \mathbf{2e^-} \rightarrow \mathbf{H_2} \tag{2-42}$$

$$\mathbf{2\,H_2CO_3} + \mathbf{2e^-} \rightarrow \mathbf{H_2} + \mathbf{2HCO_3^-} \tag{2-43}$$

$$\mathbf{2H_2S} + \mathbf{2e^-} \rightarrow \mathbf{H_2} + \mathbf{2HS^-} \tag{2-44}$$

$$\mathbf{2\,H_2O} + \mathbf{2e^-} \rightarrow \mathbf{H_2} + \mathbf{2OH^-} \tag{2-45}$$

The mass transfer flux between the bulk and the surface for each species can be calculated using mass transfer coefficients, $K_{m,j}$:

$$\mathbf{N_{e,j}} = \mathbf{k_{m,j}}\left(\mathbf{c_{bulk,j}} - \mathbf{c_{surface,j}}\right) + \mathbf{k_{m,j}}\,\frac{\mathbf{z_j\,F}}{\mathbf{R\,T}}\,\mathbf{c_{bulk,j}}\,\Delta\mathbf{\Phi} \tag{2-46}$$

Here $c_{bulk,j}$ is the concentration of the species j in the bulk, z_j is the electric charge of species j and $k_{m,j}$ is mass transfer coefficient of species j which can be calculated using the Eisenberg correlation [28] for a rotating cylinder electrode:

$$\mathbf{Sh = 0.0791\,Re^{0.7}\,Sc^{0.356}} \tag{2-47}$$

alternatively, by using Berger and Hau correlation [29] for single phase turbulent flow inside a pipe:

$$\mathbf{Sh = 0.0165\,Re^{0.86}\,Sc^{0.33}} \tag{2-48}$$

The last term $\Delta\Phi$ is the electro-migration migration due to the establishment of potential gradients due to the separation of the major species (Na^+ and Cl^-).

Substituting the flux density due to electrochemical reactions and mass transfer into the mass conservation equation, the final equation can be written:

$$\mathbf{\Delta x}\,\frac{\partial\,\mathbf{c_{surface,j}}}{\partial\,\mathbf{t}} = -\,\frac{\mathbf{i_j}}{\mathbf{n_j\,F}} + \mathbf{k_{m,j}}\left(\mathbf{c_{bulk,j}} - \mathbf{c_{surface,j}}\right) + \mathbf{k_{m,j}}\,\frac{\mathbf{z_j\,F}}{\mathbf{R\,T}}\,\mathbf{c_{bulk,j}}\Delta\mathbf{\Phi} + \mathbf{\Delta x\,R_j} \tag{2-49}$$

There produce 12 equations for the ten minor species (H_2S, HS^-, S^{2-}, CO_2, H_2CO_3, HCO_3^-, CO_3^{2-}, OH^-, H^+, and Fe^{2+}), and two for the major species (Na^+ and Cl^-). The terms major and minor refer to the magnitude of the concentrations, with (Na^+ and Cl^-) exceeding the concentration of other species by orders of magnitude.

There are 13 unknowns (12 unknown surface concentrations and one potential gradient $\Delta\Phi$), and the final equation is the electroneutrality equation:

$$\sum \mathbf{z_j}\, \mathbf{c_{surface,j}} = \mathbf{0} \tag{2-50}$$

Solving all these equations simultaneously, the surface concentrations and surface current density can be calculated.

The model solves both the time dependent and the steady state version of the system. The model can predict the concentrations in the bulk, the concentrations at the surface and the corrosion rate. Also, the model can be modified to predict the film formation of both iron carbonate and iron sulphide. The advantages of this model over the others are that the model is relatively easy to be implement and is more computationally efficient. The model can also be modified easily to study the effect other species such as acetic acid, oxygen…etc.

2.12 Limitations of the Available CO_2 Corrosion Mechanistic Models

To date, an adequate modelling of CO_2 corrosion has not been achieved. This is partly due to the complexity of the process of CO_2 corrosion, which depends on chemical reactions, mass transfer and electrochemical reactions. Each process can be controlled by different reaction rate coefficients and parameters. Many studies were carried out to model the process of CO_2 corrosion. These models which are reviewed in this part still lack a lot of information due to the different reaction constants which were used to model the chemical reactions without giving any reasonable explanation or incorrect assumptions to calculate the fluxes of the reactive species. On the other hand, important parameters such as the effect of surface roughness received no attention at all. All models were validated using the lab setups such as rotating cylinder electrode, flow loop and autoclave. Samples which were tested in these setups were polished using 1200 grit sandpaper. This means that all tested samples were relatively smooth compared to a pipeline [103]. Thus, all models have ignored the effect of surface roughness.

On other hand, all the models in the literature came to an agreement that the surface pH differs from the one in the bulk due to the electrochemical reactions.

However, the values of the surface pH were not validated with the experimental results.

Table **2-2** summarises the most important models of CO_2 corrosion. The table presents the limitations and errors of the reviewed models. Also, the parameters that were not studied by other researchers. Therefore, more work needs to be done to model the CO_2 corrosion. The work should focus on modelling CO_2 corrosion using the well-documented reaction rate constants and electrochemical fluxes, validating the bulk and surface pH and incorporating the effect of roughness into the model.

Table **2-2** follows a colour coded system (see below).

🟩	Green indicates that both equations and assumptions used are accurate.
🟥	Red indicates that either equations or assumptions used are inaccurate.

Models	Solver	Bulk chemical reaction rate constants	Electrochemical fluxes	Bulk pH	Surface pH	Roughness
Gray et al. [99]	Time-dependent	Not well studied [101]	Well formulated	Low- high pH	Not validated	Not studied
Dayalan et al. [100]	Time-dependent	Not well studied [101]	The assumption of direct reduction of bicarbonate in low pH bulk environment	Low- high pH	Not validated	Not studied
Nordsveen et al. [33]	Time-dependent	well studied	Incorrect βa and βc equations	Low- high pH	Not validated	Not studied
Remita et al. [58]	Steady state	well studied	Equations were limited to low bulk pH	Limited to low pH pH=<4	Not validated	Not studied
Zheng et al. [25]	Steady state	well studied	Well formulated	Low- high pH	Not validated	Not studied
The current study	Time-dependent and steady state	well studied	Well formulated	Low- high pH	validated	Studied in one direction

Table 2-2 Limitations of the reviewed mechanistic CO_2 corrosion models and the constraints from the present model.

Mass Transfer in CO_2 Environments

As mentioned earlier, the basis of electrochemical measurement techniques is to monitor the change of potential of the working electrode. Applying a potential will disturb the equilibrium potential (ocp). This process is called polarisation. Polarisation refers to the situation in which an electrochemical reaction is controlled by a slow step in the reaction sequence. Thus, polarisation is classified into three types: activation polarisation, resistance polarisation and concentration polarisation.

2.13 Activation Polarisation

Whenever the ocp is disturbed, activation polarisation results from the change in activation energies. Activation polarisation is caused by a slow electrode reaction. This polarisation can be either positive or negative depending on the displacement of the electrode potential. If the applied potential is positive then the polarisation is termed as anodic or positive while being cathodic or negative when the applied potential is negative [78].

Figure **2-25** shows the relationship of the anodic reaction which oxidises iron. The potential (E) is plotted on the Y-axis. The potential increases or moves to a more positive potential. The current (i) is plotted as log value on the X-axis. The increase of the potential increases the current. The activation polarisation curve is the straight line extending from the lower potential on the left (point number 1) to the higher potential on the right (point number 2). The slope of the line represents the anodic Tafel slope (β_a) [104].

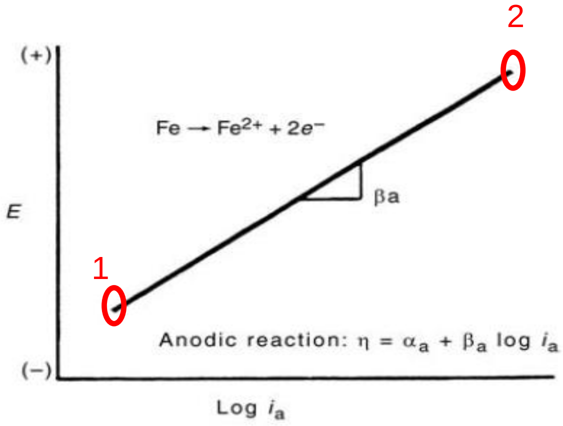

Figure 2-25 Activation polarisation curve of the anodic reaction of iron [104].

The increase in potential due to the anodic potential similar to Figure **2-25** leads to generate more iron ions (Fe^{2+}) at the surface and more electrons are left at the metal surface.

While the activation curve for the cathodic reaction of hydrogen ions (reduction of hydrogen ions) which illustrated in Figure **2-26**. The axes are similar to Figure **2-25**. The slope of the line represents the cathodic Tafel slope β_c. The cathodic activation polarisation is the line extending from point 1 to point 2. The reduction reaction increases as the potential becomes more negative. This means more hydrogen ions and electrons are consumed at the surface. It is worth mentioning that i_a is the rate of generation of electrons and i_c is the rate of consumption of electrons.

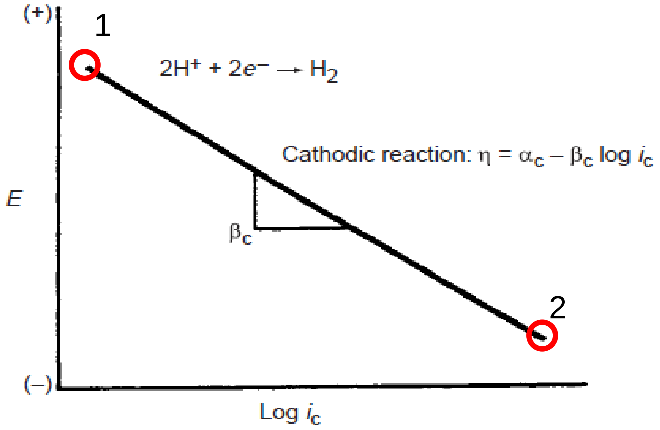

Figure 2-26 Activation polarisation curve of the cathodic reaction of the hydrogen ions [104].

The anodic reaction (Figure **2-25**) and cathodic reaction (Figure **2-26**) are combined in Figure **2-27**. Figure **2-27** shows the activation polarisation for both anodic and cathodic reactions under steady state. As mentioned earlier, the potential of the intersection of the anodic and cathodic curve is called E_{corr} and the current at this point is called i_{corr}.

As shown in Figure **2-28**, there are three types of activation polarisation. These types are anodic control, cathodic control or mixed control. Basically, the type of control can be determined from the slope of the anodic and cathodic curves (β_a and β_c). The polarisation is under cathodic control when the slope of cathodic (reduction) is higher than the slope of anodic (oxidation) curve. While the polarisation is under anodic control when the slope of oxidation curve is greater than the slope of reduction curve. Finally, the polarisation is under mixed control when the corrosion rate is equally sensitive to shifts in the anodic and the cathodic reaction [104].

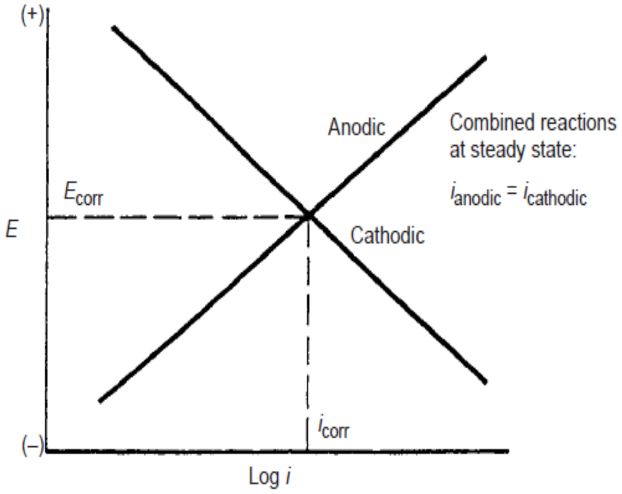

Figure 2-27 Combined anodic and cathodic reactions with activation polarisation [104].

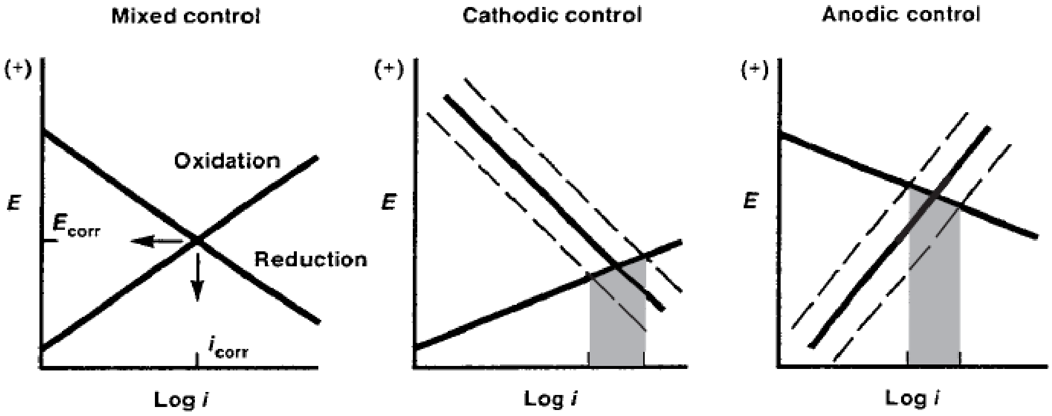

Figure 2-28 Schematic diagrams of the types of activation polarisation [104].

2.14 Resistance Polarisation

Generally, the total polarisation at an electrode is the sum of three components which are the activation polarisation, the concentration polarisation and the resistance polarisation. However, ohmic resistances are negligible unless the reaction itself or a complementary reaction produces films on the electrode surface [50].

2.15 Concentration Polarisation or Mass Transfer Controlled Mechanism

When the corrosion is controlled by the supply of the reactant or the removal of the product from the surface, this is called concentration polarisation. In this case, the ions are produced or consumed at the electrode faster than they can diffuse to or from the solution. Concentration polarisation becomes important when the current density reaches its maximum limit. The current in this case is called the limiting current density. The limiting current represents the maximum possible reduction in a system. At this region, it is not similar to the activation controlled system, the change in potential has no effect on the current and can be represented by the area at which current becomes insensitive to potential variation [36]. The effect of concentration on the cathodic polarisation curves is shown in Figure **2-29**.

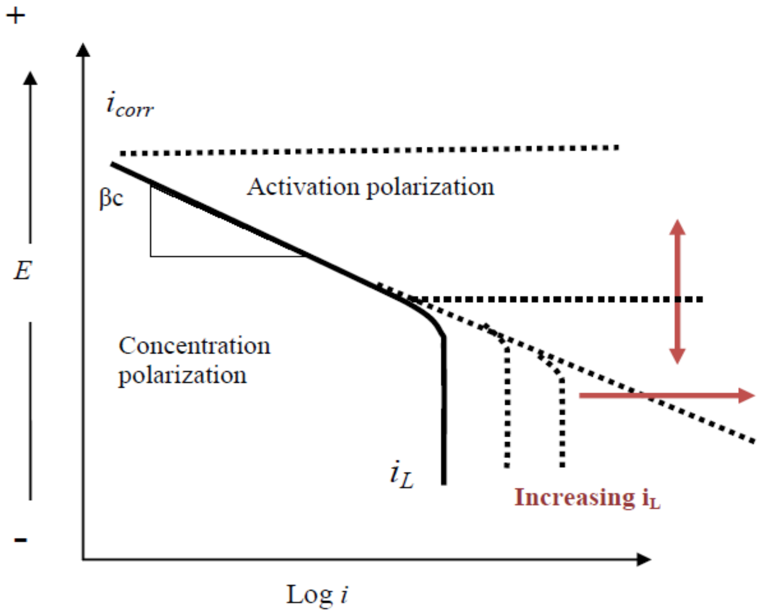

Figure 2-29 Onset of concentration polarisation at more reducing potentials for a cathodic reduction reaction [105].

The value of current density can be calculated using the equation which is derived from Fick's law under steady state diffusion. The equation can be written in the following form:

$$J = \frac{i}{nF} = D\frac{(C_b - C_s)}{\delta} \tag{2-51}$$

where J is the flux of the species transported to the surface given (mol/ m^2 s), C_s and C_b are the concentrations of the species at the surface and in the bulk of solution respectively (Molar), D is the diffusion coefficient (m^2/s), δ is the thickness of the mass transfer boundary layer (m) and i is the current density arising from mass transport to the surface (A/m^2).

When the high charge transfer reaction drains the concentration near the surface and makes it zero, the limiting current density (i_{lim}) rises and the rate of cathodic reaction on the metal surface depends on the mass transfer rate of the species. Thus, equation (2-51) becomes:

$$\mathbf{i_{lim}} = \frac{\mathbf{n\ F\ D\ C_b}}{\boldsymbol{\delta}} \qquad (2\text{-}52)$$

Mass transfer coefficient, K_m, is the ratio of the diffusion coefficient to the thickness of mass transfer boundary layer. Thus, the limiting current equation will be:

$$\mathbf{i_{lim}} = \mathbf{n\ F\ k_m\ C_b} \qquad (2\text{-}53)$$

In CO_2 corrosion, mass transfer is a function of geometry, velocity and physical properties of the fluid and concentration of species in the bulk [106, 107]. Mass transfer has been studied by many researchers. The limiting current is a combination of two elements. However, less attention has been paid to the effect of the surface finish on the mass transfer in the CO_2 environment. In the next section, a review of the primary elements of carbon dioxide corrosion limiting currents and factors affecting the mass transfer processes is provided. The section will emphasize on the role of surface roughness.

2.16 Mass Transfer Measurement Methods

Experimental investigation of the mass transfer is vital as it gives an indication of the concentration gradient of species. In the case of corrosion, the process of corrosion is highly controlled by mass transfer. Determining the value of mass transfer coefficient can help to predict the value of the corrosion rate. Also, the mass transfer at the metal surface can also determine whether corrosion product films are formed or not [108]. Many methods were proposed in the literature to measure the mass transfer experimentally. However, the naphthalene sublimation technique and limiting current method are the most widely experimental procedures used in mass transfer measurements [109, 110].

Naphthalene sublimation is an easy method to conduct the mass transfer measurements. It has been used to determine the local mass transfer coefficients by coating test samples with naphthalene. The coated specimens are installed in the test sections. The difference between the initial naphthalene coated surface profile or weight and the final naphthalene coated surface profile or weight will be used to obtain the mass transfer coefficient [109]. The method can be easily fabricated and installed. However, this method has many limitations. The method gives time averaged values which makes it difficult to predict the transient stage. Also, at a low flow velocity, a long time is required to monitor the change in the naphthalene coating [109]. Naphthalene sublimation is the ideal method to study the mass transfer during evaporation and condensation. However, it is not the best method to study the mass transfer in flow systems [111].

On the other hand, the limiting current technique is an electrochemical method. This method enables the measurement of mass transfer coefficient in different flow and geometry conditions [110]. The term limiting current refers to the maximum rate of current efficiency at which any increase in potential will not change the value of current. Thus, the limiting current is determined by the plateau zone on the cathodic polarisation curves [108]. The limiting current technique has been used by many researchers to obtain the mass transfer for different geometries [112, 113]. This results from this method can be obtained rapidly. Also, it gives the time averaged mass transfer. Nevertheless, the limiting current technique can be used to study the mass transfer for complex geometries.

The limiting current technique and its many advantages over conventional heat and mass transfer measurement methods have been discussed by Landau [114] amongst others. The main advantage of this technique is that the results can be obtained quickly. As the limiting current matches the instantaneous mass transfer rate, fluctuations in the mass transfer can be studied. However, the limiting current technique has a number of drawbacks. First, the purity of the solution is essential so any contamination might lead to inaccuracies. Second, the concentration of the reactive species and temperature must be carefully controlled. Finally, the hydrodynamic conditions must be fully defined for any mass transfer measurements [108].

2.17 Limiting Current in CO_2 Environments

In low pH environment such as the N_2 environments at pH 4, when a cathodic polarisation is conducted, the limiting current is indicated by a plateau zone on the polarisation curve. In this case, the dominant reaction is the Hydrogen evolution reaction (HER).

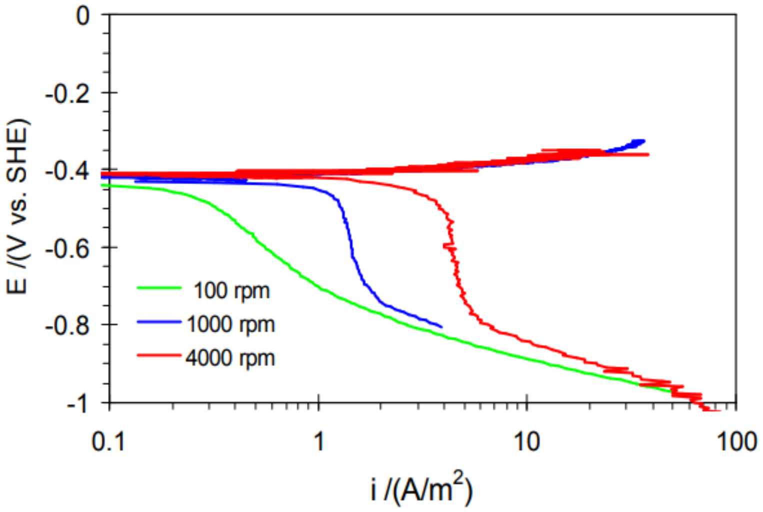

Figure 2-30 Potentiodynamic sweep conducted in HCl solution at pH 4 purged with N_2, T=22°C and 3% NaCl using a rotating cylinder electrode [115].

The value of limiting current is quite sensitive to the change in flow velocity. Nesic et al. [115] studied the limiting current of hydrogen ions in an N_2 environment using a rotating cylinder electrode. Their results are shown in Figure **2-30** and revealed that the increase in rotation speed leads to an increase in limiting current values as more hydrogen ions can transfer from the bulk and react at the surface via the hydrogen evolution reaction. With the exception of the reduction of water (which only becomes significant at high pH or very low overpotentials), this is the only cathodic reaction in the system. It has been shown previously by Stern [28] that the rate of the hydrogen-evolution reaction proceeds only as fast as hydrogen can diffuse from the bulk to the surface. In this case, the mass transfer of hydrogen ions can be calculated using equation (2-53).

Mass transfer is a function of flow geometry; mass transfer equation has the dimensionless number form:

$$\mathbf{Sh} = \mathbf{a}\ \mathbf{Re}^{\mathbf{b}}\ \mathbf{Sc}^{\mathbf{c}}. \tag{2-54}$$

where a, b and c are constants determined by experiments, Sh is the dimensionless Sherwood number representing the ratio of convective mass transport and molecular diffusion $(\mathrm{Sh} = \frac{\mathrm{k\,d}}{\mathrm{D}})$, Re is dimensionless Reynolds number representing the ratio of the inertial force and viscous forces $(\mathrm{Re} = \frac{\rho\,\mathrm{V}\,\mathrm{d}}{\mu})$, Sc is dimensionless Schmidt number representing the ratio of molecular momentum transport to molecular diffusion mass transport $(\mathrm{Sc} = \frac{\mu}{\rho\,\mathrm{D}})$ where: k is the mass transfer coefficient (m/s), d is the diameter (m), D is the diffusion coefficient (m^2/s), V is velocity of the flow (m/s), ρ is the density (kg/m^3) and μ is the dynamic viscosity (kg/m.s).

In 1977, Berger and Hau [29] studied the mass transfer inside a smooth pipe and presented equation (2-55). This equation is the most widely used to calculate the mass transfer for a turbulent single phase flow inside pipes.

$$\mathbf{Sh} = \mathbf{0.0165}\ \mathbf{Re}^{\mathbf{0.86}}\mathbf{Sc}^{\mathbf{0.33}} \tag{2-55}$$

In 1954, Eisenberg et al. [116] conducted a comprehensive study on mass transfer on a smooth RCE surface. They employed the limiting current technique to measure mass transfer utilising the ferriferrocyanide redox reaction in alkaline solutions. Their data for turbulent conditions was correlated with Equation (2-56).

$$\mathbf{Sh} = \mathbf{0.0791}\ \mathbf{Re}^{\mathbf{0.7}}\mathbf{Sc}^{\mathbf{0.356}}. \tag{2-56}$$

Equation (2-56) is not the only mass transfer relationship developed for the RCE. Silverman [117] reported other available correlations in the literature. A number of these correlations are listed in Table **2-3**.

Correlation	Experimental Conditions	Reference
$Sh = 0.0791\ Re^{0.7}\ Sc^{0.356}$	Ferricyanide-ferrocyanide on nickel electrode, $10^3 < Re < 10^5$	Eisenberg et al. [116]
$Sh = 0.0964\ Re^{0.7}\ Sc^{0.356}$	Ferricyanide-ferrocyanide on platinum electrode, $10^3 < Re < 2 \times 10^4$	Morrison et al. [118]
$Sh = 0.0791\ Re^{0.69}\ Sc^{0.41}$	Cathodic deposition of copper from copper sulfate, $10^4 < Re < \sim 5 \times 10^5$	Robinson and Gabe [119]
$Sh = 0.0489\ Re^{0.748}\ Sc^{0.356}$	Derived from curve-fit of Theodorsen and Regier tests [120] over range of $200 < Re < 4 \times 10^5$	Silverman [121]

Table 2-3 Reported correlations to calculate mass transfer for a hydrodynamic smooth cylinder [117].

One point to stress is that the correlations here are based on a straight line fit (from a log-log relationship) to what is actually a non-linear relationship. This was demonstrated in the work of Makrides and Hackerman [122] who reported a change in the relationship between mass transfer and the Reynolds number exponent over $10^3<Re<10^4$, compared to the range $3x10^4<Re<10^5$. However the correlation developed by Eisenberg et al. [116] is most often used to characterise the mass transfer behaviour of hydrogen ions for a smooth RCE.

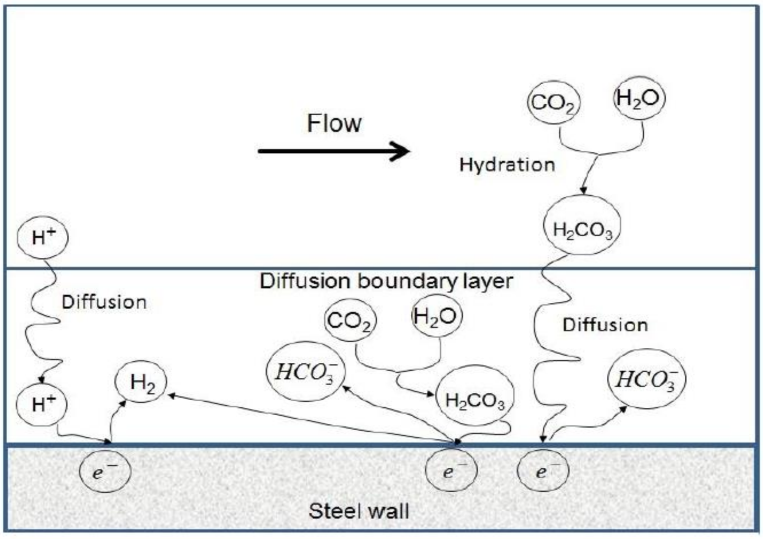

Figure 2-31 Diffusion of hydrogen ions and carbonic acid through the diffusion boundary layer and hydration of aqueous CO_2 in the bulk and within the boundary layer [123].

On other hand, in CO_2-containing environments, CO_2 dissolves in water and hydrates to form carbonic acid which later partially dissociates and is responsible for the high corrosion rates observed for steel in CO_2 containing brines [31]. Hydrogen ions and carbonic acid transfer from the bulk to the surface through the mass transfer boundary layer, as shown schematically in Figure **2-31**.

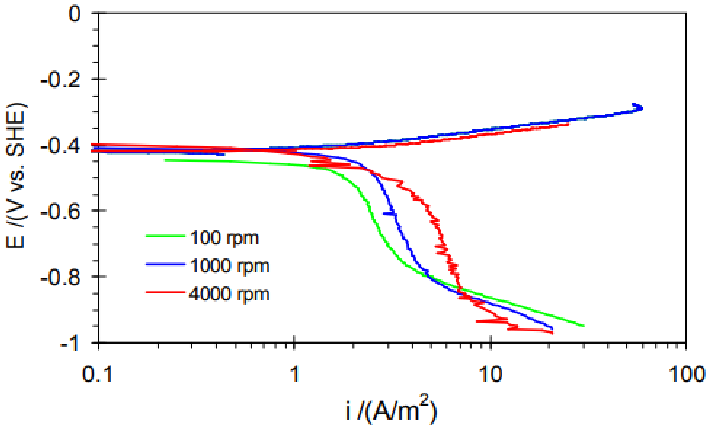

Figure 2-32 Potentiodynamic sweep conducted in a CO_2 solution at pH=4, T=22 °C and 3% NaCl using a rotating cylinder electrode [115].

Nesic et al. [115] conducted their experiments at pH 4 and 25ºC in CO_2 environments using an RCE. Cathodic Tafel sweeps (displayed in Figure **2-32**) showed that the limiting current increases as the rotation speed increases. Comparison between the values of limiting current results in N_2 (Figure **2-30**) and CO_2 environments (Figure **2-32**) is shown in Figure **2-33**.

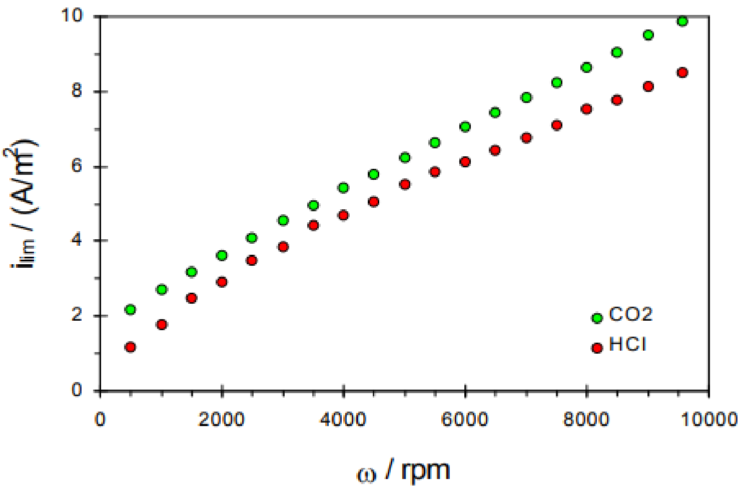

Figure 2-33 Limiting currents for a CO_2 and a HCl solution at pH4, T=22°C measured potentiostatically using a rotating cylinder electrode [115].

It is clearly seen that the value of the limiting current in the CO_2 system is higher than the one in the N_2 system at the same pH. This increase in limiting current is attributed to the presence of H_2CO_3 which was initially believed by Schmitt and Rothmann [32] to be directly reduced at the steel surface:

$$\mathbf{2H_2CO_3 + 2e \rightarrow H_2 + 2HCO_3^-} \tag{2-57}$$

However, more recent research [25, 33] has shown that the reaction actually occurs via the buffering effect at the steel surface.

In the case of CO_2, the limiting current can be divided into two components; one related to the diffusion of H^+ (quantified by the limiting current in the N_2 system) and the other associated with the role of H_2CO_3 which is quantified by the gap between the two curves in Figure **2-33**. Firstly, it appears that the observed gap between the two curves in Figure **2-33** is insensitive to flow over the rpm ranges considered, remaining relatively constant. This is consistent with previous studies and Vetter [124] first proposed an equation to determine the magnitude of the limiting current of the carbonic acid component:

$$\mathbf{i_{lim\ H2CO3} = F\ C_{b,H2CO3}\sqrt{\boldsymbol{K_{-1}}\ D_{H2CO3}}}\ . \tag{2-58}$$

where: $C_{b,H2CO3}$ is the bulk concentration of carbonic acid (mol/m^3), K_{-1} is the backward reaction rate constant of hydration of carbonic acid (1/s) and D_{H2CO3} is the diffusion coefficient of carbonic acid (m^2/s).

However, research by Nesic et al. [115] evaluated Vetter's model and found that at high rpm (beyond ~6000 rpm) the $i_{lim\ H2CO3}$ component began to increase slightly with increasing speed, indicating that the limiting current can be influenced by flow at higher speeds. The phenomenon was attributed to the change in relative thickness between the reaction layer and diffusion layer and the fact that Vetter's model was derived for stagnant conditions or systems where the reaction layer is much smaller than the diffusion layer. Based on this work, Nesic et al. [115] proposed a modification to Vetter's model using a 'flow factor':

$$\mathbf{i_{lim\ H2CO3} = f_1\ F\ C_{b,H2CO3}\sqrt{\boldsymbol{K_{-1}}\ D_{H2CO3}}}\ . \tag{2-59}$$

where

$$\mathbf{f_1} = \frac{1+e^{-2\zeta}}{1-e^{-2\zeta}} = \boldsymbol{coth\zeta}. \tag{2-60}$$

where: f_1 is flow factor and ζ is the ratio of the diffusion layer δ_m to the reaction layer δ_r. both diffusion layer and reaction layer can be calculated using the following equations:

$$\boldsymbol{\delta_m} = \frac{\boldsymbol{D}}{\boldsymbol{k_m}} \tag{2-61}$$

$$\boldsymbol{\delta_r} = \sqrt{\frac{\boldsymbol{D}}{\boldsymbol{K_{-1}}}} \tag{2-62}$$

The process is similar in pipe flow, at higher velocities (>1 m/s), it was reported that using Vetter's correlation to calculate the limiting currents measured in loop experiments always underpredicts the value of the limiting current [81].

Thus, for low and intermediate velocities, Vetter's equation is still being used. However, at high velocities a flow factor must be applied so that the modified Vetter's equation can be used to predict the correct values of the carbonic acid limiting current.

2.18 Factors Influencing the Mass Transfer in CO_2 Environments

In CO_2 corrosion, in low pH environments, the rates of the electrochemical reactions depend on the transport of reactive species towards the metal surface. The mass transport generally occurs via molecular diffusion. Molecular diffusion occurs due to concertation gradient near the metal surface. Whereas, convective mass transfer occurs as a result of flow of the solution over a metal [33]. Many factors affect the value of mass transfer. Some of these factors are widely studied such as: the effect of flow and temperature while other factors have received less attention such as the effect of surface roughness. In the next section, these factors will be reviewed. Furthermore, a detailed review of the literature dealing with the effect of surface roughness will be presented to show its effect on mass transfer. In addition, the major correlation of mass transfer with respect to surface roughness will be highlighted.

2.18.1 Effect of Flow Velocity

In low pH and film-free conditions, an increase in velocity increases the corrosion rate. In this case, the system is under mass transfer control. Accordingly, the increase in velocity enhances the mass transfer of species from the bulk to the surface. Thus, the corrosion rate will increase. The increase in velocity will thin the diffusion boundary layer. Thus, the resistance against species diffusion to the surface will reduce and the mass transfer will increase [33].

2.18.2 Effect of Temperature

Temperature is a key influence on the mass transfer coefficient. Temperature has a significant influence on the physical properties of the solution. The increase in temperature enhances the molecular diffusivity of species, so the mass transport increases. On other hand, the liquid viscosity will decrease as the temperature increases so the mass transfer will increase. Therefore, temperature has a significant effect on the mass transfer especially at higher temperatures [125].

2.18.3 Effect of Surface Finish

Although the effects of surface roughness on momentum and heat transfer have been studied widely, comparatively few studies have considered the effect of surface roughness on mass transfer [126]. The latter is of particular importance in corrosive environments when the electrochemical response of the surface is influenced by the transport of electrochemically active species to and from the steel surface. One key example is in the transportation of carbon dioxide (CO_2)-containing process fluids using carbon steel pipelines in the oil and gas industry [127].

Studies which have considered the influence of roughness on mass transfer characteristics involve geometries such as rectangular ducts [128], pipes [129], the rotating disk [130] and the rotating cylinder [112]. The early work by King and Howard [131] and Ibl [132] in the 1930s and 1960s respectively, showed that in diffusion-controlled environments surface roughness has a major effect on the rate of metal dissolution. These observations were supported a few years later from the work of Ibl [132] and by Brenan and Trass [133] who studied the effect of roughness on the dissolution of crystalline surfaces by roughening the surfaces of glass tubes by coating them with molten solids. Their results showed that the rate of mass transfer increased fourfold with the increase in surface roughness height from ~2.5 to 10 µm over a Reynolds number range from 8,000 to 60,000.

The systematic study of the effects of surface roughness on mass transfer is complicated by the diverse geometrical forms of roughness. It is believed that the increase or decrease in mass transfer mainly depends on the nature of the rough surface, specifically the number of roughness elements per unit area, as well as their shape, height, distribution and their orientation with respect to the flow [134].

In 1962, Levich [135] proposed a theoretical correlation for the Sherwood number in pipe geometries in the form Sh=f(α), where:

$$\boldsymbol{\alpha = f_p^{0.25} Re^{0.5} Sc^{0.25} \left(\frac{\bar{d}}{e}\right)^{0.5}} . \tag{2-63}$$

where: f_p is pipe friction factor, $\bar{d}$ is the diameter of the pipe (m) and e is the average distance from peak to valley (m).

This was validated experimentally in 1968 by Mahato and Shemilt [136], who studied the effect of surface roughness on the dissolution of an iron pipe by water in turbulent flow conditions, and proposed the following correlation:

$$\mathbf{Sh = 13.4 + 0.125 f_p^{0.25} Re^{0.5} Sc^{0.25} \left(\frac{\bar{d}}{e}\right)^{0.5}} . \tag{2-64}$$

Building on this research, in the 1980s, Sedahmed et al. [137] determined the rate of mass transfer at the inner wall of a rough tube using the electrochemical method of measuring the limiting current of the cathodic reduction of potassium ferricyanide in sodium hydroxide. The roughness was achieved by creating V-threads in the inner surface of the pipe with a peak to valley height 0.047 to 0.833 mm. Tests performed over a Reynolds number range of 5,000 to 40,000 revealed that surface roughness increased mass transfer by 10% to 115% depending on the degree of roughness and the Reynolds number. Based on their results, they developed the following relationship using the Stanton number (St):

$$\mathbf{St = 0.183Re^{-0.15}Sc^{-0.66}\left(\frac{e}{\bar{d}}\right)^{0.313}\left(\frac{L}{\bar{d}}\right)^{-0.33}}. \qquad (2\text{-}65)$$

where: St is Stanton number, $St = \frac{Sh}{Re\,Sc}$ and L is length of the transfer surface (m).

In relation to the rotating cylinder electrode (RCE), which is the focus of this study, consideration is afforded here exclusively to the latter in single-phase flow environments, which is particularly useful for this application given its ability to generate turbulence at low rotation rates and the fact that a number of empirical relationships already exist (in the turbulent flow regime) for a number of transport properties associated with the geometry [117].

One of the main approaches towards characterising mass-transfer behaviour for the RCE geometry is to determine the mass-transfer coefficient (k) and convert it into the Sherwood number (Sh). By plotting this value against Reynolds number (Re) it is possible to compare with existing correlations for complete mass-transfer control. Selection of an appropriate correlation is a critical step in this process as it is important to ensure that the correlation chosen is valid over the range of experimental conditions analysed.

The generation of surface roughness of a material through wet-grinding (sample preparation), erosion, corrosion, deposition or other processes will modify the hydrodynamic and mass-transfer boundary layers and consequently change the mass-transfer characteristics. Several physical explanations for the effect of surface roughness on mass transfer have been proposed in the literature. Surface roughness, for example, is assumed to disturb the viscous sublayer and the turbulence generated to reduce the resistance to mass transfer and penetrate into the valleys between the roughness peaks. Although it is understood that surface roughness will influence the Sherwood vs Reynolds number relationship from that of a smooth surface, defining this relationship quantitatively is challenging. This is attributed to the fact that a systematic study of the effects of surface roughness on mass transfer is complicated by the diverse geometrical forms of roughness. It is believed that the change in mass transfer characteristics mainly depends on the nature of the rough surface, specifically the number of roughness elements per unit area, as well as their shape, height, distribution and orientation/alignment to the flow direction [134].

One of the first studies to evaluate the effect of surface roughness on mass transfer was the work of Theodersen and Reiger [120]. Experiments were conducted with sand fixed onto smooth RCEs and indicated that the size of the sand grain relative to the cylinder diameter influenced the drag coefficient. However, above a certain critical Reynolds number (Re_{crit}), the drag coefficient became independent of Reynolds number. Theodersen and Reiger proposed the following relationship between friction factor and the height of surface roughness irregularities:

$$\frac{\mathbf{1}}{\sqrt{\frac{\mathbf{f_c}}{\mathbf{2}}}} = \mathbf{1.25} + \mathbf{5.76 \log}\left(\frac{\mathbf{d}}{\mathbf{e}}\right) \qquad (2\text{-}66)$$

Where: f_c is the rotating cylinder electrode friction factor and d is the diameter of the rotating cylinder electrode (m).

Noting here that this equation has been adapted to be a function of the cylinder diameter and not the radius, as in the original expression, its range of validity was found to depend on the friction length through the following relationship:

$$\frac{\mathbf{e}}{\mathbf{d}^{+}} \geq \mathbf{3.3} \qquad (2\text{-}67)$$

d^{+} is friction length (m) $= \frac{\tau}{\rho}$, where τ is shear stress (Pa) and ρ is density (kg/m^3).

Both Makrides and Hackerman [122] and Kappessar et al. [138] have examined this relationship, with the latter authors reporting results for platinised titanium electrodes under cathodic control. Kappessar et al. [138] confirmed the equations reported by Theodersen and Reiger and proposed the following equation to determine critical Reynolds number Re_{crit}.

$$\mathbf{Re_{crit}} = \mathbf{18.2}\left(\frac{\mathbf{d}}{\mathbf{e}}\right)^{\mathbf{1.18}} \tag{2-68}$$

Kappessar et al. studied the effect of surface roughness on mass transfer in an oxygen environment. They concluded that the friction factor might become independent of the Reynolds numbers when the Reynolds numbers are higher than Re_{crit} (equation (2-68)).

Based on these observations, it is clear that surface roughening has an important influence on the Sherwood vs Reynolds number correlation. This change in relationship is related to the enhancement of mass transfer due to boundary layer disruption, but is also due to the deviation in actual surface area from the projected area with increased roughening.

Although the former observations of the role of surface roughness appear to suggest a simple relationship between mass transfer and roughness, other RCE studies highlight a much more complicated correlation. It appears that the exponent of the Reynolds number in the relation with Sherwood number depends on the geometrical form of roughness. For instance, Gabe et al. [139] examined the Sherwood vs Reynolds number relationship for multiple forms of rough surfaces. The Reynolds exponent was shown to vary from 0.61 to 1 depending on whether the RCE surface roughness was in the form of knurled diamond pyramids, longitudinal fins, cylindrical wire wrapping or a metal powder deposit. Some studies have also suggested that the Reynolds number exponent tends to 1 as the roughness height increases [30, 140], although this is argued to be too simplistic [117]. In contrast, Makanjuola and Gabe [31] actually discovered that for certain RCE geometries, the exponent is 1 for lower Reynolds number, but reduces to 0.578 at higher values. This suggests an even more complex relationship whereby the Reynolds exponent varies with the geometry or roughness, the magnitude of roughness and the Reynolds number itself.

Finally, Sedahmed et al. [141] evaluated the effect of machining fins (or longitudinal grooves) into an RCE on mass transfer. The d/e ratios considered were from 17 to 54. Interestingly, they reported that the friction factor remained sensitive to Reynolds number, even when the critical Reynolds number for each particular sample roughness was exceeded.

It is clear there are quite contrasting relationships between friction factor and Reynolds number in the literature. Some studies [120, 138] report no sensitivity of friction factor to Reynolds number above a critical Reynolds number, while other authors [141] observe a clear dependency of friction factor on Reynolds number above the reported critical value. Therefore care needs to be taken when applying such equations to particular studies to ensure the appropriate Sherwood number vs Reynolds number correlation is used.

2.19 Open Research Constraints of Effect of Roughness on Mass Transfer in a CO_2 Environment

The above review demonstrates that there is a need for greater awareness and understanding of the role of surface roughening on mass transfer. Researchers studied how the increase in surface roughness enhances the mass transfer. As mentioned earlier, that mass transfer is controlled by the value of roughness, roughness orientation and Reynolds numbers. The literature reported different roughness orientation. Gabe and Makanjuola [112] studied the effect of roughness on mass transfer using different samples. Their samples orientation was knurled diamonds pyramids. On other hand, Sedahmed at al. [141] examined mass transfer of longitudinal rectangular grooves. Furthermore, Holland [140] studied the effect of metal powder deposit on an RCE on the mass transfer. Thus, the literature has focused on specific geometries. Axial grooves which are parallel to the direction of flow has received less consideration within the literature compared to others. Few studies have focused on the relationship between surface roughness and mass transfer in an RCE system for this kind of roughness, Gabe and Makanjuola [112] and Poulson [30] have developed correlations for the Sherwood number. Poulson [30] suggested that surface roughness prevailed over the system geometry in terms of influencing mass transfer and proposed the following relationship:

$$\mathbf{Sh = 0.01\,Re\,Sc^{0.33}} \qquad 3000 < Re < 50{,}000 \qquad (2\text{-}69)$$

The relationship was based on data from very rough RCE geometries (d/e=87) as well as numerous other geometries with various forms of roughening patterns [30]. However, Poulson does not explain why the correlation is independent of surface roughness.

The correlation by Gabe and Makanjuola [112] was developed for cylindrical wire wrapping which is similar to the geometry considered here:

$$\mathbf{Sh} = \mathbf{0.0062\ Re\ Sc^{0.356}} \qquad 210 < \mathrm{Re} < 240{,}000 \qquad (2\text{-}70)$$

This correlation is valid for Reynolds values (210- 240,000), with wire diameters ranging from 0.05 to 0.125 mm diameter.

The importance of this kind of roughness was shown by Postlethwaite [142]. Postlethwaite [142] revealed that the surface of the pipe was roughened as a result of erosion-corrosion of aqueous slurries of sand inside the pipe. The shape of the roughness (shown Figure **2-34**) is axial grooves which makes this type of roughness significant for both industrial applications.

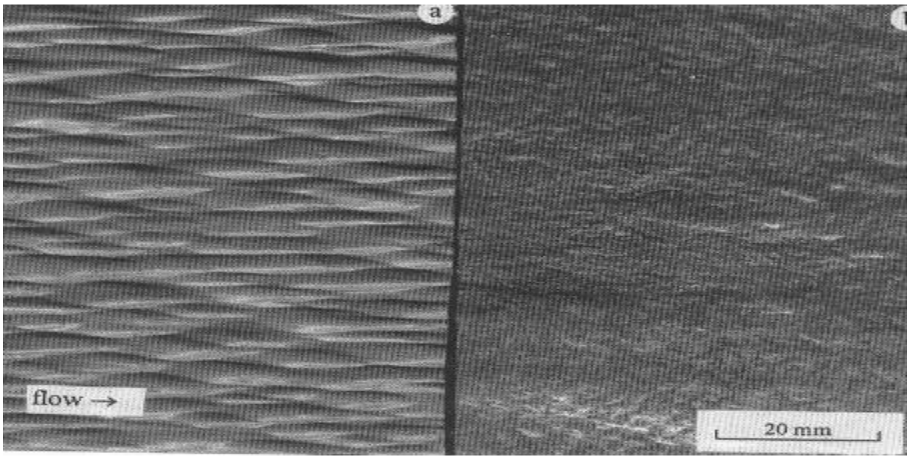

Figure 2-34 Roughened surface as a result of erosion-corrosion of aerated aqueous slurries of sands inside a pipe [142].

The effect of surface roughness has not been studied in a CO_2 environment. The available literature of mass transfer in CO_2 environments has shown that the limiting current of carbonic acid can be affected by flow. In more specific cases, Nesic et al. [115] reported that the increase of rotating speed (more than 6000 rpm) leads to an increase in the limiting current of carbonic acid. Thus, Vetter's correlation needs to be modified by applying a correction factor. The question will arise, if the surface roughness has changed, does the available correlation (Vetter's correlation) need to be modified to account for the change in surface roughness.

The main points which were not covered by the literature and will be studied later are first, manufacturing RCE samples with axial grooves and testing them in an

N_2 solution at pH=3 to check the validity of the available correlations and conclude if a new correlation needs to be obtained. Second, testing the RCE samples in the CO_2 environment and checking whether Vetter's correlation needs to be changed to take into account the effect of surface roughness.

Near Surface pH Measurements

pH has been defined as a scale to specify the acidity and basicity of an aqueous solution. pH represents the negative logarithm scale of the activity of the hydrogen ions [143]. Thus, pH can be calculated using the following equation:

$$\mathbf{pH} = -(\mathbf{log_{10}\, C_{H+}}) \qquad (2\text{-}71)$$

where $\mathrm{C_{H+}}$ is the activity of hydrogen ions (Molar).

Measurement of solution pH is vital for different applications. Classic glass pH electrodes have been used to measure pH of different aqueous solutions [144]. As mentioned in the previous section, CO_2 corrosion is highly influenced by pH. However, local surface conditions or surface pH values can differ from that the values in bulk when an electrochemical process is producing or consuming either hydrogen ions (H^+) or hydroxyl ions (OH^-). The mechanism and rates of electrochemical reactions are affected by the surface pH [32]. Corrosion of carbon steel in carbon dioxide environments occurs primarily by electrochemical reactions. In the absence of the protective film, three main electrochemical reactions occur at the corroded surface. Two are cathodic and one is anodic. The cathodic reactions (Equations (2-72) and (2-73)) which are the hydrogen evolution reaction and carbonic acid reaction (via a buffering effect) and the anodic reaction (Equation (2-74)) which is the dissolution of iron that is actually believed to occur through a number of complex, intermediate reactions as described by Nesic et al. [66].

$$\mathbf{2\ H^{+}{}_{(aq)} + 2e^{-} \rightarrow H_{2(g)}} \qquad (2\text{-}72)$$

$$\mathbf{2\ H_2CO_{3\,(aq)} + 2e^{-} \rightarrow H_{2(g)} + 2\ HCO^{-}_{3(aq)}} \qquad (2\text{-}73)$$

$$\mathbf{Fe_{(s)} \rightarrow Fe^{2+}{}_{(aq)} + 2\ e^{-}} \qquad (2\text{-}74)$$

These reactions are strongly influenced by pH [145]. The experimental results by Nesic et al. have revealed that both bulk pH and surface pH has a strong effect on corrosion of carbon steel in a CO_2 environment [23]. Bulk pH can be measured using the glass pH probe, while surface pH cannot be measured directly using the glass pH probe. A better understanding of corrosion of metals requires measuring the surface pH. Therefore, empirical and semi-empirical models which are based on thermodynamic and transport theories have helped to give a quantification of the surface pH. The experimental studies of near surface pH were limited to biological and medical applications and few publications dealt with the near surface pH related to CO_2 corrosion. The available techniques to measure the near surface pH will be reviewed in detail to highlight the advantages and disadvantages of each method.

2.20 Experimental Methods to Measure the Near Surface pH

The existing methods to measure the near surface pH (NSP) outlined in the literature have been classified as direct and indirect methods. These methods are as follow:

2.20.1 Indirect Near Surface pH Measurement Method

One technique uses a semiconductor contact to observe the distribution of pH. The semiconductor contact sensor is made of a silicon semiconductor covered with silicon nitride. The surface of the sensor (point A in Figure **2-35**) is uniform and divided into multiple measurement points. Each point responds individually to the change of pH. The resulting change in capacitance as a response to the pH can be recorded with a generated photocurrent [146].

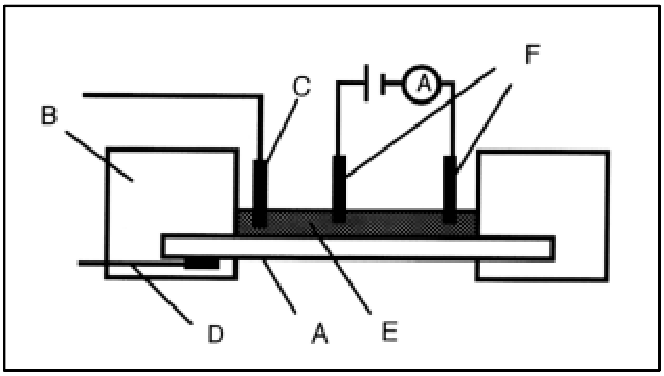

Figure 2-35 Electrochemical cell and indirect pH measurement setup. A: pH sensor, B: Holder, C: Glass pH probe, D: Ohmic contact, E: Electrolyte, F: Pt electrodes [146].

This kind of cell is expensive and complicated. It requires a number of elements which are neither cheap nor easy to design and manufacture.

2.20.2 Direct Surface pH Measurement Methods

In some research, traditional pH probes (standard glass pH probe) were modified to measure surface pH [147]. This method is called mesh capped probe [147]. Nevertheless, various solid state metals have been used to measure the surface pH to replace the traditional pH probe. This kind of electrode is fabricated by depositing various metals or metal oxides on substrates. The choice of metal oxide and substrates depends on the applications. Einerhand et al. [148] introduced a PdO probe which was used to measure the pH of whole blood. The probe was coated with a Nafion film to prevent the PdO probe from dissolving in Cl^- contained solutions. Later, the experiments by Grubb et al. [149] demonstrated that the PdO probe suffers from redox interference. Fog et al. [150] surveyed different metal oxides including PtO_2, RuO_2, TiO_2 and IrO_2 and SnO_2. Their experiments examined pH sensitivity, the range of working pH and redox interference of each probe. Their results indicated that IrO_2 is the most promising probe due to its fast pH response and wide working pH ranges.

Iridium oxide probes have received considerable attention in recent years. These probes have good stability even at high temperature up to 250°C [151, 152]. The iridium oxide probes were divided according to the fabrication method of the probes. Table **2-4** shows examples of the methods which were used to prepare iridium oxide pH electrodes.

Method	Precursor method/ Substrate	Reference
Sol- gel	IrO_x/ Ti	Da Silva et al. 2008 [153]
Thermal oxidation	IrO_x/ Pt	Song et al. 1998 [154]
Sputtering	IrO_2 /Al_2O_3	Kreider 1991 [155]
Electrodeposition	IrO_2/ Ag, Cu and Co IrO_2/ stainless steel	Marzok 2003 [156] Martinez et al. 2009 [157]

Table 2-4 Different methods to prepare iridium oxide pH electrodes.

The direct method is the most widely used by researchers due to its reliability, economic feasibility and ease of manufacture compared to the indirect method.

The mesh capped probe and methods to prepare the iridium oxide probes will be reviewed in more detail in the next sections.

2.20.2.1 Mesh- Capped Probe

Various designs were used to study the interfacial pH using the mesh technique but the submerged impinging jet mesh probe cell and static mesh capped probe are the most well-known.These designs have been used by many researchers to study the solution/ metal interface. In 1997, Deslouis et al. [158] used this method to characterise the surface pH during the reduction of dissolved oxygen in an impinging jet setup. The set up which was used in their experiments are shown in Figure **2-36**. A 0.5 mm gold mesh was used as a working electrode. A flat pH probe was fixed on the mesh using teflon tape. A platinum grid was used as a counter electrode and a calomel electrode (CE) was used as a reference electrode. The mass transfer results from electrochemistry were used to calculate the surface pH. The results of the mass transfer were matched with the surface pH results from the mesh. The increase in mass transfer leads to higher surface pH. However, their measurements suffered some discrepancies due to the fact that a motionless volume of solution is trapped in the holes of the grid which affect the real value of surface pH.

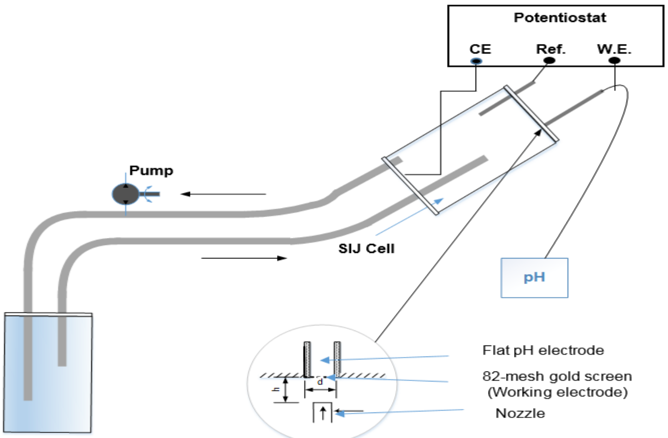

Figure 2-36 Interfacial pH measurements of dissolved oxygen in a submerged impinging jet setup [158].

Later, Tlili et al. [159] used the same technique to study the effect of surface pH on precipitation of calcium carbonate. Their results showed the importance of surface pH on the rate of precipitation of calcium carbonate.

In more recent study, Han et al. [32] studied the surface pH of mild steel during the corrosion process in a CO_2 environment using a mesh-capped probe. Han et al. [32] used carbon steel mesh as a corroded metal. pH probe was placed in contact with the mesh. The experiments were run in static solutions saturated with either CO_2 or N_2 with different bulk pH (4, 5 and 6). Also, they examined the effect of HAc on the surface pH. The surface pH measurements were recorded as the mesh corrodes. In both cases (CO_2 or N_2), the results have shown a big difference between the surface pH and bulk pH.

The advantages of this technique are: it is simple to design, flexible and low-cost compared with other techniques. However, this technique has many disadvantages such as fragility and difficulties to implement the mesh capped probe to be used in a dynamic system such as: pipe flow wall or thin flow channel cell (TCFC).

2.20.2.2 Sol-Gel Method

The Sol-gel or dip coating method has been used to fabricate flexible iridium oxide pH probes. This method is mainly used to fabricate microelectrodes. Sol-gel can be used to fabricate an array of pH sensors similar to Figure **2-37** [160].

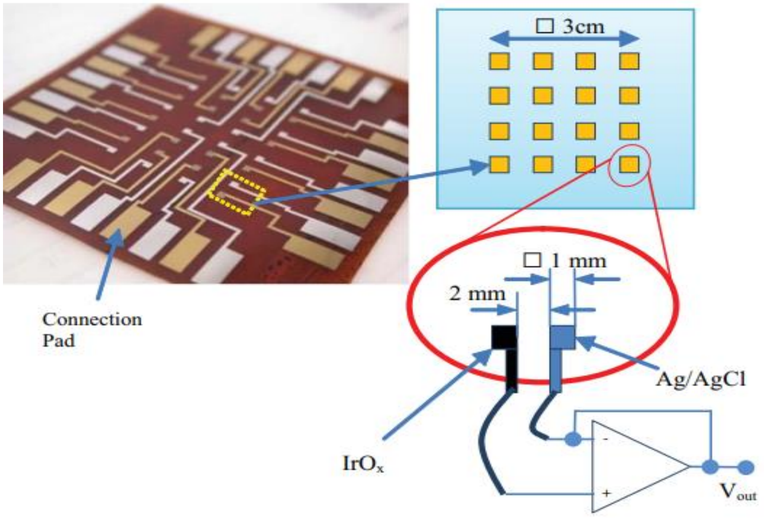

Figure 2-37 Photo of a pH sensor array. The array includes 16 individual pH sensors [160].

pH sensors can be prepared by coating substrates with iridium oxide using the sol-gel method. The sol-gel method is a coating method. The coating solution is prepared by mixing 0.5 g iridium chloride with 21 mL methanol and 5mL acetic acid. The coating process is carried out by immersing the whole substrate in the solution. The dipped substrate was taken out using a dip coating apparatus. The quality of coating and sensitivity of the electrode is highly controlled by the withdrawal rate. The reported literature has recommended 0.5 mm/sec for the withdrawal rate.

Also, a significant improvement in the thickness and quality of the coating was shown when the dipping process was repeated more than once. In some cases, the dipping process is followed by heat treatment to improve the adhesion of the film [160].

The method is suitable to achieve low cost pH electrodes. However, the challenge of the sol-gel method can be attributed to its drying process. The drying process might lead to cracks in the iridium oxide film due to its dehydration. Tadanori et al. were suggested using some additives to improve the coating [161].

2.20.2.3 Thermal Oxidation

This method is carried out by oxidising a pure iridium to form iridium oxide using potentiodynamic cycling (cyclic voltammetry) method. Many authors have used this method to fabricate the pH electrodes by depositing iridium on substrates using cyclic voltammetry in dilute acid, usually sulfuric acid (H_2SO_4) [151, 154, 162]. Authors reported different parameters that control the iridium oxide film. These parameters are acid concentration, number of cycles and scan rate.

Song et al. [154] studied the fabrication of iridium oxide film in 0.5 molar H_2SO_4 aqueous solution. They used cyclic voltammetry with a scan rate of 50 mV/s and different exposure time (2, 4, 8 and 24 hr). Their results showed that as the exposure time increased the stability of the film increased.

The main advantage of this type of electrodes is high sensitivity of electrodes compared to others. The thermal oxidation pH probes are very sensitive and responsive to the change in pH. However, the best mechanism of preparing these probes is still under debate.

2.20.2.4 Sputtering

The sputtering method was mainly used for neural stimulation electrodes [21, 163]. Iridium oxide electrodes are fabricated by sputtering iridium (sputtering target) in an oxygen environment. Iridium reacts to form iridium oxide and this is called reactive sputtering. The behaviour of sputtered iridium oxide changes depending on the exposure time. Kreider [155] studied the stability of iridium oxide in high temperature and pressure saline solution. Sputtered iridium oxide probe was prepared in 0.4 Pa mixed oxygen- Argon environment in a ratio 1:1. Iridium was deposited on alumina substrates and tested at temperatures 30°C to 240°C. His results showed that in low temperature saline solutions the probe was stable even after 24 hrs of exposure. However, at high temperature the pH sensitivity decreased as the exposure time increased.

The main disadvantage of this method is the high cost of iridium oxide sputtering targets which makes this method expensive.

2.20.2.5 Electrodeposition

Yamanaka [164] first proposed electrodeposition of iridium oxide to fabricate pH probes. Yamanaka suggested the procedure for electrodeposition. After that researchers significantly improved the electrodeposition procedure. The electrodeposition method is carried out by preparing the iridium oxide solution. The solution preparation procedure is shown in Figure **2-38**. After that the electrodeposition procedure was done using a three electrode cell. The electrodeposition was carried out by a mean of cyclic voltammetry. The thickness of the coating is mainly controlled by number of cycles, scan rate and scan range [165].

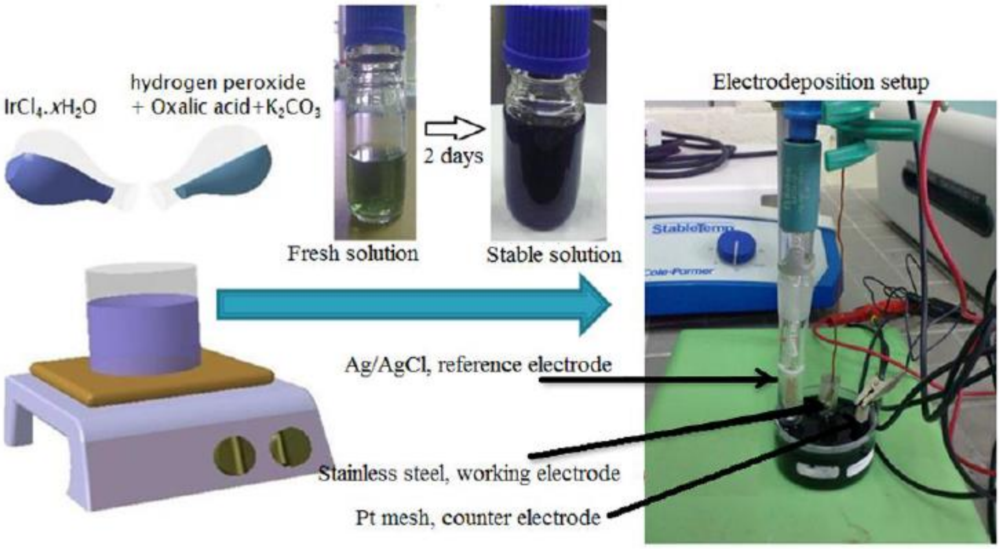

Figure 2-38 Iridium oxide solution preparation and electrodeposition method [165].

The process of electrodeposition does not require high temperatures to achieve good iridium oxide coating. The fabricated sensor using electrodeposition has fast response and good repeatability.

2.20.2.6 Assessment of Iridium Oxide pH Electrodes

Iridium has numerous impressive qualities due to its sensitivity to the change of pH. Iridium has been used to fabricate the pH probes. As mentioned earlier in the previous section, there are four primary methods to fabricate these electrodes. These methods are sol-gel, thermal oxidation, sputtering and electrodeposition. Each method has advantages and disadvantages. Thermal oxidation is the easiest method to prepare iridium oxide but it requires using solid iridium (Ir) which is expensive. Similarly, sol-gel is an easy method to achieve low cost pH electrodes. However, the drying process is quite challenging due to the possibility of cracking of the iridium film. Also, sputtering is the most reliable method but the use of an expensive Ir target makes this method expensive and requires experience to achieve good coating. Finally, the electrodes fabricated using the electrodeposition method appears to have the same benefits as the sputtered method without the cost of Ir target. This makes the electrodeposition method the most popular methods to prepare pH probes.

The choice of the method of fabrication highly depends on the application where the electrodes will be used. For example, in biological applications Marzouk et al. [166] used pH electrodes fabricated with sputtering methods to measure extracellular pH in ischemic rabbit papillary muscle. Furthermore, O'Hare et al. [167] tried to measure the pH in the cultured intervertebral disc by adjusting the probes fabricated with oxidation method. Their results showed that these pH electrodes are unstable. Also, the iridium oxide film dissolved in high chloride media. Despite the high cost of the sputtering method it is still the most popular method to fabricate pH probes for biological and medical applications. On other hand, in corrosive environments such as CO_2 corrosion which is the interest of this thesis, few studies have focused on measuring the surface pH during corrosion. Mesh probes have been used to measures the surface pH during corrosion of carbon steel in the CO_2 environment [32]. Later, Zhu et al. [168] measured the surface pH during corrosion of 316L stainless steel in the CO_2 environment using probes manufactured by an electrodeposition method. Kakooei et al. [165] studied the electrodeposition technique in more detail taking into account the effect of different parameters on iridium oxide films. Their results support using the electrodeposition technique to measure the surface pH due to its unique pH sensing properties compared to other techniques.

From the above we can conclude that the near surface pH during carbon steel uniform corrosion in CO_2 environment still needs to be studied as the process of corrosion is controlled by the surface pH. The study should focus on fabricating the iridium oxide pH probes using an electrodeposition method as it is recommended by the literature, measuring the near surface pH during the corrosion of carbon steel samples in CO_2 environment, replicating the near surface pH results of the mesh probe to check the reliability of the reported results and to compare the results of both methods. The results of the iridium oxide probe will show if the iridium oxide probe is reliable enough to be used for near surface pH measurements in CO_2 environments.

2.21 Electrodeposited Iridium Oxide Probe (Preparation and Methodology)

2.21.1 Iridium Oxide Solution

Yamanaka [164] first presented the fabrication of iridium oxide pH electrodes using the electrodeposition method. Yamanaka [164] proposed the procedure to prepare the iridium oxide solution which is based on $(NH_4)_2[IrCl_6]$ and complex oxalate component. Later, many authors tried to modify and improve the procedure without giving any proper justification [169-171]. In 2003 Marzouk [156] in his valuable work optimised the preparation procedure to prepare the electrodeposition solution by mixing $IrCl_4$ as iridium source, hydrogen peroxide, oxalic acid and potassium carbonate. Marzouk justified using $IrCl_4$ instead of $(NH_4)_2[IrCl_6]$ as the solution takes less time (three days) to accomplish dark blue colour compared to 7 days in Yamanaka's procedure. Marzouk showed that the colour development from dark yellow or green to dark blue or purple is the sign of maturity of the solution and formation of iridium oxide. The change in the solution colour means that the solution is ready for electrodeposition on substrates [156]. Marzouk's procedure was later studied by many researchers and concluded is the best procedure to prepare iridium oxide solution [145, 165, 168].

2.21.2 The Electrodeposition of Iridium Oxide

Researchers have used cyclic voltammetry for iridium oxide electrodeposition [145, 156, 168]. Cyclic voltammetry (CV) is an electrochemical technique where the potential of the electrode is scanned forward and backwards between predefined limits. The resultant current is measured as a function of the applied potential. CV can be used for different purposes such as studying the electroactive species in solution, determining the electron stoichiometry of a system and electrodeposition process. So the focus will be on CV in electrodeposition [172].

CV has been used to deposit iridium oxide on substrates. According to Figure **2-39**, the potential starts from the low potential (-0.5 V) and scans toward a high potential (0.65) and then scans back towards starting potential. The increase in current peaks as the cycles increases, indicating the formation of an iridium oxide film. Also, when the cycles increase this leads to an increase in the thickness of the iridium film. During the potential scan two redox processes in the oxidation region can be assigned. These processes (A1, A2, C1 and C2) are shown in Figure **2-39**. The first one is (A1 and C1) is assigned to $Ir^{III} \leftrightarrow Ir^{IV}$ transition. While the second one is (A2 and C2) is assigned $Ir^{IV} \leftrightarrow Ir^{V}$ transition.

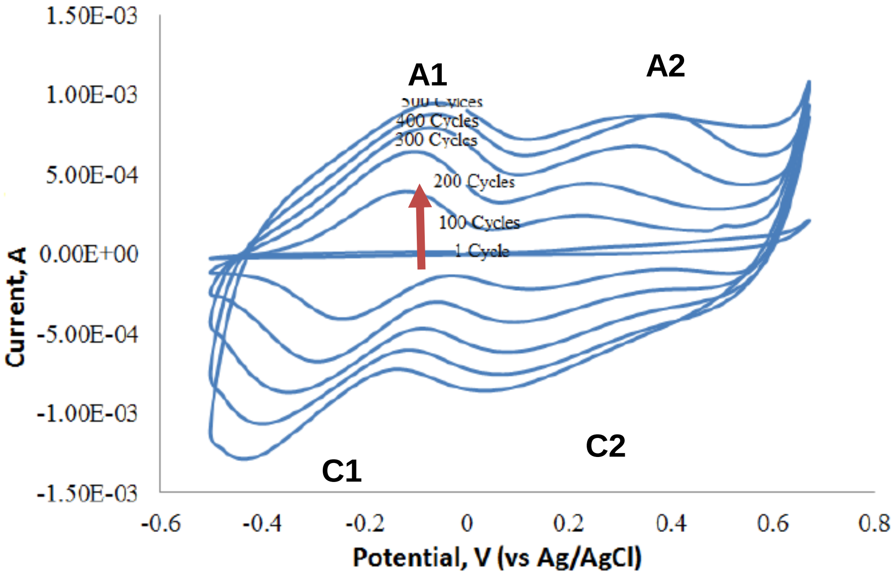

Figure 2-39 Electrodeposition of iridium oxide on stainless steel samples using cyclic voltammetry [165].

These two redox processes are important as they mainly control the characteristic of the film. Thus, choosing the correct scan range is essential to achieve the best iridium oxide film. The literature reported the scan ranges of different substrates for examples the scan range for stainless steel is (-0.5 to o.65) V, titanium (0 to 1) V and platinum (0.2 to 0.75) V all versus (Ag/AgCl) [145, 165, 168].

CV is controlled by three parameters which are scan range, number of cycles and scan rate. The scan range depends on the type of substrates.

On the other hand, Kakooei et al. [173] studied the effect of the other two parameters on the iridium oxide film on stainless steel samples and found these parameters are significant (as shown in Figure 2-40). They reported that the increase of the number of cycles leads to enhanced iridium thickness which leads to a decrease in the response of the probe. Furthermore, they concluded that the most efficient probe is not the one with the thickest iridium oxide film [173].

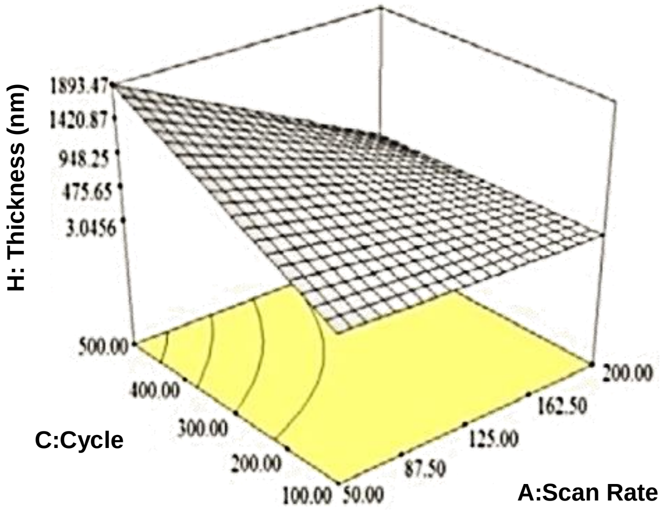

Figure 2-40 Response surface and contour plot of IrOx coating thickness (nm) as a function of the number of cycles and scan rate at room temperature [173].

Kakooei et al. suggested (100 to 300) cycles and (50 mV/s) as the optimum number of cycles and scan rate to achieve good iridium oxide coating [173].

2.21.3 Iridium Oxide Probe Sensing Mechanism and Response to pH

As mentioned earlier, pH is the activity of the hydrogen ions. Thus, the evaluation of alkalinity or acidity is based on a comparison scale. This scale represents the effective concentration of hydrogen ions. The pH scale has the range from 0 to 14. The pH has been measured using glass electrodes. The glass pH probe is a combination of indicating electrode and reference electrode in a single electrode. The indicating electrode is made of a material sensitive to the activity of H^+ [174]. The reference electrode in this kind of probes is either a calomel electrode or a silver-silver chloride (Ag/AgCl) electrode. The mechanism of working of this type of electrodes is that on immersion the hydrogen ions in solution exchange electrons with the electrode which creates a potential. The amplifier transmits the potential difference between the two electrodes and converts it to pH units [174]. The relation between the potential and pH can be defined using the Nernst equation (2-7). The equation can be modified and presented in the following formulae:

$$\mathbf{E} = \mathbf{\mathring{E}} - \frac{\mathbf{R\,T}}{\mathbf{F}}\,\mathbf{ln}\;a_{H+} \qquad (2\text{-}75)$$

$$\mathbf{E} = \mathbf{\mathring{E}} - \frac{\mathbf{R\,T}}{\mathbf{M\,F}}\,\mathbf{log}\;a_{H+} \qquad (2\text{-}76)$$

$$\mathbf{E} = \mathbf{\mathring{E}} - \frac{\mathbf{R\,T}}{\mathbf{M\,F}}\,\mathbf{pH} \qquad (2\text{-}77)$$

where: E is the measured potential (mV) at temperature T (Kelvin), E° is standard potential (mV), R is the molar gas constant (8.3144 J/ mol.K), M is a factor to convert Ln to Log (2.303), F is Faraday constant (96485 C/mol) and T is temperature (Kelvin).

Therefore, at a given temperature equation (2-77) can be used to calculate pH, where E° is the slope of the calibration curves. The value of E° slightly changes as the temperature changes similar to Figure **2-41**. Thus the reading needs to be corrected to take into account the effect of temperature.

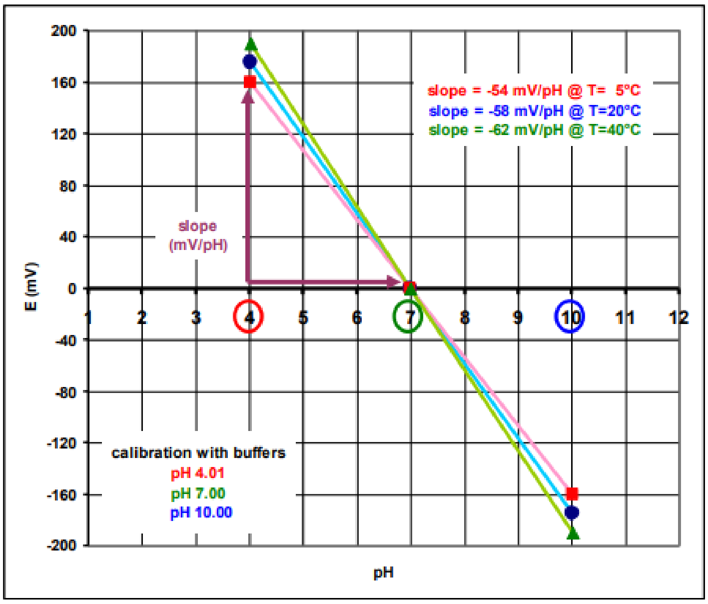

Figure 2-41 Effect of temperature on the Nernst slope of a pH calibration [175].

On the other hand, the mechanism of the iridium oxide probe is a little different from the standard glass probe. The response of the iridium probe does not depend on the solution- electrode interface. It depends on H^+ activity and oxidation state of IrOx. The response of the iridium oxide probe to the change in pH is related to the transition between two oxidation states of an electroactive couple (Ir(III) oxide and Ir(IV) oxide) [176]. The reaction can be written as follows:

$$\textbf{Ir(IV) oxide} + \mathbf{qH^+} + \mathbf{ne^-} \leftrightarrow \textbf{Ir(III) oxide} + \mathbf{rH_2O}. \tag{2-78}$$

where q, n, and r are stoichiometric coefficients.

In the case of electrodeposited iridium oxide, the iridium film is very hydrous as it forms in an aqueous solution. During the hydration process, IrO_2 hydrates to form Ir_2O_3 similar to reaction (2-79). The pH response is likely associated to electrons exchanged during the hydration reaction [176].

$$\mathbf{2[IrO_2(OH)_2\,2H_2O]^{2-} + 3H^+ + 2e^- \leftrightarrow [Ir_2O_3(OH)_3\,3H_2O]^{3-} + 3H_2O} \tag{2-79}$$

The Nernst equation can be used to calculate the potential. The question can be written in the following form [177].

$$\mathbf{E = E^{\circ} - \frac{R\,T}{n\,F}\,\ln \frac{[[Ir_2O_3(OH)_3\;3H_2O]^{3-}]}{[[IrO_2(OH)_2\;2H_2O]^{2-}]^2}}. \tag{2-80}$$

The Nernstian response which represents the slope of the calibration curves of iridium oxide when calibrated in three buffer solution (4,7 and 9) varies depending on substrates and the thickness of iridium oxide. The results of Kakooei et al. [165] in Figure **2-42** showed that the electrodeposited iridium oxide on stainless steel has the Nernstian response of (60 to 75) mV Vs. (Ag/AgCl). The change in the Nernstian response can be attributed to the change in iridium oxide thickness. As the iridium oxide became thicker the response reduces.

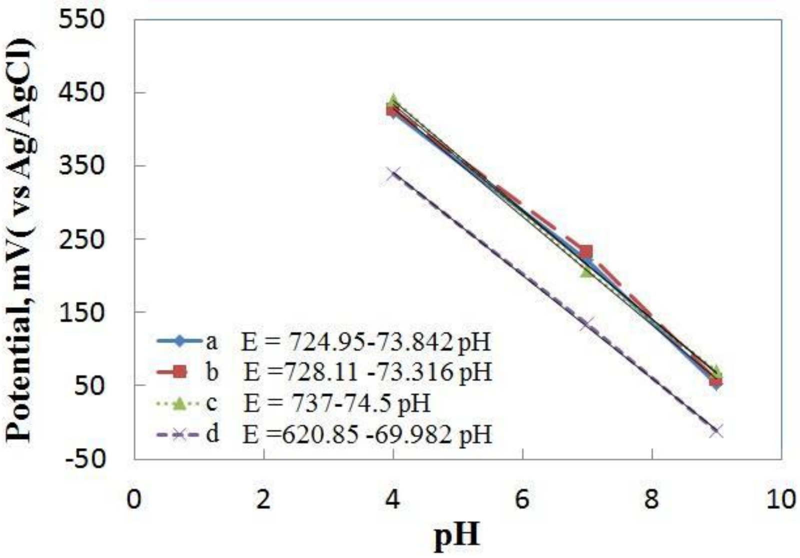

Figure 2-42 The response of the iridium oxide electrodes to a series of universal buffer solutions [165].

Chapter 3 Experimental Methods

This chapter focuses on the experimental component of the thesis. This studies the effect of roughness on the mass transfer in both N_2 and CO_2 environments. The limiting current technique is used to measure the mass transfer of H^+ for the case of N_2 and the combined mass transfer of H^+ and H_2CO_3 for the case of CO_2. The results in the N_2 environment are used to assess the validity of the reported correlations in the literature to predict the mass transfer for rough surfaces. On the other hand, the results in the CO_2 environment assess if the surface roughness has any effect on the value of limiting current in the CO_2 environment.

Experiments were also conducted to investigate the near surface pH using both the mesh capped probe technique and the electrodeposited iridium oxide probe technique. The experimental results of the near-surface pH measurements in CO_2 environments will be used as a benchmark to compare these results with the surface pH results from the mechanistic models to assess the reliability of this type of models.

Furthermore, the experiments explore the effect of roughness on the corrosion rate in the CO_2 environments. Electrochemical measurements were taken in the form of LPR measurements.

3.1 Effect of Roughness on Mass Transfer

This section provides the experimental procedure which is used to study the role of surface roughness on mass transfer. The experimental work is divided into a number of stages: initially, the first stage starts with preparation of samples and solution. This stage includes the way to manufacture the samples and the analysis of surface topography using white light interferometry. The results of the surface analysis can be used in the next stage to see how the surface factors affect the mass transfer. In the second stage, the smooth samples are tested in an N_2 environment using an RCE setup. Results from this stage are compared against well-known theoretical correlations to check their validity. Later, the samples with different surface roughness are tested in the same environment as smooth samples. The results from these samples provide an understanding of the surface roughness that can affect the mass transfer of X65 carbon steel in a low pH deaerated environment emphasising the sensitivity of this process. Furthermore, the results are compared first against the smooth samples and second against the correlations of rough samples to highlight the validity of these correlations and to check if a new correlation will need to be obtained. The final stage is carried out in a CO_2 environment to see how the surface roughness will affect the value of the mass transfer of carbonic acid. Figure 3-1 provides an overview of the tests done to study the role of surface roughness on mass transfer and the subsequent analysis.

Figure 3-1 Summary of roughness effects on the mass transfer experiments.

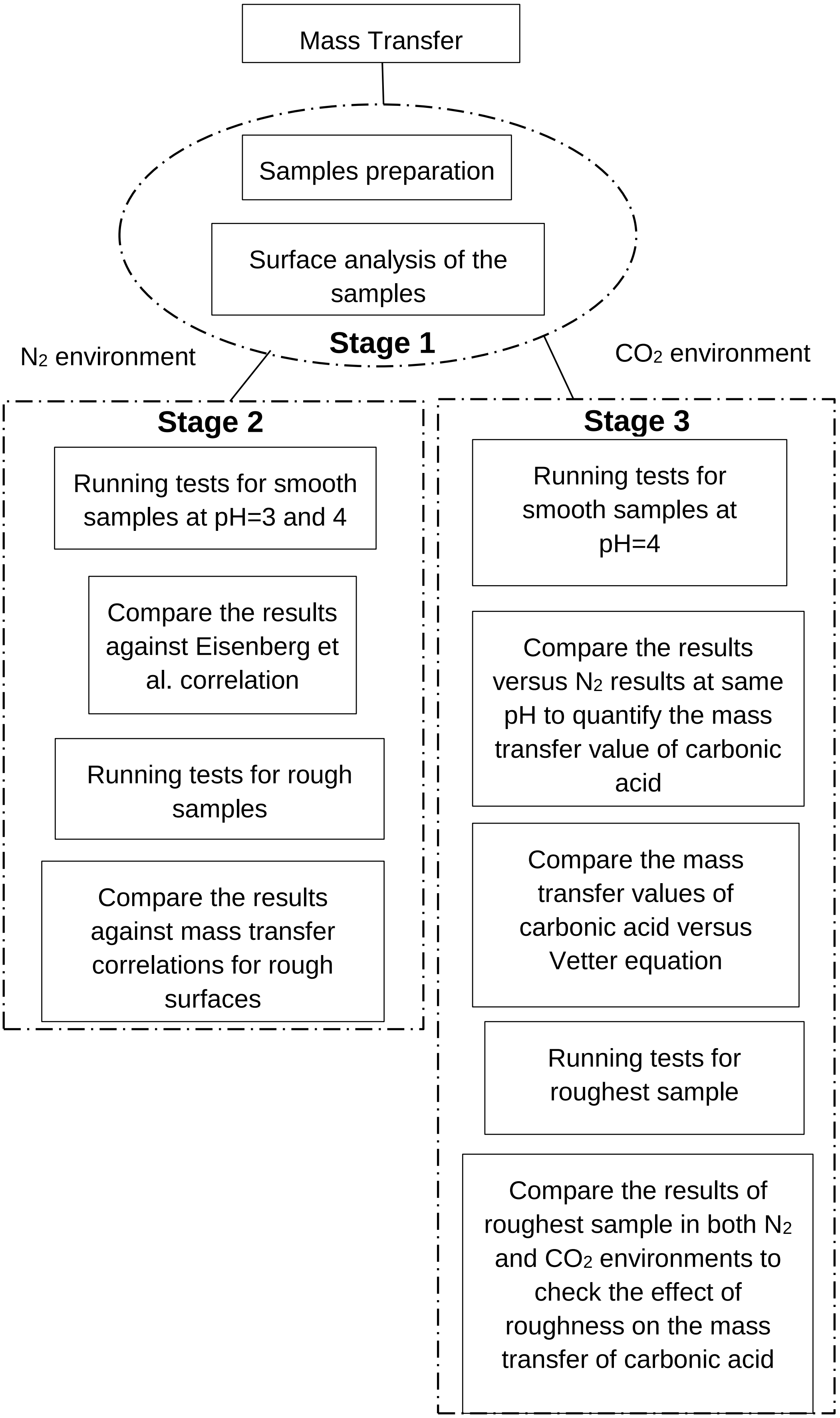

3.1.1 Materials and Sample Preparation

Four RCE samples with different surface finishes were prepared using a hardinge lathe. Various speed feeds and cut depths are selected to ensure each sample set would be consistent. Three samples are rough and one is smooth. The electrodes were made of carbon steel X65 with 1.2 cm diameter and 1 cm length. The surface texture of the samples was analysed using white light interferometry, a non-contact optical technique for surface height measurements which is capable of resolving surface topography down to tens of nanometers.

X65 (UNS K03014) is the material used in this project as the corroding sample. The steel elements composition is shown in Table 3-1. The table shows iron as the primary element while the content of carbon is below 2.5 wt%.

Table 3-1 X-65 carbon steel elemental composition in weight percentage.

C	Si	P	S	Mo	Ni	Nb	V	Mn	Fe
0.150	0.220	0.025	0.002	0.170	0.090	0.054	0.057	1.422	97.810

3.1.1.1 Surface Profilometry

White light interferometry was used to characterise the surface roughness of the samples and to quantify the actual surface area of the samples. It is a spectroscopic technique which is based on the interference between wave fronts of light beams exiting the same source and allowing the measurement of small surface irregularities.

The NPFLEX 3D Machine at the University of Leeds which is manufactured by Bruker acts as an optical device that divides a beam of white light exiting a single source into two beams and then recombines them in order to create an interference pattern.

The surface of the carbon steel sample is first cleaned with acetone and then dried with air before the roughness analysis with light interferometry.

3.1.2 Equipment and Test Conditions

Experiments were conducted in a 1L glass cell at atmospheric pressure and 25^{o}C. A three electrode setup (Figure 3-2) was employed for all experiments. The setup comprises a working electrode (RCE sample), a reference electrode (Ag/AgCl) and a counter electrode (platinum). Electrochemical measurements were performed using a potentiostat (ivium COMPACTSTAT.h) connected to a computer.

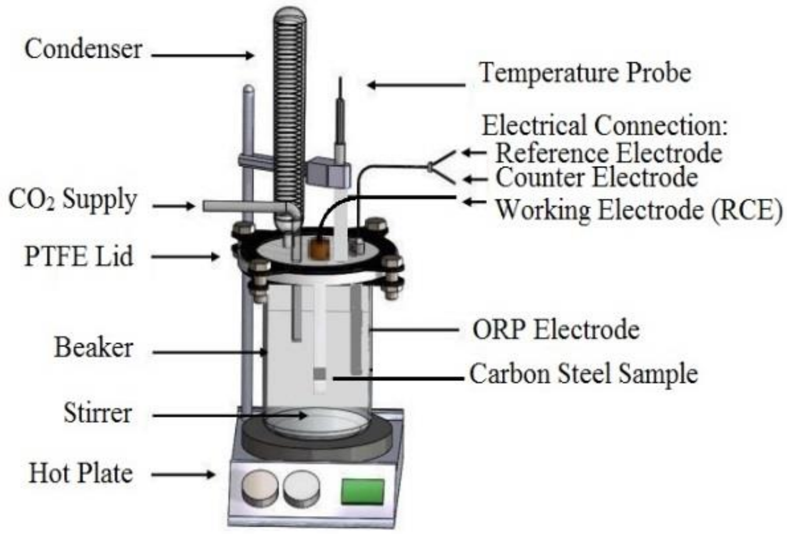

Figure 3-2 Schematic of the RCE three electrode cell.

The tests were performed at rotational velocities between 1000 and 4000 rpm in a 1 wt.% NaCl solution saturated with either nitrogen (N_2) or carbon dioxide (CO_2) gas for 24 hours prior to the experiments to ensure that the system was free from oxygen. Bubbling of gas into the electrolyte was also maintained over the duration of each experiment and temperature was controlled with the aid of a hotplate and thermocouple. The pH of the system was initially measured using a pH probe directly immersed into the electrolyte and adjusted to the desired value using either dilute hydrochloric acid (HCl) or sodium bicarbonate ($NaHCO_3$). The full matrix of test conditions evaluated is provided in Table 3-2.

Table 3-2 Experimental test matrix.

Working Environment	N_2, CO_2	Uncertainty
pH	3, 4	± 0.03
Temperature	25°C	±0.1
Total Pressure	1bar	
NaCl Concentration	1wt.%	± 0.1
Rotation Speed	1000 – 4000 RPM	± 10

3.1.3 Mass transfer Measurements Using the Limiting Current Technique

The glass vessel was filled with 1L of 1 wt.% NaCl solution and CO_2 or N_2 gas was bubbled into the electrolyte for 24 hours to saturate the solution and remove oxygen. When required, the pH of the solution was adjusted through the addition of either dilute HCl or $NaHCO_3$. Prior to each experiment the samples were degreased with acetone, rinsed with distilled water and then dried with compressed air before mounting onto the RCE shaft. The open circuit potential of the material was then allowed to stabilise for 10 minutes before starting the experiment.

To determine the mass transfer in each system, the limiting current technique was implemented. This methodology has been used by many researchers, e.g. [112, 126, 138], and been shown to provide reliable results in relation to the mass transfer of species.

The technique works by performing cathodic potential sweeps on the working electrode and evaluating the point at which current becomes insensitive to potential variation. This point is known as the limiting current and in this region, it has been shown that the hydrogen evolution reaction can proceed only as fast as H^+ ions can diffuse from the bulk solution to the surface. This enables the mass transfer coefficient to be determined using Equation (3-1)

$$\mathbf{k} = \frac{\mathbf{i_{lim}}}{\mathbf{A\ z\ F\ C_b}}. \qquad (3\text{-}1)$$

where: i_{lim} is the limiting current (Amp/m^2), A is the area (m^2), z is the number of electrons exchanged per mole of reactants and C_b is the bulk concentration (mol/m^3).

The limiting current technique was implemented to calculate the mass transfer in both N_2 and CO_2 environments. All cathodic sweeps were performed individually, starting from 15 mV above the Open Circuit Potential (OCP), and finishing at approximately -400 mV vs OCP at a scan rate of 0.5 mV/s.

3.1.3.1 Mass Transfer Measurements for Smooth and Rough Surfaces in N_2 Environments

Experiments were run at pH 3 in an N_2 environment to characterise the mass transfer of hydrogen ions. In the N_2 environments, the hydrogen evolution reaction is the dominant reaction. The mass transfer results of the N_2 environment will be used to subtract the effect of hydrogen ions from the total limiting current in the CO_2 environments to calculate the carbonic acid limiting current value.

The limiting current technique was used to check the limiting current of hydrogen ions as a function of rotation speed for a smooth surface. Tests were performed in pH 3 solution saturated with N_2. The results of mass transfer were checked against the Eisenberg et al. [28] correlation to assess the validity of this correlation and to check how the mass transfer is changing with the change of the rotation speed.

The work by Eisenberg et al. [28] conducted a comprehensive study on mass transfer from a smooth RCE surface. Their data for turbulent conditions was correlated with (3-2) and is most often used to characterise mass transfer behaviour of a smooth RCE geometry. Based on this relationship for smooth surfaces, the Eisenberg et al. correlation [28] suggests that the mass transfer coefficient is proportional to $U_{RCE}^{0.7}$ for the RCE.

$$\mathbf{Sh = 0.0791\ Re^{0.70} Sc^{0.356}}. \tag{3-2}$$

On other hand, tests performed on rough surfaces in N_2 environments enabled the influence of surface roughness on mass transfer of hydrogen ions to be evaluated. The increase in surface roughness leads to an increase in the actual area. Thus, all the results of the rough samples were corrected with the true surface area in order to show the effect of surface roughness on mass transfer. Also, the results were compared against well-known equations for rough surfaces to check the validity of these equations.

3.1.3.2 Comparison Between Mass Transfer Measurements for Smooth and Rough Surfaces in N_2 and CO_2 Environments

For smooth surfaces, experiments in CO_2 environments were used to assess the combined limiting current for both H^+ and H_2CO_3 (i.e. that associated with the buffering effect of carbonic acid) [59] at pH 4 to understand the sensitivity of each component to rotation speed. Thus, limiting current measurements were used to check the mass transfer in N_2 and CO_2 environments. The difference in limiting current in both cases (N_2 and CO_2) represents the limiting current of carbonic acid ($i_{lim,H2CO3}$). The limiting current of carbonic acid has been estimated using Vetter's correlation Equation (3-3) [124]. Thus, the experimental results were compared against Vetter's correlation [124] to evaluate the accuracy of this correlation.

$$\mathbf{i_{lim\ H_2CO_3} = F\ C_{b,H_2CO_3}\ \sqrt{k_{-1}\ \ D_{H_2CO_3}}\ .} \tag{3-3}$$

While in case of rough surfaces, tests were performed at the highest speed, 4000 rpm, in both N_2 and CO_2 environments at pH 4 enabled the influence of surface roughness on the limiting current of carbonic and how this component changes with the change of the surface roughness. Finally, Vetter's formula [124] which has been used to calculate the limiting current for carbonic acid is assessed to check if a correction factor needs to be applied for the case of rough surfaces.

3.2 Near Surface pH Measurements

The surface pH measurements were limited to few applications such as medical and biological applications. However, few studies focused on studying the surface pH during corrosion of carbon steel in CO_2 environments. Han et al. [32] studied the near surface pH using the mesh capped probe. This method has many limitations including the fragility of pH probe and difficulties to implement this design for flowing systems.

Developments in metal oxide pH probes have helped researchers to study the near surface pH in corrosive environments. Zhu et al. [168] used iridium oxide probes to study the surface pH of stainless steel samples in saline solution. Also, Da Silva et al. [178] studied the effect of surface pH on the initiation of pits in high Cl^- contents solution.

Thus, the experimental work of the near surface pH compares the iridium oxide probe results which were not used before to measure surface pH with the mesh capped probe results. Comparison of both experiments will help to evaluate the results of both techniques. Also, it will identify the best method to measure the surface pH for corroded surfaces for both static and dynamic conditions.

The near surface pH experimental work is divided into a number of parts; the first part is the design and setup of the mesh-capped probe and the second part is preparation and deposition of iridium oxide on substrates and the third is the equipment and test conditions.

3.2.1 Mesh Capped pH Probe

A commercial pH probe which is designed to monitor the surface pH was employed in the surface pH measurement in CO_2 environments. The probe was fitted in its place (as shown in Figure **3-3**) using a compression fitting. The pH probe was calibrated using standard buffer solutions before each experiment. A fine mild steel single mesh was cut to circular shape to fit the size of the compression cap. The mesh was analysed using SEM/EDX technique (which will be reviewed later) and found to have the properties shown in Table **3-3** and Table **3-4**.

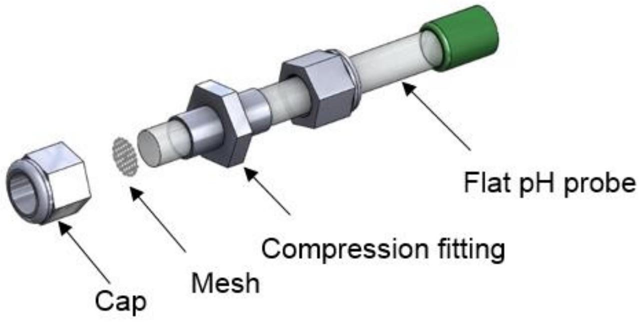

Figure 3-3 A schematic of surface pH design.

Mesh Type	Single
Mesh Size	60 per 2.54 cm
Mesh wire diameter	0.1905 mm
Mesh open area	30 %

Table 3-3 Mild steel mesh properties.

C	O	Si	Mn	Fe
0.19	5.63	0.17	0.33	93.68

Table 3-4 Mild steel mesh elemental composition in weight percentage.

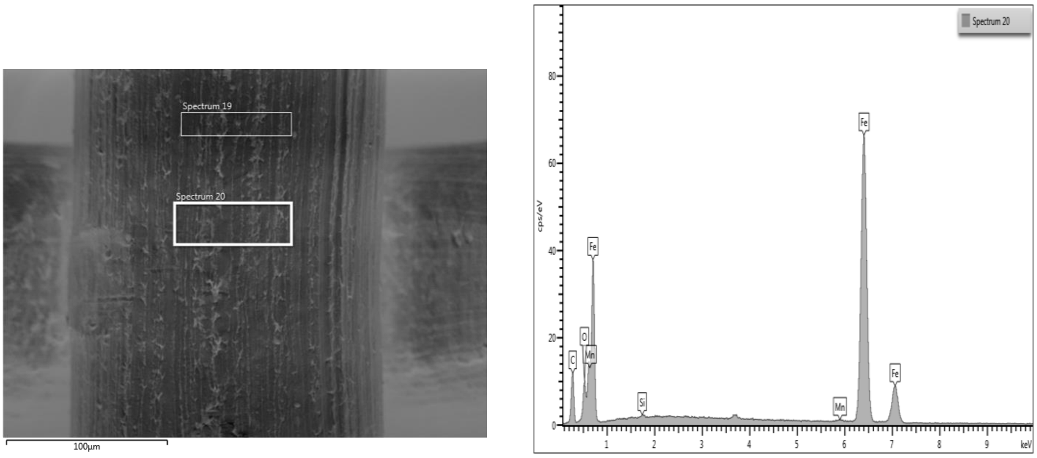

Figure 3-4 SEM and EDx images of a single sheet mesh.

Before each experiment, the mesh was cut and cleaned with acetone and distilled water then dried with compressed air. The cap was tightened well into the fitting. Then, the probe was deployed in the solution. The tests were run for 4 hours and the surface pH values were recorded every 30 mins. Each experiment was repeated at least two times to check the repeatability of the tests.

3.2.2 Scanning Electron Microscopy (SEM) and Energy Dispersive X-ray (EDX)

SEM is a quantitative surface analysis technique which is used to analyse the surface of the mesh sample. The machine provides high resolution images. The machine is the Carl Zeiss EVO MA15 (Shown in Figure 3-5) which requires sample preparation prior analysis. The sample was mounted on the sample holder using double sided tape. The edges of the sample were painted with a conductive graphite paint to form a bridge between the top of the sample and sample holder. After sample preparation, the SEM machine was vented and opened and the sample was adjusted securely on to the stage. The machine was closed and vacuumed. Then, the SEM analysis was done using the machine.

The same machine was used for the EDX analysis. EDX analysis was used to characterise the elements of the mesh. EDX is a micro-analytical technique which is used in conjunction with the SEM. EDX provides a report about the chemical characterisation of the scanned sample.

Figure 3-5 An image of Carl Zeiss EVO MA15 SEM and EDX machine.

3.2.3 The Iridium Oxide Probe

In this case, experiments were carried out by deposition of iridium oxide on stainless steel 316L samples. The samples were machined to 2 mm diameter. Electrodes were connected to the wire and then all areas were insulated with PTFE insulator except the surface area where iridium oxide was deposited. Electrodes were polished with sandpaper to roughen the surface, degreased with acetone, rinsed with distilled water and then dried with compressed air.

3.2.3.1 Iridium Oxide Solution

The solution was prepared using the procedure suggested by Marzouk [156]. This procedure was also used by other researchers to prepare iridium oxide solution [145, 165, 168]. The solution was prepared by dissolving 150 mg Iridium (IV) chloride in 100 ml distilled water. The solution was stirred for 15 mins, followed by addition of 1 ml H_2O_2. 10 mins later, 365 mg of oxalic acid dihydrate was added. After 10 mins of stirring, the solution pH was increased slowly and adjusted to 10.5 by adding potassium carbonate. A light green colour solution was obtained. The solution was left from two to three days to age and achieve a dark blue solution. After that the solution will be ready for electrodeposition.

3.2.3.2 Electrodeposition Procedure

The process of electrodeposition of iridium oxide was performed using a multichannel ivium potentiostat. The process was done by depositing iridium oxide on the substrates at room temperature using a standard three electrode cell. The electrodeposition was carried out using the cyclic voltammetry (CV) technique. A working electrode was the metal (stainless steel) and a reference electrode (Ag/AgCl) and a counter electrode (platinum). 300 cycles and a scan rate of 50 mV/s were used to produce a good iridium oxide coating. The scan range was between -0.5 to 0.65 V (vs Ag/ AgCl). After the electrodeposition, the probe was soaked in water overnight and later calibrated using three standard buffer solutions (4, 7 and 10). The open circuit potential (OCP) of the probe was monitored until a stable reading was achieved.

3.2.3.3 Equipment and Test Conditions

Experiments were conducted in a 1L glass cell at atmospheric pressure. The three electrode setup was employed for the experiments.

The tests were performed in a 1 wt.% NaCl solution saturated with carbon dioxide (CO_2) gas for 24 hours prior to the experiments to ensure that the system was free from oxygen. Bubbling of gas into the electrolyte was also maintained over the duration of each experiment and temperature was controlled with the aid of a hotplate and thermocouple. The pH of the system was initially measured using a glass pH probe directly immersed into the electrolyte and adjusted to the desired value using either dilute hydrochloric acid (HCl) or sodium bicarbonate ($NaHCO_3$). The full matrix of test conditions evaluated for both cases is provided in Table **3-5**.

Working Environment	**CO_2**	**Uncertainty**
pH	4,5 and 6	± 0.05
Temperature	25 °C	±0.1
Total Pressure	1 bar	
NaCl Concentration	1 wt.%	± 0.1

Table 3-5 Experimental test matrix for the near surface pH tests.

The carbon steel samples were cut to the desired dimensions of 25 mm diameter and a 2 mm hole drilled in the middle of the samples. The machined coupons were initially soldered to the wire and then mounted in nonconductive resin. The exposed area of the samples was polished using different sizes of abrasive sand paper. The samples were then degreased with acetone, rinsed with distilled water and dried with compressed air. The iridium oxide probes were fitted in the samples' hole (as shown in Figure **3-6**) so the in-situ near surface pH measurement can be obtained.

In both cases, the experiments were run in static conditions. The experimental results of the mesh capped probe were compared against the iridium oxide probe to reveal how comparable they were.

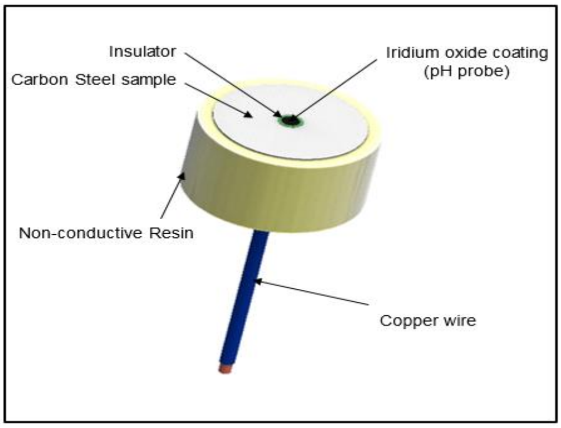

Figure 3-6 Schematic of iridium oxide probe impeded in a carbon steel sample.

3.3 Effect of Roughness on Corrosion Rates

The surface roughness of pipes has a roughness of order of the 20 microns and may even exceed 50 microns [179], yet laboratory experiments in CO_2 environments tend to be with samples which are wet-ground to sub-micron surface finishes (i.e. 1200 grit SiC paper). This is despite the fact that surface roughness is believed to contribute significantly towards corrosion rates in CO_2-containing environments [33] based on the notion that surface topography can affect the electrochemical response of the corroding material.

Given that some of the electrochemical processes on carbon steel surfaces in CO_2 environments are influenced by mass-transfer (particularly in solutions close to pH 4). Numerous studies have shown rough surfaces can enhance mass-transfer, there is clearly a need for greater awareness and fundamental understanding of the role of surface roughening on corrosion rates in CO_2 environments and how this relates to the transport of species to and from the steel surface and the impact that this has on material dissolution.

In relation to experimentally observing the effect of surface roughness, the Rotating Cylinder Electrode (RCE) provides a convenient means of generating a uniform reaction environment for fundamental and engineering studies of corrosion and mass-transfer under open-circuit, controlled potential or constant current conditions, and is the experimental apparatus of choice for this study. This part utilises the Linear Polarisation Resistance (LPR) technique in conjunction with the RCE to study the effect of surface roughness on carbon steel corrosion rate in CO_2 environments.

3.3.1 Materials and Sample Preparation

Four RCE samples (similar to the one used in mass transfer experiments) with different surface finishes were prepared using a hardinge lathe. The electrodes shown in Figure 3-7 were made of carbon steel X65 with 1.2 cm diameter and 1 cm length.

Figure 3-7 Images of the RCE samples with different surface roughnesses.

3.3.2 Corrosion Rate Measurements

Prior to each experiment the samples were degreased with acetone, rinsed with distilled water and then dried with compressed air before mounting onto the RCE shaft. The open circuit potential of the material was then allowed to stabilise for 10 minutes before starting each experiment. Following stabilisation of the OCP, *in situ* corrosion rates were recorded by means of the DC LPR technique. LPR measurements were conducted by polarising the sample ±15 mV with respect to the open circuit potential, scanning at a rate of 0.25 mV/s to obtain a polarisation resistance, R_p (Ohm.cm^2). LPR measurements were undertaken every 10 minutes over a total period of 3 h.

In all experiments, the solution resistance, R_s (Ohm.cm^2) was determined after LPR measurements were complete using electrochemical impedance spectroscopy (EIS). This consisted of polarising the sample ±5 mV vs. the OCP using a frequency range from 20 kHz to 0.1 Hz. The value of R_s was subtracted from R_p to produce a charge-transfer resistance, R_{ct} (Ohm.cm^2) which was used to determine the corrosion rate behaviour with time:

$$\mathbf{R_{ct} = R_p - R_s} \tag{3-4}$$

Potentiodynamic measurements were also performed on each sample at the end of the 3 hours test. This technique was used to generate Tafel polarisation curves to determine the anodic and cathodic Tafel constants (β_a and β_c, respectively in mV/decade) and ultimately an appropriate Stern-Geary coefficient (B) to enable calculation of corrosion rates from the values of R_{ct} determined as a function of time in each experiment.

Tafel polarisation curves were also collected by performing individual anodic and cathodic sweeps starting at OCP and scanning to either 250 mV or -500 mV vs. OCP, respectively at a scan rate of 0.5 mV/s. Only one Tafel curve (either anodic or cathodic) was generated at the end of each experiment as significant polarisation can alter the surface characteristics.

From the polarisation curves produced, it was possible to determine β_a and β_c by measuring their respective gradients over regions where linearity was observed between the applied voltage and the natural log of the measured current. The Tafel slope measurements were used to determine the Stern-Geary coefficient (B), and the corrosion current density, i_{corr} (mA/cm^2):

$$\mathbf{B = \frac{\beta_a \beta_c}{2.303(\beta_a + \beta_c)}} \tag{3-5}$$

$$\mathbf{i_{corr} = \frac{\beta_a \beta_c}{2.303 R_{ct}(\beta_a + \beta_c)}} \tag{3-6}$$

where β_a and β_c are the Tafel constants representing the anodic and cathodic Tafel slopes of corrosion process in (V/decade). The i_{corr} value obtained was used in combination with Faraday's Law and the measured values of R_{ct} to determine the corrosion rate (CR) in mm/year

$$\mathbf{CR} = \frac{\mathbf{3.27 i_{corr} M_{Fe}}}{\mathbf{n\rho}} \qquad (3\text{-}7)$$

where 3.27 is a conversion factor (mm.g/(mA.cm.year)), M_{Fe} is the atomic mass of iron = 55.845 g/mol, n=2 is the number of electrons generated in the anodic reaction per mole of iron and ρ the density of iron (g/cm^3).

Each experiment was repeated at least twice and the values of corrosion rate reported in this work reflect the average of multiple LPR measurements over both 3 hour tests complete with errors bars which indicate the maximum and minimum corrosion rates determined from the individual measurements across all experiments.

3.3.3 Corrosion Rate Measurements for Smooth Samples under Dynamic Conditions

A series of experimental measurements of corrosion rate for RCE systems in aqueous CO_2 solutions was carried out. For smooth RCE samples, corrosion rate values from the RCE experiments were studied by varying the solution pH and the rotational speed of the RCE. The effect of velocity was studied at pH=4, 5 and 6. The rotation speed started with 1000 rpm (0.628 m/s) and increased up to 4000 rpm (2.512 m/s). The full matrix of test conditions evaluated is provided in Table 3-6.

Table 3-6 Experimental test matrix of corrosion rate experiments for smooth samples.

Working Environment	**CO_2**
pH	4, 5 and 6
Temperature	25°C
Total Pressure	1bar
NaCl Concentration	1wt.%
Rotation Speed	1000 – 4000 rpm

3.3.4 Corrosion Rate Measurements for Rough Samples under Static Conditions

It is generally accepted that an increase in surface roughness leads to higher corrosion rates, since rough surfaces have a larger interfacial area with the corrosive environment and can induce localised mass transfer between surface peaks [180]. Few studies have quantified the effect of the increase in surface area on the values of corrosion rates in CO_2 environments. For example, Asma et al. [103] studied the effect of surface polishing on corrosion rates at room temperature, pH 5.5, 3wt.% NaCl and for carbon steel BS970. Six different sand papers were used to apply different surface finish on samples.

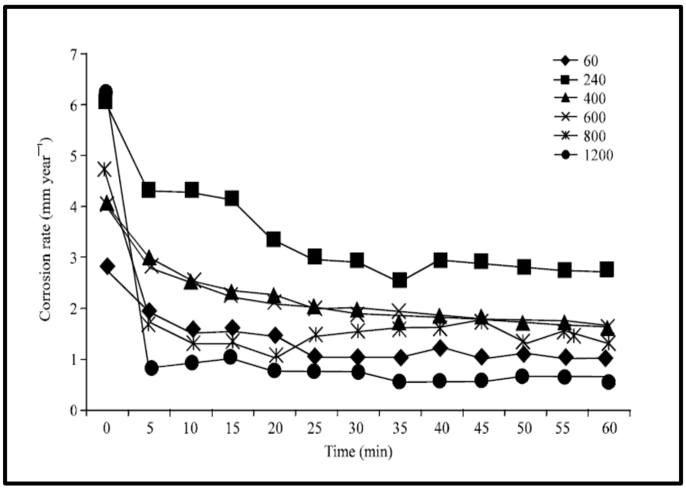

Figure 3-8 Average corrosion rate of mild steel samples with different surface roughness in CO_2 saturated environment at pH=5.5, 22°C and 1000 rpm [103].

As shown in Figure 3-8, their results revealed that the increase in the degree of roughness leads to an increase in corrosion rate. This was attributed to the larger surface area which is in contact with the corrosive environment. However, in their work they did not correct the corrosion rate results with the actual surface area. So it is not easy to quantify how the mass transfer affects the values of corrosion when results are normalised with the actual surface area.

The first series of experiments on rough surfaces were carried out in static conditions. Tests were performed with four samples of different surface finishes of carbon steel X65 in a 1 wt.% NaCl solution saturated with carbon dioxide (CO_2) gas. The pH and temperature were 4 and 25°C respectively.

3.3.5 Corrosion Rate Measurements for Rough Samples under Dynamic Conditions

The tests were extended to cases of turbulent flow over rough carbon steel X65 surfaces. All current densities, and hence the corrosion rate, were scaled with respect to the total surface area measured using light interferometry. Tests were performed with four samples of different surface finishes in a 1wt.% NaCl solution saturated with carbon dioxide (CO_2) gas. The pH was adjusted to 4 and the temperature was 25°C. The conditions of the test are provided in Table 3-7.

Table 3-7 Experimental test matrix for rough samples under dynamic conditions.

Working Environment	**CO_2**
pH	4
Temperature	25°C
Total Pressure	1bar
NaCl Concentration	1wt.%
Rotation Speed	1000 – 4000 rpm

Chapter 4 Experimental Results – Smooth Surfaces

The following chapter includes the results and the analysis obtained from experiments conducted on smooth samples. The results of the smooth samples cover different experiments starting with mass transfer of smooth samples, near surface pH measurements and ending with corrosion rate experiments. In all cases, the experiments were repeated at least two times and error bars are included to show the repeatability of the results. The experiments were very repeatable and the maximum percentage difference among the repeated test was less than 11%.

4.1 Mass transfer Results for Smooth Samples

4.1.1 Mass Transfer Measurement for Smooth Surfaces in N_2 Environments

Experiments were initially conducted on smooth RCE samples (0.5 µm) in N_2 environments at pH 3 to obtain definitive limiting currents as a function of the rotation speed. Figure 4-1 provides examples of selected cathodic sweeps obtained and indicates that the limiting currents are clearly flow dependent. At pH=3 in an N_2 saturated environment, the increase in velocity leads to an increase in limiting current values as more H^+ ions are able to transfer from the bulk solution and react at the surface via the hydrogen-evolution reaction:

$$\mathbf{2H^{+}_{(aq)} + 2e^{-} \rightarrow H_{2(g)}} \tag{4-1}$$

With the exception of the reduction of water (which only becomes significant at high pH or very negative overpotentials), this is the only cathodic reaction in the system when the solution is de-aerated with N_2. It has been shown previously by Stern [181] that the limiting rate of the hydrogen-evolution reaction proceeds only as fast as hydrogen can diffuse from the bulk to the surface.

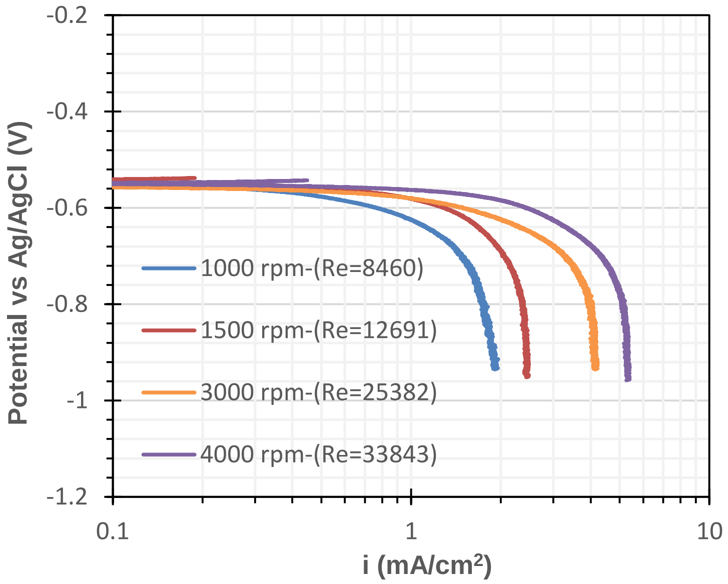

Figure 4-1 Potentiodynamic sweeps conducted in HCl solution at pH 3 purged with N_2, T=25 °C and 1 wt.% NaCl using a smooth RCE sample surface.

Mass transfer coefficient values were determined from the limiting currents of the cathodic Tafel sweeps determined from the experiments conducted for each case shown in Figure 4-1 using Equation (3-1). The Eisenberg et al. [28] correlation has been used to calculate the mass transfer for smooth samples. Thus, the limiting current results of the smooth RCE samples were compared against the Eisenberg et al. correlation. The calculated coefficients are plotted against Reynolds number in Figure 4-2 against the Eisenberg et al. correlation and an excellent agreement is obtained as the results have a 8% maximum deviation and 5.5% average deviation from the proposed relationship. These results demonstrate the validity of the technique employed in the context of H^+ ion diffusion and indicates that for a ‘smooth’ RCE surface, the mass transfer coefficient is proportional to $U_{RCE}^{0.7}$.

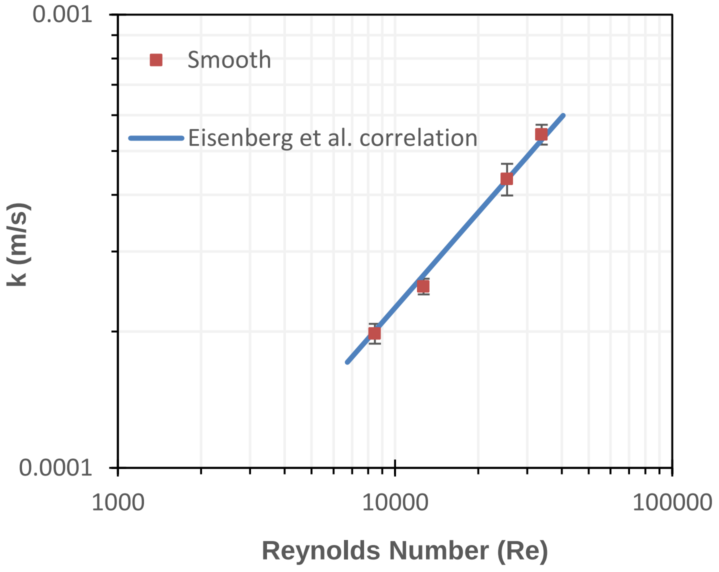

Figure 4-2 Comparison of mass transfer coefficient for a smooth surface with the Eisenberg et al. correlation.

4.2 Mass Transfer from Smooth Surfaces in CO_2 Environments

For smooth surfaces in the N_2 environment at pH 3, when a cathodic sweep is conducted, the limiting current is clearly flow dependent. In this section, N_2 experiments are compared with CO_2-containing environments at pH 4 to determine the role of CO_2 on the observed limiting currents.

In CO_2-containing environments, CO_2 dissolves in water and is hydrated to form carbonic acid.

$$\mathbf{CO_{2(aq)} + H_2O_{(l)} \rightarrow H_2CO_{3(aq)}} \quad (4\text{-}2)$$

Carbonic acid is a weak acid which partially dissociates and is responsible for the high corrosion rates observed for steel in CO_2 containing brines [33].

$$\mathbf{H_2CO_{3(aq)} \rightarrow H^+_{(aq)} + HCO^-_{3(aq)}} \quad (4\text{-}3)$$

$$\mathbf{HCO^-_{3(aq)} \rightarrow H^+_{(aq)} + CO^{2-}_{3(aq)}} \quad (4\text{-}4)$$

Figure 4-3 and Figure 4-4 show cathodic Tafel sweeps conducted at pH 4 and 25ºC in N_2 and CO_2-saturated environments, respectively, on a smooth sample. The value of limiting current in the CO_2 system is clearly higher than in the N_2 system at the same pH. This increase in limiting current is attributed to the presence of H_2CO_3 which was initially believed by DeWaard and Milliams [57] to be directly reduced at the steel surface through the reaction:

$$\mathbf{2H_2CO_{3(aq)} + 2e^- \rightarrow H_{2(g)} + 2HCO_{3(aq)}^-} \tag{4-5}$$

However, more recent research [58, 59] has shown that the reaction actually occurs via a buffering effect at the steel surface.

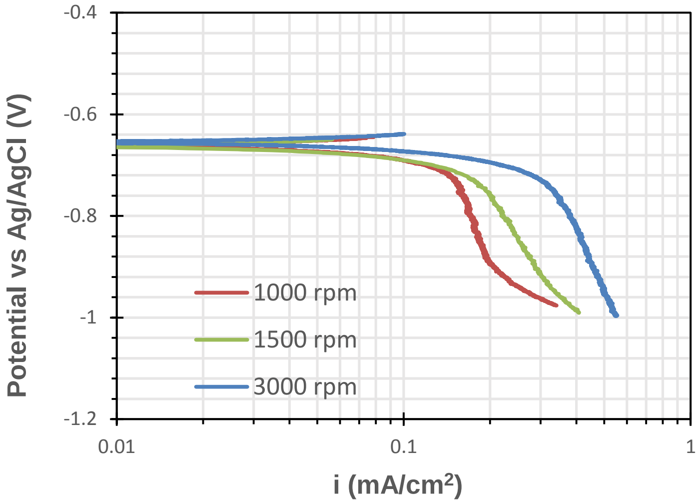

Figure 4-3 Potentiodynamic sweeps conducted in N_2 solution at pH 4, T=25 °C, 1 wt.% NaCl and different RCE speeds on a smooth sample.

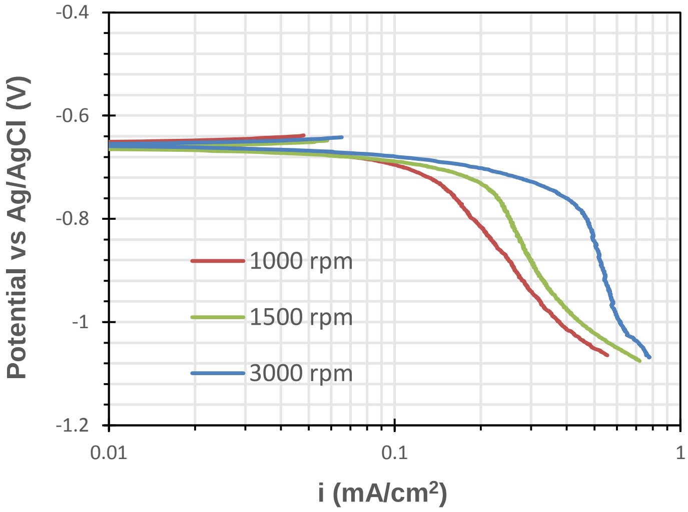

Figure 4-4 Potentiodynamic sweeps conducted in CO_2 solution at pH 4, T=25 °C, 1 wt.% NaCl and different RCE speeds on a smooth sample.

Limiting currents were recorded over the range of 1000 to 4000 rpm in both HCl (N_2) and CO_2 solutions using cathodic polarisation sweeps at pH 4 and 25°C for the smooth sample after correction for the water reduction reaction (determined by extending the cathodic polarisation sweeps to more negative potentials). The corresponding limiting currents in N_2-saturated environments are compared with those obtained previously at pH 3 and are provided in Figure 4-5(a) for the smooth sample. This figure confirms the measurement of mass transfer at low pH but also validates the corrections implemented for the water reduction reaction which enable the limiting currents to be determined more precisely, particularly at lower rotation speeds.

Figure 4-5(b) shows the difference between limiting currents observed in the N_2 and CO_2-saturated environments at pH 4. This pH was chosen as opposed to a lower pH to enable the difference between the two limiting currents to be more easily visualised (i.e. to prevent dominance of the mass-transfer controlled H^+ reduction reaction and its total contribution to the limiting current).

If it is assumed that both H^+ and H_2CO_3 play a role in the cathodic reactions, the limiting current can be divided into two components; one related to the diffusion of H^+ (quantified by the limiting current in the N_2 system) and the other associated with the role of H_2CO_3 which is quantified by the gap between the two curves in Figure 4-5(b), and is also shown more clearly in Figure 4-5(c).

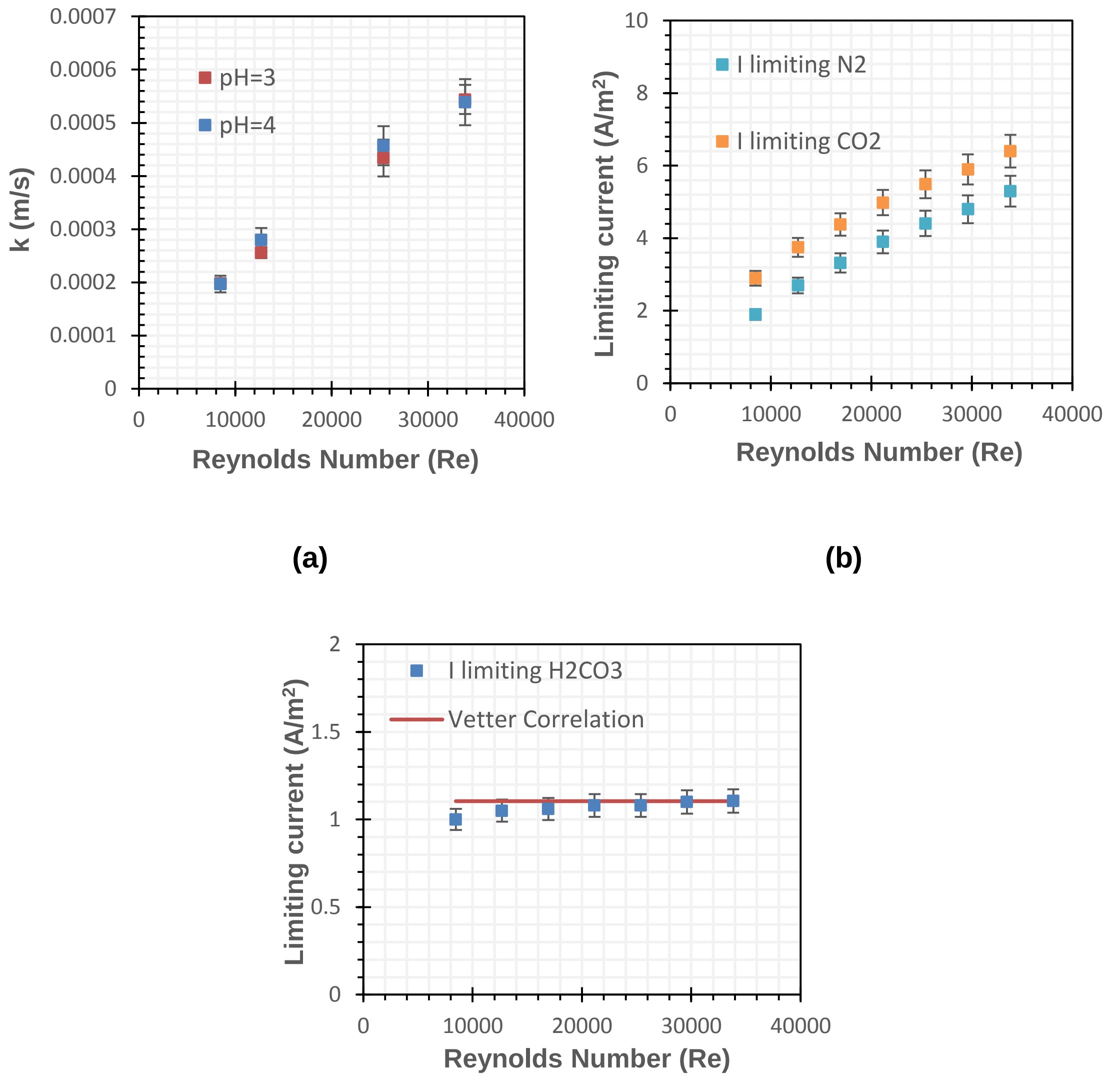

(a) **(b)**

(c)

Figure 4-5 (a) Comparison between mass transfer coefficient for smooth samples in N_2 solution at pH 3 and pH=4 T=25 °C, 1 wt.% NaCl and different RCE speeds (b) Limiting currents for smooth samples in CO_2 and N_2 solution at pH 4, T=25 °C, 1 wt.% NaCl and different RCE speeds (c) Comparison between Vetter's correlation and limiting currents of H_2CO_3.

Firstly, it appears that the observed gap between the two curves depicted in Figure 4-5(c) is insensitive to flow over the rpm ranges considered, remaining relatively constant. This is consistent with previous studies and Vetter [124] first proposed an equation to determine the magnitude of the limiting current of the carbonic acid component:

$$\mathbf{i}_{\mathbf{lim}\,\mathbf{H_2CO_3}} = \mathbf{F}\ \mathbf{C}_{\mathbf{b},\mathbf{H_2CO_3}}\sqrt{\mathbf{k}_{-1}\ \mathbf{D}_{\mathbf{H_2CO_3}}}\ . \tag{3-3}$$

This model is shown in Figure 4-5(c) and demonstrates a good agreement with the experimental data collected here for smooth samples up to 4000 rpm. However, research by Nesic et al. [115] evaluated Vetter's model and found that at high rpm (beyond ~6000 rpm) the $i_{\mathrm{lim\ H2CO3}}$ component began to increase slightly with increasing speed, indicating that the limiting current can be influenced by flow at higher speeds. The phenomenon was attributed to the change in relative thickness between the reaction layer and diffusion layer and the fact that Vetter's model was derived for stagnant conditions or systems where the reaction layer is much smaller than the diffusion layer. Based on this work, Nesic et al. [115] proposed a modification to Vetter's model using a 'flow factor':

$$\mathbf{i}_{\mathbf{lim}\,\mathbf{H_2CO_2}} = \mathbf{F}\ \mathbf{f_1}\ \mathbf{C}_{\mathbf{b},\mathbf{H_2CO_3}}\sqrt{\mathbf{k}_{-1}\ \mathbf{D}_{\mathbf{H_2CO_3}}}\ . \tag{4-6}$$

where

$$\mathbf{f_1} = \frac{1+e^{-2\zeta}}{1-e^{-2\zeta}} = \boldsymbol{coth}\zeta. \tag{4-7}$$

Unfortunately, the experimental data produced at higher rotation speeds resulted in noise from the cathodic Tafel sweeps which produced ambiguity over the limiting current values required to validate this response.

4.3 Near surface pH Measurements

4.3.1 Iridium Oxide Probe Responses

The prepared iridium oxide probes were calibrated and tested before being used in corrosion experiments. The probes showed good responses and stability over time. All pH sensors demonstrated an excellent linear correlation in the entire pH range. The calibration curves for iridium oxide probes were obtained prior to each experiment. The curves were consistent even after being tested several times and stored for several weeks. The results in Figure **4-6** show that the calibration curves of the same iridium oxide probe when calibrated using universal standard pH buffer solutions. The curves showed a linear Nernstian response with a sensitivity of -65 ± 5 mV /pH Vs. (Ag/AgCl). The Nernstian response of the probes came in agreement with the recommended range by Kakooei et al. [165]. They suggested the range (60 to 75) mV/ pH Vs. (Ag/AgCl) for the best response of electrodeposited iridium oxide probes. Thus, the calibration results demonstrate the reliability and repeatability of the pH sensors.

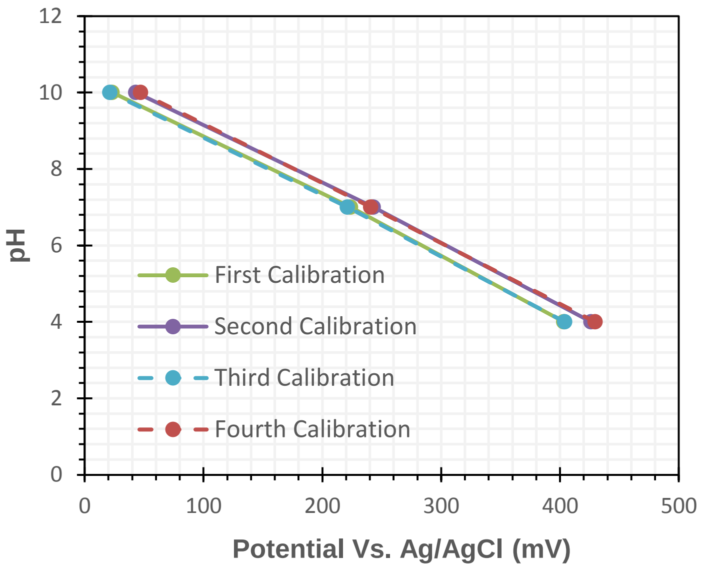

Figure 4-6 Calibration curve for the potential responses of the iridium oxide probes when calibrated with a series of standard buffer solutions prior to each experiment.

4.3.2 Stability of Iridium Oxide Probe

Stability is one of the vital features of the pH probe. The measurements of the probe should be stable over a period of time when placed in an environment where pH is constant and there are no reactions or additives which affect the value of pH. In order to test the stability of the iridium oxide probe, experiments were run in three different solutions under static conditions. The solutions were distilled water with 1wt.% NaCl saturated with CO_2. The pH values of the solutions were measured using a glass pH probe and the values are 3.89, 5.00 and 6.00 respectively. Figure **4-7** provides ocp values of the probe over time. The ocp results of the probes are fairly constant with time. Generally, the increase in solution pH leads to a decrease in potential. This comes in agreement with the calibration curves. The percentage difference between the traditional pH probe reading and the iridium oxide probe for solutions with bulk pH (3.89, 5,00 and 6,00) are (0.1, 1 and 1.5%) respectively. The results support the reliability of the iridium pH probes.

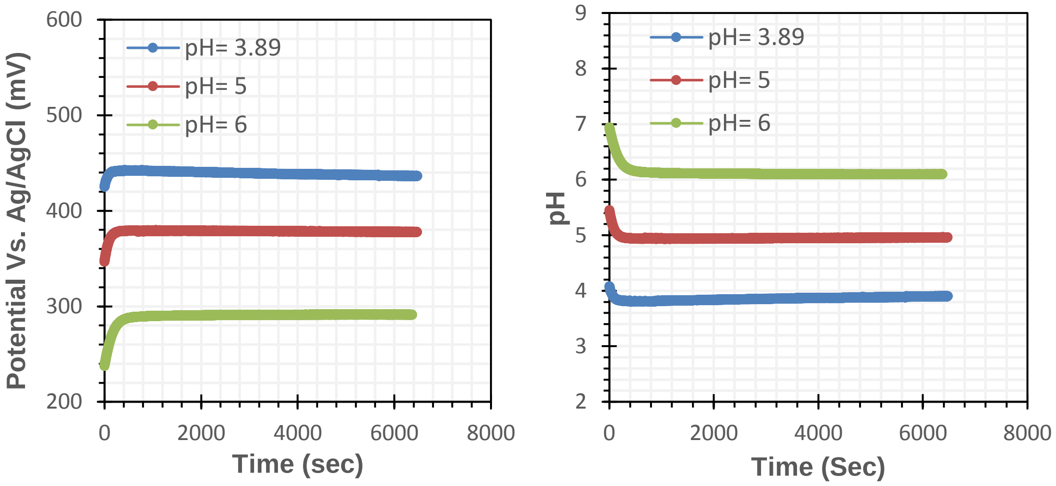

Figure 4-7 Stability of the iridium pH probes in 1wt.% solutions saturated with CO_2 with different pH (3.89, 5.00 and 6.00).

4.3.3 Near Surface pH Measurements: Comparison Between Mesh Capped Probe and Iridium Oxide Film Probe

The near surface pH measurements during corrosion of carbon steel samples were carried out using the two techniques. Tests were run for 4 hours in a solution saturated with CO_2. The solution is water with 1wt.% NaCl. The working conditions were 25°C and pH (4, 5 and 6). With the mesh capped probe, the surface pH measurements were recorded every 30 minutes. While in the case of iridium oxide probe, the ocp of the probe was recorded every second. In addition, the solution bulk pH was also measured using a glass pH probe to compare the surface results against it. Figure **4-8** shows the near surface pH for both techniques. The results are fairly similar for both cases. The surface pH is higher than the one in the bulk due to the electrochemical reactions which occur at the corroding surface. The results in Figure **4-8** reflect that the surface pH has a dependency on bulk pH. It is obvious that the difference in pH between the bulk and the surface decreases as the bulk pH increases. This can be attributed to hydrogen ions concentration. For example, at pH=6 the concentration of hydrogen ions are two orders less than the concentration at pH=4 thus less hydrogen ions diffuse from the bulk and react at the surface.

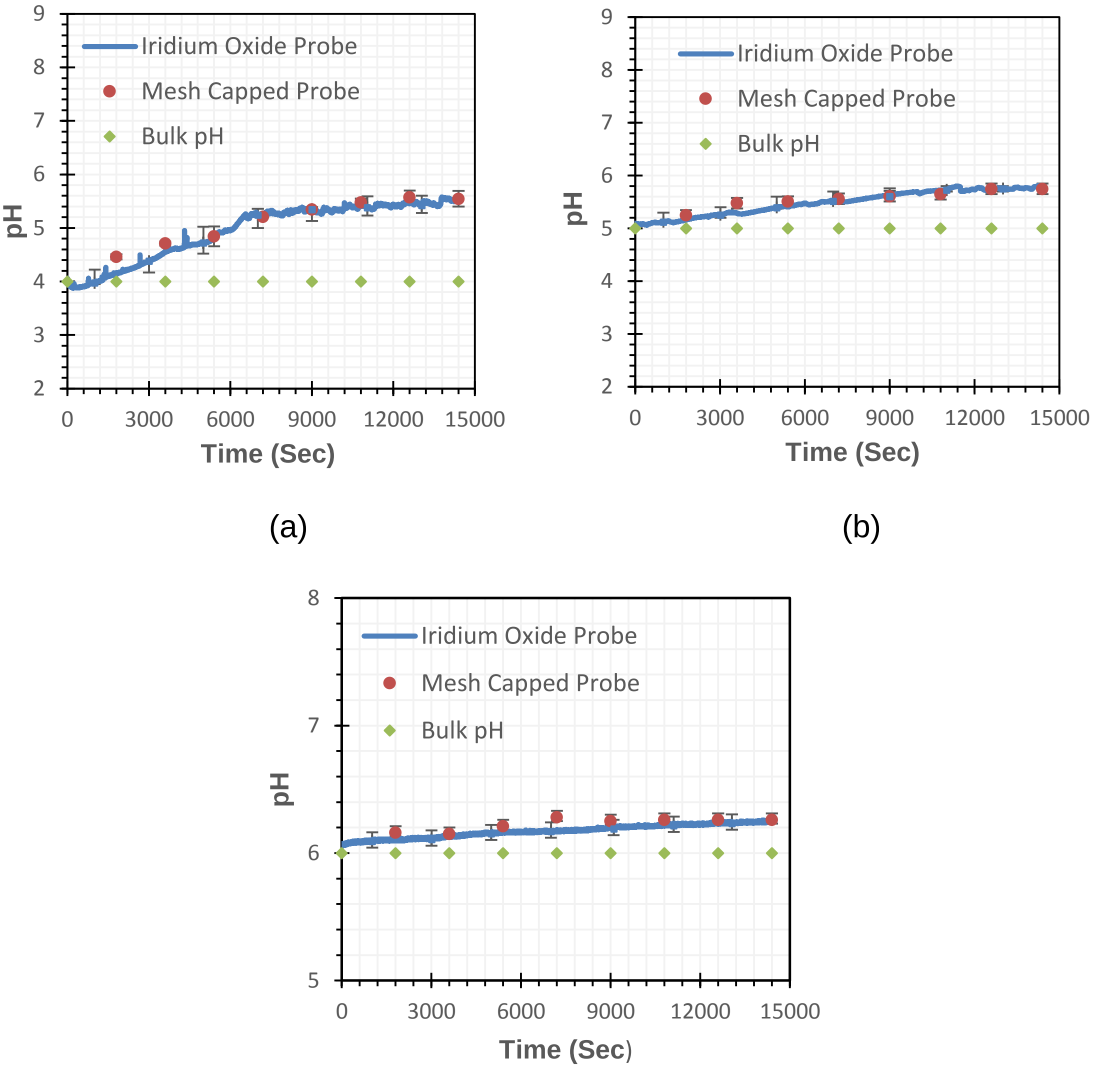

(a)

(b)

(c)

Figure 4-8 Comparison between the near surface pH measurements of Iridium oxide probe and the Mesh capped probe with time in a solution saturated with CO_2 with 1% wt. NaCl, temperature 25°C and bulk pH a) pH= 4, b) pH= 5 and c) pH=6.

4.4 Corrosion Rates from Smooth Samples

4.4.1 Corrosion Rate Measurements for Smooth Samples Under Dynamic Conditions

Initial tests were performed to observe the effect of speed and pH on CO_2 corrosion. The tests were performed for a solution of 1wt.% NaCl dissolved in distilled water with different pH values.

The value of corrosion rate was calculated using the measured polarisation resistance. However, solution resistance affects the value of the charge transfer resistance. Thus, the solution resistance should be added to the charge transfer resistance according to equation (3-4). Figure 4-9 shows the electrochemical impedance of the RCE sample for working conditions of 25°C, pH=4, 1%NaCl and 1000 rpm. The solution resistance represents the first value Z' when Z''=0. The main parameters that affect the solution resistance are temperature and ionic strength which are maintained constant in all experiments therefore the results of solution resistance did not change during the experiments.

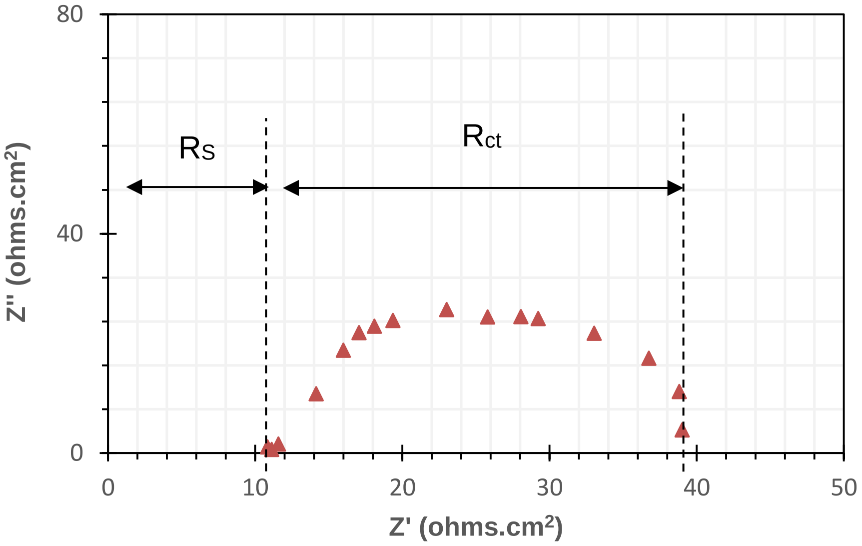

Figure 4-9 Nyquist plot indicating solution resistance in an RCE at 1000 rpm, pH=4, 1%NaCl and temperature 25°C.

Another important parameter is the value of Stern-Geary coefficient (B). This was initially set to 26 as it was assumed that both anodic and cathodic Tafel constants were equal to 120 mV/decade. Later, the values were corrected based on the cathodic and anodic Tafel values. The gradient of the anodic and cathodic branches are obtained from Figure 4-10 where β_a is approximately 48 mV/decade and β_c is approximately 111 mv/ decade.

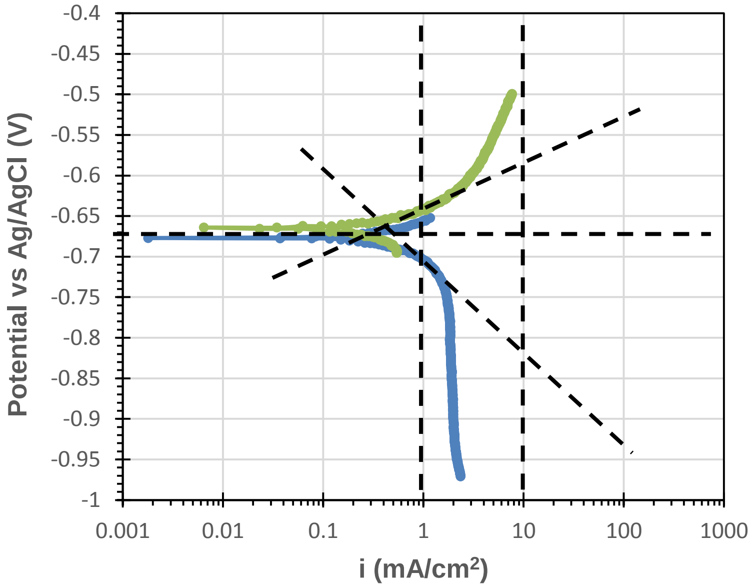

Figure 4-10 Cathodic and anodic Tafel plot for temperature 25°C, pH=4, 1wt.%NaCl for an RCE set up saturated with CO_2.

Figure 4-11 shows the experimental corrosion rate results for smooth samples under different rotation speeds and various pH values. The results show that the value of corrosion rate decreases as the pH increases. Also, the figure shows that at pH=4 corrosion rate increases with rotational speed, indicating that mass-transfer from the bulk is essential, whereas for the higher pH values, where the bulk concentration of H^+ is orders of magnitude smaller, mass transfer of H^+ ions is far less essential.

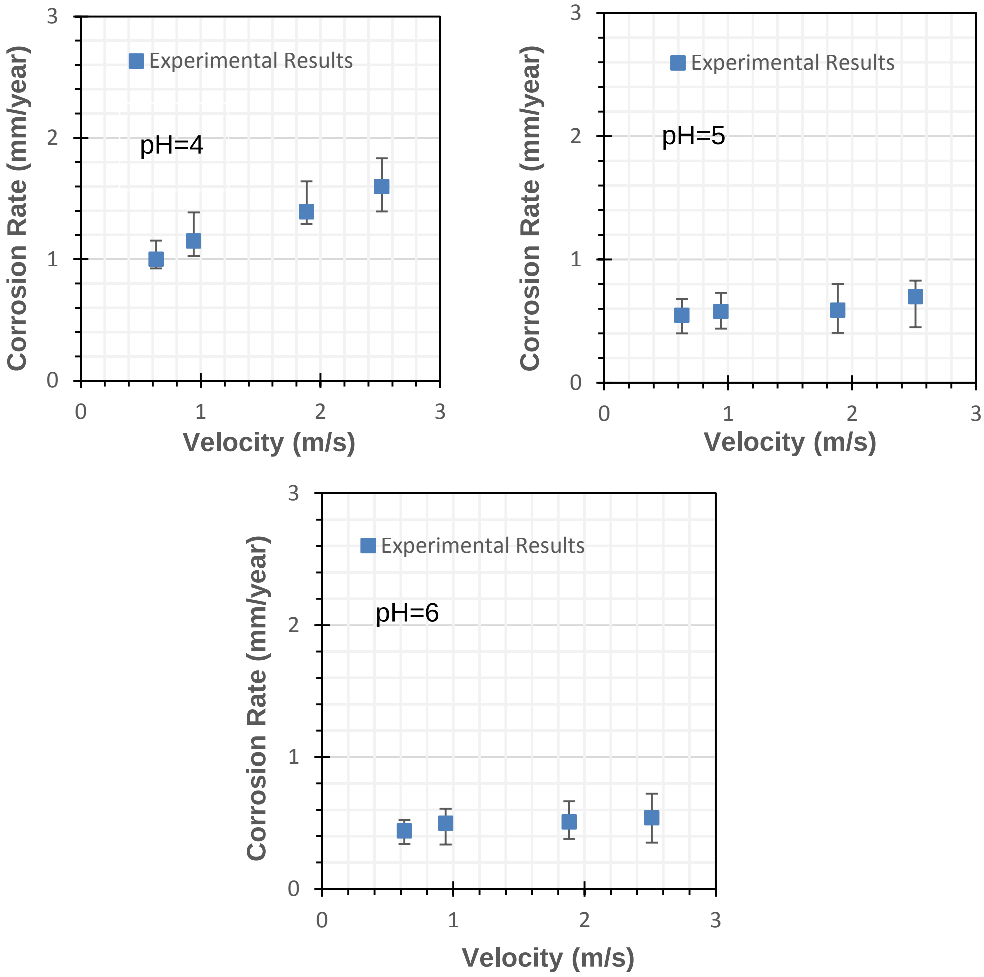

Figure 4-11 Experimental corrosion rates at 1 bar total pressure, temperature 25°C, various pH, and different rotation speeds for a smooth RCE.

Chapter 5 Mass Transfer and Corrosion Rates from Rough Surfaces

The following chapter includes the results obtained from experiments conducted in an RCE setup. The results cover two parts, the first part is the effect of roughness on mass transfer and the second part is the effect of roughness on corrosion rate. In all cases, results were repeated at least twice and error bars are included to show the repeatability of the results. The experiments were reasonably repeatable and the maximum percentage difference among the repeated test was less than 13%.

5.1 Effect of Surface Roughness on Mass Transfer

The results in this part covered the three stages presented in Figure 3-1. The results of these stages are presented in the following subsections starting with the results of the surface analysis and ending with how the surface roughness affects the limiting current of carbonic acid.

5.1.1 Non-Contact Profilometry Results

The surface texture of all four RCE samples was analysed over their entire length using white light interferometry. Example 2D and 3D profiles are provided in Figure 5-1 for the second roughest RCE sample (6 µm roughness). Each RCE surface consists of forms of peaks and valleys and a value of ‘e’ was assigned to each sample which represents the average distance between the peaks and valleys [134].

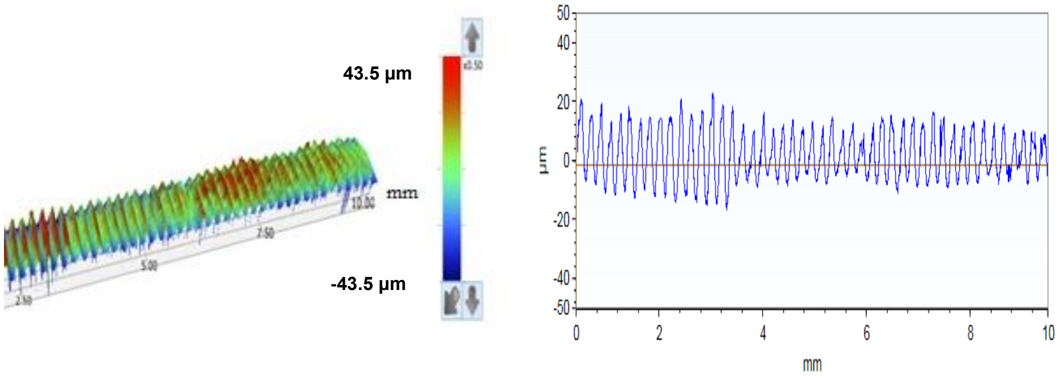

(a) **(b)**

Figure 5-1 (a) 3D and (b) 2D profile of second roughest RCE sample considered in this study(6 µm).

This value is displayed in Table **5-1** along with the d/e ratio (which is commonly assumed to influence mass-transfer [180]) and the ratio of the real area (A_R) to the projected is (A_P). Table **5-1** indicates that the machining process is able to produce a range of RCE surface roughness from very smooth (with a real area very similar to the projected area) up to 34 µm, which is analogous to that of steel pipelines delivered to coatings yards [103] and has an actual area ~1.23 times that of the smooth surface.

Table 5-1 RCE surface properties of the four samples considered in this study.

Sample	Roughness height (e) µm	(d/e)	(A_R/A_p)
Smooth	0.5	24000	1.004
Rough	6	2000	1.108
	20	600	1.219
	34	353	1.234

5.1.2 Influence of Roughness on Mass Transfer in N_2 Environments at pH 3

In flow conditions for the smooth RCE sample, the rate of mass transfer to the steel surface was determined by finding a mass transfer coefficient, k, using equation (3-1) which requires an input of the steel surface area. In this instance, the projected and actual surface areas of the smooth sample were very similar and no compensation for area effects was required to determine the enhancement of mass transfer.

For rough samples, however, equation (3-1) should consider the true surface area (A_R) to account for surface area effects and decouple their contribution from mass transfer enhancement:

$$\mathbf{k_R} = \frac{\mathbf{i_{lim,H^+}}}{\mathbf{A_R\ z\ F\ C_{b.H^+}}}. \qquad (5\text{-}1)$$

In the next series of experiments, all four RCE samples of different roughness (0.5, 6, 20 and 34 µm) were evaluated across a range of rotation speeds from

1000 to 4000 rpm (Re=8460 to 33843) at pH 3 in an N2 environment to elucidate the effect of roughness on mass transfer. **(b)**

Figure 5-2 provides examples of the cathodic Tafel polarisation sweeps conducted on RCE samples with different surface roughness values at 1000 rpm in a pH 3 N_2-saturated 1 wt.% NaCl solution.

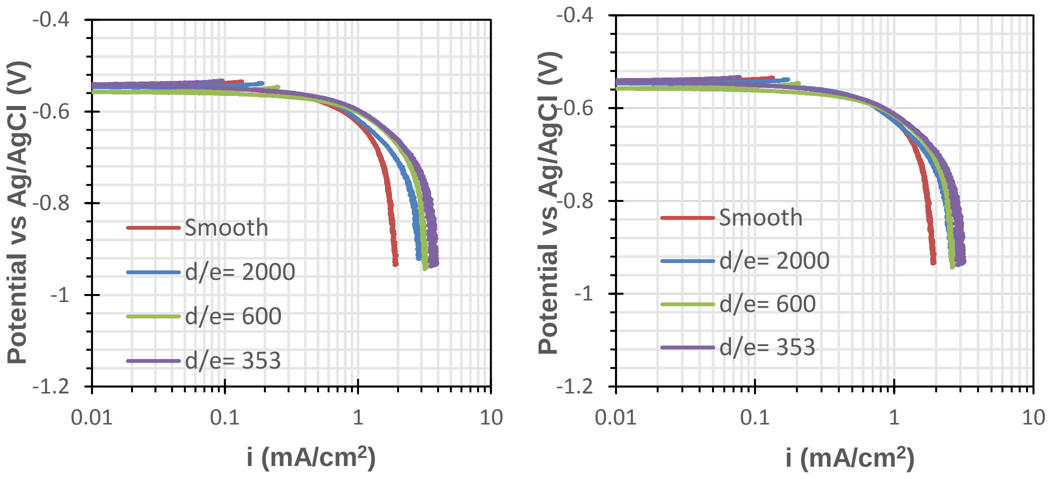

(a) (b)

Figure 5-2 Potentiodynamic sweeps conducted in a HCl solution at pH 3 purged with N2, T=25 °C, 1 wt.% NaCl, 1000 rpm: (a) without correcting the current density for the true area (b) with correction of current density for the true area.

Figure 5-2 (a) and Figure 5-2 (b) show the difference in sweep profiles when the current density is determined based on the projected area or the actual area of the X65 steel surfaces, respectively. There is a small but discernible difference between the two sets of profiles, particularly at the higher levels of roughness (d/e = 353 in particular). This indicates that compensating for the actual area is essential in order to determine the true effect of surface roughening on the rate of mass transfer. These results support the observations of Makanjuola and Gabe [31] who demonstrated the importance of accounting for the increased surface area as a result of roughening to fully understand the effect on mass transfer. Using RCE experiments they found that the observed 80% enhancement in mass transfer coefficient was reduced to less than 10% when the true surface area is used instead of the projected area. Such an approach allows the increased area effects to be decoupled from the true enhancement of mass transfer due to the hydrodynamic effects induced by surface roughness. In practice, of course, from the perspective of understanding *overall* mass-transfer enhancement, it is sufficient and much more convenient to adopt the conventional approach of simply using the projected surface area. Figure 5-3 shows the percentage of enhancement of mass transfer coefficient from that of a smooth surface (where the projected area is very similar to the actual surface area) for each surface roughness value at various Reynolds number. Figure 5-3 (a) and (b) indicate the level of enhancement when the limiting current was derived based on projected and true surface area, respectively. Generally, with the exception of the highest rotation speeds of 3000 and 4000 rpm (Re=25382 and 33843) for the roughest sample (d/e = 353), the percentage enhancement in mass transfer increases with both surface roughening and Reynolds number. At 1000 rpm (Re=8460), the percentage increase in mass-transfer from a smooth surface for d/e values of 2000, 600 and 353 is 50, 69 and 89%, respectively when values are based on projected areas. However, these values reduce to 35, 38 and 54% when the true areas are considered, indicating that the increased area of the sample is responsible for a significant increase in mass transfer. At the highest rotation speed of 4000 rpm (Re=33843), the enhancement is 69, 96 and 112% for d/e values of 2000, 600 and 353, respectively when projected area is used. The percentage increase reduces to 52, 61 and 72% when the true surface area is used.

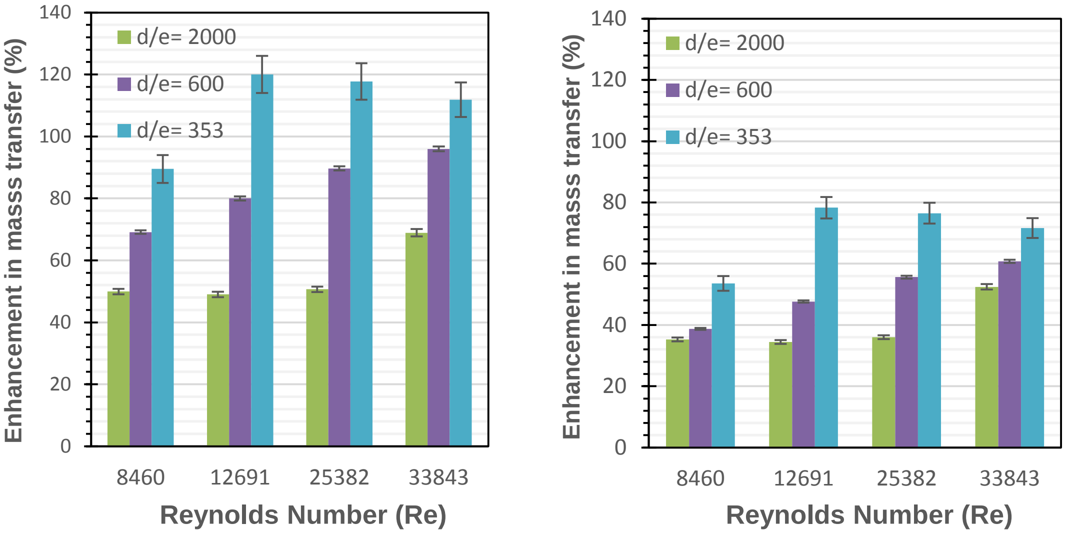

(a) **(b)**

Figure 5-3 Percentage enhancement in mass transfer coefficient from that determined for a smooth RCE sample as a function of surface roughness and velocity in N_2 solution, T=25°C, 1 wt.% NaCl and pH=3 for limiting currents (a) based on projected area (b) with correction for the true area.

Figure **5-4** expresses the limiting currents extracted from Figure **5-2** (b) (which are based on the true steel surface area) as mass transfer coefficients against the RCE surface velocity. The data is supplemented with the additional tests performed using the same four samples at the higher rotation speeds to enable correlations to be established. Expressing the results based on the actual area of each sample enables the true effect of mass-transfer enhancement to be visualised and decoupled from the effect of increased area. Referring to Figure **5-4**, the increase in sample roughness clearly leads to an increase in the rate of mass transfer, even when the real surface area of each sample is taken into account. Busse et al. [182] studied turbulent flow past an irregular rough surface based on a scan of a rough graphite surface, which they used as a no-slip boundary in Direct Numerical Simulations (DNS) of the turbulent flow. Their DNS predicted a number of flow features which could explain enhanced mass transfer over rough surfaces, including a significant increase in wall-normal flow fluctuations within roughness layers, strong upwards motions at the upstream faces of roughness peaks and recirculating flow regions between the peaks.

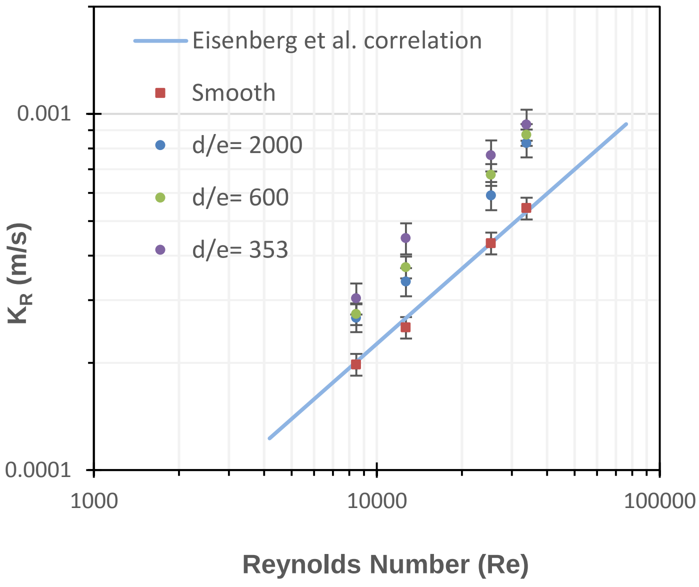

Figure 5-4 Measured and predicted mass transfer coefficient as a function of surface roughness and velocity in an N_2 solution, T=25°C, 1 wt.% NaCl and pH=3 for limiting currents corrected using the actual surface area of each sample.

The results in Figure 5-4 also reflect that mass transfer has some dependency on the d/e ratio, as increasing the roughness (or reducing d/e) served to enhance mass transfer for a given rotation speed.

Although few studies have focused on the relationship between surface roughness and mass transfer in an RCE system for the particular roughness pattern considered in this work, Gabe and Makanjuola [112] and Poulson [30] have developed correlations for the Sherwood number which are worthy of comparison with the values determined here.

Poulson [30] suggested that surface roughness prevailed over the system geometry in terms of influencing mass transfer and proposed the following relationship:

$$\mathbf{Sh = 0.01\, Re\, Sc^{0.33}} \qquad 3000 < Re < 50{,}000 \qquad (5\text{-}2)$$

The relationship was based on data from very rough RCE geometries (d/e=87) as well as numerous other geometries with various forms of roughening patterns [30]. However, Poulson does not explain why the correlation is independent of surface roughness.

The correlation by Gabe and Makanjuola [112] was developed for cylindrical wire wrapping which is similar to the geometry considered here:

$$\mathbf{Sh} = \mathbf{0.0062\ Re\ Sc^{0.356}} \qquad 210 < \mathrm{Re} < 240{,}000 \qquad (5\text{-}3)$$

This correlation is valid for Reynolds values (210- 240,000), with wire diameters ranging from 0.05 to 0.125 mm diameter. These two relationships are compared with the results obtained in this study within Figure 5-5 for two of the rough surfaces considered within the RCE (i.e. d/e = 2000 and 353). Note that for ease of comparison with previous studies and the complexities associated with determining actual area, all experimental data from this point onwards is based on the projected area. The fluid properties and diffusion coefficients used in the calculation of the Sherwood and Reynolds numbers here, as well as specific fluid properties utilised in subsequent calculations are provided in Table **5-1** and Table 5-2 for reference.

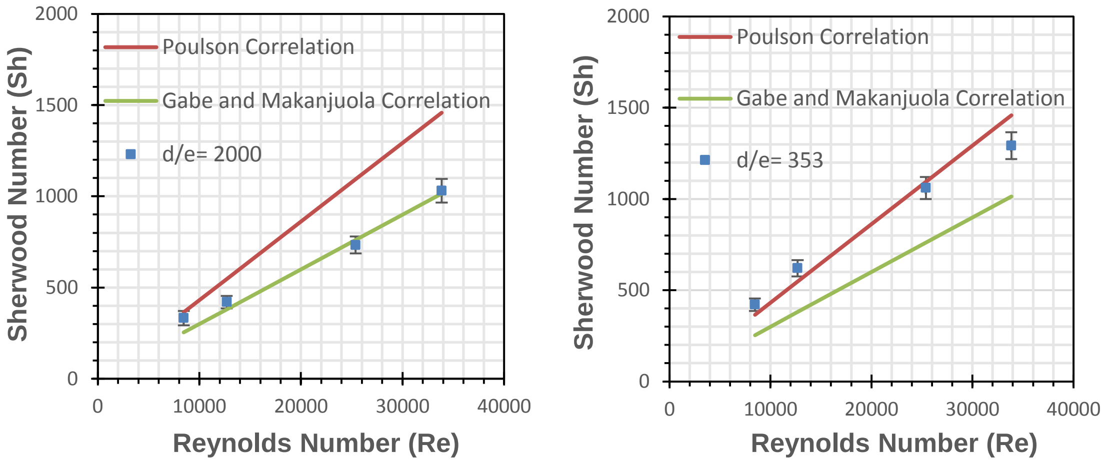

(a) **(b)**

Figure 5-5 Comparison between the Poulson [30] and Gabe and Makanjuola correlation [112] with experimental Sherwood number based on sample projected area for: (a) d/e=2000 (b) d/e= 353.

Table 5-2 Fluid and species properties [8].

Density	$\rho(T) = 1152.3 - 0.5116\, T_K$
Dynamic viscosity	$\mu(T) = \mu_{ref} \times 10^{\frac{1.3272(20-T_C)-0.001053(20-T_C)^2}{T_C+105}}$
Diffusion coefficient	$D = D_{ref}\left(\frac{T_K}{T_{ref}}\right)\left(\frac{\mu_{ref}}{\mu}\right)$
T_{ref} is the reference temperature = 20°C , μ_{ref}=1.002 kg/(m.s) T_K is the temperature in K T_c is the temperature in °C	

Table 5-3 Reference diffusion coefficients for each species [8].

Species	**Diffusion Coefficients (m^2/s)**
H^+	9.312×10^{-9}
H_2CO_3	2×10^{-9}

Figure 5-5 shows that the Poulson correlation produces a closer agreement with the roughest RCE sample considered (d/e = 353). This is expected given that the model was developed for RCE samples with d/e values of 87. However, it is also important to point out here that the roughness pattern on the RCE samples consisted of perpendicular grooves which have been shown to generate significant enhancement of mass transfer compared to other patterns and orientations [31].

As mentioned previously, a d/e value of 87 for RCE samples analysed by Poulson equated to roughness elements which exceed that of the viscous sublayer thickness. In the context of this work, the viscous sublayer thickness, δ, can be estimated by setting y^+=5 [183] where:

$$\mathbf{y^+} = \frac{\delta\, \rho\, U_f}{\mu}. \tag{5-4}$$

The friction velocity is a function of wall shear stress τ_w

$$\mathbf{U_f} = \sqrt{\frac{\tau_w}{\rho}}. \tag{5-5}$$

and the wall shear stress can be calculated from the Fanning friction factor

$$\tau_w = \frac{f_c}{2} \rho\, U_{RCE}^2 \qquad (5\text{-}6)$$

where

$$U_f = \sqrt{\frac{f_c}{2} U_{RCE}^2}. \qquad (5\text{-}7)$$

Hence

$$y^+ = \frac{\delta\, \rho \sqrt{f_c}}{\sqrt{2}\, \mu} U_{RCE}. \qquad (5\text{-}8)$$

and the thickness of the viscous sublayer, δ, can be estimated by

$$\delta = \frac{5\sqrt{2}\, \mu}{\rho\, \sqrt{f_c}\, U_{RCE}}. \qquad (5\text{-}9)$$

where: y^+ is the dimensionless height, δ is the thickness of viscous sublayer (m), U_f is the friction velocity (m/s) and τ_w is the Wall shear stress (Pa).

This estimate of the viscous sublayer thickness, for various RCE speeds, is compared against the surface roughness, e, in Table 5-4. It shows that the viscous sublayer thickness is close to e for the largest surface roughness at the higher RCE speeds of 3000 and 4000 rpm and it is therefore not surprising that roughness plays a role in influencing mass transfer, a finding that is consistent with Dawson and Trass [184]. However for the flows considered here, with Schmidt numbers around Sc~100, even when the roughness is well immersed within the viscous sublayer, it can still disturb the thinner mass transfer boundary layer, leading to enhancement of mass transfer. This is described comprehensively in Nesic et al. [185].

Table 5-4 Estimates of viscous sublayer thickness as a function of RCE speed in comparison to surface roughness of 0.5, 6, 20 and 34 µm.

RCE rpm	Re	Viscous sublayer (δ) (µm)
1000	8460	97.8
2000	12691	69.3
3000	25382	38.4
4000	33843	30.1

With regards to the correlation by Gabe and Makanjuola, this model provides a good estimate of Sherwood number at low roughness (d/e=2000). However, the agreement degrades with high roughness (d/e=353) with a maximum deviation of approximately 26%.

Both the Poulson and the Gabe and Makanjuola correlations agree well with specific degrees of roughness evaluated in this study. This can be attributed to the fact that these correlations were developed for a particular roughness (d/e=87 in the case of Poulson) or small roughness ranges (wire winding with diameters 0.05, 0.1 and 0.125 mm in the case of Gabe and Makanjuola). The results generated here are clearly sensitive to the degree of surface roughness and consequently suggest that there is a need for a new correlation which also accounts for the value of d/e.

The correlation proposed here is derived from the experimental results based on the projected surface area to produce a correlation which can be more easily utilised by other researchers who are unable to measure, or experience difficulties estimating, the actual surface area.

From Figure 5-6, it can be determined that for rough cylinders, the mass transfer coefficient increases with $Re^{0.8}$ and is sensitive to d/e. Therefore, a modified correlation for Sherwood number is suggested:

$$\mathbf{Sh} = \frac{\mathbf{k\ d}}{\mathbf{D_{H^+}}} = \frac{\mathbf{f}_c}{\mathbf{2}}\ \mathbf{Re^{0.8}\ Sc^{\ 0.356}} \qquad (5\text{-}10)$$

where

$$\frac{\mathbf{f}_c}{\mathbf{2}} = \mathbf{0.175}\left(\frac{\mathbf{e}}{\mathbf{d}}\right)^{\mathbf{0.17}} \qquad (5\text{-}11)$$

This correlation is compared with the entire set of experimental data collected in this study for rough samples in Figure 5-6, producing a maximum deviation of around 7.5% and average deviation of around 3%. The correlation is valid for the Reynolds number range of 8500 to 33850 and d/e from 353 to 2000. Note that the Reynolds numbers exponent has been shown to be sensitive to the roughness pattern, ranging from 0.61 for perpendicular fins to 1 for knurled diamond pyramids [117], whereas the (e/d) exponent reported by Sedahmed et al. [141] for perpendicular fins is 0.2.

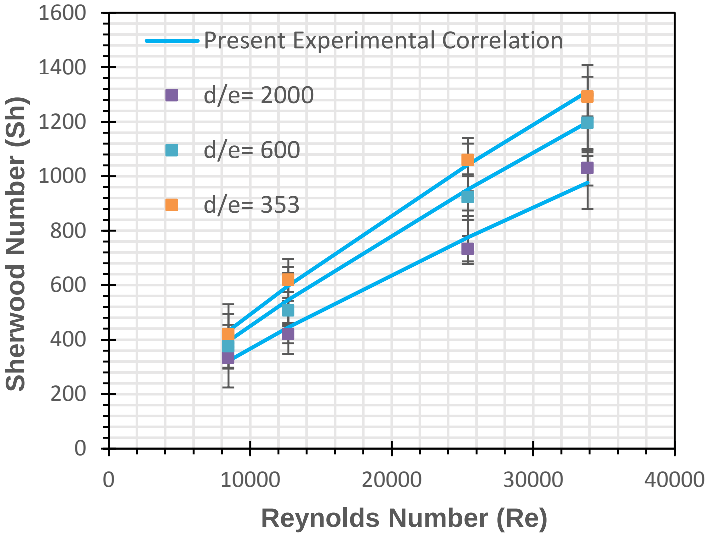

Figure 5-6 Sherwood number vs Reynolds number for different degrees of roughness.

5.1.3 Influence of Surface Roughness in CO_2 and N_2 Environments at pH 4

The results of the smooth samples demonstrated the validity of Vetter's correlation. However, based on the research by Nesic et al. [115], and the fact that modifying surface roughness has the ability to disrupt mass transfer in the boundary layer, a final set of measurements were performed at 4000 rpm (the highest speed at which reliable electrochemical measurements could be obtained) on surfaces of different roughness values to establish whether the value of $i_{lim\ H2CO3}$ is influenced by surface roughness at the conditions considered in this study. Results provided in Figure 5-7 show that for the cases considered here, up to 4000 rpm, the effect of surface roughness on $i_{lim\ H2CO3}$ is only minor, the variation being within experimental error. Consequently for the range of experimental conditions considered in this work, equation (3-3) can be used to estimate $i_{lim\ H2CO3}$ without further modification for surface roughening effects.

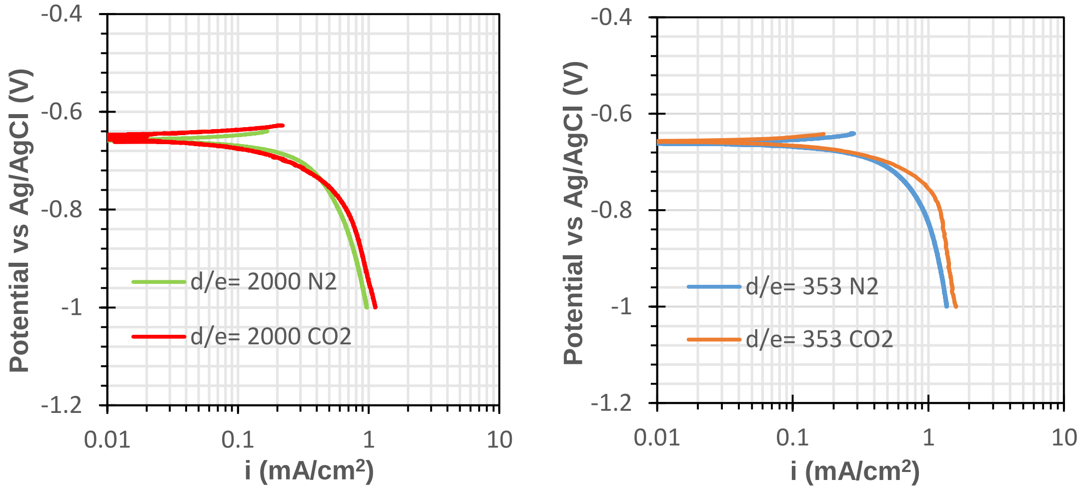

Figure 5-7 Comparison between potentiodynamic sweeps conducted in CO_2 and N_2 solution at pH 4, T=25 °C, 1 wt.% NaCl, 4000 rpm and different surface roughness based on sample projected area.

5.2 Effect of Surface Roughness on Corrosion Rates

The experimental work which is presented in this part reveals the effect of surface roughness on the value of corrosion rates. The experimental work is divided into two parts: the first part is testing the rough samples in static conditions and assessing how the projected area affects the corrosion rate and the second part is comparing the corrosion rates of samples with different surface roughness under different rotating speeds.

Electrochemical measurements were taken in the form of LPR measurements. The experiments were repeated at least two times to ensure consistency and repeatability of data.

5.2.1 Corrosion Rates for Rough Samples under Static Conditions

Tests were performed with four samples (0.5, 6, 20 and 34) µm of different surface finishes of X65 carbon steel in a 1 wt.% NaCl solution saturated with CO_2. The samples were connected to an RCE shaft and left in a stagnant state. The pH of the solution was adjusted to 4. The results of corrosion are normalised based on their actual surface area determined by profilometry, as opposed to their projected area. Figure 5-8 presents the corrosion rate results after correcting with the real surface area. It is clear that correcting for area leads to no significant change in corrosion rates across all rough surfaces, indicating that the machining process does not influence the dissolution of the steel.

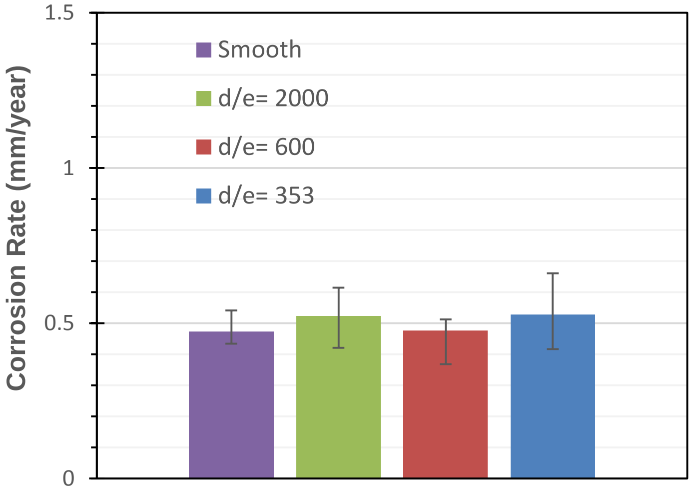

Figure 5-8 Static corrosion rate experimental results at 1 bar total pressure in a CO_2-saturated 1 wt.% NaCl solution at pH=4, temperature 25°C, for different surface finishes after correcting for the total surface area. Note: area ratios are shown in Table 5-1.

5.2.2 Corrosion Rates for Rough Samples under Dynamic Conditions

The results of tests for samples with different surface roughness are studied as a function of velocity. The tests were performed in a solution saturated with CO_2. 1wt. % NaCl was dissolved in water and the pH adjusted to 4. The tests were run for 3 hours. The results shown in Figure 5-9 confirm the stability of the corrosion rate values with time through all the experiment for all samples with different surface roughness.

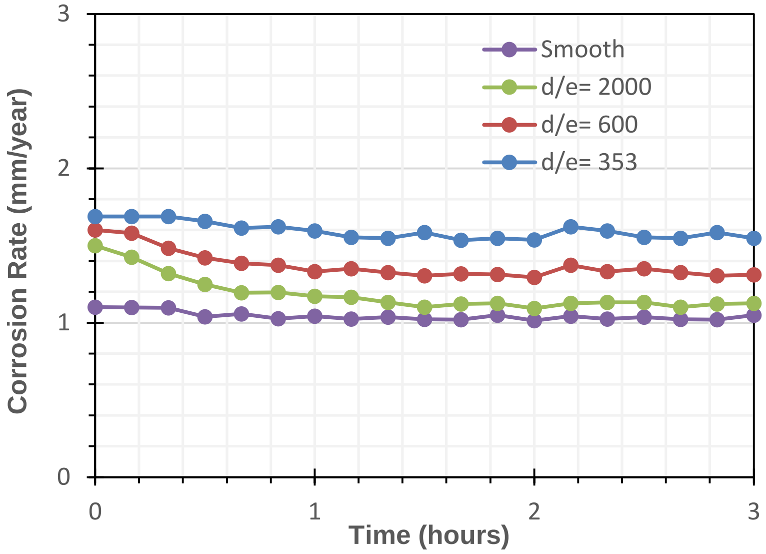

Figure 5-9 The experimental corrosion rate results corrected with true surface area versus time at 1 bar total pressure, temperature 25°C, pH=4, and rotation speed= 1000 rpm for different surface finishes.

Figure 5-10 (a) shows the experimental corrosion rate results as a function of RCE velocity for each of the four different roughness values. It is obvious that the corrosion rate increases with the speed and surface roughness. Figure 5-10 (b) indicates the level of enhancement when the corrosion rates were derived based on the true surface area. For example, at 1000 rpm percentage increase in corrosion rates from a smooth surface for d/e values of 2000, 600 and 353 is 18, 34 and 51%, respectively. While, at 3000 rpm the corrosion rate increases by roughly 12, 22 and 31 %, for d/e values of 2000, 600 and 353 compared to the smooth sample. At the highest rotation speed of 4000 rpm (Re=33843), the enhancement is 19, 28 and 35% for d/e values of 2000, 600 and 353, respectively

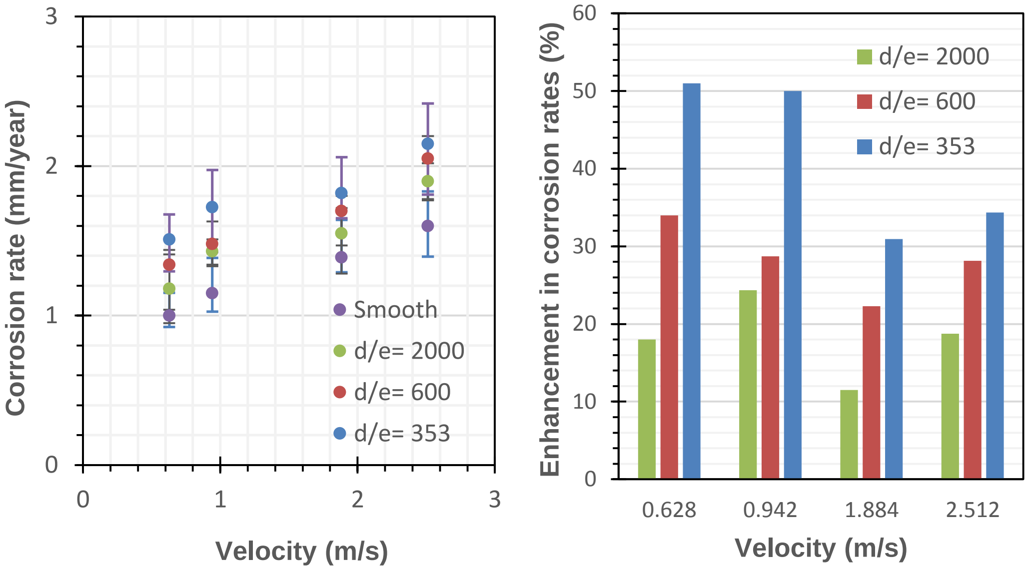

(a) **(b)**

Figure 5-10 Experiment results at 1 bar total pressure, 25°C, pH=4, and different rotation speeds for different surface finishes.

Chapter 6 Modelling of Carbon Steel Corrosion in CO_2 Environments in Film Free Conditions.

6.1 Background

A large amount of research has been published to understand the complex CO_2 corrosion processes over the past few decades [186, 187]. The recent review of CO_2 corrosion models by Kahyarian et al. [101] identified three categories: *empirical*, *semi-empirical* and *mechanistic*. Empirical/semi-empirical ones are simple models, developed when there is limited fundamental understanding of the physical phenomena, often taking the form of statistical fits based on experimental data or correlation factors. Although these can be useful for representative conditions for which they have been designed, they should be used with caution outside their range of application. Important examples of empirical/semi-empirical models include those of deWaard & Milliams [57] and Pots et al. [188]. A number of useful reviews of such models have appeared in the literature, see e.g. Olson [92] and Nesic [23].

Some mechanistic models have been developed to provide a physical basis for corrosion rate predictions and to address the inherent limitations of empirical and semi-empirical models, Kahyarian et al. [101]. Elementary mechanistic models de-couple the main physicochemical phenomena in corrosion processes, namely mass transfer, charge transfer and chemical reactions, and use parameters which have a sound theoretical foundation. Examples of these are widely used in corrosion engineering analyses (see e.g. Sundaram et al. [189], Han et al. [190]) but their neglect of homogeneous chemical reactions is a serious shortcoming.

These limitations have been addressed in more comprehensive mechanistic models based on the Nernst-Planck equation for mass conservation. Nordsveen et al. [33] solved the Nernst-Planck equation to describe the time-dependent mass transfer of species in the boundary layer using a computationally expensive multi-node approach. The computational requirements of their multi-node approach were alleviated by Remita et al. [58] who used a simplified, steady-state form of the Nordsveen et al. [33] model, which may be sufficient for practical purposes of corrosion rate estimation. Zheng et al. [27] recently proposed a novel, and much more computationally efficient, 2-node approach to predicting corrosion rates in cases of mixed CO_2/H_2S corrosion, which calculates the surface concentrations and corrosion rates at corroding surfaces using mass transfer coefficients and bulk concentrations of each species.

The following sections focus on assessing the use of the multi-node model that developed by Nordsveen et al. [33]. The model covers the process of corrosion including chemical reactions in the bulk solution, electrochemical reactions at the surface and transport of species between the bulk and surface and vice versa.

The model is first validated against corrosion rate results from the literature. Also, the pH gradient across the boundary layer will be compared to the near surface pH experiments to check the reliability of this kind of model to predict the surface pH.

Furthermore, the two-node methodology which is developed by Zheng et al. [27] will be used to build a model. The model will be compared versus the multi-node model to show the advantages and disadvantages of each model. Finally, the new correlation based on mass-transfer coefficients for RCE samples with rough surfaces obtained from experiments in Chapter 5 will be used to predict corrosion rates for flow over rough surface.

6.2 Multi-Node Model Description

The multi-node modelling approach for CO_2 corrosion developed by Nordsveen et al. [33] is described in this section. This model integrates through the boundary layer to calculate the concentration of each species at a series of points in the boundary layer by accounting for transport of species to and from the bulk. The assumption in this model include:

- Homogeneous chemical reactions in the bulk.
- Diffusion of species through the boundary layer.
- Electrochemical reactions at the steel surface, which cause a flux of species there.
- Transport of species to and from the bulk, including convection and diffusion through the boundary layer.

The governing equation for the concentrations of species c_j, of species j, is:

$$\frac{\partial \mathbf{c_j}}{\partial \mathbf{t}} = -\frac{\partial \mathbf{N_j}}{\partial \mathbf{x}} + \mathbf{R_j} \tag{6-1}$$

where R_j is the rate of chemical reaction of species j and N_j is the flux of species j due to diffusion in the positive x-direction (away from the steel surface). t is the time and x is the spatial coordinate (distance from the steel surface). There are seven species to be accounted for, namely CO_2 , H_2CO_3 , HCO_3^-, CO_3^{2-}, OH^-, H^+ and Fe^{2+}.

6.2.1 Bulk Chemistry Model

For CO_2 corrosion, the water chemistry is determined by the combined effects of carbon dioxide hydration, carbonic acid dissociation, bicarbonate ion dissociation and water dissociation. These reactions are respectively

$$\mathbf{CO_2}_{\,(g)} \Leftrightarrow \mathbf{CO_2}_{\,(aq)} \tag{6-2}$$

$$\mathbf{CO_2}_{\,(aq)} + \mathbf{H_2O} \Leftrightarrow \mathbf{H_2CO_3}_{(aq)} \tag{6-3}$$

$$\mathbf{H_2CO_3}_{(aq)} \Leftrightarrow \mathbf{H^+}_{(aq)} + \mathbf{HCO_3^-}_{(aq)} \tag{6-4}$$

$$\mathbf{HCO_3^-}_{(aq)} \Leftrightarrow \mathbf{H^+}_{(aq)} + \mathbf{CO_3^{2-}}_{(aq)} \tag{6-5}$$

$$\mathbf{H_2O} \Leftrightarrow \mathbf{H^+}_{(aq)} + \mathbf{OH^-}_{(aq)} \tag{6-6}$$

The rates of each of these reactions depend on temperature, CO_2 partial pressure and ionic strength [33]. Choosing the reaction rate constant is not an easy task. In the literature, the values of forward and backward reaction constants vary from one reference to another. The reaction coefficients are used here after a careful review of the literature. The reaction rate constants used here are given in Table **6-1**.

Constant	Source
$K_{sol}\frac{14.5}{1.00258}\times 10^{-(2.27+5.65\times10^{-3}\times T_f-8.06\times10^{-6}\times T_f^2+0.075\times I)}$ (molar/bar)	[191]
$K_{wa} = 10^{-(29.3868-0.0737549\times T_k+7.47881\times 10^{-5}\times T_k^2)}$ molar^2	[192]
$K_{b\,wa} = 7.85\times10^{10}$ M^{-1} s^{-1}	[193]
$K_{hy} = 2.58\times10^{-3}$	[194]
$K_{f\,hy} = 10^{329.85-110.541\times\log T_k-\frac{17265.4}{T_k}}$ s^{-1}	[194]
$K_{ca} = 387.6\times$ $10^{-(6.41-1.594\times10^{-3}\,T_f+8.52*10^{-6}\,T_f^2-3.07\times10^{-5}\,P-0.4772\times I^{0.5}+0.118\times I)}$ (molar)	[191]
$K_{f\,ca} = 10^{5.71+0.0526\times T_c-2.94\times10^{-4}\,T_c{}^2+7.91\times10^{-7}\times T_c{}^3}$ s^{-1}	[195]
$K_{bi} =$ $10^{-(10.61-4.97\times10^{-3}\,T_f+1.331*10^{-5}\times T_f^2-2.624\times10^{-5}\,P-1.166\times I^{0.5}+0.3466\times I)}$ (molar)	[191]
$K_{f\,bi} = 10^9$ s^{-1}	[33]
$K = k_f/k_b$	Estimated
Note: T_f is the temperature in degree Fahrenheit, T absolute temperature in Kelvin, T_c is the temperature in Celsius, I is the ionic strength in molar, and p is the total pressure in psi.	

Table 6-1 Equilibrium reaction rate constants.

In the bulk solution, the equations for the 6 different species ($\mathrm{CO_2}$, $\mathrm{H_2CO_3}$, $\mathrm{HCO_3^-}$, $\mathrm{CO_3^{2-}}$, $\mathrm{OH^-}$ and $\mathrm{H^+}$) are created as follows. Firstly, CO_2 molecules are consumed by carbonic acid hydration:

$$\mathbf{R_{CO_2}} = \frac{\mathbf{d}}{\mathbf{dt}}(\mathbf{c_{CO_2}}) = \mathbf{K_{b,hy}\,c_{H_2CO_3} - K_{f,hy}c_{CO_2}} \tag{6-7}$$

$\mathrm{K_{f,hy}}$ and $\mathrm{K_{b,hy}}$ are forward and backward reaction rate constants of carbonic acid hydration.

H_2CO_3 is created by carbonic acid hydration and carbonic acid dissociation:

$$\mathbf{R_{H_2CO_3} = \frac{d}{dt}\left(c_{H_2CO_3}\right) = -\left(K_{b,hy}\, c_{H_2CO_3} - K_{f,hy} c_{CO_2}\right) - \left(K_{f,ca}\, c_{H_2CO_3} - K_{b,ca} c_{H^+}\, c_{HCO_3^-}\right)} \quad \text{(6-8)}$$

$K_{f,ca}$ and $K_{b,ca}$ are the forward and backward reaction rate constants of carbonic acid dissociation.

HCO_3^- ions are created by carbonic acid dissociation and bicarbonate ion dissociation:

$$\mathbf{R_{HCO_3^-} = \frac{dc_{HCO_3^-}}{dt} = \left(K_{f,ca}\, c_{H_2CO_3} - K_{b,ca} c_{H^+}\, c_{HCO_3^-}\right) - \left(K_{f,bi}\, c_{HCO_3^-} - K_{b,bi} c_{H^+}\, c_{CO_3^{2-}}\right)} \quad \text{(6-9)}$$

$K_{f,bi}$ and $K_{b,bi}$ are forward and backward reaction rate constants of bicarbonate ion dissociation.

CO_3^{2-} ions are created by bicarbonate ion dissociation:

$$\mathbf{R_{CO_3^{2-}} = \frac{dc_{CO_3^{2-}}}{dt} = \left(K_{f,bi}\, c_{HCO_3^-} - K_{b,bi} c_{H^+}\, c_{CO_3^{2-}}\right)} \quad \text{(6-10)}$$

OH^- ions are created from water dissociation:

$$\mathbf{R_{OH^-} = \frac{dc_{OH^-}}{dt} = K_{f,wa} - K_{b,wa} c_{H^+}\, c_{OH^-}} \quad \text{(6-11)}$$

$K_{f,wa}$ and $K_{b,wa}$ are forward and backward reaction rate constants of water dissociation.

H^+ ions are created by carbonic acid dissociation, bicarbonate ion dissociation and water dissociation:

$$\mathbf{R_{H^+} = \frac{dc_{H^+}}{dt} = \left(K_{f,ca}\, c_{H_2CO_3} - K_{b,ca} c_{H^+}\, c_{HCO_{3,}^-}\right) + \left(K_{f,bi}\, c_{HCO_{3,}^-} - K_{b,bi} c_{H^+}\, c_{CO_{3,}^{2-}}\right) + \left(K_{f,wa} - K_{b,wa} c_{H^+}\, c_{OH^-}\right)} \quad \text{(6-12)}$$

Equations (6-7) to (6-12) for the 6 different species (CO_2 , H_2CO_3 , HCO_3^-, CO_3^{2-}, $OH^-$and H^+) in the bulk are solved using an efficient Newton-Raphson numerical scheme implemented in Python. The chemistry model obtained in this section is the foundation for the electrochemical corrosion model. Therefore it is vital to calculate the concentrations accurately.

6.2.2 Flux of Species

The flux of species N_j is made up of contributions from diffusion, electro-migration and convection. Here we will ignore the effect of electro-migration due to a small electrical potential difference between the bulk solution and the surface water layer, which is significant only for the transport of major species (Na^+ and Cl^-) [27], hence:

$$\mathbf{N_j = -D_j \frac{\partial c_j}{\partial x} + c_j v} \tag{6-13}$$

where D_j is the molecular diffusivity of species j and v is the instantaneous velocity. A well-established statistical technique is to divide the instantaneous velocity into a time-averaged and a turbulent-fluctuating component. Close to a solid surface the former is parallel to the surface and does not contribute to the transport of species in the direction normal to the metal surface. The turbulent convection term ($c_j v$) can be approximated by a turbulent diffusivity term, $-D_t \frac{\partial c_j}{\partial x}$, which means that:

$$\mathbf{N_j = -(D_j + D_t) \frac{\partial c_j}{\partial x}} \tag{6-14}$$

where: D_j is the molecular diffusivity coefficient (m^2/s) and D_t is the turbulent diffusivity coefficient (m^2/s).

The turbulent diffusivity D_t is a function of distance from the metal surface. Davis reported the following equation [196]:

$$\mathbf{D_t = 0.18 \left(\frac{x}{\delta}\right)^3 \frac{\mu}{\rho}} \tag{6-15}$$

where δ is the boundary layer thickness (m).

The liquid boundary layer thickness is typically a function of the Reynolds number (Re). Wang and Nesic [197] have given a correlation that can be used for pipe flow.

$$\boldsymbol{\delta = 25\, Re^{(-7/8)} d} \tag{6-16}$$

where d is the hydraulic diameter (m) and Re = ρUd/μ is the Reynolds number, U is the bulk velocity, ρ is the density (Kg/m^3) and μ is the dynamic viscosity (Pa). The properties of (density and viscosity) and the molecular diffusivity of the species (D_j) are modelled as a function of temperature. These properties are given in Table **6-2**.

Density	$\rho(T) = 1152.3 - 0.5116T$
Dynamic viscosity	$\mu(T) = \mu_{ref} \times 10^{\frac{1.3272(20-T)-0.001053(20-T)^2}{T+105}}$
Diffusion coefficient	$D = D_{ref}\left(\frac{T}{T_{ref}}\right)\left(\frac{\mu_{ref}}{\mu}\right)$
T_{ref} is the reference temperature =20°C , μ_{ref}=1.002 kg/(m.s)	

Table 6-2 Species properties as a function of Temperature [33].

The diffusion coefficient of the species at reference temperatures can be found in the literature. The coefficients are collected in Table **6-3**.

Species	Diffusion Coefficients (m^2/s)	Reference
CO_2	1.96×10^{-9}	[198]
H_2CO_3	2×10^{-9}	[199]
HCO_3^-	1.105×10^{-9}	[33]
CO_3^{2-}	0.92×10^{-9}	[199]
H^+	9.312×10^{-9}	[33]
OH^-	5.26×10^{-9}	[33]
Fe^{2+}	0.72×10^{-9}	[199]

Table 6-3 Reference diffusion coefficient of species used in the current model.

Hence the total diffusivity for species j is a function of the position in the boundary layer:

$$\mathbf{D_j}^{\mathbf{total}}(\mathbf{x}) = (\mathbf{D_j} + \mathbf{D_t}(\mathbf{x})) \tag{6-17}$$

and

$$\mathbf{N_j} = -\mathbf{D_j}^{\mathbf{total}}(\mathbf{x})\frac{\partial \mathbf{c_j}}{\partial \mathbf{x}} \tag{6-18}$$

6.2.3 Electrochemical Reactions

The rate of the electrochemical reactions at the metal surface depends on the surface concentrations of species involved in the electrochemical reactions and the temperature [33]. The cathodic reactions are given by the reduction of hydrogen, carbonic acid (via a buffering effect) and water reduction respectively

$$\mathbf{2\ H^+{}_{(aq)} + 2e^- \rightarrow H_{2(g)}} \tag{6-19}$$

$$\mathbf{2\ H_2CO_{3\,(aq)} + 2e^- \rightarrow H_{2(g)} + 2\ HCO^-_{3(aq)}} \tag{6-20}$$

$$\mathbf{2\ H_2O_{(l)} + 2e^- \rightarrow H_{2(g)} + 2\ OH^-{}_{(aq)}} \tag{6-21}$$

It is important to stress that carbonic acid has been shown to contribute to the cathodic reaction via a buffering effect whereby it is transported to the steel surface and dissociates, resulting in the reaction shown in equation (6-19), hence there is a distinction in the pathway, but the ultimate hydrogen evolution reaction is the same.

The anodic reaction is given by equation (6-22), although this is a simplification and is actually believed to occur through a number of complex, intermediate reactions as described by Nesic et al. [66].

$$\mathbf{Fe_{(s)} \rightarrow Fe^{2+}{}_{(aq)} + 2\ e^-} \tag{6-22}$$

Since the electrochemical reactions involve the exchange of electrons, the reaction rate represents the rate at which electrons are released or consumed. These exchange current densities can be calculated using the following formula:

$$\mathbf{i} = \pm \mathbf{i_0} \times \mathbf{10}^{\pm\left(\frac{\mathbf{E}-\mathbf{E_{rev}}}{\mathbf{b}}\right)} \tag{6-23}$$

where E is the potential of the corroding surface (V) and E_{rev} is the reversible potential of a specific reaction (V). A positive sign refers to the anodic reaction and a negative sign refers to a cathodic one. The exchange current densities take the general form

$$\mathbf{i_o} = \mathbf{i_{ref}} \left(\frac{\mathbf{c_{H+}}}{\mathbf{c_{H+,ref}}}\right)^{\mathbf{a1}} \left(\frac{\mathbf{c_{co2}}}{\mathbf{c_{co2,ref}}}\right)^{\mathbf{a2}} \left(\frac{\mathbf{c_{H2CO3}}}{\mathbf{c_{H2CO3,ref}}}\right)^{\mathbf{a3}} \mathbf{e}^{\frac{-\Delta \mathbf{H}}{\mathbf{R}}\left(\frac{\mathbf{1}}{\mathbf{T}}-\frac{\mathbf{i}}{\mathbf{T_{ref}}}\right)} \tag{6-24}$$

where the reference parameter values and exponents a_1, a_2 and a_3 for each of the reactions are given in Table **6-4**.

The exchange current density is $i_o = \mathrm{i}_{\mathrm{ref}} \left(\frac{c_{H+}}{c_{H+,ref}}\right)^{a1} \left(\frac{c_{co2}}{c_{co2,ref}}\right)^{a2} \left(\frac{c_{H2CO3}}{c_{H2CO3,ref}}\right)^{a3} e^{\frac{-\Delta H}{R}\left(\frac{1}{T}-\frac{i}{T_{ref}}\right)}$											
	$\mathrm{i}_{\mathrm{ref}}$	a_1	$c_{H+,ref}$	a_2	$c_{co2,ref}$	a_3	$c_{H2CO3,ref}$	ΔH	$\mathrm{T}_{\mathrm{ref}}$	$\mathrm{E}_{\mathrm{rev}}$	b
	$\frac{A}{m^2}$		Molar		Molar		Molar	$\frac{KJ}{mol}$	°C	V	V
$2H^+ + 2e \rightarrow H_2$	0.05	0.5	10^{-4}	0	N/A	0	N/A	30	25	$\frac{-2.303RT}{F}pH$	$\frac{2.303\ RT}{0.5\,F}$
$2H_2CO_3 + 2e \rightarrow HCO_3 + H_2$	0.018	- 0.5	10^{-5}	0	N/A	0.5	10^{-4}	50	20	$\frac{-2.303RT}{F}pH$	$\frac{2.303\ RT}{0.5\,F}$
$2H_2O + 2e \rightarrow H_2 + 2OH^-$	0.002	0	N/A	0	N/A	0	N/A	35	25	$\frac{-2.303RT}{F}pH$	$\frac{2.303\ RT}{0.5\,F}$
$Fe \rightarrow Fe^{2+} + 2e$	0.1 (RCE) 1 (pipe)	2 for PH<4 1 for 4<PH<5 0 for PH>5	10^{-4}	1 for P_{CO2} <1bar 0 for P_{CO2} >1bar	0.0366	0	N/A	37.5	25	-0.488	$\frac{2.303\ RT}{1.5\,F}$

Table 6-4 Current density parameters for the cathodic and anodic reactions [25, 33, 200].

For the hydrogen reduction reaction, the total current density i_{H^+} is given by the following expression of the charge transfer-controlled exchange current, $i_{\alpha\, H+}$, and the mass-transfer limiting current $\mathbf{i_{lim,H^+} = F\, k_{m,H^+}\, c_{b,H^+}}$, Zheng et al. [25], namely

$$\frac{\mathbf{1}}{\mathbf{i_{H+}}} = \frac{\mathbf{1}}{\mathbf{i_{\alpha\, H+}}} + \frac{\mathbf{1}}{\mathbf{i_{lim\, H+}}} \tag{6-25}$$

The total current density of carbonic acid is calculated similarly, with

$$\frac{\mathbf{1}}{\mathbf{i_{H2CO3}}} = \frac{\mathbf{1}}{\mathbf{i_{\alpha\, H2CO3}}} + \frac{\mathbf{1}}{\mathbf{i_{lim\, H2CO3}}} \tag{6-26}$$

where

$$\mathbf{i_{lim\, H2CO3} = f_1\, F\, C_{b,H2CO3} \sqrt{K_{b,hy}\ D_{H2CO3}}\ .} \tag{6-27}$$

where: f_1 is flow factor, $C_{b,H2CO3}$ is the bulk concentration of carbonic acid (mol/m^3 and F is Faraday constant (96485 C/mol).

For spontaneous corrosion the potential, E, at the corroding surface can be found by equating the total cathodic and anodic current densities:

$$\sum_{I}^{n_a} i_a = \sum_{I}^{n_c} i_c \tag{6-28}$$

Once E is determined, the electrochemical fluxes of species can be calculated

$$\mathbf{N_{out,i}} = \pm \frac{\mathbf{i_i}}{\mathbf{n_i\, F}} \tag{6-29}$$

where n_i is the number of moles of electrons created per mole of species in the ith electrochemical reaction: n_i=1 for all cathodic reactions and 2 for the anodic reaction. A positive or negative sign is taken for cathodic and anodic reactions, respectively.

6.3 Comparison of the present multi-node model implementation against that of Nordsveen et al. [33]

The multi-node model implementation in this thesis mainly differs from that used by Norsdveen et al [33] in terms of the chemical and electro-chemical reaction rate constants used. The present implementation uses the most up to date constants which are based on a firm theoretical and experimental background.

The research by Kahyarian et al. [201] studied extensively the anodic branch of Tafel slope (b_a) in CO_2 saturated environments. They found that the anodic branch correlates well with $\frac{2.303\ R\ T}{1.5\ F}$. Also, they stressed the effect of temperature on the anodic Tafel slope.

Similarly, Zheng [202] studied the effect of CO_2 on the cathodic reactions during corrosion. He concluded that the hydrogen evolution reaction does not change with the presence of CO_2. This is in agreement with Nordsveen's conclusion. However, Zheng argued about the equation of the cathodic Tafel slope (b_c) of Nordeseen et al. and found that b_c fits perfectly with $\frac{2.303\ R\ T}{0.5\ F}$. His value of the cathodic Tafel slope is consistent with other researchers [101, 200].

Also, Zheng [202] has shown that the current density equation of carbonic acid which was used by Nordsveen et al. is not accurate and suggested a better equation which is shown in Table **6-4**. This equation is used in the Multi-Node model.

Finally, Nordsveen et al. [33] ignored the contribution of water reduction to the total cathodic current densities. Researchers have shown that the direct reduction of water still has an effect on corrosion and causes an increase in the total cathodic current density [200, 203].

Nordsveen et al. model [33]	Present multi-node model
$b_a = 0.03$ for PH<4 $b_a = 0.08$ for 4<PH<5 $b_a = 0.12$ for PH>5	$b_a = \frac{2.303\ RT}{1.5\ F}$
$b_c = \frac{2.303\ RT}{2F}$	$b_c = \frac{2.303\ RT}{0.5\ F}$
$i_{o,H2C03} = 0.06\ (\frac{c_{H+}}{10^{-5}})^{-0.5}\ (\frac{c_{H2CO3}}{10^{-4}})$ $e^{\frac{-50}{R}(\frac{1}{T}-\frac{i}{T_{ref}})}$	$i_{o,H2C03} = 0.018\ (\frac{c_{H+}}{10^{-5}})^{-0.5}\ (\frac{c_{H2CO3}}{10^{-4}})^{0.5}$ $e^{\frac{-50}{R}(\frac{1}{T}-\frac{i}{T_{ref}})}$
$i_{o,H20} = 0$	$i_{o,H20} = 0.002\ e^{\frac{-35}{R}(\frac{1}{T}-\frac{i}{T_{ref}})}$

Table 6-5 Comparison of parameters and reaction rate constants between the Nordsveen et al. [33] and the Multi-Node corrosion model.

6.4 Corrosion Rate Predictions

6.4.1 Initial and Boundary Conditions

Uniform concentrations of species in chemical equilibrium are used as initial conditions for all the species. These equilibrium conditions are also used as boundary conditions in the bulk where it is assumed that all species are thoroughly mixed by turbulence. The bulk chemistry is calculated using the equations specified in section 6.2.1.

At the metal surface, zero flux is specified for the species not involved in the electrochemical reactions. For species j involved in electrochemical reactions at the metal surface, the flux at the metal surface can be determined from equation (6-29).

Three cathodic reactions and one anodic reaction occur at the surface. Thus, the flux of these reactions can be written:

$$\mathbf{N_{H_2CO_3}} = -\frac{\mathbf{i_{H_2CO_3}}}{\mathbf{F}} \tag{6-30}$$

$$\mathbf{N_{HCO_3^-}} = \frac{\mathbf{i_{H_2CO_3}}}{\mathbf{F}} \tag{6-31}$$

$$\mathbf{N_{OH^-}} = \frac{\mathbf{i_{H_2O}}}{\mathbf{F}} \tag{6-32}$$

$$\mathbf{N_{H^+}} = -\frac{\mathbf{i_{H^+}}}{\mathbf{F}} \tag{6-33}$$

$$\mathbf{N_{Fe^{2+}}} = \frac{\mathbf{i_{Fe}}}{\mathbf{2F}} \tag{6-34}$$

6.4.2 Numerical Method

The governing equations (6-1) for the species concentrations in the boundary layer are solved using a Finite Volume (FV) approach in which there are a total of nFV across the boundary layer, with a total of nFV+1 flux boundaries, since each FV has an upstream and downstream flux boundary. The unknown values of the concentration freedoms, c_j, are represented at the centres of the FVs and the species fluxes, N_j, are specified at the boundaries of the FVs. These are shown in the following figures, where FV 0 is adjacent to the steel surface and nFV-1 is adjacent to the bulk liquid.

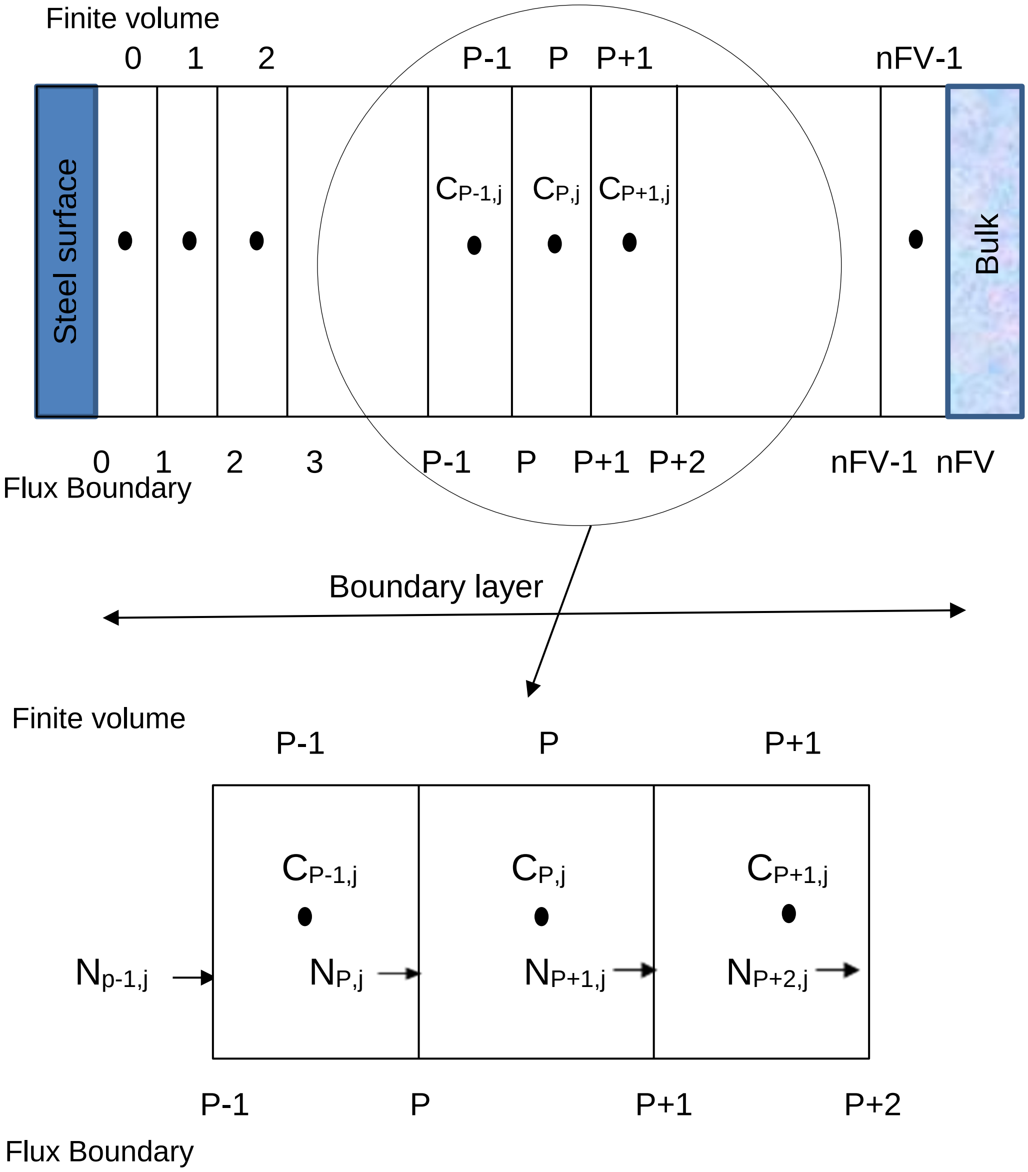

Figure 6-1 Sketch of the control volume used for discertization of the computational domain.

Consider the pth FV which has concentration freedoms $c_{p,j}$, where $c_{p,j}$ represents the jth species concentration at the middle of the pth Finite Volume. The pth Finite Volume has concentration fluxes $N_{p,j}$ flowing into it and $N_{p+1,j}$ flowing out of it. Since all the equations are strongly and non-linearly coupled through the chemical reaction, they all have to be solved simultaneously, together with the boundary conditions including the non-linear surface charge balance. Note that due to the importance of the electrochemical reaction terms, a non-uniform grid, with larger grid density near the steel surface, will be needed.

Integrating the transport equation over the pth Finite Volume of width Δx_p results in the following discretised equations:

$$\frac{\left(\mathbf{c}_{\mathbf{p,j}}^{\mathbf{n+1}} - \mathbf{c}_{\mathbf{p,j}}^{\mathbf{n}}\right)}{\Delta \mathbf{t}} \Delta \mathbf{x}_{\mathbf{p}} = -\mathbf{N}_{\mathbf{p+\frac{1}{2},j}}^{\mathbf{n+1}} + \mathbf{N}_{\mathbf{p-\frac{1}{2},j}}^{\mathbf{n+1}} + \mathbf{R}_{\mathbf{p,j}}^{\mathbf{n+1}} \Delta \mathbf{x}_{\mathbf{p}} \tag{6-35}$$

where:

- $c_{p,j}^{n+1}$= concentration of species j in the pth Finite Volume at time step n+1
- $c_{p,j}^{n}$= concentration of species j in the pth Finite Volume at time step n
- $N_{p+\frac{1}{2},j}^{n+1}$ = flux of species j at the p+1st flux boundary at time step n+1
- $N_{p-\frac{1}{2},j}^{n+1}$ = flux of species j at the pth flux boundary at time step n+1
- $R_{p,j}^{n+1}$ = rate of change of species j in pth Finite Volume at time step n+1 due to homogeneous chemical reactions
- Δx_p = width of Finite Volume p
- $\Delta t = t_{n+1} - t_n$ is the nth time step (usually constant time steps are used)

This can be rewritten as:

$$\mathbf{c}_{\mathbf{p,j}}^{\mathbf{n+1}} - \mathbf{c}_{\mathbf{p,j}}^{\mathbf{n}} = \mathbf{r}_{\mathbf{p}} \left(-\mathbf{N}_{\mathbf{p+\frac{1}{2},j}}^{\mathbf{n+1}} + \mathbf{N}_{\mathbf{p-\frac{1}{2},j}}^{\mathbf{n+1}} \right) + \Delta \mathbf{t}\, \mathbf{R}_{\mathbf{p,j}}^{\mathbf{n+1}} \tag{6-36}$$

where $r_p=\Delta t/\Delta x_p$.

Note that in the Newton iteration solution procedure described below it will be necessary to calculate both the flux and chemical reactions terms and their derivatives with respect to their associated freedoms..

6.4.2.1 Chemical Reactions Terms and Derivatives

The rates of the chemical reactions within the pth Finite Volume only depend on the concentration freedoms associated with that Finite Volume, i.e. $R_{p,j} = R_{p,j}(c_{p,k})$ only. Hence the only non-zero terms in the chemical reaction Jacobian are the $\frac{\partial R_{p,j}^{n\prime}}{\partial c_{p,i}^{n\prime}}$ terms. These can be calculated from the chemical reaction terms.

6.4.2.2 Flux Terms and Derivatives

The flux terms are:

$$\mathbf{N}_{\mathbf{j}} = -\mathbf{D}_{\mathbf{j}}^{\mathbf{total}}(\mathbf{x}) \frac{\partial \mathbf{c}_{\mathbf{j}}}{\partial \mathbf{x}} \tag{6-37}$$

which means that we need a way of estimating the concentration gradients, $\frac{\partial c_j}{\partial x}$ at each flux boundary. To calculate the fluxes $N_{p-1/2,j}$ and $N_{p+1/2,j}$ associated with Finite Volume p, we use a quadratic representation of the concentration fields. In terms of Figure 6-2:

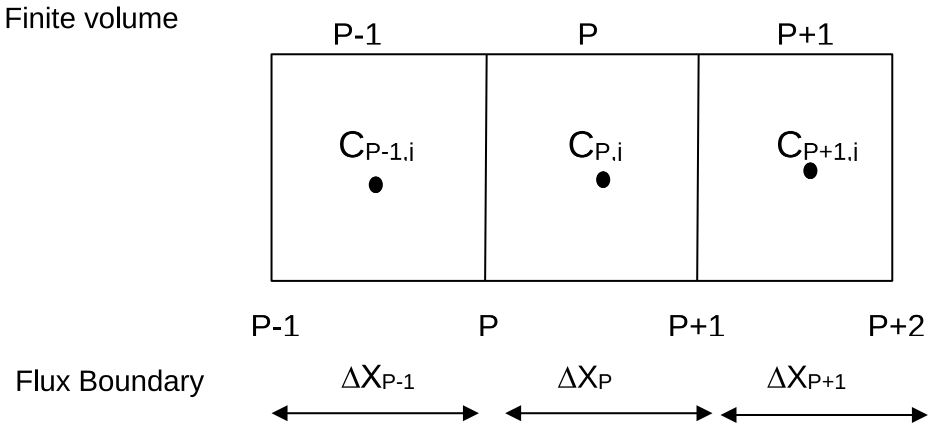

Figure 6-2 A quadratic representation of the concentration fields.

In terms of Figure 6-2, for each species j fit a quadratic through the species concentration freedoms with x'=0 at the upstream boundary of FV p-1 and $x'=\Delta x_{p-1}+\Delta x_p+\Delta x_{p+1}$ at the downstream boundary of FV p+1, so that:

- $c_j = c_{p-1,j}$ at $x' = (\Delta x_{p-1})/2$
- $c_j = c_{p,j}$ at $x' = \Delta x_{p-1} + (\Delta x_p)/2$
- $c_j = c_{p+1,j}$ at $x' = \Delta x_{p-1} + \Delta x_p + (\Delta x_{p+1})/2$

Within FV p the derivatives of the fluxes $N_{p,j}$ and $N_{p+1,j}$ with respect to the freedoms $c_{p-1,j}$, $c_{p,j}$ and $c_{p+1,j}$ can be calculated analytically using the quadratic representation of the concentration field c_j within that FV.

At flux boundary 0, corresponding to the steel surface, $N_{0,j}$ fluxes and their derivatives are given in terms of the electrochemical reactions.

At flux boundary 1, $N_{1,j}$ fluxes and their derivatives are calculated by derivatives at the upstream boundary of FV 1 in terms of the freedoms $c_{0,j}$, $c_{1,j}$, $c_{2,j}$.

For internal flux boundaries where $2 \leq i \leq nFV-2$ then the fluxes and their derivatives $N_{i,j}$ can be calculated in two ways:

- by calculating concentration gradients and their derivatives at the upstream boundary of FV i: $\frac{dc_{i,j}}{dx}_u$ in terms of freedoms $c_{i-1,j}$, $c_{i,j}$, $c_{i+1,j}$

- by calculating concentration gradients and their derivatives at the downstream boundary of FV (i-1): $\frac{dc_{i,j}}{dx}_d$ in terms of freedoms $c_{i-2,j}$, $c_{i-1,j}$, $c_{i,j}$

In practice for flux boundaries 2 ≤ i ≤nFV-2 the concentration gradients and their derivatives will be calculated by using the harmonic mean of these two gradients in order to smooth out unphysically large concentration gradients that may arise early in the time-integration process, hence:

$$\frac{\mathbf{dc_{i,j}}}{\mathbf{dx}} = \mathbf{2}\frac{\frac{\mathbf{dc_{i,j}}}{\mathbf{dx}}_{\mathbf{u}} \times \frac{\mathbf{dc_{i,j}}}{\mathbf{dx}}_{\mathbf{d}}}{\left(\frac{\mathbf{dc_{i,j}}}{\mathbf{dx}}_{\mathbf{u}} + \frac{\mathbf{dc_{i,j}}}{\mathbf{dx}}_{\mathbf{d}}\right)} \tag{6-38}$$

$$\mathbf{N_{i,j}} = -\mathbf{D_j}^{\mathbf{total}}(\mathbf{x_i})\frac{\partial \mathbf{c_{i,j}}}{\partial \mathbf{x}} \tag{6-39}$$

where x_i is the location of the ith flux boundary in the boundary layer.

At flux boundary nFV-1, $N_{nFV-1,j}$ fluxes and their derivatives are calculated by derivatives at the downstream boundary of FV nFV-2 in terms of the freedoms $c_{nFV-3,j}$, $c_{nFV-2,j}$, $c_{nFv-1,j}$

The derivatives of these fluxes need to be determined too, so that the corrosion equations can be solved using Newton iteration. These can be determined analytically and their harmonic means will be calculated numerically. The derivatives $\frac{\partial N^{n'}_{p-\frac{1}{2},j}}{\partial c^{n'}_{k,i}}$ and $\frac{\partial N^{n'}_{p+\frac{1}{2},j}}{\partial c^{n'}_{k,i}}$ are calculated using Finite Differences.

6.4.3 Numerical Solution of the Time-Dependent Equations

The Newton iteration solution procedure used here requires linearization of terms to create the equations to be solved, ignoring second order terms or higher, we can use:

$$\mathbf{N^{n+1}_{p+\frac{1}{2},j}} = \mathbf{N^{n'}_{p+\frac{1}{2},j}} + \frac{\partial \mathbf{N^{n'}_{p+\frac{1}{2},j}}}{\partial \mathbf{c^{n'}_{k,i}}}\left(\mathbf{c^{n+1}_{k,i}} - \mathbf{c^{n'}_{k,i}}\right) \tag{6-40}$$

$$\mathbf{N^{n+1}_{p-\frac{1}{2},j}} = \mathbf{N^{n'}_{p-\frac{1}{2},j}} + \frac{\partial \mathbf{N^{n'}_{p-\frac{1}{2},j}}}{\partial \mathbf{c^{n'}_{k,i}}}\left(\mathbf{c^{n+1}_{k,i}} - \mathbf{c^{n'}_{k,i}}\right) \tag{6-41}$$

$$\boldsymbol{R^{n+1}_{p,j}} = \boldsymbol{R^{n'}_{p,j}} + \frac{\partial \boldsymbol{R^{n'}_{p,j}}}{\partial \boldsymbol{c^{n'}_{k,i}}}\left(\boldsymbol{c^{n+1}_{k,i}} - \boldsymbol{c^{n'}_{k,i}}\right) \tag{6-42}$$

where n’ refers to the values of the freedoms at an intermediate time step $t_n \le t_{n'} \le t_{n+1}$.

Hence the linearized form of the discretized equations becomes:

$$\mathbf{c}_{\mathbf{p,j}}^{\mathbf{n+1}} + \mathbf{r}_{\mathbf{p}} \frac{\partial \mathbf{N}^{\mathbf{n}'}_{\mathbf{p+\frac{1}{2},j}}}{\partial \mathbf{c}_{\mathbf{k,i}}^{\mathbf{n}'}} \mathbf{c}_{\mathbf{k,i}}^{\mathbf{n+1}} - \mathbf{r}_{\mathbf{p}} \frac{\partial \mathbf{N}^{\mathbf{n}'}_{\mathbf{p-\frac{1}{2},j}}}{\partial \mathbf{c}_{\mathbf{k,i}}^{\mathbf{n}'}} \mathbf{c}_{\mathbf{k,i}}^{\mathbf{n+1}} - \Delta \mathbf{t} \frac{\partial \mathbf{R}_{\mathbf{p,j}}^{\mathbf{n}'}}{\partial \mathbf{c}_{\mathbf{k,i}}^{\mathbf{n}'}} \mathbf{c}_{\mathbf{k,i}}^{\mathbf{n+1}} = \mathbf{c}_{\mathbf{p,j}}^{\mathbf{n}} + \mathbf{r}_{\mathbf{p}} \left(\mathbf{N}^{\mathbf{n}'}_{\mathbf{p-\frac{1}{2},j}} - \mathbf{N}^{\mathbf{n}'}_{\mathbf{p+\frac{1}{2},j}} \right) + \mathbf{r}_{\mathbf{p}} \left(\frac{\partial \mathbf{N}^{\mathbf{n}'}_{\mathbf{p+\frac{1}{2},j}}}{\partial \mathbf{c}_{\mathbf{k,i}}^{\mathbf{n}'}} \mathbf{c}_{\mathbf{k,i}}^{\mathbf{n}'} - \frac{\partial \mathbf{N}^{\mathbf{n}'}_{\mathbf{p-\frac{1}{2},j}}}{\partial \mathbf{c}_{\mathbf{k,i}}^{\mathbf{n}'}} \mathbf{c}_{\mathbf{k,i}}^{\mathbf{n}'} \right) + \Delta \mathbf{t} \mathbf{R}_{\mathbf{p,j}}^{\mathbf{n}'} - \Delta \mathbf{t} \frac{\partial \mathbf{R}_{\mathbf{p,j}}^{\mathbf{n}'}}{\partial \mathbf{c}_{\mathbf{k,i}}^{\mathbf{n}'}} \mathbf{c}_{\mathbf{k,i}}^{\mathbf{n}'} \qquad \text{(6-43)}$$

The iterative solution process of solving the above linear system of equations proceeds as follows. At the start of each time step the intermediate freedoms, $\mathbf{c}_{\mathbf{k,i}}^{\mathbf{n}'}$, are initialised to the (known) freedoms at the end of the previous time step, i.e. $\mathbf{c}_{\mathbf{k,i}}^{\mathbf{n}'} = \mathbf{c}_{\mathbf{k,i}}^{\boldsymbol{n}}$. The intermediate freedoms are then used to calculate the highly nonlinear terms associated with the flux of species terms and their derivatives and the homogeneous chemical reaction terms and their derivatives in equation (6.40). These new values are then used in the updated system of linear equations, which are then solved to determine the updated values of the intermediate terms, $\mathbf{c}_{\mathbf{k,i}}^{\mathbf{n}'}$. This iterative procedure continues until the maximum difference between the updated freedoms in two successive iterations is below a specified error tolerance. This error tolerance, *tol*, takes the form *tol=CΔt* where *C* is a specified error constant and *Δt* is the time step being used. Once the maximum difference is below the error tolerance the solution at the next time step, t_{n+1}, is set to the latest intermediate solution, i.e. $\mathbf{c}_{\mathbf{k,i}}^{\mathbf{n+1}} = \mathbf{c}_{\mathbf{k,i}}^{\mathbf{n}'}$.

Under-relaxation often needs to be used to avoid divergence of the solution process. At each time step, the corrosion rate is predicted by calculating:

$$\mathbf{CR}_{\mathbf{mmy}} = \mathbf{1.16\ i}_{\mathbf{Fe}} \qquad \text{(6-44)}$$

6.5 Multi-Node Model Validation and Sensitivity Analysis

Any model cannot be trusted before comparing its data with other models and experimental values. The film free CO_2 model is verified by comparing its results against the experimental results from the literature.

First, the chemical part of the model should be able to predict the concentration of species in the bulk when the pH is known. Also, it should be able to predict the concentration of other species in the bulk when pH is unknown. Second, a sensitivity analysis needs to be carried out to check the effect of the number of terms in the model on the values of the predicted corrosion rate. These terms include: number of finite volume (nFV) and time step (Δt). Third, the model should be validated against the corrosion rates results from other models and pipe experiments form the literature. Finally, the pH gradient across the boundary layer will be compared against the near surface pH results in Chapter 4 to check the accuracy of the model results.

6.5.1 Chemical Solver Results

In a CO_2 environment, the model predicts the concentration of species in the bulk solution over a wide temperature range. Solving the concentration of the species in the bulk for a known bulk pH and assuming equilibrium, Figure **6-3** depicts the concentrations for variable pH at a temperature of 25°C and p_{CO2} = 0.97 bar.

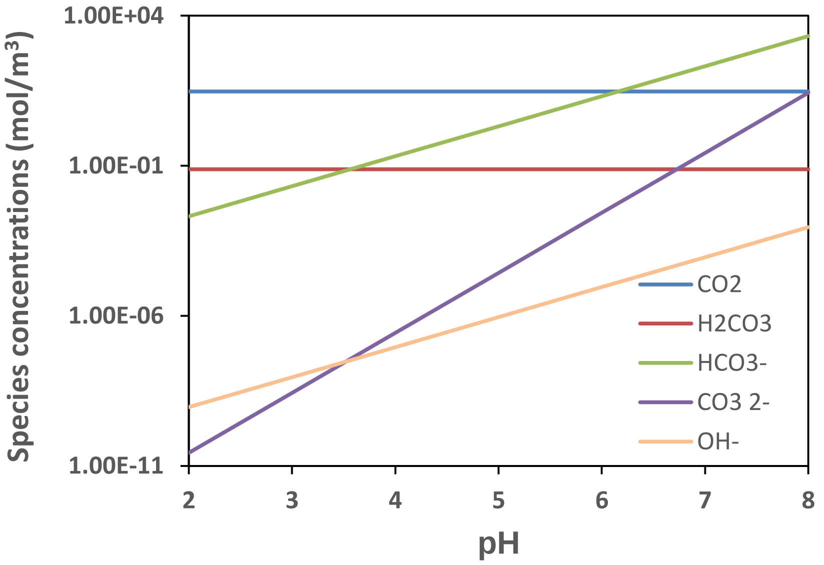

Figure 6-3 Species concentrations at different pH values, 1bar total pressure, temperature 25°C and 1wt.% NaCl.

Solutions of the bulk chemistry solver are validated against the experimental results of Meyssami et al. [204] and Tanupabrungsun et al. [205]. These are shown in Figure **6-4**.

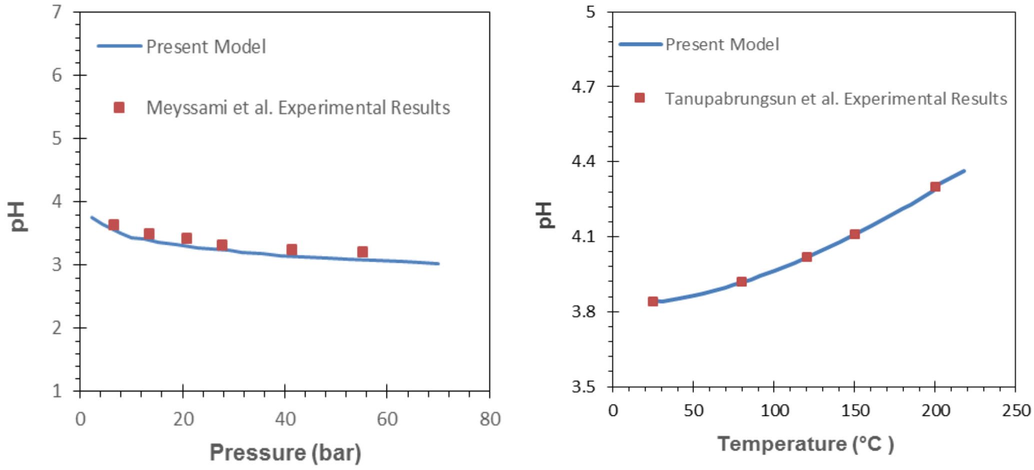

Figure 6-4 Validation of bulk chemistry predictions against Meyssami et al. [204] and Tanupabrungsun et al. [205].

The agreement is excellent in both cases. The results indicate that the model can predict the pH in the bulk accurately.

6.5.2 Sensitivity Analysis

The first set of results show typical forms of output from the numerical model. This has been set up for the problem with 1 bar partial pressure, 20°C, flow velocity 1m/s, 1wt.% NaCl, 0.01m pipe diameter and pH 6. Figure **6-5** shows the corrosion rate as a function of time. From Figure **6-5**, the initial corrosion rate is high due to the iterative numerical process before the corrosion rate settles down to a steady value.

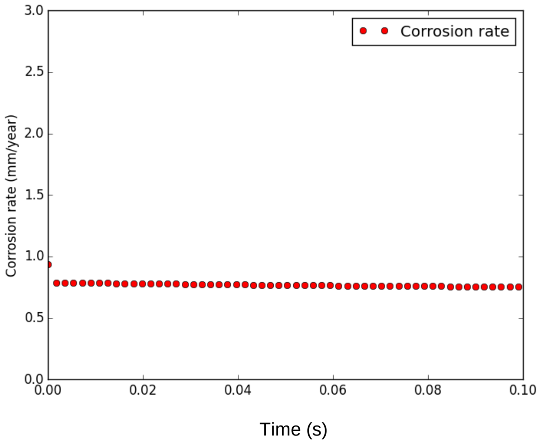

Figure 6-5 Predicted corrosion rate as a function of time for 1 bar CO_2 partial pressure, temperature 20°C, flow velocity 1m/s, 1wt.% NaCl, 0.01m pipe diameter and pH 6.

The accuracy of the output of the model is directly dependent on a number of terms in the model. These terms are the number of finite volumes, tolerance and the time step. For example, a high number of finite volumes will produce results with high accuracy. However, it will require a large amount of computational time and memory to obtain the corrosion rates. The following table shows the effect of the number of finite volume (nFV) on the numerical predictions of corrosion rate in mm/year for the case of 1 bar partial pressure, 20°C, flow velocity 1m/s, 1%wt. NaCl, 0.01m pipe diameter and pH 6. The corrosion rates have achieved an effective steady state, with a fixed time step of $\Delta t=0.05s$.

Table 6-6 Steady-state corrosion rate with different nFV for 1 bar CO_2 partial pressure, temperature 20°C, flow velocity 1m/s, 1wt.% NaCl, 0.01m pipe diameter and pH 6.

nFV	**Corrosion rate (mm/year)**
75	0.787
100	0.787
150	0.787

Table **6-6** shows that the corrosion rate is not sensitive to the change of nFV for nFV≥75.

On other hand, the model converges and reaches steady state when the difference in successive iterations is below a specified error tolerance. Thus, different tolerances have been used to check their effect on the model predictions. Table 6-7 shows the effect of the tolerance on the numerical predictions of corrosion rate in mm/year for the case of 1 bar partial pressure, 20°C, flow velocity 1m/s, 1%wt. NaCl, 0.01m pipe diameter and pH 6. The corrosion rates reached an effective steady state, with nFV=75 and a fixed time step of $\Delta t=0.05s$.

Table 6-7 Steady-state corrosion rate with different tolerance for 1 bar CO2 partial pressure, temperature 20°C, flow velocity 1m/s, 1wt.% NaCl, 0.01m pipe diameter and pH 6.

Tolerance	**Corrosion rate (mm/year)**
5e-4	0.787
5e-5	0.787
5e-6	0.780

Table 6-7 shows that the corrosion rate is not sensitive to the change in the tolerance. Thus, Tol=5e-5 was picked to provide a balance between the solution accuracy and numerical calculations.

Also, the time step must be chosen in such a way that it resolves time-dependent features and it maintains the solution stability. A wrong time step may lead to incorrect corrosion rate values if the chemical reactions do not reach an equilibrium. The use of an implicit time integration scheme allows the use of a larger time step than for an explicit scheme. The following table shows the effect of the number of time steps (Δt) on the numerical predictions of corrosion rate in mm/year for the case of 1 bar partial pressure, 20°C, flow velocity 1m/s, 1wt.% NaCl, 0.01m pipe diameter and pH 6. The corrosion rates have achieved an effective steady state, with nFv=75 and tol=5e-5.

Table 6-8 Steady-state corrosion rate with time step Δt for 1 bar CO_2 partial pressure, temperature 20°C, flow velocity 1m/s, 1%wt. NaCl, 0.01m pipe diameter and pH 6.

Δt (s)	**Corrosion rate (mm/year)**
0.1	0.746
0.08	0.755
0.05	0.787

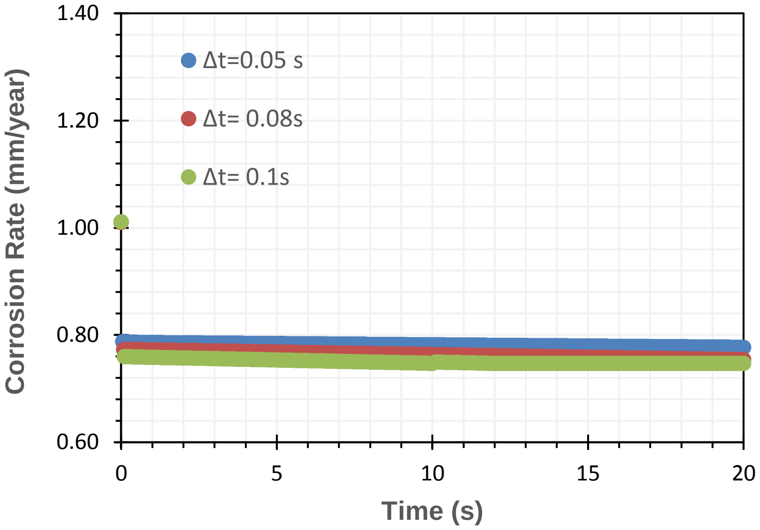

Figure 6-6 Corrosion rate with time step ∆t for 1 bar CO2 partial pressure, temperature 20°C, flow velocity 1m/s, 1%wt. NaCl, 0.01m pipe diameter and pH 6.

Table **6-8** and Figure 6-6 show that the corrosion rate slightly changes with the change of ∆t for ∆t ≤0.1. As the calculations are time-consuming for the computer with Intel Xenon 3.5 GHz processor and 16 GB installed memory, therefore, all the following results are obtained using nFV=75 and ∆t=0.1s, which is a suitable balance between efficiency and accuracy.

6.5.3 Corrosion Rates Verification

6.5.3.1 Comparison Against Nordsveen et al. [33]

The film free multi-node model is verified by comparing the corrosion rate predictions versus the results from Nordsveen et al. [33] and the published experimental results from Nesic et al. [81]. The working conditions were 20°C, flow velocity 1m/s, 1%wt. NaCl, 0.01m pipe diameter and three different pH values (4, 5 and 6). From Figure **6-7**, it is clear that the present multi-node model predictions are closer to the experimental results than the model implementation by Nordsveen et al. [33]. Thus, from Table 6-9, the predictions of the present multi-node model with the updated reaction constants appear to be more accurate than the original Nordsveen et al. [33] paper.

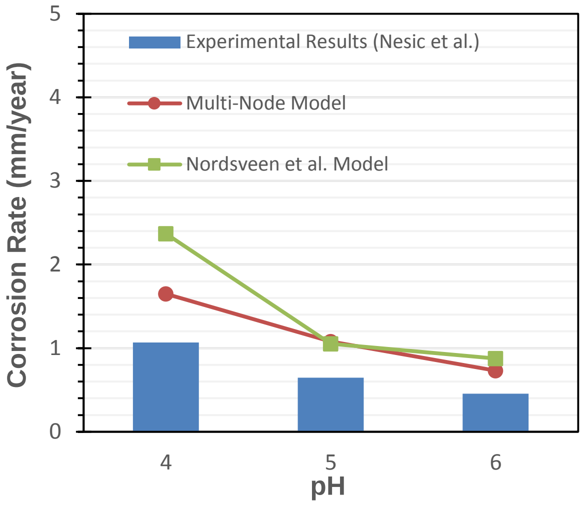

Figure 6-7 Comparison between the multi-node model predictions for pipe flow aginst experiments [81] and predictions of Nordsveen et al. [33] at 1 bar CO_2 partial pressure, 20°C, d=0.01 m and various pH values (4, 5 and 6).

Table 6-9 Comparison between the multi-node model predictions for pipe flow aginst experiments [81] and predictions of Nordsveen et al. [33] at 1 bar CO_2 partial pressure, temperature 20°C, d=0.01 m and various pH values (4, 5 and 6).

pH	Multi-Node Model	Nordsveen et al. Model	Experimental Results
4	1.65	2.36	1.06
5	1.08	1.05	0.64
6	0.74	0.87	0.45

6.5.3.2 Corrosion Rate Predictions for Pipe Flows

The corrosion rate predictions obtained here are now compared with the pipe flow loop experiments for different pH values and flow speeds from Nesic et al. [81]. In these experiments, the flow loop with diameter (0.01m) was filled with 56 L of solution (water and 1wt.% NaCl) then CO_2 was bubbled for 24 hours prior the experiments. The experiments were done at 1 bar carbon dioxide partial pressure and 20°C temperature.

Figure **6-8** shows that the present corrosion model predictions agree reasonably well with the experimental results of Nesic et al. [81]. The prediction that corrosion rates are independent of flow speed for pH=6 indicates that the process is surface chemical controlled rather than mass transfer controlled in these cases.

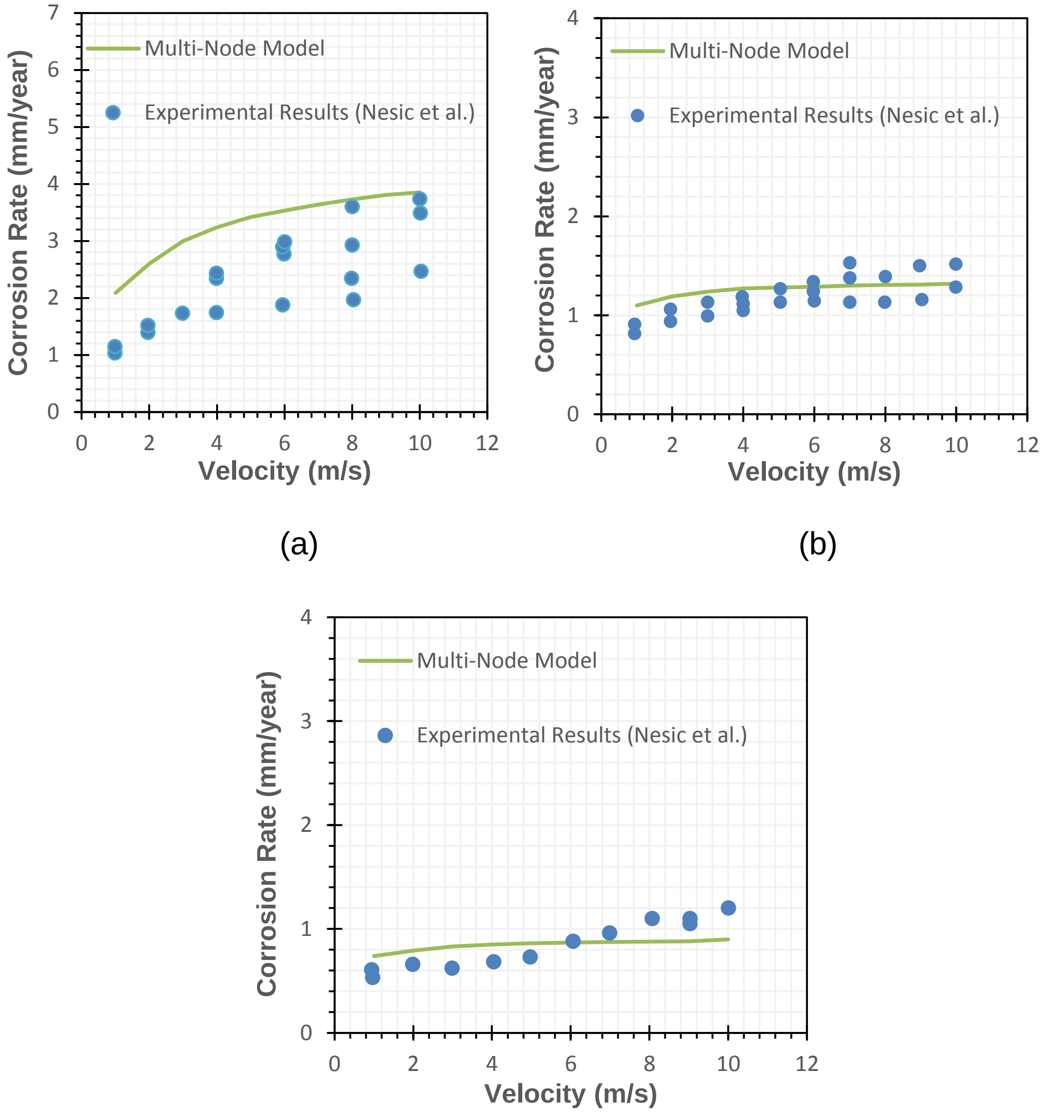

(a)

(b)

(c)

Figure 6-8 Comparison between the multi-node model predictions for pipe flow aginst Nesic et al. experiments [81] at 1 bar total pressure, d=0.01 m, temperature 20°C and various pH values a)pH=4, b)pH= 5 and c)pH=6.

6.5.4 Concentration Gradient/ Surface pH Prediction

As mentioned earlier in previous sections, the electrochemical reactions are highly influenced by the surface concentration of the species. The concentration of the species differs from the one in the bulk as the reactive species diffuse from the bulk and react at the surface. The increase of the concentration of the reactive species will lead to an increase in the rate of the electrochemical reactions. This will lead to an increase in the value of corrosion rates [33].

One of the main factors that affect the corrosion rates is pH. pH represents the activity of hydrogen ions in a solution. pH is recognised as a key local parameter that influences electrochemical reaction mechanisms and rates [32]. Also, researchers have shown that pH controls the formation of iron carbonate [206, 207]. However, the effect of the protective film is not within the scope of this thesis. The electrochemical reactions are still being controlled by the surface pH. Calculating the correct surface pH is essential to predict the correct corrosion rates.

The developed CO_2 mechanistic model is able to predict the concentration gradient of species very near the corroding surface for different conditions. Furthermore, the model is able to predict the pH gradient in the near surface region. To illustrate this aspect of the model, the model was run for the conditions similar to the experiments run by Lee et al. [208]. The experiments were run in a pipe flow test rig. The working conditions are 0.1 m pipe diameter, temperature 20°C, flow velocity 1m/s, P_{CO2} 1bar and pH 6. In this case, the produced results are shown in Figure **6-9** (a) and represent the concentration deviation from surface to bulk. The concentration deviation is negative for some species as the bulk concentration is greater than the surface concentration. This means species are consumed at the surface. The concentration deviation is positive for some species as the surface concentration is greater than the bulk concentration. This means species are produced at the surface. At pH 6 there are few hydrogen ions (H^+) in the bulk. Thus, the pH gradient is very small. The result in Figure **6-9** (b) shows the pH deviation between the bulk and the surface. The surface pH increases as the hydrogen ions are consumed at the surface.

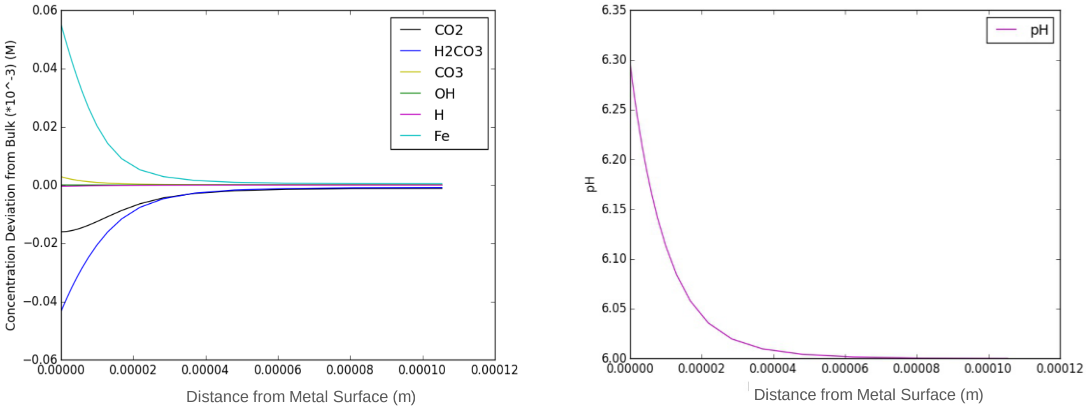

(a) (b)

Figure 6-9 Model output as a function of distance from steel surface for 0.1 m pipe diameter, temperature 20°C, flow velocity 1m/s, P_{CO2} 1bar and pH 6 (a) Deviation of dissolved species from the bulk values (b) pH gradient between the surface and bulk.

In this case, the predicted corrosion rate (0.75 mm/year) is close to the experimental value (0.68 mm/year) reported by Lee et al. [208]. The deviation between the experimental value and the theoretical value is about 10%.

Even though both the theoretical and experimental corrosion rates agree well, it is not enough to compare the corrosion rates only. The surface pH also needs to be validated with the experimental results to make sure that all the assumptions for the electrochemical reactions are correct.

In the CO_2 literature, the only way to calculate the surface pH is via the mechanistic models. However, the near surface pH experiments presented in Chapter 4 can be used to compare the experimental results and the model results. Thus, the surface pH results are compared versus the surface pH experiments. These experiments were run in solutions with various pH values under static conditions. Thus, the model needs to be modified for the static condition.

In static environments, species are transported from high concentration regions to low concentration regions via diffusion. The process is similar in the CO_2 static environment. Species generated from chemical reactions in bulk transport to the surface via diffusion. Similarly, the generated species at the surface transfer to the bulk using the same mechanism. To model this, equation (6-14) needs to be modified by ignoring the turbulent diffusivity coefficient (D_t) term. Thus, equation (6-14) can be written in the following form:

$$\mathbf{N_j} = -(\mathbf{D_j})\frac{\partial \mathbf{c_j}}{\partial \mathbf{x}} \tag{6-45}$$

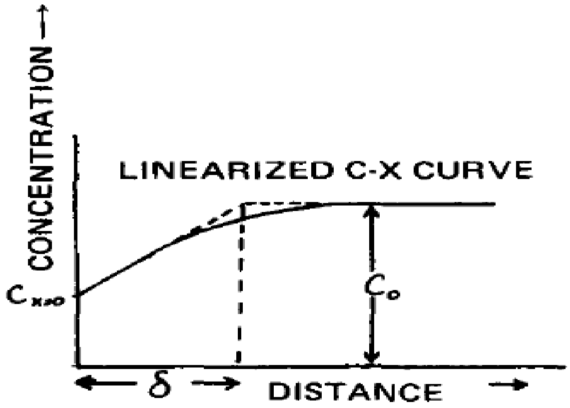

Figure 6-10 Concentration versus distance from the electrode interface [209].

The diffusion of species occurs within a small distance from the metal surface under the influence of the concentration gradient. As shown in Figure **6-10**, this distance is called the concentration boundary layer (δ). Walker and Holt [209] estimated the thickness of the boundary layer to be 300 µm. In more up to date research, Nesic et al. estimated the thickness of the liquid boundary layer in the CO_2 solution at room temperature to equal 250 µm [209]. Thus, equation (6-16) will be replaced by the value 250 µm. Otherwise, the model will be the same and nothing will be changed.

The model runs for conditions similar to the static surface pH experiments. The tests were run in static conditions for a solution saturated with CO_2 at 25°C, 1%wt. NaCl, 1 bar total pressure and pH 4, 5 and 6. The species and pH gradient are shown in Figure **6-11**. It very clear that as the bulk pH increases, the pH deviation between the surface pH and bulk pH decreases. This can be attributed to the hydrogen ions, as the pH increases this means that the hydrogen ions concentration decrease. Thus, fewer hydrogen ions diffuse from the bulk and react at the surface.

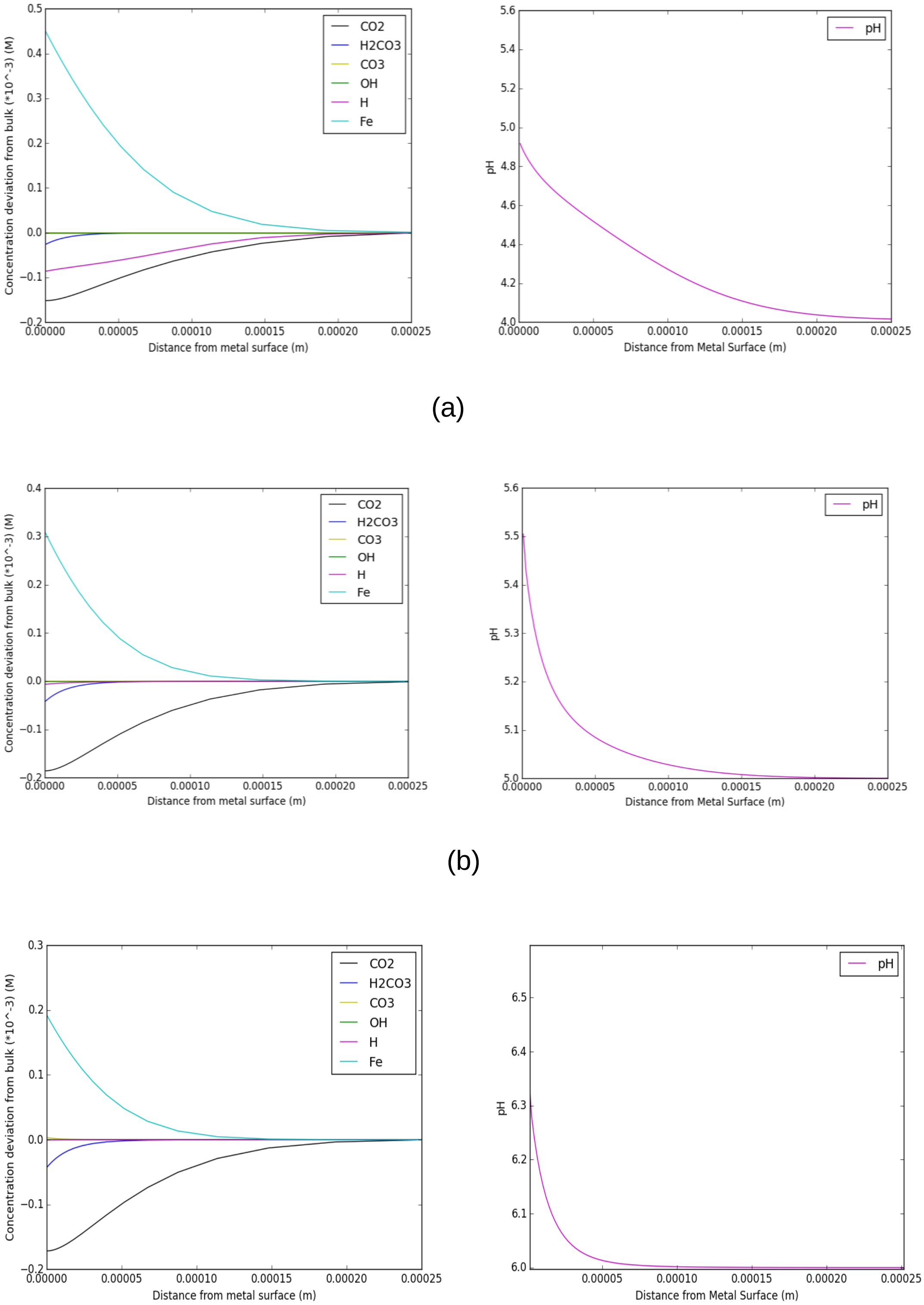

(a)

(b)

(c)

Figure 6-11 Species deviation and pH gradient between the surface and bulk as a function of distance from steel surface for a static solution saturated by CO_2, temperature 25°C, P_{CO2} 1bar and various bulk pH a) pH=4, b) pH=5 and c) pH=6**.**

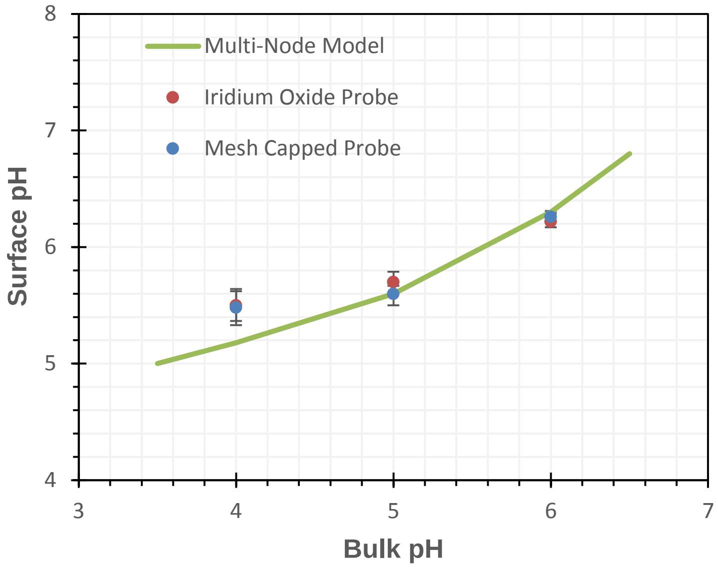

Figure 6-12 Comparison between the model surface pH predictions and experimental results from the Mesh and Iridium oxide probes for a static solution saturated by CO_2, temperature 20°C, P_{CO2} 1bar and various bulk pH.

From Figure **6-12**, the trend of both the model predictions and the experimental results are similar. In both cases, as the bulk pH increases the pH deviation between the surface and bulk decreases. The model shows a reasonable agreement with the experimental results. At low pH (pH=4) the model under-predicts the surface pH. Whereas, at higher (pH=5 and pH=6) the model prediction is very accurate. From Figure **6-12**, the discrepancy between the model results and iridium oxide results is (5.5, 2.5 and 1.2)% for pH=4, 5 and 6 respectively. Whereas, the discrepancy between the model results and mesh probe results is (4.4, 1.6 and 0.6) % for pH=4, 5 and 6 respectively.

These results suggest that the model can be used to predict the surface pH in CO_2 environments reasonably accurately, with greater accuracy for higher bulk pH conditions.

6.6 Two-Node Corrosion Modelling

This model is based on the computationally-efficient 2-node approach, proposed recently by Zheng et al. [27], which calculates species concentrations at the corroding surface in a thin surface water film of thickness Δx by accounting for homogeneous chemical reactions, mass transfer of species and electrochemical reactions at the corroding surface. This has been proposed as a more computationally-efficient alternative to the multi-node model described above. This leads to the equation

$$\frac{\partial \mathbf{c}_{\mathbf{s,j}}}{\partial \mathbf{t}} = \frac{\left(\mathbf{N}_{\mathbf{in,j}} - \mathbf{N}_{\mathbf{out.j}}\right)}{\Delta \mathbf{x}} + \mathbf{R}_{\mathbf{j}} \tag{6-46}$$

where $c_{s,j}$ is the surface concentration of species j, $N_{in,j}$ is the flux of species j from the bulk into the surface water film, $N_{out,j}$ is the flux of species out of the surface water film due to the electrochemical reactions and R_j is the rate of chemical reaction of species j in the surface water film, see Figure **6-13**. There are 7 species to be accounted for, namely CO_2, H_2CO_3, $\mathrm{HCO_3^-}$, $\mathrm{CO_3^{2-}}$, $\mathrm{OH^-}$, $\mathrm{H^+}$ and Fe^{2+}.

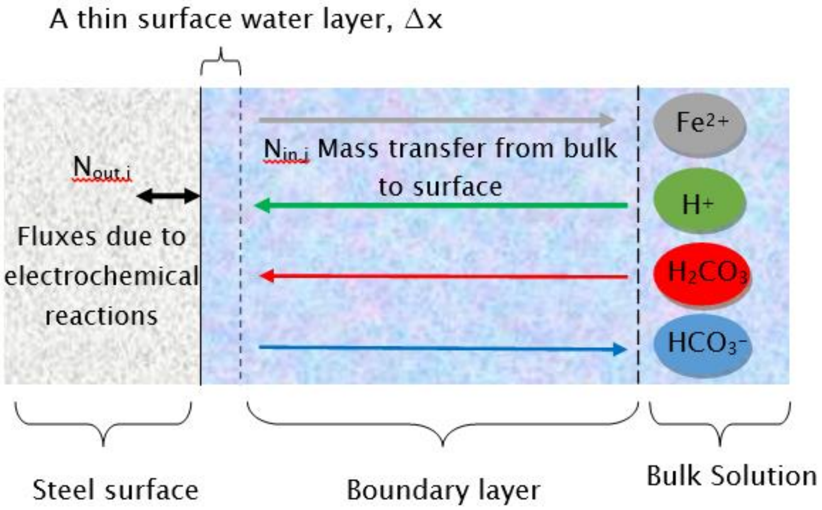

Figure 6-13 A Schematic diagram of the two-node model.

6.6.1 Mass Transfer Fluxes

The mass transfer fluxes, $N_{in,j}$ are given by

$$\mathbf{N}_{\mathbf{in,j}} = \mathbf{k}_{\mathbf{m,j}}(\mathbf{c}_{\mathbf{b,j}} - \mathbf{c}_{\mathbf{s,j}}) \tag{6-47}$$

where $k_{m,j}$ (m/s) and $c_{b,j}$ (mol/m^3) are the mass transfer coefficient and bulk concentration of species j respectively. Mass transfer coefficients are generally functions of the geometry and of the Reynolds, Schmidt and Sherwood numbers. Thus, the mass transfer coefficient for turbulent single phase flow inside a pipe can be calculated using the Berger and Hau [23] correlation:

$$\mathbf{Sh} = \mathbf{0.165\ Re^{0.86} Sc^{0.33}} \tag{6-48}$$

where the Sherwood number Sh=(kd)/D, in terms of the mass-transfer coefficient, k (m/s), RCE diameter, d (m), and diffusion coefficient D (m^2/s), the

Reynolds number Re=(U_{RCE} d)/ υ, where υ is the kinematic viscosity (m^2/s) and the Schmidt number Sc= υ/D.

For an RCE the following Eisenberg correlation [24] has been shown to be accurate for smooth surfaces

$$\mathbf{Sh = 0.0791\ Re^{0.7} Sc^{0.356}} \tag{6-49}$$

6.6.2 Electrochemical Fluxes

Three cathodic reactions and one anodic reaction are assumed to occur at the corroded surface. The cathodic reactions are the reduction of hydrogen, carbonic acid (via a buffering effect) and water reduction. While, the only anodic reaction is the iron dissolution. The rate of electrochemical reactions are computed using equation (6-24), where the reference parameter values for each of the reactions are given in Table **6-4**.

6.6.3 Chemical Reactions

For CO_2 corrosion, the water chemistry is determined by the combined effects of carbonic acid hydration, carbonic acid dissociation, bicarbonate ion dissociation and water dissociation.

Similar to the Multi-Node model, equations (6-7) to (6-12) for the 6 different species (CO_2 , H_2CO_3 , HCO_3^-, CO_3^{2-}, $OH^-$and H^+) are solved using an efficient Newton-Raphson numerical scheme implemented in Python.

6.6.4 Steady-state Two-Node Corrosion Model

This study investigates the effect of CO_2 on corrosion rates in non-film-forming conditions where corrosion rate attains a steady-state. As mentioned earlier, the model is formulated in terms of values at two nodes. The first node represents the values in the bulk and the second node those at the surface. These three processes are connected using equation (6-46), leading to:

$$\Delta\,\mathbf{x}\frac{\partial\,\mathbf{C_{surface,i}}}{\partial\,\mathbf{t}} = -\frac{\mathbf{i_i}}{\mathbf{n_i\,F}} + \mathbf{K_{m,i}}\left(\mathbf{C_{bulk,i}} - \mathbf{C_{surface,i}}\right) + \Delta\,\mathbf{x} * \mathbf{R_i} \tag{6-50}$$

Equation (6-50) is written for each of the species. The boundary conditions are:

- The species at the surface are under equilibrium. Therefore all equilibrium coefficients applied in the bulk can be used at the surface.

- The flux at the surface (N_{out}) due to the electrochemical reactions is zero for non-reactive species. While the flux for the reactive species can be calculated using equation (6-24).

The steady state equations boundary conditions can be rearranged to yield:

$$
\begin{aligned}
\mathbf{0} = -\frac{\left(\mathbf{i}_{\mathbf{H}^+} + \mathbf{i}_{\mathbf{H_2o}} + \mathbf{i}_{\mathbf{H_2CO_3}}\right)}{\mathbf{F}} &+ \mathbf{k}_{\mathbf{m,H}^+}\left(\mathbf{c}_{\mathbf{H}_\mathbf{b}^+} - \mathbf{c}_{\mathbf{H}_\mathbf{s}^+}\right) \\
&- \mathbf{k}_{\mathbf{m,OH}^-}\left(\mathbf{c}_{\mathbf{OH}_\mathbf{b}^-} - \mathbf{c}_{\mathbf{OH}_\mathbf{s}^-}\right) + \mathbf{k}_{\mathbf{m,CO_2}}\left(\mathbf{c}_{\mathbf{CO_{2,b}}} - \mathbf{c}_{\mathbf{CO_{2,s}}}\right) \\
&- \mathbf{k}_{\mathbf{m,CO_3^{2-}}}\left(\mathbf{c}_{\mathbf{CO_{3,b}^{2-}}} - \mathbf{c}_{\mathbf{CO_{3,s}^{2-}}}\right) \\
&+ \mathbf{k}_{\mathbf{m,H_2CO_3}}\left(\mathbf{c}_{\mathbf{H_2CO_{3,b}}} - \mathbf{c}_{\mathbf{H_2CO_{3,s}}}\right)
\end{aligned}
\tag{6-51}
$$

$$
\mathbf{K}_{\mathbf{wa}} = \mathbf{c}_{\mathbf{H}_\mathbf{s}^+}\mathbf{c}_{\mathbf{OH}_\mathbf{s}^-}
\tag{6-52}
$$

$$
\mathbf{0} = \mathbf{k}_{\mathbf{m,CO_2}}\left(\mathbf{c}_{\mathbf{CO_{2,b}}} - \mathbf{c}_{\mathbf{CO_{2,s}}}\right) + \Delta\mathbf{x}(\mathbf{K}_{\mathbf{b,hy}}\,\mathbf{c}_{\mathbf{H_2CO_{3,s}}} - \mathbf{K}_{\mathbf{f,hy}}\mathbf{c}_{\mathbf{CO_{2,s}}})
\tag{6-53}
$$

$$
\begin{aligned}
\mathbf{0} = \mathbf{k}_{\mathbf{m,CO_2}}\left(\mathbf{c}_{\mathbf{CO_{2,b}}} - \mathbf{c}_{\mathbf{CO_{2,s}}}\right) &+ \mathbf{k}_{\mathbf{m,H_2CO_3}}\left(\mathbf{c}_{\mathbf{H_2CO_{3,b}}} - \mathbf{c}_{\mathbf{H_2CO_{3,s}}}\right) \\
&+ + \mathbf{k}_{\mathbf{m,HCO_3^-}}\left(\mathbf{c}_{\mathbf{HCO_{3,b}^-}} - \mathbf{c}_{\mathbf{HCO_{3,s}^-}}\right) \\
&+ \mathbf{k}_{\mathbf{m,CO_3^{2-}}}\left(\mathbf{c}_{\mathbf{CO_{3,b}^{2-}}} - \mathbf{c}_{\mathbf{CO_{3,s}^{2-}}}\right)
\end{aligned}
\tag{6-54}
$$

$$
\mathbf{c}_{\mathbf{H}_\mathbf{s}^+}\mathbf{c}_{\mathbf{HCO_{3,s}^-}} = \mathbf{K}_{\mathbf{Ca}}\,\mathbf{c}_{\mathbf{H_2CO_{3,s}}}
\tag{6-55}
$$

$$
\mathbf{c}_{\mathbf{H}_\mathbf{s}^+}\mathbf{c}_{\mathbf{CO_{3,s}^{2-}}} = \mathbf{K}_{\mathbf{bi}}\mathbf{c}_{\mathbf{HCO_{3,s}^-}}
\tag{6-56}
$$

These 6 equations are solved using a Newton-Raphson numerical scheme. The computer program is written for this purpose, in the Python language.

Once the current density is calculated, the corrosion rate (CR (mm/year)) can be obtained using the formula:

$$
\mathbf{CR} = \mathbf{1.16} \times \mathbf{i}_{\mathbf{cathodic}}
\tag{6-44}
$$

where:

$$
\mathbf{i}_{\mathbf{cathodic}} = \mathbf{i}_{\mathbf{H}^+} + \mathbf{i}_{\mathbf{H_2o}} + \mathbf{i}_{\mathbf{H_2CO_3}}
\tag{6-57}
$$

6.7 2-Node Model Corrosion Rate Predictions

6.7.1 Comparison Against Multi-Node Model and Pipe Flow Results

The corrosion rate predictions obtained from the 2-node model are now compared with the corrosion Multi-Node predictions for different pH values and flow speeds and pipe flow loop experiments from Nesic et al. [81].

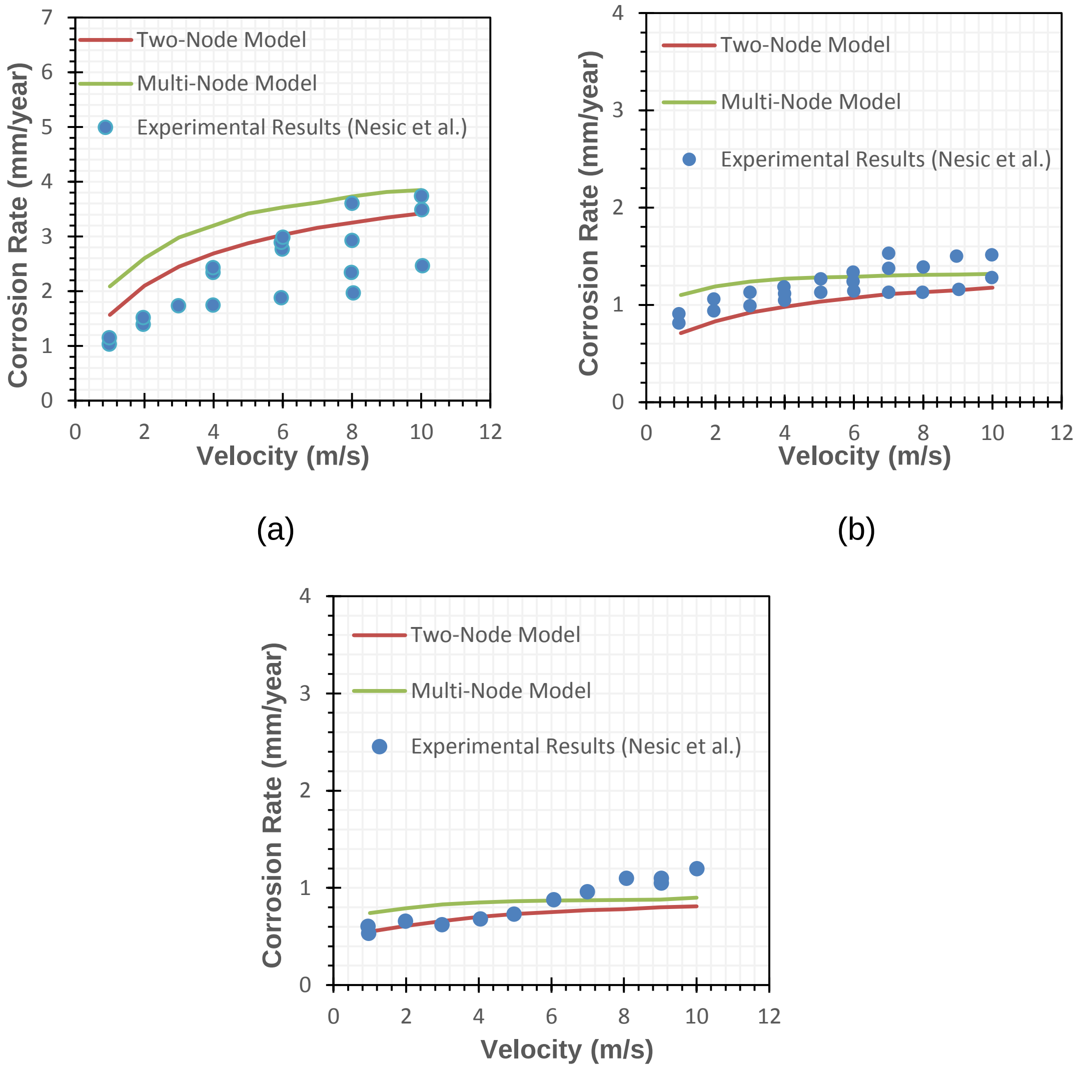

(a) (b)

(c)

Figure 6-14 Comparison between two-node model predictions and multi-node model predictions for pipe flow aginst Nesic et al. experiments [28] at 1 bar CO_2, d=0.01 m, 20°C and various pH values a) pH=4, b) pH=5 and c) pH=6.

The results presented in Figure **6-14** reveal that the two-node corrosion model predictions agree well with both the experimental and theoretical results of the multi-node model. At pH=4 the two-node model predictions are more accurate than the multi-node ones, while at high pH (pH=5 and 6), the results of the multi-node model are more accurate than the two-node corrosion model. Note, however, that the predictions of the two-node model can be obtained in only a few seconds on a desk-top computer with an Intel Xenon 3.5 GHz processor and 16 GB installed memory, compared to multi-node ones which typically take in excess of 20 minutes in order to predict the corrosion rate.

6.7.2 Corrosion Rate Validation for Smooth RCE Samples

The results of the two-node model are compared with the experimental results for a smooth RCE given in Section 4.4.1, with corrosion rate values from the RCE experiments compared with the model's predictions by varying the solution pH and the rotational speed of the RCE. The effect of velocity was studied at pH=4, 5 and 6. The rotation speed started with 1000 rpm (0.628 m/s) and increased up to 4000 rpm (2.512 m/s).

Figure **6-15** shows that for pH=4 corrosion rate increases with rotational speed, indicating that mass transfer from the bulk is important, whereas, for the higher pH values, where the bulk concentration of H^+ is orders of magnitude smaller, mass transfer of H^+ ions is far less important. This leads to a reduction in the cathodic consumption of H^+ ions and a corresponding reduction in corrosion rate. Good agreement was obtained between the model predictions and the experimental results for all cases considered, with the discrepancies within the margins of experimental error. The average difference between the model and the experiments is about 10, 7 and 15 % for pH=4, 5 and 6 respectively.

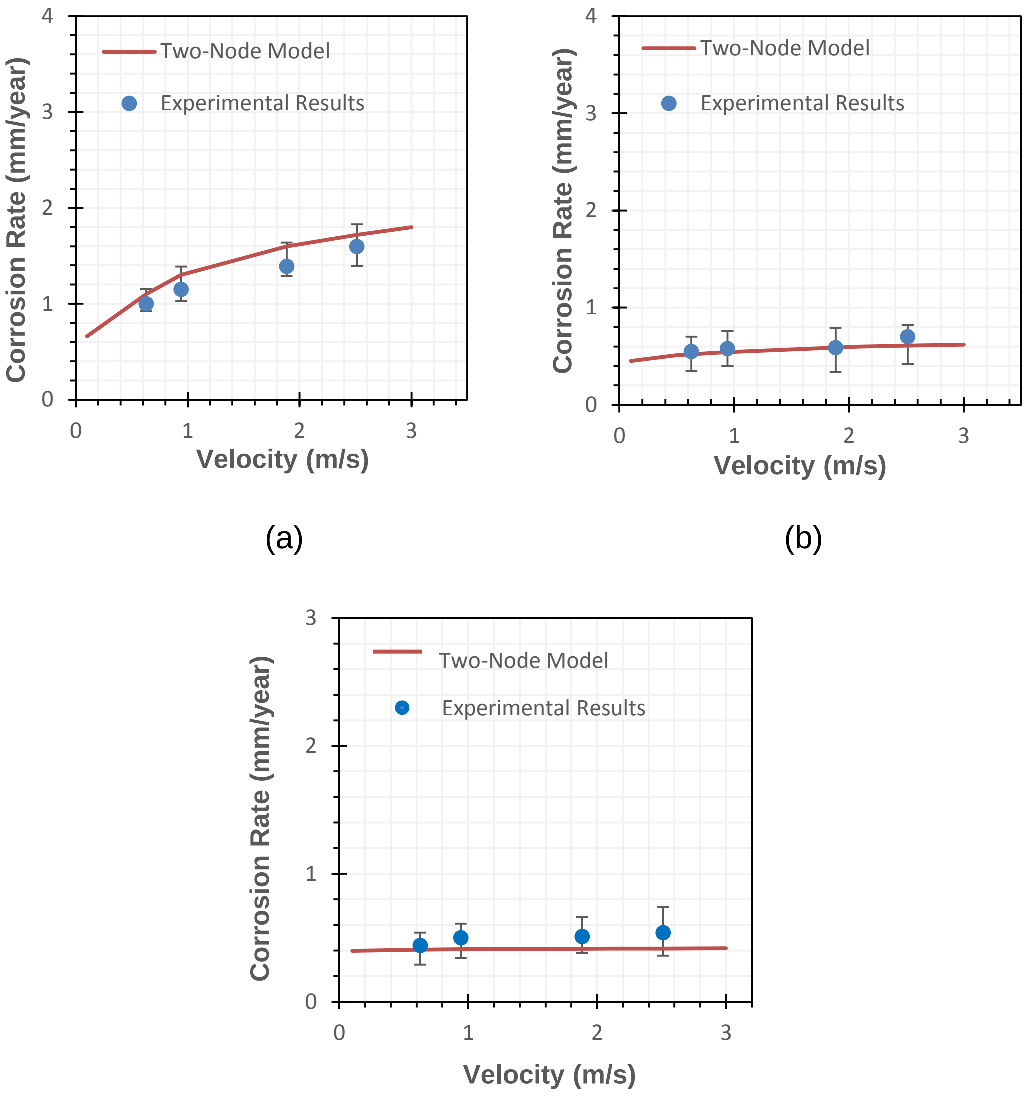

(a)

(b)

(c)

Figure 6-15 Comparisons between experimental and theoretical corrosion rates at 1 bar total pressure, 25°C, different rotation speeds for a smooth RCE and various pH a) pH=4, b) pH=5 and c) pH=6.

6.7.3 Model Corrosion Rate Validation for Rough RCE Samples

These tests were then extended to cases of turbulent flow over rough carbon steel X65 surfaces. The mass transfer coefficients used in the two-node corrosion model are calculated using the new correlation for mass transfer to rough RCE surfaces proposed in (Chapter 5) where

$$\mathbf{Sh} = \frac{\mathbf{k\ d}}{\mathbf{D_{H^+}}} = \frac{\mathbf{f_c}}{\mathbf{2}}\ \mathbf{Re^{0.8}\ Sc^{\ 0.356}} \tag{5.10}$$

where

$$\frac{\mathbf{f}_c}{\mathbf{2}} = \mathbf{0.175}\left(\frac{\mathbf{e}}{\mathbf{d}}\right)^{\mathbf{0.17}} \tag{5.11}$$

All current densities, and hence the corrosion rate, were expressed with the projected surface area. Figure **6-16** shows the experimental and theoretical corrosion rate results as a function of RCE velocity for each of the four different roughness values. The red dotted line represents model predictions which have been not validated against the experimental results. while the continuous red line represents validated model predictions. It is clear that the corrosion rate increases with the surface roughness. For example, at 3000 rpm the corrosion rate increases by 22, 46 and 57 % as the surface roughness increases from d/e=2000 to d/e=600 and d/e=353 respectively. The modified 2-node model also agrees very well for all roughness cases with average discrepancies of 10, 6, 5.6 and 12.5 % in comparison with the experiments for the four roughness cases. The average difference between the model and the experiments is around 8% and the maximum deviation is about 19%.

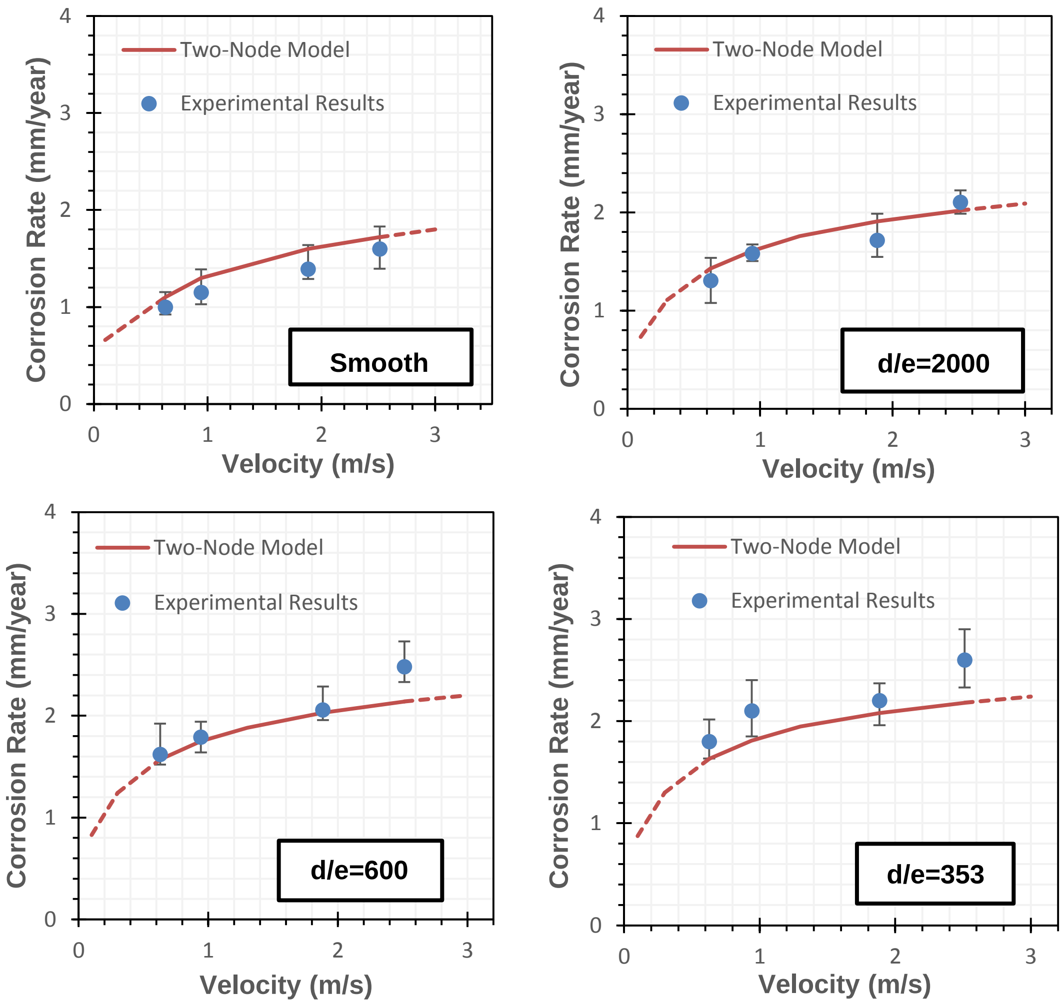

Figure 6-16 Comparisons between model results and experimental results at 1 bar total pressure, 25°C, pH=4, and different rotation speed for different surface finishes.

Several explanations for the effect of surface roughness on increasing corrosion rate have been discussed in the literature. It is generally assumed that the roughness peaks disturb the viscous layer and the turbulence generated reduces the resistance to mass transfer across the concentration boundary layer and in the valleys between the roughness peaks [184]. The analysis of mass transfer intensification is based on behaviour of turbulent eddies. These eddies penetrate into a cavity on a wall causing deceleration in their motion due to viscous friction with the surface. The process of decceleration is totally non uniform. Inside these cavities, the non-uniformity causes formation of such areas where turbulence fluctuations have relatively high kinetic energies at distances from the surface which are significantly smaller than the diffusive layer thickness calculated assuming the wall is smooth [135].

6.7.4 Model Corrosion Rate Results for Rough RCE Samples under Different Working Conditions

In the previous sections, the comparison between the results of the two-node model with the experimental results from both the present study and the literature have demonstrated the reliability of the model. Thus, the validated model was used to predict the effect of temperature and the effect of CO_2 partial pressure on corrosion rates for rough RCE samples.

Figure 6-17 shows the effect of increasing temperature on the corrosion rates for three RCE samples with surface roughness of (d/e= 2000, 600 and 353). The increase of temperature leads to an increase in the corrosion rate.

In low pH (pH=4) and a film free condition, temperature accelerates all the processes involved in corrosion including: electrochemical reactions, transport of species and chemical reactions. Thus, the corrosion rates increased with the increase of the temperature. For example, at 3000 rpm (1.884 m/s) and d/e= 2000, the corrosion rate increases by 51% and 121% at temperature 50°C and 80°C respectively. while, at 3000 rpm (1.884 m/s) and d/e= 600, the corrosion rate increases 49% and 119% at temperature 50°C and 80°C respectively. On the other hand, at 3000 rpm (1.884 m/s) and d/e= 353, the corrosion rate increases 48% and 117% for temperature 50°C and 80°C respectively. The average increase of the corrosion rate at 50°C is around 55, 52 and 51% for d/e= 2000, 600 and 353 respectively and the The average increase of the corrosion rate at 80°C is around 131, 126 and 123 % for d/e= 2000, 600 and 353 respectively. While, the maximum increase of the corrosion rate at 50°C is around 63, 60 and 57% for d/e= 2000, 600 and 353 respectively and the maximum increase of the corrosion rate at 80°C is around 152, 144 and 140 % for d/e= 2000, 600 and 353 respectively.

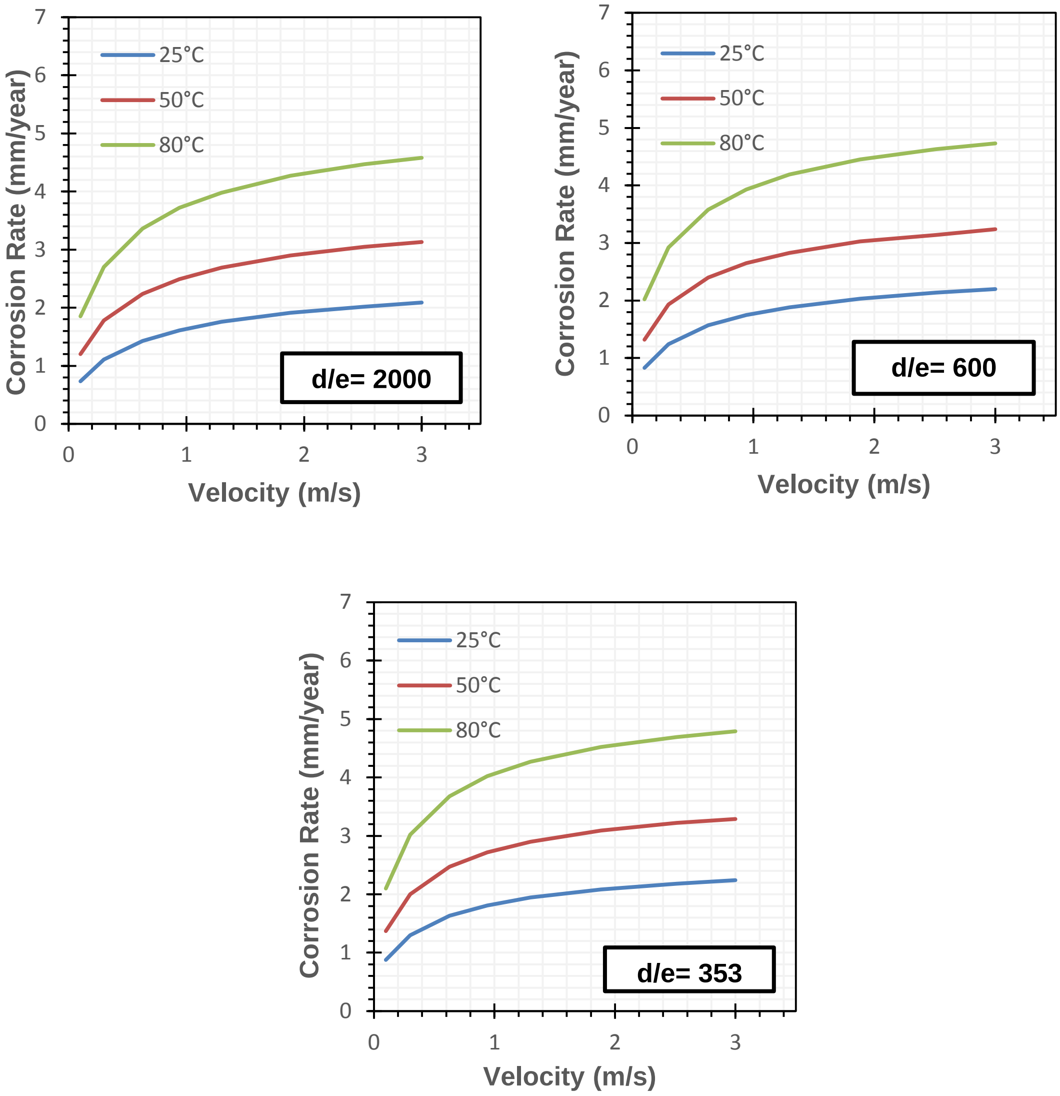

Figure 6-17 Predicted corrosion rates of a two-node model for different surface finishes at 1 bar total pressure, pH=4, and different rotation speed and various temperature values 25°C, 50°C and 80°C.

Figure 6-18 shows the effect of increasing CO_2 partial pressure on corrosion rates for three RCE samples with surface roughness of (d/e= 2000, 600 and 353). It can be seen that corrosion rate increases when CO_2 partial pressure increases; this might be caused by increasing either the total pressure or the molar concentration of CO_2 in the gas phase. This means the concentrations of reactive species are increased, leading to a significant increase in the corrosion rate. The average increase of the corrosion rate at 5 bar is around 71, 64 and 116% for d/e= 2000, 600 and 353 respectively and the average increase of the corrosion rate at 10 bar is around 143, 129 and 122 % for d/e= 2000, 600 and 353 respectively. While, the maximum increase of the corrosion rate at 5 bar is around 134, 117 and 110% for d/e= 2000, 600 and 353 respectively and the maximum increase of the corrosion rate at 10 bar is around 276, 242 and 229 % for d/e= 2000, 600 and 353 respectively.

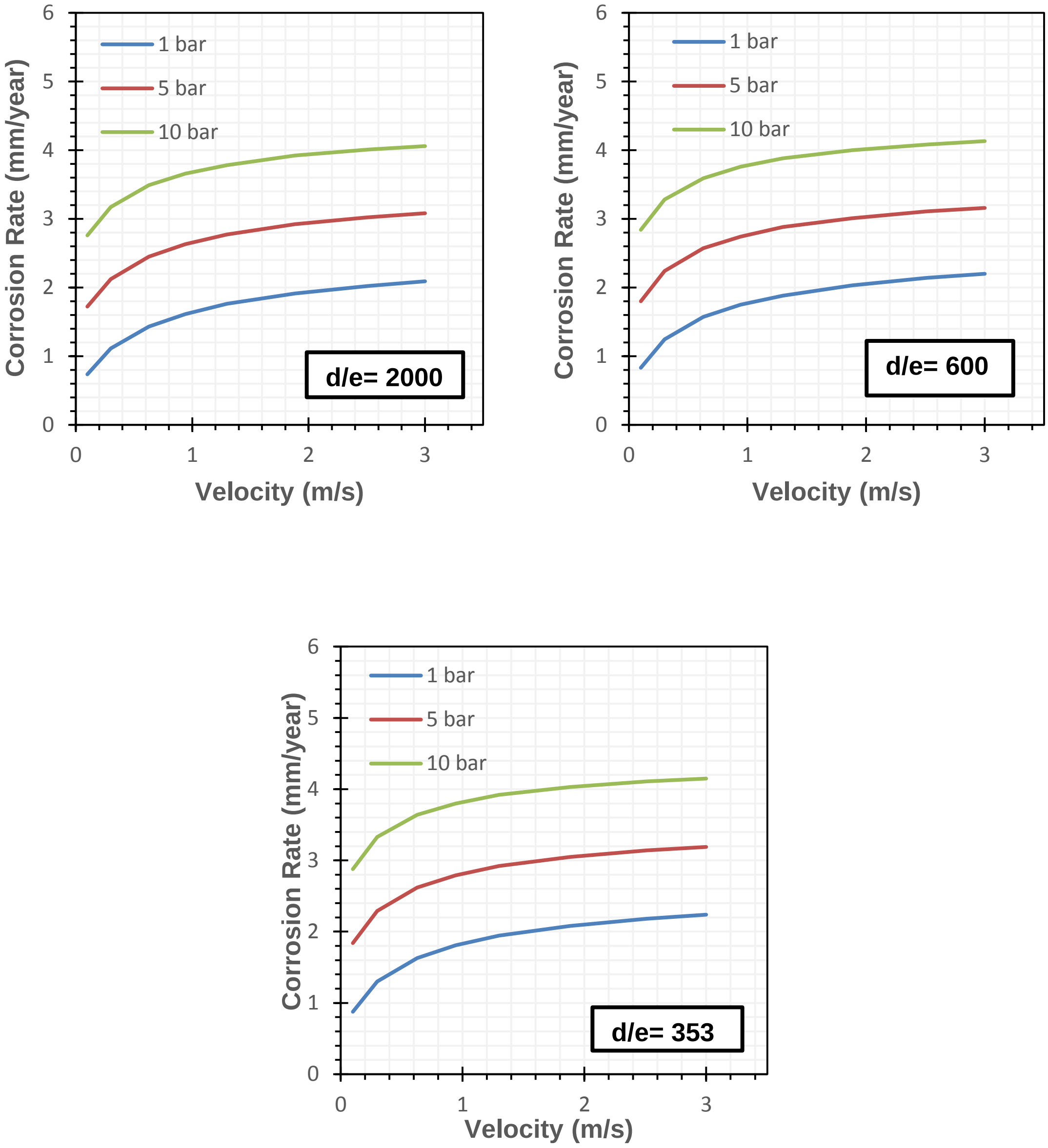

Figure 6-18 Predicted corrosion rates of a two-node model for different surface finishes at 25°C, pH=4, and different rotation speed and various partial pressure values 1 bar, 5 bar and 10 bar.

Chapter 7 Conclusions and Future Work

7.1 Introduction

This thesis has used experimental and numerical methods to understand how surface roughness influences both mass transfer and corrosion rates in CO_2 environments. It has also assessed the validity of the available mass transfer correlations for surfaces with different roughness and the use of different techniques to measure the surface pH.

7.2 Overall Discussion

The purpose of the discussion section is to review the overarching themes and proposed methodologies. The discussion is divided into the following key areas:

- The effect of surface roughness on mass transfer.
- The effect of surface roughness on corrosion rates.
- Evaluation of surface pH measurement methods.
- The usefulness and key role of the CO_2 mechanistic models to predict the corrosion rates and surface pH.
- Corrosion rate predictions of rough surfaces under different working conditions.

7.2.1 The Effect of Surface Roughness on Mass Transfer

In the case of mass transfer, the use of limiting current technique to measure the mass transfer is very well established in the field. The technique was employed to measure the mass transfer for both smooth and rough samples.

The experimental results in (Chapter 5) showed the difference in sweep profiles when the current density is determined based on the projected area or the actual area of the X65 steel surfaces. The results showed a noticeable difference between the two sets of profiles. This difference increased as the surface roughness increased (d/e = 353 in particular). This observation indicates the importance of accounting for the increased surface area. This comes in agreement with Makanjuola and Gabe [31] who demonstrated the need to express the results based on the actual area. The mass transfer results revealed that the increase in sample roughness leads to an increase in the rate of mass transfer, even when the real surface area of each sample is taken into account. The explanation of the enhancement of mass transfer was explained by Busse et al. [182] who studied turbulent flow past an irregular rough surface based on a scan of a rough graphite surface. They concluded that there is enhanced mass transfer over rough surfaces, including a significant increase in wall-normal flow fluctuations within roughness layers, strong upwards motions at the upstream faces of roughness peaks and recirculating flow regions between the peaks.

An interesting observation in these tests showed that mass transfer has some dependency on the d/e ratio, as increasing the roughness (or reducing d/e) served to enhance mass transfer for a given rotation speed.

The comparison between the experimental results and two relationships from the literature (Gabe and Makanjuola correlation and Poulson correlation) [30, 112] showed that the Poulson correlation produces a closer agreement with the roughest RCE sample considered (d/e = 353). While, the Gabe and Makanjuola correlation produces a closer agreement with the lowest roughness RCE sample considered (d/e = 2000). The results generated are clearly sensitive to the degree of surface roughness and consequently suggest that there is a need for a new correlation which also accounts for the value of d/e. It is therefore not surprising that roughness plays a role in influencing mass transfer, a finding that is consistent with Dawson and Trass [184]. However for the flows considered here, with Schmidt numbers around Sc~100, even when the roughness is well immersed within the viscous sublayer, it can still disturb the thinner mass transfer boundary layer (As shown in Figure **7-1**), leading to enhancement of mass transfer.

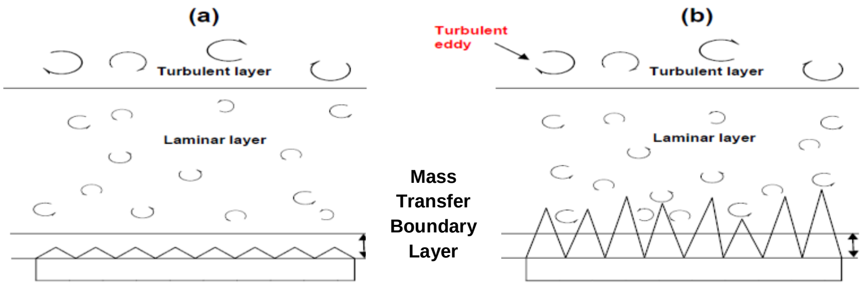

Figure 7-1 Schematic illustration of the mass-transfer boundary layer for (a) smooth surfaces and (b) rough surfaces under turbulent flow [210].

From the above, the results obtained in these experiments have shown that surface roughness is a complex factor as the mass transfer is highly affected by changes of it. Also, the comparison with the correlations from literature has revealed that it is not possible to obtain a universal mass transfer correlation for all kinds of roughness. Thus, each roughness orientation has to be treated individually, and a particular correlation has to be obtained for each roughness pattern.

While in the CO_2 environments, the Vetter correlation has been used to estimate the magnitude of the limiting current of the carbonic acid component. The work by Nesic et al. [115] suggested that the surface roughness might disturb the mass transfer in the boundary layer. However, the tests were performed at 4000 rpm indicate that the effect of the surface is minor and Vetter’s correlation is still being used to estimate the limiting current of carbonic acid ($i_{lim\ H2CO3}$) without any modification.

7.2.2 The Effect of Surface Roughness on Corrosion Rates

In the case of corrosion rates, the Linear Polarisation Resistance (LPR) technique was used to measure the corrosion rate. The experiments were run for 3 hours to make sure that the corrosion rate achieved a steady state.

The early set of experiments were run for smooth samples in an RCE setup. The results were not surprising as the value of corrosion rate decreased as the pH increased. Also, at low pH (pH=4) the corrosion rate showed flow dependence. The corrosion rate increased with rotational speed, indicating that mass-transfer from the bulk is influential, whereas for the higher pH values, where the bulk concentration of H^+ is orders of magnitude smaller, mass transfer of H^+ ions is far less influential.

For the case of rough surfaces, the static tests were performed with four RCE samples (0.5, 6, 20 and 34) µm of different surface finishes. The results of corrosion are normalised based on their actual surface area determined by profilometry, as opposed to their projected area The results shown in Figure 5-8 indicate that correcting for area leads to no significant change in corrosion rates across all rough surfaces, indicating that the machining process does not influence the dissolution of the steel.

For the case of rough surfaces and under dynamic conditions, the results shown in Figure 5-10 displayed the experimental corrosion rate results based on the true surface area. It is very clear that the corrosion rate increased with the speed and surface roughness. The reason behind this can be attributed to the enhancement in mass transfer. The increase in surface roughness disturbs the thinner mass transfer boundary layer leading to an increase in mass transfer. Thus, the corrosion rate increases.

7.2.3 Evaluation of Surface pH Measurement Methods.

Very few studies have reported in the literature to measure surface pH. It is believed that the surface pH controls the electrochemical reactions [32]. Thus, the ability to measure and predict surface pH is essential to understand the process of corrosion in the CO_2 environment.

As discussed in Chapter 2, there were several reasons for using the mesh capped pH probes and the iridium oxide probes. In the case of mesh capped probe, the method was used by Han et al. [32] to study the surface pH in the CO_2 environments. The method is easy to fabricate however the method is only limited to static systems. In the case of iridium oxide probes, the most important of which were cheap compared to others, the fabricated sensor has fast response and good repeatability and no need for heat treatment.

The first set of results in Figure **4-7** revealed the response of probes over a period of time (2 hours) in three solutions with different pH. The probes showed a fast response and stability. The probes first slightly overpredict the value of pH and after few seconds dropped and stabilised to predict the bulk pH. The maximum difference between the traditional pH probe reading and the iridium oxide probe was about 1.5%. These results confirmed that the iridium oxide is stable over time and can be used to measure pH.

The iridium oxide probes were only limited to biological and medical applications and never been used to measure surface pH for the case of CO_2 corrosion. Comparisons of surface pH results in the static CO_2 environments between the iridium probes and the mesh capped were plotted in Figure **4-8**. The results in both cases were very similar. The results have shown that the surface pH is higher than the one in the bulk due to the electrochemical reactions which occur at the corroding surface. Also, the surface pH has a dependency on bulk pH. It is obvious that the difference in pH between the bulk and the surface decreases as the bulk pH increases. This can be attributed to hydrogen ions concentration. For example, at pH= 6 the concentration of hydrogen ions is two orders less than the concentration at pH=4 thus less hydrogen ions diffuse from the bulk and react at the surface. These results support the fact that the iridium oxide probes can be used to measure the surface pH during corrosion of carbon steel. Furthermore, these results demonstrated that the iridium oxide probes could be effectively utilised in the future to measure the surface pH for dynamic systems.

7.2.4 The Role of Mechanistic CO_2 Corrosion Models for Predicting Corrosion Rates and Surface pH.

Two mechanistic models for CO_2 corrosion were implemented in Chapter 6. The first one is the multi-node model and the second one is the two-node model. Both of these models rely on the accurate prediction of solution chemistry in the bulk solution. The chemical term of these models was validated against the results from the literature. The model is capable of predicting the solution bulk pH accurately.

In the multi-node model, the model solves the time-dependent corrosion problem. The present implementation of the multi-node model, with more up-to-date reaction rate constants, has been shown to provide more accurate predictions than the original Nordsveen et al. [33] implementation.

The present implementation of the multi-node model has been successfully calibrated against data from the literature. This data was carefully controlled pipe flow corrosion experiments under different environmental parameters in film free conditions. The results displayed in Figure **6-8** showed that the model predictions agreed reasonably well with the experimental results. At low pH (pH=4), both the model and the experimental results were monotonically increased as the flow speed increased. The reason is that the process in these cases is mass transfer controlled. The increase of flow speed increased the mass transfer thus more reactive species transported from bulk to surface which cause the corrosion rate to be increased. On the other hand, at high pH (pH=6), the process is chemical controlled. Thus, the corrosion rates were independent of flow speed. Furthermore, the multi-node predications were compared against the near surface pH measurements in static conditions. The results plotted in Figure **6-12** indicating that the model showed a reasonable agreement with the experimental results.

The present implementation of the two-node model proposed by Zheng et al. [202] enables the steady state corrosion rates in CO_2 environments to be determined at a fraction of the cost of the corresponding multi-node solutions. Comparison of the two-node model, multi-node model and the experimental results for pipe flow revealed that the two-node predications were within an acceptable level of agreement.

The comparison between the two-node model and the smooth RCE experiments showed that the model predictions were within the experimental error bars which accentuate the accuracy of this model. The results plotted in Figure **6-15** illustrated that at pH=4 the corrosion rate increased with rotational speed, indicating that mass transfer from the bulk is important, whereas, for the higher pH values, where the bulk concentration of H^+ is orders of magnitude smaller, mass transfer of H^+ ions is far less important. This leads to a reduction in the cathodic consumption of H^+ ions and a corresponding reduction in corrosion rate.

7.2.5 Corrosion Rate Predictions of Rough Surfaces Under Different Working Conditions.

The final stage of the discussion comprises the results of the two-node model for surfaces with different roughness. Also, the effect of temperature and CO_2 partial pressure on the corrosion rate of rough surfaces was analysed in this stage.

The modified two-node model also agreed very well for all roughness cases. The comparisons between the experimental and theoretical results could be deduced that the corrosion rates increased with the surface roughness. The explanation of this increase in corrosion rate that the roughness peaks disturb the viscous layer and the turbulence generated reduces the resistance to mass transfer across the concentration boundary layer and in the valleys between the roughness peaks [184].

Furthermore, the results in Figure 6-17 and Figure 6-18 display the effect of temperature and CO_2 partial pressure on the corrosion respectively. In both cases, the increase of temperature and partial pressure led to an increase in the corrosion rates. The explanation of increase of corrosion rates as the temperature increased that temperature accelerates all the processes involved in corrosion including electrochemical reactions, transport of species and chemical reactions. Thus, the corrosion rates increased with the increase of the temperature. On the other hand, when CO_2 partial pressure increases; this might be caused by increasing the molar concentration of CO_2. This means the concentrations of reactive species are increased, leading to a significant increase in the corrosion rate.

7.3 Conclusions summary

In this concluding part, the questions raised in the aim and objectives section have been addressed and the main findings in this study are summarised as follows:

- Surface roughness is a complex parameter. Thus, there is a need for greater awareness and understanding of the role of surface roughening on mass transfer. Mass transfer is controlled by the value of roughness, roughness orientation and Reynolds numbers.
- Surface roughness is an important factor that affects the value of the mass transfer. In the N_2 environment at pH=3, the increase of surface roughness led to an increase in the value of limiting current. Thus, the mass transfer increased.
- The available correlations for the roughness pattern similar to the roughness picked in this study were shown to be inadequate. Thus, a new correlation was proposed which is a function of roughness (d/e) to predict the mass transfer with a high degree of accuracy. It is important to stress that it is impossible to obtain a universal mass transfer equation for all types of surface roughness.
- In the CO_2 environment, surface roughness has a minor effect on the limiting current of carbonic acid ($i_{lim,H2CO3}$). Thus, Vetter's correlation can still be used without any modification.
- A number of experimental methods were proposed in the literature to measure the surface pH. However, the mesh-capped and iridium oxide probes were used to measure the surface pH in the CO_2 environments. The results of both methods were fairly similar.

- The results of the Iridium oxide probes demonstrated that these probes can be promoted in the future to measure the surface pH for dynamic systems. Also, this design can be implemented to track the surface pH during the formation of iron carbonate.
- The surface pH is strongly affected by the bulk pH. The difference between the surface pH and the bulk increased as the bulk pH decreased as the hydrogen ions increased.
- A mechanistic multi-node model is implemented in this study to predict the nature of the near-surface region in the absence of protective films. The model takes into account the mechanisms of the CO_2 corrosion process, the rates of the different electrochemical reactions, the rates of the mass transfer processes, various equilibrium reactions in the system. The model was successfully calibrated against the experimental results from the literature. Furthermore, the model reasonably predicted the static surface pH results.
- The two-node model was developed to overcome the long duration to process the numerical calculations in the multi-node model. Comparison between the two-node model and multi-node model demonstrated the reliability of the two-node model to predict the corrosion rates.
- Both the two-node model and the experimental results for an RCE setup supported the fact that the corrosion rate is highly sensitive to flow at low pH and less sensitive to flow at high pH.
- The two-node model can predict the corrosion rates for both smooth and rough RCE surfaces.

7.4 Recommendations For Future Work

Although the study has highlighted several findings concerning the value of combined modelling and experimental approaches to understand the effect of surface roughness on the mass transfer, corrosion rate and near-surface pH measurements in CO_2 environments, there is a multitude of avenues that the work can be carried forward.

The outcome of this study opens the way to further and deepen knowledge of corrosion behaviour of the carbon steel under different working conditions. Specific recommendations for future work include:

- Explore the effect of more roughness patterns such as knurled diamond pyramids, longitudinal fins and metal deposit at low pH in N_2 environments to check the validity of the correlations in the literature. Also, study the effect of these roughness patterns on the limiting current of carbonic acid in CO_2 environments to check the validity of Vetter's correlation for each case.
- Develop a flow cell to create an efficient method to measure the surface pH for flowing systems as shown in schematic in Figure **7-2**. The flow cell will help to study the effect of hydrodynamics on both corrosion rates and surface pH under different working conditions.
- Implement the iridium oxide probe to measure the surface pH in H_2S environments.

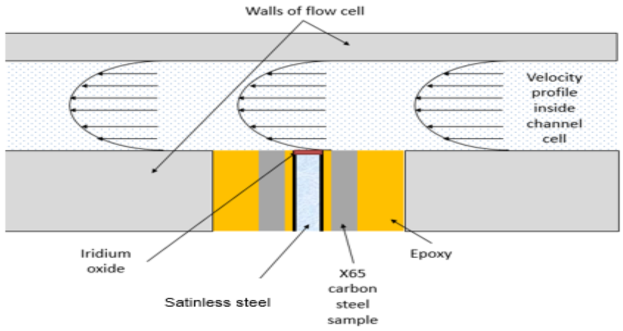

Figure 7-2 Schematic for flow for surface pH measurements for future work.

- Use the iridium oxide probe to measure the surface pH during the precipitation of iron carbonate ($FeCO_3$). This will help to model the $FeCO_3$ as a function of surface pH because all the $FeCO_3$ precipitation models are a function of bulk pH.
- Develop the mechanistic model to take into account the effect of the surface film, the effect of H_2S and wettability.
- Iron carbonate is an efficient way to inhibit corrosion. Thus, link the saturation ratio and surface pH with film formation will help to create a more robust mechanistic CO_2 corrosion model.

References

1. McCafferty, E., *Introduction to corrosion science*. 2010: Springer Science & Business Media.
2. Hu, H., et al., *The role of renewable energy consumption and commercial services trade in carbon dioxide reduction: Evidence from 25 developing countries.* Applied Energy, 2018. **211**: p. 1229-1244.
3. Agency, I.E., *Oil market report*. 2017.
4. Stephen, P. and G. Hillard, *OPEC and world oil security.* Energy Policy, 2017.
5. Nguyen, T.-V., et al., *Life performance of oil and gas offshore platforms–site-scale integration and exergy-based assessment.* Energy, 2014. **73**: p. 282-301.
6. Kermani, M. and D. Harr. *The impact of corrosion on oil and gas industry*. in *Giornata di studio IGF S. Donato Milanese 1996*. 2008.
7. Fosbøl, P.L., K. Thomsen, and E.H. Stenby, *Improving Mechanistic CO2 Corrosion Models*. NACE International.
8. Attanasi, E.D. and P.A. Freeman, *Commercial possibilities for stranded conventional gas from Alaska's North Slope.* Natural resources research, 2014. **23**(1): p. 175-193.
9. Abduh, M., *The 50 Major Engineering Failures.* 2008.
10. Administration, U.D.o.T.P.a.H.M.S., *Serious incidents by cause, US pipelines.* 2015.
11. Kermani, M.B. and A. Morshed, *Carbon Dioxide Corrosion in Oil and Gas ProductionA Compendium.*
12. Bennett, L.H., et al., *Economic effects of metallic corrosion in the United States. Part 1*. 1978, National Bureau of Standards, Washington, DC (USA); Berman (Edward B.) Associates, Inc., Marblehead, MA (USA).
13. Roberge, P.R., *Handbook of corrosion engineering. 2000.* Table. **3**: p. 242.
14. Koch, G.H., et al., *Corrosion cost and preventive strategies in the United States*. 2002.
15. Jensen, D.L., et al., *The solubility of rhodochrosite (MnCO 3) and siderite (FeCO 3) in anaerobic aquatic environments.* Applied geochemistry, 2002. **17**(4): p. 503-511.
16. Hunter, M.L., et al., *The agenda-setting power of stakeholder media.* California management review, 2011.
17. Barker, R.J., *Erosion-corrosion of carbon steel pipework on an offshore oil and gas facility*. 2012: University of Leeds.
18. Ropital, F. and Y. Chauvin, *Corrosion and degradation of metallic materials: understanding of the phenomena and applications in petroleum and process industries*. 2010: Editions technip.

19. Patel, K.K., M. Mehta, and T.R. Singh, *Application of homotopy analysis method in one-dimensional instability phenomenon arising in inclined porous media.* American Journal of Applied Mathematics and Statistics, 2014. **2**(3): p. 106-114.
20. Stansbury, E.E. and R.A. Buchanan, *Fundamentals of electrochemical corrosion*. 2000: ASM international.
21. Van Ooyen, A., et al., *Iridium oxide deposited by pulsed dc-sputtering for stimulation electrodes.* Journal of Micromechanics and Microengineering, 2009. **19**(7): p. 074009.
22. Schweitzer, P.A., *Encyclopedia of corrosion technology*. Vol. 20. 2004: CRC Press.
23. Nešić, S., *Key issues related to modelling of internal corrosion of oil and gas pipelines – A review.* Corrosion Science, 2007. **49**(12): p. 4308-4338.
24. Nesic, S., et al., *Mechanistic Modeling for CO2 Corrosion with Protective Iron Carbonate Films*. NACE International.
25. Zheng, Y., et al., *Electrochemical Model of Mild Steel Corrosion in a Mixed H2S/CO2 Aqueous Environment.* CORROSION/2014, paper, 2014(3907).
26. Nesic, S., J. Postlethwaite, and S. Olsen, *An electrochemical model for prediction of corrosion of mild steel in aqueous carbon dioxide solutions.* Corrosion, 1996. **52**(4): p. 280-294.
27. Zheng, Y., et al., *Advancement in Predictive Modeling of Mild Steel Corrosion in CO2-and H2S-Containing Environments.* Corrosion, 2016. **72**(5): p. 679-691.
28. Eisenberg, M., C. Tobias, and C. Wilke, *Ionic mass transfer and concentration polarization at rotating electrodes.* Journal of the Electrochemical Society, 1954. **101**(6): p. 306-320.
29. Berger, F. and K.-F.-L. Hau, *Mass transfer in turbulent pipe flow measured by the electrochemical method.* International Journal of Heat and Mass Transfer, 1977. **20**(11): p. 1185-1194.
30. Poulson, B., *Mass transfer from rough surfaces.* Corrosion Science, 1990. **30**(6): p. 743-746.
31. Makanjuola, P. and D. Gabe, *A study of roughness and mass transfer enhancement for the rotating cylinder electrode.* Surface Technology, 1985. **24**(1): p. 29-44.
32. Han, J., et al., *Mesh-capped probe design for direct pH measurements at an actively corroding metal surface.* Journal of applied electrochemistry, 2010. **40**(3): p. 683-690.
33. Nordsveen, M., et al., *A mechanistic model for carbon dioxide corrosion of mild steel in the presence of protective iron carbonate films-Part 1: Theory and verification.* Corrosion, 2003. **59**(5): p. 443-456.
34. Shrier, L., R. Jarman, and G. Burstein, *Corrosion—Metal/Environment Reactions, Jordan Hill.* Oxford: Butterworth-Heinemann, 1995. **2**: p. 3-2.

35. Trethewey, K.R. and J. Chamberlain, *Corrosion for science and engineering.* 1995.

36. Ahmad, Z., *Principles of corrosion engineering and corrosion control*. 2006: Butterworth-Heinemann.

37. Brondel, D., et al., *Corrosion in the oil industry.* Oilfield review, 1994. **6**(2): p. 4-18.

38. Bradford, S., *Corrosion control. 2.* 2001.

39. Atkins, P. and J. De Paula, *Elements of physical chemistry*. 2013: Oxford University Press, USA.

40. Levinovitz, A.W. and N. Ringertz, *The Nobel Prize: the first 100 years*. 2001: World Scientific.

41. Tait, W.S., *An introduction to electrochemical corrosion testing for practicing engineers and scientists*. 1994: PairODocs Publications.

42. Stojek, Z., *The Electrical Double Layer and Its Structure*, in *Electroanalytical Methods: Guide to Experiments and Applications*, F. Scholz, Editor. 2002, Springer Berlin Heidelberg: Berlin, Heidelberg. p. 3-8.

43. Barnartt, S., *Primary current distribution around capillary tips used in the measurement of electrolytic polarization.* Journal of the Electrochemical Society, 1952. **99**(12): p. 549-553.

44. Han, J., et al., *Roles of passivation and galvanic effects in localized CO2 corrosion of mild steel.* CORROSION/2008, paper, 2008. **8332**.

45. Bockris, J.O.M. and A.K. Reddy, *Modern electrochemistry 2B: electrodics in chemistry, engineering, biology and environmental science*. Vol. 2. 1998: Springer Science & Business Media.

46. Perez, N., *Electrochemistry and Corrosion Science. 2004*. Kluwer Academic.

47. Celestine, O.N. and E. Okechukwu, *Review of Corrosion Kinetics and Thermodynamics of CO2 and H2S Corrosion Effects and Associated Prediction/Evaluation on Oil and Gas Pipeline System.* International Journal of Scientific & Technology Research, 2012. **1**(4): p. 156-162.

48. Scully, J.R., *Polarization resistance method for determination of instantaneous corrosion rates.* Corrosion, 2000. **56**(2): p. 199-218.

49. G102-89, A., *Standard Practice for Calculation of Corrosion Rates and Related Information from Electrochemical Measurements.* Reapproved 1999, 1999.

50. Taleb, W., *Nanotechnology for corrosion control Silsesquioxane based nanofillers for iron carbonate film enhancement*. 2016, University of Leeds.

51. Papavinasam, S., *Corrosion control in the oil and gas industry*. 2013: Elsevier.

52. 15156-2, N.M.I., *Petroleum and Natural Gas Industries—Materials for Use in H2S-Containing Environments in Oil and Gas Production—Part 2:*

Cracking-Resistant Carbon and Low Alloy Steels, and the Use of Cast Irons. 2003.

53. Nesic, S., et al., *Advancement in Predictive Modeling of Mild Steel Corrosion in Co2 and H2S Containing Environments*. NACE International.
54. Dugstad, A., *Fundamental Aspects of CO2 Metal Loss Corrosion - Part 1: Mechanism*. NACE International.
55. Nesic, S., et al. *Mechanistic Modeling for CO2 Corrosion with Protective Iron Carbonate Films*. in *CORROSION 2001*. 2001. NACE International.
56. Nesic, S., *Effects of multiphase flow on internal CO2 corrosion of mild steel pipelines.* Energy & Fuels, 2012. **26**(7): p. 4098-4111.
57. De Waard, C. and D. Milliams, *Carbonic acid corrosion of steel.* Corrosion, 1975. **31**(5): p. 177-181.
58. Remita, E., et al., *Hydrogen evolution in aqueous solutions containing dissolved CO 2: quantitative contribution of the buffering effect.* Corrosion Science, 2008. **50**(5): p. 1433-1440.
59. Tran, T., B. Brown, and S. Nesic, *Corrosion of Mild Steel in an Aqueous CO2 Environment – Basic Electrochemical Mechanisms Revisited*. NACE International.
60. George, K. and S. Nešic, *Investigation of carbon dioxide corrosion of mild steel in the presence of acetic acid—part 1: basic mechanisms.* Corrosion, 2007. **63**(2): p. 178-186.
61. Uhlig, H.H., *Uhlig's corrosion handbook*. Vol. 51. 2011: John Wiley & Sons.
62. Videm, K. and A. Dugstad, *Corrosion of carbon steel in an aqueous carbon dioxide environment Part 1.* Mater. Performance;(United States), 1989. **28**(3).
63. Bockris, J.M., D. Drazic, and A. Despic, *The electrode kinetics of the deposition and dissolution of iron.* Electrochimica Acta, 1961. **4**(2): p. 325-361.
64. Schmitt, G., *Investigations Into the Corrosion Mechanism of Mild Steel in Oxygen Free Carbon Dioxide Solutions. II. Kinetics of Iron Dissolution.* Werkst. Korros., 1978. **29**(2): p. 98-100.
65. Hurlen, T., et al., *Effects of carbon dioxide on reactions at iron electrodes in aqueous salt solutions.* Journal of electroanalytical chemistry and interfacial electrochemistry, 1984. **180**(1-2): p. 511-526.
66. Nesic, S., et al., *Electrochemical properties of iron dissolution in the presence of CO2 Corrosion'96 NACE.* USA, paper, 1996. **3**.
67. Nesic, S., *Carbon Dioxide Corrosion of Mild Steel*, in *Uhlig's Corrosion Handbook*. 2011.
68. Schmitt, G., *Fundamental Aspects of CO2 Metal Loss Corrosion. Part II: Influence of Different Parameters on CO2 Corrosion Mechanism*. NACE International.

69. Fang, H., et al. *General CO2 corrosion in high salinity brines*. in *CORROSION 2006*. 2006. NACE International.

70. Nešic, S., et al., *A mechanistic model for carbon dioxide corrosion of mild steel in the presence of protective iron carbonate films-Part 2: A numerical experiment.* Corrosion, 2003. **59**(6): p. 489-497.

71. De Waard, C., U. Lotz, and D. Milliams, *Predictive model for CO2 corrosion engineering in wet natural gas pipelines.* Corrosion, 1991. **47**(12): p. 976-985.

72. Tomson, M. and M. Johnson. *How ferrous carbonate kinetics impacts oilfield corrosion*. in *SPE International Symposium on Oilfield Chemistry*. 1991. Society of Petroleum Engineers.

73. Snesic, S., S. Wang, and K. George, *High Pressure CO2 Corrosion Electrochemistry and the Effect of Acetic Acid*. NACE International.

74. Suhor, M.F., et al., *Corrosion Of Mild Steel In High CO2 Environment: Effect Of The Feco3 Layer*. NACE International.

75. Arumugam, S., N. Tajallipour, and P.J. Teevens. *Modeling the Influence of Iron Carbonate Scale Morphology in Sweet Corrosion Prediction*. in *CORROSION 2014*. 2014. NACE International.

76. Gao, M., X. Pang, and K. Gao, *The growth mechanism of CO2 corrosion product films.* Corrosion Science, 2011. **53**(2): p. 557-568.

77. Sun, W. and S. Nesic, *Basics revisited: kinetics of iron carbonate scale precipitation in CO2 corrosion.* Corrosion/2006, paper, 2006(06365).

78. Sun, W., et al., *A study of protective iron carbonate scale formation in CO2 corrosion.* AIChE, Austin, Texas, 2004.

79. Tanupabrungsun, T., *Thermodynamics and kinetics of carbon dioxide corrosion of mild steel at elevated temperatures*. 2013: Ohio University.

80. Ning, J., B. Brown, and S. Nesic. *Verification of Pourbaix Diagrams for the H2S-H2O-Fe System at 25 oC*. in *ICMT Ohio University Advisory Board Meeting,(March, 2012)*. 2012.

81. Nešic, S., G.T. Solvi, and J. Enerhaug, *Comparison of the rotating cylinder and pipe flow tests for flow-sensitive carbon dioxide corrosion.* Corrosion, 1995. **51**(10): p. 773-787.

82. Davies, J.T., *Turbulence Phenomena: An Introduction to the Eddy Tranfer of Momentum Mass and Heat Particulary*. 1972: Academic Press.

83. Ukpai, J.I., *Erosion-corrosion characterisation for pipeline materials using combined acoustic emission and electrochemical monitoring*. 2014, University of Leeds.

84. Winston, R., *Uhlig's corrosion handbook.* 2000.

85. Ciaraldi, S.W., *Why Asset Integrity Implementation Often Fails.* Journal of Petroleum Technology, 2012. **64**(07): p. 64-65.

86. Kermani, B. and L.M. Smith, *A Working Party Report on CO2 Corrosion Control in Oil and Gas Production: Design Considerations*. Vol. 688. 1997: Maney Pub.

87. Crolet, J.L., N. Thevenot, and S. Nesic, *Role of conductive corrosion products on the protectiveness of corrosion layers*. 1996, NACE International, Houston, TX (United States).

88. Burkle, D.P., *Understanding the Formation of Protective FeCO3 on to Carbon Steel Pipelines during CO2 Corrosion*. 2017, University of Leeds.

89. Schmitt, G., et al. *A probabilistic model for flow induced localized corrosion*. in *CORROSION 2000*. 2000. NACE International.

90. Structx.com. *Galvanic Series (electrochemical series). [online]* (2018). Available from: http://structx.com/Material_Properties_001.html.

91. Nesić, S., J. Postlethwaite, and M. Vrhovac, *CO2 corrosion of carbon steel-from mechanistic to empirical modelling*. 1997.

92. Olsen, S., *CO2 Corrosion Prediction by Use of the NORSOK M-506 Model - Guidelines and Limitations*. NACE International.

93. Nyborg, R., *CO2 CORROSION MODELS FOR OIL AND GAS PRODUCTION SYSTEMS.* NACE international, 2010. **Houston,Texas**(paper No.10371).

94. Mishra, B., et al., *Development of a predictive model for activation-controlled corrosion of steel in solutions containing carbon dioxide.* Corrosion, 1997. **53**(11): p. 852-859.

95. De Waard, C., U. Lotz, and A. Dugstad. *Influence of Liquid Flow Velocity on CO~ 2 Corrosion: A Semi-Empirical Model*. in *CORROSION-NATIONAL ASSOCIATION OF CORROSION ENGINEERS ANNUAL CONFERENCE-*. 1995. NACE.

96. Lotz, U., *Velocity effects in flow induced corrosion.* 1993.

97. Ikeda, A., M. Ueda, and S. Muka, *CO2 behaviour of carbon and Cr steels in Hausler RH Giddard HP.* Corrosion, 1983. **39**: p. 131-137.

98. Gray, L.G., et al., *Mechanism of carbon steel corrosion in brines containing dissolved carbon dioxide at pH 4.* Corrosion/89, paper, 1989(464).

99. Gray, L.G., et al., *Effect of pH and temperature on the mechanism of carbon steel corrosion by aqueous carbon dioxide.* Corrosion/90, paper, 1990. **40**.

100. Dayalan, E., et al., *CO2 Corrosion Prediction in Pipe Flow Under FeCO3 Scale-Forming Conditions*. NACE International.

101. Kahyarian, A., M. Singer, and S. Nesic, *Modeling of uniform CO 2 corrosion of mild steel in gas transportation systems: A review.* Journal of Natural Gas Science and Engineering, 2016. **29**: p. 530-549.

102. Linter, B. and G. Burstein, *Reactions of pipeline steels in carbon dioxide solutions.* Corrosion science, 1999. **41**(1): p. 117-139.

103. Asma, R., P. Yuli, and C. Mokhtar, *Study on the effect of surface finish on corrosion of carbon steel in CO2 environment.* Journal of Applied Sciences, 2011. **11**(11): p. 2053-2057.

104. Davis, J.R., *Corrosion: Understanding the basics*. 2000: ASM International.

105. Ismail, A., *Seawater as a hydraulic fluid; corrosion mechanisms and rates of engineering materials*. 2014, University of Leeds.

106. Rahmani, M. and J.E. Strutt, *Hydrodynamic Modeling of Corrosion of Carbon Steels and Cast Irons in Sulfuric Acid*. 1992: Materials Technology Institute of the Chemical Process Industries.

107. Chen, T.-Y., A. Moccari, and D.D. Macdonald, *Development of controlled hydrodynamic techniques for corrosion testing.* Corrosion, 1992. **48**(3): p. 239-255.

108. Sydberger, T. and U. Lotz, *Relation between mass transfer and corrosion in a turbulent pipe flow.* Journal of the Electrochemical Society, 1982. **129**(2): p. 276-283.

109. Goldstein, R. and H. Cho, *A review of mass transfer measurements using naphthalene sublimation.* Experimental Thermal and Fluid Science, 1995. **10**(4): p. 416-434.

110. Wilk, J., *A review of measurements of the mass transfer in minichannels using the limiting current technique.* Experimental Thermal and Fluid Science, 2014. **57**: p. 242-249.

111. Mendes, P.S., *The naphthalene sublimation technique.* Experimental Thermal and Fluid Science, 1991. **4**(5): p. 510-523.

112. Gabe, D. and P. Makanjuola, *Enhanced mass transfer using roughened rotating cylinder electrodes in turbulent flow.* Journal of Applied Electrochemistry, 1987. **17**(2): p. 370-384.

113. Mahato, B.K. and L.W. Shemilt, *Effect of surface roughness on mass transfer.* Chemical Engineering Science, 1968. **23**(2): p. 183-185.

114. Gomaa, H., A.M. Al Taweel, and J. Landau, *Mass transfer enhancement at vibrating electrodes.* Chemical Engineering Journal, 2004. **97**(2–3): p. 141-149.

115. Nesic, S., et al., *Superposition of Diffusion and Chemical Reaction Controlled Limiting Currents-Application to CO2 Corrosion.* Journal of Corrosion Science and engineering, 1995. **1**(3).

116. Eisenberg, M., C. Tobias, and C. Wilke. *Mass transfer at rotating cylinders*. in *Chem. Eng. Prog. Symp. Ser*. 1955.

117. Silverman, D., *The rotating cylinder electrode for examining velocity-sensitive corrosion-a review.* Corrosion, 2004. **60**(11): p. 1003-1023.

118. Morrison, B., et al., *Kinetic studies using a rotating cylinder electrode: Part I. Electron transfer rates in ferrous/ferric sulfate on platinum.* Journal of electroanalytical chemistry and interfacial electrochemistry, 1986. **215**(1-2): p. 151-160.

119. Robinson, D. and D. Gabe, *High Speed Electrodeposition of Copper from Conventional Sulphate Electrolytes.* Transactions of the IMF, 1970. **48**(1): p. 35-42.

120. Theodorsen, T. and A. Regier, *Experiments on drag of revolving disks, cylinders, and streamline rods at high speeds.* 1944.

121. Silverman, D., *Simplified equation for simulating velocity-sensitive corrosion in the rotating cylinder electrode at higher Reynolds numbers.* Corrosion, 2003. **59**(3): p. 207-211.

122. Makrides, A. and N. Hackerman, *Dissolution of Metals in Aqueous Acid Solutions II. Depolarized Dissolution of Mild Steel.* Journal of The Electrochemical Society, 1958. **105**(3): p. 156-162.

123. Pots, B., *Mechanistic models for the prediction of CO corrosion rates under multi-phase flow conditions*. 1995, NACE International, Houston, TX (United States).

124. Vetter, K.-J., S. Bruckenstein, and B. Howard, *Electrochemical Kinetics: Theoretical Aspects: Sections 1, 2 and 3 of Electrochemical Kinetics: Theoretical and Experimental Aspects*. 1967: Academic Press.

125. Jin, H., et al., *Experimental study of oxygen mass transfer coefficient in bubble column with high temperature and high pressure.* Chemical engineering & technology, 2004. **27**(12): p. 1267-1272.

126. Sedahmed, G. and L. Shemilt, *Forced convection mass transfer at rough surfaces in annuli.* Letters in Heat and Mass Transfer, 1976. **3**(6): p. 499-511.

127. Hu, X. and A. Neville, *CO2 erosion–corrosion of pipeline steel (API X65) in oil and gas conditions—A systematic approach.* Wear, 2009. **267**(11): p. 2027-2032.

128. Tantirige, S. and O. Trass, *Mass transfer at geometrically dissimilar rough surfaces.* The Canadian Journal of Chemical Engineering, 1984. **62**(4): p. 490-496.

129. Postlethwaite, J. and U. Lotz, *Mass transfer at erosion‐corrosion roughened surfaces.* The Canadian Journal of Chemical Engineering, 1988. **66**(1): p. 75-78.

130. Cornet, I., W. Lewis, and R. Kappesser, *EFFECT OF SURFACE ROUGHNESS ON MASS TRANSFER TO A ROTATING DISC.* TRANS INST CHEM ENG, 1969. **47**(7): p. 222-226.

131. King, C.V. and P.L. Howard, *Heat Transfer and Diffusion Rates at Solid-Liquid Boundaries.* Industrial & Engineering Chemistry, 1937. **29**(1): p. 75-78.

132. Ibl, N., *Advances in electrochemistry and electrochemical engineering: edited by P. Delahay and CW Tobias, vol. 1 (edited by P. Delahay) 326 pages, $12, Interscience, New York 1961*. 1962, Pergamon.

133. Brenan, W.C. and O. Trass, *52nd Nat. Meeting of A. I. Ch. E. (1964).*

134. Gabe, D. and F. Walsh, *The rotating cylinder electrode: a review of development.* Journal of Applied Electrochemistry, 1983. **13**(1): p. 3-21.

135. Levich, V.G., *Physicochemical hydrodynamics*. 1962: Prentice Hall.

136. Mahato, B., S. Voora, and L. Shemilt, *Steel pipe corrosion under flowconditions—I. An isothermal correlation for a mass transfer model.* Corrosion Science, 1968. **8**(3): p. 173IN7191IN9191-180IN8190IN15193.

137. Sedahmed, G., M.N. Soliman, and N. El-Kholy, *Effect of surface roughness on the rate of mass transfer to a pipe wall in the mass transfer entry region.* The Canadian Journal of Chemical Engineering, 1981. **59**(6): p. 693-696.

138. Kappesser, R., I. Cornet, and R. Greif, *Mass transfer to a rough rotating cylinder.* Journal of the Electrochemical Society, 1971. **118**(12): p. 1957-1959.

139. Gabe, D.R., et al., *The rotating cylinder electrode: its continued development and application.* Journal of Applied Electrochemistry, 1998. **28**(8): p. 759-780.

140. Holland, F.S., *Method of producing metal powder*. 1977, Google Patents.

141. Sedahmed, G., et al., *Mass transfer at rotating finned cylinders.* Journal of Applied Electrochemistry, 1979. **9**(5): p. 563-566.

142. Postlethwaite, J., *Erosion-corrosion in single and multiphase flow.* Uhlig's Corrosion Handbook: p. 249.

143. Bates, R.G., *Determination of pH: theory and practice.* Determination of pH: theory and practice., 1964.

144. Safi, R., R.K. Agarwal, and S. Banerjee, *Numerical simulation and optimization of CO 2 utilization for enhanced oil recovery from depleted reservoirs.* Chemical Engineering Science, 2016. **144**: p. 30-38.

145. Steegstra, P. and E. Ahlberg, *In situ pH measurements with hydrous iridium oxide in a rotating ring disc configuration.* Journal of Electroanalytical Chemistry, 2012. **685**: p. 1-7.

146. Yoshinobu, T., et al., *Application of chemical imaging sensor to electro generated pH distribution.* Japanese journal of applied physics, 1998. **37**(3B): p. L353.

147. Hessami, S. and C.W. Tobias, *In‐situ measurement of interfacial pH using a rotating ring‐disk electrode.* AIChE journal, 1993. **39**(1): p. 149-162.

148. Einerhand, R., W. Visscher, and E. Barendrecht, *pH measurement in strong KOH solutions with a bismuth electrode.* Electrochimica acta, 1989. **34**(3): p. 345-353.

149. Grubb, W. and L. King, *Palladium-palladium oxide pH electrodes.* Analytical Chemistry, 1980. **52**(2): p. 270-273.

150. Fog, A. and R.P. Buck, *Electronic semiconducting oxides as pH sensors.* Sensors and Actuators, 1984. **5**(2): p. 137-146.

151. Burke, L.D., J.K. Mulcahy, and D.P. Whelan, *Preparation of an oxidized iridium electrode and the variation of its potential with pH.* Journal of electroanalytical chemistry and interfacial electrochemistry, 1984. **163**(1-2): p. 117-128.

152. Yao, S., M. Wang, and M. Madou, *A pH electrode based on melt-oxidized iridium oxide.* Journal of the electrochemical society, 2001. **148**(4): p. H29-H36.

153. Da Silva, G., et al., *Development of low-cost metal oxide pH electrodes based on the polymeric precursor method.* analytica chimica acta, 2008. **616**(1): p. 36-41.

154. Song, I., K. Fink, and J. Payer, *Metal oxide/metal pH sensor: Effect of anions on pH measurements.* Corrosion, 1998. **54**(1): p. 13-19.

155. Kreider, K., *Iridium oxide thin-film stability in high-temperature corrosive solutions.* Sensors and Actuators B: Chemical, 1991. **5**(1-4): p. 165-169.

156. Marzouk, S.A., *Improved electrodeposited iridium oxide pH sensor fabricated on etched titanium substrates.* Analytical chemistry, 2003. **75**(6): p. 1258-1266.

157. Martinez, C.C.M., R.E. Madrid, and C.J. Felice, *A pH sensor based on a stainless steel electrode electrodeposited with iridium oxide.* IEEE Transactions on Education, 2009. **52**(1): p. 133-136.

158. Deslouis, C., et al., *Interfacial pH measurement during the reduction of dissolved oxygen in a submerged impinging jet cell.* Journal of applied electrochemistry, 1997. **27**(4): p. 482-492.

159. Tlili, M., et al., *Influence of the interfacial pH on electrochemical CaCO3 precipitation.* Journal of The Electrochemical Society, 2003. **150**(11): p. C765-C771.

160. Nguyen, C.M., et al., *Sol-gel iridium oxide-based pH sensor array on flexible polyimide substrate.* IEEE Sensors Journal, 2013. **13**(10): p. 3857-3864.

161. Hashimoto, T., et al., *pH Sensors Using 3d-Block Metal Oxide-Coated Stainless Steel Electrodes.* Electrochimica Acta, 2016. **220**: p. 699-704.

162. Hitchman, M.L. and S. Ramanathan, *Evaluation of iridium oxide electrodes formed by potential cycling as pH probes.* Analyst, 1988. **113**(1): p. 35-39.

163. Carroll, S. and R.P. Baldwin, *Self-calibrating microfabricated iridium oxide pH electrode array for remote monitoring.* Analytical chemistry, 2010. **82**(3): p. 878-885.

164. Yamanaka, K., *Anodically electrodeposited iridium oxide films (AEIROF) from alkaline solutions for electrochromic display devices.* Japanese journal of applied physics, 1989. **28**(4R): p. 632.

165. Kakooei, S., M.C. Ismail, and B.A. Wahjoedi, *Electrochemical study of iridium oxide coating on stainless steel substrate.* Int. J. Electrochem. Sci, 2013. **8**(3).

166. Marzouk, S.A., et al., *Measurement of extracellular pH, K+, and lactate in ischemic heart.* Analytical biochemistry, 2002. **308**(1): p. 52-60.

167. O’Hare, D., K.H. Parker, and C.P. Winlove, *Metal–metal oxide pH sensors for physiological application.* Medical Engineering and Physics, 2006. **28**(10): p. 982-988.

168. Zhu, Z., et al., *A fabrication of iridium oxide film pH micro-sensor on Pt ultramicroelectrode and its application on in-situ pH distribution of 316L stainless steel corrosion at open circuit potential.* Sensors and Actuators B: Chemical, 2017.

169. Lu, Y., et al., *Anodically electrodeposited iridium oxide films microelectrodes for neural microstimulation and recording.* Sensors and Actuators B: Chemical, 2009. **137**(1): p. 334-339.

170. Pikulski, M. and W. Gorski, *Iridium-based electrocatalytic systems for the determination of insulin.* Analytical chemistry, 2000. **72**(13): p. 2696-2702.

171. Terashima, C., et al., *Electrodeposition of hydrous iridium oxide on conductive diamond electrodes for catalytic sensor applications.* Journal of Electroanalytical Chemistry, 2003. **544**: p. 65-74.

172. Kissinger, P.T. and W.R. Heineman, *Cyclic voltammetry.* Journal of Chemical Education, 1983. **60**(9): p. 702.

173. Kakooei, S., M.C. Ismaila, and B. Ari-Wahjoedia. *Electrodeposition of Iridium Oxide by Cyclic Voltammetry: Application of Response Surface Methodology*. in *MATEC Web of Conferences*. 2014. EDP Sciences.

174. Hilliard, E.T., *Fabrication and Testing of a Micro-scalable pH Sensor for Implanted Biomedical Use*. 2011, University of Pittsburgh.

175. Phmeters.com, *http://www.phmeters.com/docs/pH_Electrochemistry_White_Paper.pdf*. 2010.

176. Kim, Y.-J., et al., *A novel pH microsensor with a built-in reference electrode.* 2003.

177. Khalil, M., et al., *Electrodeposition of Iridium Oxide Nanoparticles for pH Sensing Electrodes.* Journal of The Electrochemical Society, 2016. **163**(9): p. B485-B490.

178. da Silva, M.M., et al., *Near-surface solution pH measurements during the pitting corrosion of AISI 1020 steel using a ring-shaped sensor.* Journal of Electroanalytical Chemistry, 2016. **780**: p. 379-385.

179. Fogg, G. and J. Morse. *Development of a new solvent-free flow efficiency coating for natural gas pipelines*. in *Rio Pipeline 2005 Conference and Exposition, IBP1233*. 2005.

180. Evgeny, B., T. Hughes, and D. Eskin, *Effect of surface roughness on corrosion behaviour of low carbon steel in inhibited 4 M hydrochloric acid under laminar and turbulent flow conditions.* Corrosion Science, 2016. **103**: p. 196-205.

181. Stern, M., *The electrochemical behavior, including hydrogen overvoltage, of iron in acid environments.* Journal of the electrochemical society, 1955. **102**(11): p. 609-616.

182. Busse, A., M. Lützner, and N.D. Sandham, *Direct numerical simulation of turbulent flow over a rough surface based on a surface scan.* Computers & Fluids, 2015. **116**: p. 129-147.

183. Reiss, L.P. and T.J. Hanratty, *An experimental study of the unsteady nature of the viscous sublayer.* AIChE Journal, 1963. **9**(2): p. 154-160.

184. Dawson, D.A. and O. Trass, *Mass transfer at rough surfaces.* International Journal of Heat and Mass Transfer, 1972. **15**(7): p. 1317-1336.

185. Nesic, S., J. Postlethwaite, and D. Bergstrom, *Calculation of wall-mass transfer rates in separated aqueous flow using a low Reynolds number κ-ε model.* International journal of heat and mass transfer, 1992. **35**(8): p. 1977-1985.

186. Nešic, S. and K.-L. Lee, *A mechanistic model for carbon dioxide corrosion of mild steel in the presence of protective iron carbonate films—part 3: film growth model.* Corrosion, 2003. **59**(7): p. 616-628.

187. Nesic, S., M. Nordsveen, and A. Stangel, *A Mechanistic Model for C02 Corrosion with Protective Iron Carbonate Films.* 2001.

188. Pots, B.F.M., et al., *Improvements on de Waard-Milliams Corrosion Prediction and Applications to Corrosion Management*. NACE International.

189. Sundaram, M., et al., *Deterministic modeling of corrosion in downhole environments*. 1996, NACE International, Houston, TX (United States).

190. Han, J., J.W. Carey, and J. Zhang, *A coupled electrochemical–geochemical model of corrosion for mild steel in high-pressure CO 2–saline environments.* International Journal of Greenhouse Gas Control, 2011. **5**(4): p. 777-787.

191. Oddo, J.E. and M.B. Tomson, *Simplified calculation of CaCO3 saturation at high temperatures and pressures in brine solutions.* Journal of Petroleum Technology, 1982. **34**(07): p. 1,583-1,590.

192. Kharaka, Y.K., et al., *SOLMINEQ. 88: A computer program for geochemical modeling of water-rock interactions.* US Geological Survey Water-Resources Investigations Report, 1988. **88**: p. 4227.

193. Delahay, P., *Implications of the Kinetics of Ionic Dissociation with Regard to Some Electrochemical Processes—Application to Polarography.* Journal of the American Chemical Society, 1952. **74**(14): p. 3497-3500.

194. Palmer, D.A. and R. Van Eldik, *The chemistry of metal carbonato and carbon dioxide complexes.* Chemical Reviews, 1983. **83**(6): p. 651-731.

195. BRAMFORD, B. and C. TIPPER, *Comprehensive Chemical Kinetics, vol. 6*. 1972, Elsevier, Amsterdam.

196. Davies, J.T., *Turbulence phenomena: an introduction to the eddy transfer of momentum, mass, and heat, particularly at interfaces*. 2012: Elsevier.

197. Wang, S. and S. Nesic, *On coupling CO2 corrosion and multiphase flow models.* 2003.

198. Perry, R. and D. Green, *Handbook of chemical engineering.* pg, 1984: p. 17-6.

199. Kvarekvål, J., *A kinetic model for calculating concentration profiles and fluxes of CO -related species across the Nernst diffusion layer*. 1997, NACE International, Houston, TX (United States).

200. Fardisi, S., N. Tajallipour, and P.J. Teevens, *Predicting General Corrosion Rates In Sour Environments With the Growth of a Protective Iron Sulphide Film*. NACE International.

201. Kahyarian, A., B. Brown, and S. Nesic, *Electrochemistry of CO2 corrosion of mild steel: Effect of CO2 on iron dissolution reaction.* Corrosion Science, 2017. **129**: p. 146-151.

202. Zheng, Y., *Electrochemical mechanism and model of H2S corrosion of carbon steel*. 2015, Ohio University.

203. Song, F.M., *A comprehensive model for predicting CO2 corrosion rate in oil and gas production and transportation systems.* Electrochimica Acta, 2010. **55**(3): p. 689-700.

204. Meyssami, B., M.O. Balaban, and A.A. Teixeira, *Prediction of pH in model systems pressurized with carbon dioxide.* Biotechnology progress, 1992. **8**(2): p. 149-154.

205. Tanupabrungsun, T., et al. *Construction and verification of pourbaix diagrams for CO2 corrosion of mild steel valid up to 250 C*. in *CORROSION 2012*. 2012. NACE International.

206. Nesˇic, W.S.a.S., *Kinetics of Corrosion Layer Formation: Part 1—Iron Carbonate Layers in Carbon Dioxide Corrosion.* NACE international, 2008.

207. Sun, W. and S. Nesic, *Basics Revisited: Kinetics of Iron Carbonate Scale Precipitation in CO2 Corrosion*. NACE International.

208. Lee, K.-L.J., *A Mechanistic Moceling of CO 2 Corrosion of Mild Steel in the Presence of H 2 S*. 2004, Ohio University.

209. Walker, R. and N.S. Holt, *Determination of the Nernst diffusion layer thickness in the Hydroson agitation tank.* Surface technology, 1984. **22**(2): p. 165-174.

210. Barmatov, E., T. Hughes, and M. Nagl, *Effect of Surface Roughness and Flow on Corrosion Inhibition of Coiled Tubing Steel Under Matrix Acidizing Conditions*. NACE International.

Appendix A Velocity and Reynolds Number Calculations for an RCE

$$\mathbf{U_{RCE}} = \frac{\boldsymbol{\omega} * \boldsymbol{d_{RCE}} * \boldsymbol{\pi}}{\mathbf{60}}$$

where: U_{RCE} the peripheral RCE velocity (m/s) and ω is the rotation speed (rpm), d_{RCE} is the diameter of RCE samples (m).

$$\mathbf{Re_{RCE}} = \frac{\boldsymbol{\rho}\ \mathbf{U_{RCE}}\ \mathbf{d_{RCE}}}{\boldsymbol{\mu}}$$

For the case of RCE, the flow pattern is considered to be turbulent when Re_{RCE}>200.

ω (rpm)	U_{RCE} (m/s)	Re_{RCE}
1000	0.628	8460.9
1500	0.942	12691.4
3000	1.884	25382.7
4000	2.827	33843.8

Table A Peripheral and Reynolds number calculations for an RCE.

Appendix B Surface Roughness Profilometry Results

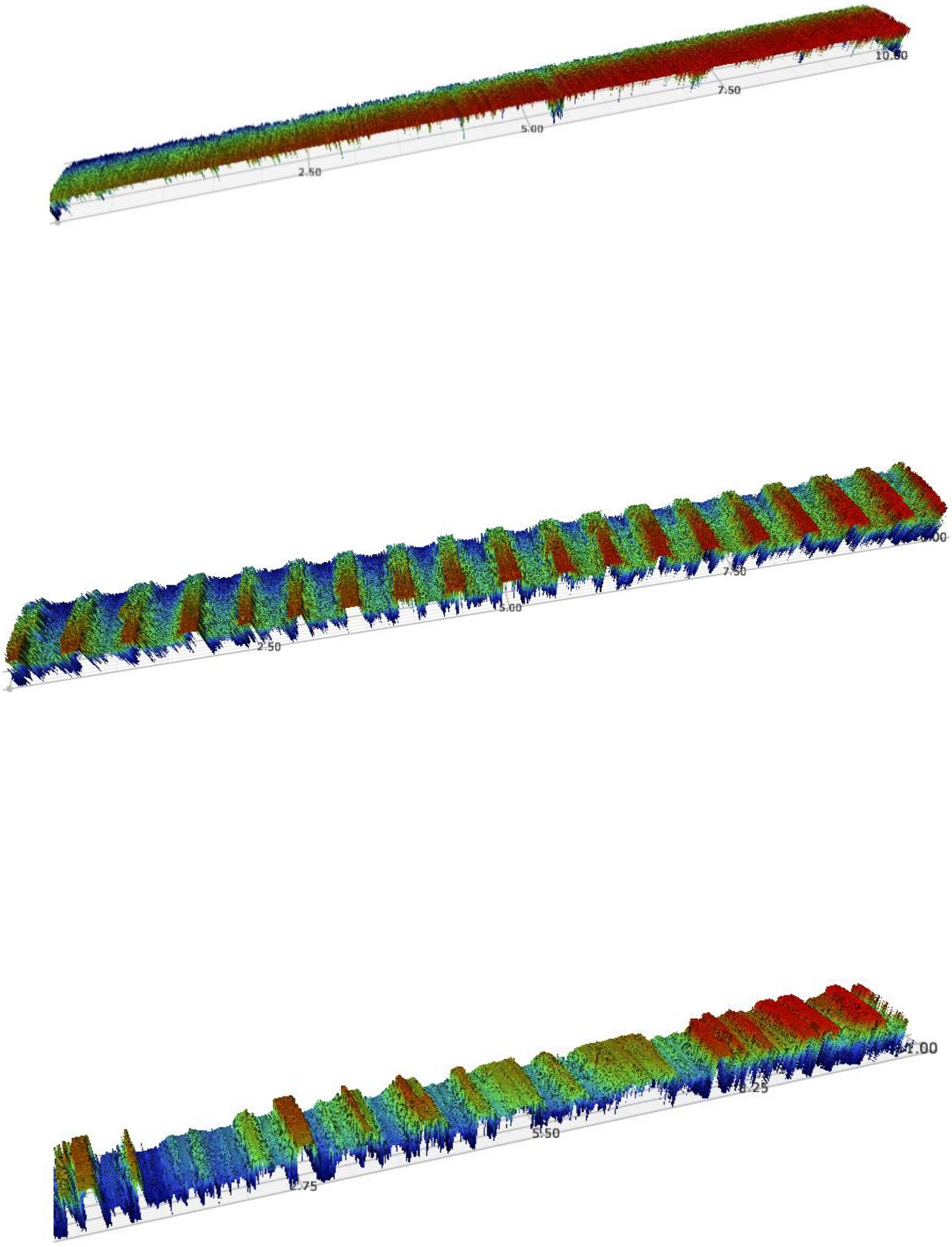

Figure A 3D profile of RCE samples with roughness (0.5, 20 and 34) µm considered in this study.

Appendix C Homogeneous Chemical Reactions

Ionic Strength, I

Ionic strength is the measure of concentration of ions in the solution, the dissociation and concentration of different salts affect on the properties of the electrolyte. The main equation to calculate the ionic strength is:

$$I = \frac{1}{2}\sum_{i=1}^{n} c_i \, z_i^2$$

Where c_i is the concentration of ion and z_i is the charge of the ion.

For 1% NaCl :

10g NaCl → $\boxed{\text{1 litre } H_2O}$

Molecular mass of NaCl = 58.44 g/mol

$$\frac{10\ g}{58.44\ \ g/mol} \times \frac{1}{1\ litter} = 0.1711\ \frac{mol}{litter}$$

$$I = \frac{1}{2}\ (\ 0.1711 * (1)^2\ + 0.1711 * (-1)^2) = 0.1711\ \frac{mol}{litter}$$

Appendix D Exact Solution for the Surface Potential

The fundamental governing equation for the current density in electrochemistry can be represented by $i = \pm i_0\ 10^{\pm\frac{E-E_{rev}}{b}}$. E in this equation denotes the potential at the surface of the metal which assumes a value such that all the electrons released in the anodic reaction are consumed in the cathodic reactions. An exact solution for the surface potential, E, can be presented as:

$$\sum i_c + \sum i_a = 0$$

so that

$$i_{H^+} + i_{H_2CO_3} +\ i_{H_2O} + i_{Fe^{2+}} = 0$$

which leads to

$$-i_{o,H}\ 10^{-\left(\frac{E-E_{rev,H}}{b_H}\right)} - i_{o,H_2CO_3}\ 10^{-\left(\frac{E-E_{rev,H_2CO_3}}{b_{H_2CO_3}}\right)} - i_{o,H_2O}\ 10^{-\left(\frac{E-E_{rev,H_2O}}{b_{H_2O}}\right)} +$$
$$i_{o,Fe}\ 10^{\left(\frac{E-E_{rev,Fe}}{b_{Fe}}\right)} = 0 \quad \text{(A1)}$$

Noting that the Tafel slope of all cathodic reactions are equal, let

$b_c=b_H=b_{H2CO3}=b_{H2O}$, $b_a=b_{Fe}$, $m=b_c/b_a$ and $p = 10^{\frac{E}{b_c}}$. Then, $10^{\frac{E}{b_a}} = 10^{\frac{E\times m}{b_c}} = p^m$.

Substituting $10^{\frac{E}{b_a}}$ and $10^{\frac{E}{b_c}}$ from the above into equation (A1) gives:

$$-i_{0,H}P^{-1}10^{\frac{E_{rev,H}}{b_c}} - i_{0,H_2CO_3}P^{-1}10^{\frac{E_{rev,H_2CO_3}}{b_c}} - i_{0,H_2O}P^{-1}10^{\frac{E_{rev,H_2O}}{b_c}}$$
$$+ i_{0,Fe}P^m 10^{\frac{-E_{rev,Fe}}{b_a}} = 0$$

so that:

$$i_{0,H}\ 10^{\frac{E_{rev,H}}{b_c}} + i_{0,H_2CO_3}\ 10^{\frac{E_{rev,H_2CO_3}}{b_c}} + i_{0,H_2O}\ 10^{\frac{E_{rev,H_2O}}{b_c}} = i_{0,Fe}P^{m+1}10^{\frac{-E_{rev,Fe}}{b_a}}$$

hence:

$$P = \left[\left(i_{0,H}\ 10^{\frac{E_{rev,H}}{b_c}} + i_{0,H_2CO_3}\ 10^{\frac{E_{rev,H_2CO_3}}{b_c}} + i_{0,H_2O}\ 10^{\frac{E_{rev,H_2O}}{b_c}}\right)\frac{10^{\frac{E_{rev,Fe}}{b_a}}}{i_{0,Fe}}\right]^{\frac{1}{m+1}}$$

From which $E=b_c \log(P)$.

Appendix E Sensitivity Analysis

Effect of the boundary layer (∆X) on the value of corrosion rate:

For the case of two-nod model, the effect of ∆X has been studied for the problem with 1 bar total pressure, 20°C, pH=4, 1wt.% NaCl and 0.01m pipe diameter.

∆X (μm)	**Corrosion rate (mm/year)**
1	1.582
10	1.581
100	1.580

From the above, it is quite clear that the effect of delta x is minor on the value of the corrosion rate.